NOISE BARRIERS

IN A COMPLEX URBAN ENVIRONMENT

KWOK MAN PUN

M. PHIL.

DEPARTMENT OF MECHANICAL ENGINEERING

THE HONG KONG POLYTECHNIC UNIVERSITY

MARCH, 2006

Certificate of Originality

I hereby declare that this thesis is my own work and that, to the best of my knowledge and belief, it reproduces no material previously published or written nor material which has been accepted for the award of any other degree or diploma, expect where due acknowledgement has been made in the text.

Kwok Man Pun

Abstract

With the rapid advancement of civilization and tremendous expansion of human population, transportation noise is one of the major environmental issues which have to be tackled. To reduce the impact from the noise pollution, various mitigation measures have been investigated and implemented. Roadside barriers are the most commonly mitigation measures adopted. By alternating the propagation of sound, the barriers manage to significantly attenuate the noise levels in the protected regions. Numerical studies on the shielding performance of the barriers have been conducted. However, there are relatively few studies taking the influence of tall buildings in urban areas into consideration to account for the efficiency of the barrier. In our study, an investigation of the acoustic performance of noise barriers in conditions commonly found in metropolitan areas is conducted.

Our study begins with the development of a measurement methodology for the acoustic impedance of a plane surface. In contrast to those standardized laboratory method, the methodology developed is in-situ in nature. The method is based on the classical spherical wave propagation theory and numerical minimization techniques. Actual quantity of impedance is obtained at the location of measurement. With the improved measurement techniques and minimization algorithm, the in-situ method developed is proved to be robust and successful.

Noise prediction model founded on the image source method for the evaluation of barriers in an urban environment is then developed. The first scenario examined consists

of a pair of parallel barriers standing aside a road which is aligned parallel to a building façade. Based on the image source method, a prediction model of the sound field of this configuration is developed. The flexibility of adopting acoustic absorptive surface is included in the model for more general applications. For the validation of the model, the predicted results are compared with the results from the boundary element method (BEM) and experimental measurement. These comparisons conclude good agreements and the accuracy of the image source model is proved.

With the success of the previous scenario, the image source model is further extended to another commonly encountered condition in urban environment. The situation taking into consideration consists of a pair of parallel barriers standing aside a road which is semi-enclosed by sky-rise buildings on both sides. Due to the additional façade surface, the multiple reflections of sound among the surfaces are much more complicated in which the complexity is almost double that of the previous case. Nevertheless, a study of the sound field in this spatial condition is processed and a complete hierarchy of the source images is outlined. In comparisons with the BEM and the laboratory measurements, the image source model demonstrates a fairly good validity. These two computationally efficient image source models successfully manage to provide a quantitative justification of the construction of roadside barriers in the planning stage.

Acknowledgements

The author is especially indebted to his co-supervisor, Prof. Li Kai Ming, for his enthusiastic approach, continued inspiration, enlightening guidance, and constant encouragement. Grateful thanks also go to his chief supervisor, Prof Leung Chun Wah, and co-supervior, Dr. Glenn Frommer, for their valuable comments and suggestions.

The author is grateful to the technical staff, Mr Tang Chow Ning, Dr. Tse Chi Sang, Mr Chan Hau Tsang and Mr Ng Piu Lun, Franco in the Department of Mechanical Engineering for their continuous support and assistance. The author wishes to thank his friends and colleagues, Dr Wong Hon Yiu, Dr Lui Wai Keung, Mr Law Ming Kan, Mr. Tang Siu Hong, Mr. Chan Chi Lung, Mr. Cheung Man Lung, Mr. Cheung Hoi Kok, Ms Leung Wai Man and Ms Lam Po Man, for their helpful discussion during the study.

Special gratitude is expressed to the Acoustics Research Centre at the University of Hull for their contribution in the development of the computer codes for the implementation in the BEM calculation. The author would like to acknowledge Mr Tim Regan from the Hewlett-Packard Company for providing the top performance computers to conduct the intensive BEM computation.

Last but not least, the author would like to thank his parents for their patience and loving care.

Table of Contents

Chapter 1 Introduction

1.1 Background

In a densely populated city with many high-rise buildings such as Hong Kong, noise pollution is one of the environmental problems that should be addressed with high priority. Dwellings, hospitals and other noise sensitive buildings are located within close proximity of major roadways. The transportation noise from the increasing traffic volume seriously deteriorates our quality of life. To reduce the impact from the noise pollution, various mitigation measures can be implemented. For instance, careful planning of the town layout, retrofitting existing roads with noise barriers and enclosures, paving roads with low-noise surface material, regulating the amount of traffic flow, and tightening the noise emission standard of vehicles.

Among the various measures, roadside barriers are one of the most extensively used methods for noise reduction. The barriers cut off the sight line propagation of sound and hence reduce the noise levels at shadow regions. In Hong Kong, for example, there are over 37 km of screen structures constructed for attenuation of noise in the past decade. It is estimated that over a hundred thousand people have benefited from these screen structures. The huge cost in constructing the large amount of barriers has stirred up public concern over the merit of the erection of barriers. To evaluate whether the barriers should be built, accurate predictions of the screening performance during the design stages are essential.

Over the second half of the past century, theoretical studies, scaled-model experiments, and full-scale field measurements have been carried out for the prediction of the acoustic performance of noise barriers. There are theoretical studies aiming to evaluate the diffraction of the sound waves with obstacles. There are also practical approximations for the predictions of the shielding effect of barriers. Despite these widespread interests, there are relatively few studies that incorporate the shielding performance of barriers in the context of a complex environment where the barriers are situated.

1.2 Objective

This study investigates the shielding performance of noise barriers in urban environments. The presence of various reflection surfaces in built-up surroundings will increase the sound pressure levels of noise due to the additional contributions of noise from reflections. Using the theoretical models for simple noise barrier alone in evaluation would overestimate the shielding performance. Correction factors are added for the adjustment for an engineering approximation. However, those simple correction factors are used with a significant degree of uncertainty. The purpose of this study is to provide an analytical model for the evaluation of barriers in an urban environment and tackle the challenge of studying the effects of reflection and diffraction analytically. Commonly encountered metropolitan conditions such as parallel barriers in front of a building façade and parallel barriers in a street canyon are included in the current study. In addition, this study intends to include effects of acoustically non-hard surfaces in the model. This offers the model to be used in more general conditions including those frequently adopted enhancements such as installing acoustic absorption materials on barrier surfaces

and using porous road pavement. For simplicity, atmospheric effects such as temperature distribution and airflow are ignored in our study.

1.3 Layout of Thesis

The thesis is arranged as follows. In Chapter 1, the background and objectives of the current studies are outlined. Reviews are given on various development and research concerning outdoor sound propagation, in-situ determination of impedance, diffraction of sound wave, shielding performance of single and parallel barriers, and performance of barriers in urban environments.

The acoustic impedance plays an essential role in the modelling of various acoustic phenomenons. In Chapter 2, the development of a methodology for an in-situ determination of the acoustic impedance of a plane surface is reported. It is intended to obtain the properties of any sound absorbents that will be installed on the surfaces of barriers for enhancing noise abatement. The method is based on the measurement of the excess attenuation and a numerical inversion technique. Comparisons of measured results on fibre glass with commonly used models are also offered.

In Chapter 3, the development of the image source model for determining the acoustic efficiency of parallel barriers in front of a building façade is demonstrated. Calculations of contributions from various ways of transmission have been discussed in detail. Hierarchies of source images contributing to the overall sound pressure level are also outlined. Calculated results from the image source method are validated with results from boundary element method (BEM) and laboratory measurements using a scaled model.

In Chapter 4, a further development of the image source model for determining the acoustic efficiency of parallel barriers in a street canyon is elaborated. Determinations and calculations of the contribution from the image sources are discussed. Predicted results from the image source model are compared with results from BEM and experimental measurements for the validation. An analysis on the effect of acoustic absorption surface is also presented.

In Chapter 5, a summary of these studies and findings are given. Some recommendations and future developments based on the present study are discussed.

1.4 Literature Review

In this section, the literature review on the related topics is presented. They include outdoor sound propagation, in-situ determination of impedance of a plane surface, the diffraction of sound wave, the shielding performance of single and parallel barriers, and the acoustic performance of barriers in urban environment.

1.4.1 Outdoor Sound Propagation

To investigate the acoustic shielding performance of a noise barrier in a high-rise city, the classical theory of outdoor sound propagation is inevitably involved. Various studies and research concerning the outdoor sound propagation conducted in the past have been reviewed.

Comprehensive reviews of outdoor sound propagation have been given by Delany [35], Piercy et al [91], Embleton [37] and Sutherland and Daigle [105]. They reviewed the general phenomena of sound propagation in complex outdoor environments and provide formulations for various effects during the spreading of sound, including distant attenuation, ground reflection, meteorological effects, turbulence, atmospheric absorption, scattering from the surroundings, etc.

For the propagation of sound in a still and homogenous atmosphere over a ground surface, sound wave can reach the receiver through the direct path and the path with ground reflection respectively. The sound waves through the direct and reflected wave paths interfere with each other at the receiver point. The impedance of the ground surface, the angle of incidence, and the path difference between direct and reflected sound paths would exert influence on the interference and, in turn, play an important role in the evaluation of the total field. The early theoretical models for sound propagating over impedance ground can be found in the studies of Rudnick [98], Lawhead and Rudnick [68], Ingard [50], Wenzel [120] , Chien and Soroka [27,28], and Attenborough et al [8]. Their details of their solutions are different but these models can be summarized in a form known as the Weyl-van der Pol formula [10]. Later Thomasson [110], Kawai et al [60], and Chandler-Wilde and Hothersall [23] proposed their models in the form of integral equations. Pirinchieva [92] demonstrated close agreement between the experimental results and the theoretical predictions.

As can be expected, the acoustic properties of the ground significantly affect the propagation of sound. Acoustically, the surface boundary can either be locally reacting or extended reaction types. For a locally reacting ground, the surface impedance is basically

independent of the incident angle of the incoming wave. On the other hand, the impedance is dependent on the angle of incident for an extended reaction ground. There are various models developed for characterizing the impedance. Delany and Bazley [34] developed an empirical formula to determine the characteristic impedance and propagation constant for a large range of absorbent materials in terms of the flow resistivity and frequency. The empirical formula is convenient to use because it only involves one ground parameter, the flow resistivity. Chessell [25] reported that the Delany and Bazley model provides a reasonable first approximation to the surface impedance in his experiments for aircraft noise over a grassy terrain. Attenborough [9] developed a rigid fibrous model predicting the acoustical characteristics of soils and sands. He used five parameters, including porosity, flow resistivity, tortuosity, steady flow shape factor, and dynamic shape factor. His model is proven to give superior predictions to the empirical formula that use flow resistivity only. Subsequent to his study, a simplified two-parameter approximation for the normal surface impedance of a non-rigidly backed layer structure was introduced [11].

1.4.2 In-situ Determination of Ground Impedance

In the study of sound propagation outdoors, the acoustic characteristics of surface are always necessary. Depending on the applications and requirements, the quantity to describe the acoustic characteristics of a surface is commonly the absorption coefficient or impedance of the surface. In general, the absorption coefficient is found in many practical applications while the impedance is used in a more scientific context. Standardized and well-known methods for measuring the absorption coefficient of materials are the reverberation chamber [7,56] and the impedance tube method [6,54,55].

For the former method, large amount of specimen are placed inside the reverberation chamber and the sound absorption coefficient is indirectly obtained from the measurement of the decay of an impulsive sound. This method is resource demanding and the absorption coefficient is calculated from an empirical reverberation formula. For the impedance tube method, specimens have to be cut into small samples and must be fitted into one end of the tube precisely and tightly for measurement. The surface impedance and absorption coefficient at normal incidence are obtained form the methods using standing wave ratio or transfer-function. For a locally reacting surface, the sound absorption coefficient for diffuse sound incidence can further be determined accordingly. The critical shortcoming of both commonly used methods is that the actual installation condition of the specimen is ignored. The measured results may not truly represent the acoustical characteristic in the real condition of practical applications. Methods of in-situ determination of the acoustical characteristic of sound absorption materials were developed in the 1980s.

Methods based on the information of reflection from a specimen surface were developed for the in-situ purpose. Ingard [51] described a procedure using a standing wave in front of the surface under investigation. In analogy to the standing wave tube, the amplitude and phase of the sound pressure has been measured. A comparison between an acoustically hard surface and the specimen yields the complex reflection factor and hence the plane wave absorption coefficient. As indicated by the authors, the assumption of plane waves is not valid at the short distances used for the measurement.

Yuzawa [122] described a technique of on-the-spot field measurement using two microphones placed exactly the same distance away from the source. The first

microphone is placed close to the surface while the second one is positioned away from the surface. By subtraction of signals from the two measurements, the magnitude of the reflection factor is found and the plane wave sound absorption coefficient can be estimated.

Davies and Mulholland [33] proposed a method to determine the impedance from measurements of the complex reflection factor. The method involved the measurement of acoustic impulses close to the surface of an absorbing material and in a free field. A short pulse with a duration of 3 ms is used which allows the separation of direct and reflected signal. Amplitude and phase characteristics of the reflected signal are thus obtained and hence the normal impedance of the material can be found.

Allard et al [1,3] also presented a method to measure the normal acoustic impedance using a two microphones technique. Two microphones used in this technique are located very close to the surface for measuring the acoustic velocity and the pressure above the sample. From the measured transfer function between the two microphones, the impedance is deduced using a full wave description of the sound field in front of an impedance plane as given by Nobile and Hayek [85].

Wilms and Heinz [121] demonstrated an in-situ methodology by means of the maximum length sequences (MLS) technique to determine the reflection factor. The basis of this procedure is the recording of impulse responses between a speaker and microphone at normal incidence of sound. The microphone is positioned half the distance between the surface of a sample and a loudspeaker. Applying time windowing to the impulse responses, the amplitudes of the direct and reflected sound are extracted.

Garai [39] presented a very similar method with the utilization of the MLS technique with greatly improved noise immunity due to the inherent cross-correlation process. Investigations on the restriction of frequency range and specimen size were made. A non-rectangular time window is suggested for analysis of the measured signals. The method is found to be inadequate at low frequency range due to the assumption of plane wave propagation.

Mommertz [79] made an improvement of incorporating a subtraction technique with the MLS based reflection method for the in-situ measurements of the complex reflection coefficients at an arbitrary angle of incidence. Two separate measurements were conducted. Based on the comparisons with experimental results from a standing wave tube, he suggested that this method can be used for normal incidence measurement for a frequency ranging from 250 Hz to 8000 Hz. This method form the basis of the standard BS 1793-5 [20] for the in-situ measurement of noise reduction device.

Li and Pascal [71] conducted an investigation on the influence of microphone vents on measurements of acoustic impedance by a two-microphone method. Two errors depending on the value of the reactive intensity at the measuring point and the mean-square pressure are studied. A correction on the mismatch of the phase between two channels was emphasized. Li and Hodgson [72] later proposed the determination method from the measurements of the impulse-response function sequentially at two locations close to the surface of the material using MLS signal and a single microphone. The phase-mismatch error that occurs with the two-microphone method is therefore

eliminated. In their study, both plane-wave and spherical-wave hypotheses are reviewed and compared.

Nocke et al [86,87] presented a method of impedance deduction from measurements of complex excess attenuation spectrum at grazing angles intended for locally reacting surfaces. Two separate measurements performed to obtain the excess attenuation are the measurement of the direct field without any reflection surface and the measurement of the total field over the impedance surface under investigation. The complex excess attenuation spectrum is then computed as the ratio of the spectrum of the total field to that of the direct field. The impedance is deduced by iterative search of the value of impedance providing the best matched theoretical excess attenuation. More efficient numerical techniques for the inversion were suggested by Blumrich and Altmann [15], Nocke [88], and Taherzadeh and Attenborough [106]. This in-situ transfer function method has been widely accepted and applications of which have been reported in various studies [12,13,16,17].

Recently, Allard et al [4,5] generalized a new deduction method based on the spherical wave reflection to include thin non-locally reacting materials with a surface impedance noticeably dependent on the angle of incidence. Instead of requiring the measurements of the complex excess attenuation transfer function, the technique they adopted takes two measurements successively over a rigid impervious surface and over the impedance surface respectively. Their prediction results show good agreement with the measurement performed using a near-field acoustical holography method.

1.4.3 Diffraction of Sound Wave

Diffraction is a phenomenon by which wavefronts of propagating waves bend in the neighborhood of obstacles. It is a classical study in optics as well as in acoustics. The exact mathematical solutions describing this phenomenon were developed by scientists over a century ago. The first rigorous solution to half plane diffraction have been obtained by Sommerfeld [104]. He solved partial differential equations which considered a two-dimensional problem of a plane wave incident on an infinitely thin and a perfectly reflecting half plane. His solution could be expressed exactly and simply in term of Fresnel integrals.

Based on the Sommerfeld's solution, Carslaw [21,22] provided an extension of solving generalized wedge diffraction problems due to cylindrical incident waves. The form of his solution however was found to be impractical. Macdonald [75] later used a different method and presented the solution in a more practical form and extended this to solve incident of spherical wave. Nevertheless, their solutions are similar and both are in terms of two integrals. The first integral represents the incident wave and the part of the diffracted wave that is associated with the incident wave. The second integral represents the reflected wave and the part of the diffracted wave that is associated with the reflected wave. Their solutions can be transformed to each other by using transformation of variables.

Rubinowics [97] transformed Kirchhoff's solution to a new diffraction formula, known as the Rubinowics-Young formula. His solution accounts the diffraction by a screen containing an aperture. The diffracted field is expressed as a line integral along the

aperture edge. This is in contrast with Kirchhoff's solution in which the diffracted field is expressed in terms of a surface integral. In addition, Rubinowics showed that the Kirchhoff solution for plane or spherical incident waves can be decomposed into two components: the unobstructed portion of the incident wave and the scattered wave due to the edge.

Copson [29], Levine and Schwinger [69,70], solved the diffraction problems by an integral approach. The exact solutions were obtained by applying the Wiener-Hopf method. The Wiener-Hopf method is a rather standard technique for solving certain types of linear partial differential equations subject to mixed boundary condition on semi-infinite geometries through a complex Fourier integral transform. It is also applicable to an integral equation of a convolution type. The details of the Wiener-Hopf method can be found in Crighton et al [30].

Pierce [90] published the formulae for the estimation of sound field at locations partially shielded from a point source by a barrier. His asymptotic expressions provided great facilitations in practical computations leading to an accurate prediction of the sound fields behind the barrier. Hadden and Pierce [41], extended their study to the diffraction of plane acoustic waves by barriers with finite acoustical impedance. They [42] further extended their study to the diffraction from a point source over a wedge. Details of the numerical technique and comparison with experimental results were presented. Their comprehensive studies laid down a solid foundation for analyzing the sound field of diffraction in geometrical acoustics.

Based on the Rubinowics-Young formula, Embleton [36] also derived a formula for the diffraction of sound by a barrier of infinite length. He assumed that the line integral is taken along the straight edge of the barrier plus a semicircular arc at infinity that connects the two ends of the barrier. Embleton's formula is convenient for numerical computation because the variable is reduced to one dimension in his integral formulation.

Tolstoy [112,113] obtained another exact and explicit solution for sound waves diffracted by wedges. His solutions are an exact representation of the field by an infinite series. The coefficients of the infinite series are given by a set of linear equations. The set of equations are solved by a simple recursion scheme. The edge diffractions are taken into account exactly without the need for any asymptotic approximation of integrals. This solution should be used with care because the infinite series converges slowly especially at high frequencies.

1.4.4 Performance of Single Noise Barrier

The growth of human activities and developments inevitably creates the problem of noise pollution. The shielding effect of screen has been adopted as a measure to obstruct the propagation of noise directly from noise sources to receivers. Studies have been carried out to explore the effectiveness of noise barrier in the past few decades.

The most direct method for investigating the acoustic performance of noise barriers is to conduct full-scale experiments or scaled model experiments. The first known graph for determining the sound attenuation in the shadow zone behind a rigid barrier due to a point source was developed by Redfearn in the 1940s [96]. The attenuation function is

given as a function of two parameters in his graphs. These are the angle of diffraction and the effective height of the barrier normalized by the sound wavelength.

Nearly 30 years later, Maekawa [76] measured the attenuation of a thin rigid barrier, with different sets of source and receiver locations, due to a spherical spreading pulsed tone of a short duration. He presented his experimental data in a chart where the attenuation is plotted against a single parameter known as the Fresnel number. The Fresnel number is the numerical ratio of path difference (the difference in distance between the diffracted path and the direct path) to the half of a sound wavelength.

In the following year, Rathe [95] presented an empirical table for sound attenuation by a thin rigid barrier due to a point source. His empirical table is based on a large number of experimental data. The attenuation is given in octave steps of frequency normalized by the reference frequency with the Fresnel number of 0.5.

Kurze and Anderson [65,66] reviewed diffraction theory from Keller [61,62], and used experimental data from Maekawa and Redfearn to derive empirical formulas for the attenuation of barrier. The attenuation was expressed as a function of relative locations of source and receiver, including the diffracted angles at the source and receiver sides. There are some common features of experimental investigations into the barrier attenuation. Firstly, the experimental studies of Redfearn, Maekawa, Rathe, and Kurze and Anderson considered a point source as an incident wave, which is practically the simplest noise source. Secondly, the Fresnel number is an elementary parameter to express the barrier attenuation. As a result, Kurze-Anderson’s formulas and Maekawa’s chart are extensively used in the engineering community due to their simplicity of use.

The ground effects on barrier shielding were observed experimentally by Scholes et al. [102] as early as in the 1970s. They conducted full-scale experiments for barrier over a grass-covered ground under different wind conditions with one dataset under zero wind condition. The interference patterns of insertion loss are shown in their data. The interference patterns are due to the superposition of direct wave and wave reflected from the ground.

Johnasson [59] suggested the usage of Ingard's theory for sound propagation and the approximate formula of Macdonald's solution by Bowman et al [18] for the calculation of the barrier attenuation over a finite impedance ground. The second term of Macdonald's solution was neglected if the source and receiver were assumed to be far from the barrier surface. He introduced Ingard's theory to calculate the sound propagation along the finite impedance ground surface. He concluded that an acoustic barrier was most effective at places where the ground attenuation is low.

Thomasson [109,110,111] calculated the barrier insertion loss by a numerical integration approach. He developed a new impedance model and introduced it into his numerical integration method based on the Fresnel-Kirchoff approximation. The impedance is governed by four parameters in his model. These four unknown parameters are estimated by fitting measured and theoretical frequency responses when source and receiver are close to the ground. His barrier diffraction theory was well matched with experimental data. He showed that interference patterns of insertion loss were found over ground with finite impedance.

Isei et al. [52,53] reported a comprehensive review on noise reduction by barriers on finite impedance ground. They compared five frequently used prediction schemes with experimental data. The five prediction schemes are Keller's geometrical diffraction theory, the Kirchhoff-Fresnel diffraction formula, Thomasson's formula, the Young-Rubinowicz formula and a modified Macdonald's formula. The ground impedance based on the work of Delany and Bazley [34], Rudnick [98], and Chessell [25] are used in four of the calculation schemes but not in that of Thomasson. They concluded that interference patterns behind a barrier are dependent on the geometrical configuration of the source, receiver, barrier and ground. They remarked that these interference effects had a bigger influence on the acoustic performance of a barrier compared to the effects of applying absorbent on the barrier or of obliquity of incidence at the barrier. They also found that there is a substantial difference in predicting A-weighted noise reduction by the five accurate schemes mentioned above, and by other simpler schemes such as that of Maekawa, and Kurze et al. The difference is more notable in the case of a soft ground.

Nicolas et al. [83] investigated the accuracy of different well-known prediction models of barrier insertion loss in the presence of the ground. They used image theory to take account of the ground effects and used the Weyl-van der Pol formula to calculate the sound propagation along a finite impedance ground surface. The ground is considered as a semi-infinite porous medium whose acoustic properties are specified using a model based on that of Delany et al. [34], Rudnick [98], and Chessell [25]. If ground effects are considered, the diffraction model of Hadden and Pierce [41,42,90] is shown to be the most accurate among the other models, such as the first-order Macdonald's approximation, the Maekawa curves and the models of Isei et al. [53]. Nicolas et al. also

mentioned that the model of Hadden and Pierce can be used in the configurations if the ground impedance on the source side and the receiver side are different.

With the advent of modern computers, the models for barrier diffraction incorporated with ground effects have shifted from analytical models and experimental studies to computationally intensive numerical schemes, such as the boundary element formulation. Hothersall, Chandler-Wilde, Crombie, and Morgan [23,45,46,80] have conducted many studies on the shielding performance of different barriers over absorbing ground.

Recently, Menounou [77] modified Maekawa's chart from a single curve with one parameter to a family of curves with two Fresnel numbers. The first Fresnel number is the conventional Fresnel number associated with the relative position of the source, the barrier, and the receiver. The second Fresnel number is defined similarly to the first Fresnel number. It represents the relative position of the image source, the barrier and the receiver. Menounou also modified the Kurze-Anderson solution and the Kirchhoff solution by introducing correction factors. The correction factors are based on the studies of the two-Fresnel number approach. Unlike studies before the 70's, the plane, cylindrical, and spherical incident waves are all considered in Menounou's studies. Her prediction models are simple to use and have the accuracy compatible with sophisticated diffraction theories.

1.4.5 Performance of Parallel Noise Barriers

Constructions of parallel barriers on both sides of a road can help to attenuate the noise level received at locations at both sides of the road. Multiple reflections of sound waves

produced by the traffic occuring between the parallel barriers create a reverberant sound field within the region. The multiple reflected sound waves may travel to the receiver directly or diffract at the top edge of the other barrier. This phenomenon results in degradation to the performance of the barriers and have been well recognized.

Hutchins and Pitcarn [48] used a laser technique to determine the acoustic wave paths generated from a source located between parallel barriers to the top of each barrier. Based on the theoretical discussion by Hurst [47] and assumption of incoherence nature of the source, they predicted the sound intensity levels at the top of barriers by summing the contributions from the principal wave propagation paths. Comparisons with upright and inclined parallel barriers were made also. Hutchins et al. [49] later presented scale-model investigations of the acoustic performance of parallel barriers with different geometrical configurations. Scaled model experiments have the advantage of permitting the control over many parameters in the experimental set-up which enables the assessment of the acoustic performance for a large range of barrier configurations to be made easily. Different barrier types were investigated and they found that a grass-covered slope surface appeared to be the most effective over the frequency range examined. They also concluded that the reflections from the inner face of the far side parallel barrier were only significant when the source was close to this surface.

Chew [26], who used Davies model [32], developed a prediction scheme for buildings situated on both sides of an expressway. Chew's model involved direct and reflected energy, both from the ground surface and multiple reflections between the parallel buildings on both sides of the expressway, and diffused energy due to scattering from the rough façade surfaces. His predictions showed that the effect of multiple reflections was

significant when the distance between the buildings on opposite sides of the road was small.

Panneton et al. [89] used the image source method to investigate the performance of parallel barriers. The authors extended the study to include absorption on inner barrier surfaces. Multiple reflections between the parallel barriers, diffraction solutions by Hadden and Pierce [41] and modified Delany-Bazley impedance model by Miki [78] were used. They presented experimental results to validate their theoretical models but only the region below the barrier top edge inside the shadow zone was investigated.

Muradali and Fyfe [81] investigated a similar diffraction-based method for the evaluation of the insertion loss of parallel barriers. Their method was based on Lam's study [67] for calculating the insertion loss of a single finite length barrier. Total sound pressure levels at the receiver were calculated by summing the contributions from a series of image sources formed by multiple reflections between the parallel barriers. Comparison of the results with BEM have been shown for validation.

Salomons et al. [100] carried out a similar investigation on parallel barriers. They used a double diffraction method and compared the results obtained from their model with those of the BEM model. They also reported that the double diffraction term was small that did not alter the predicted spectra.

In a more recent study, Cheng and Ng [24] developed a scale model and computer program based on Maekawa's prediction [76] to analyze the performance of inclined barriers. In their study, only first order reflection was considered and multiple reflections

between barriers are not considered. They found that the average noise level at low receivers behind the near side barrier could be reduced by 4, 6 and 10 dB for 125, 250 and 500 Hz, respectively, by tilting the angle of the far side barrier by over 10º.

Apart from the above theoretical studies, there were also numerous full scale experimental investigations to the performance of parallel barriers. Hajek [43] carried out field measurements to study the acoustic performance of parallel barriers of height 3 m and separation 74 m. He found that the degradation of acoustic performance behind the near side barrier due to the insertion of the far side barrier was negligible. The above finding was supported by the outdoor measurements conducted by Halliwell [44]. He reported that no evidence was found that the far side barrier would degrade the performance of the near side barrier. He suggested that in most practical situations, the traffic noise would be masked by local noise sources in the surroundings, especially if the receivers were situated far behind the barrier. Slutsky and Bertoni [103] outlined a plausible explanation of why the effect of the second barrier on the overall sound field was so small. They argued that because the separation between the parallel barriers was large, this reduced the effect of multiple reflections between them. Nelson et al [82] also reported that, even if the separation between the barriers was reduced to 33m, no significant degradation of the overall sound field was found.

On the other hand, Fleming and Rickley [38] conducted similar field tests on the acoustic performance of parallel barriers separated at a distance by 50 m in Maryland, USA. They reported that, when the far side barrier was inserted, a degradation of up to 2.8 dB(A) at 40 m behind the near side barrier was found. This change in noise levels might be perceptible by the human ears as it had been stated that the smallest change in noise level

detected by humans is about 3 dB(A). Watts [119] investigated the performance of parallel barriers by carrying out full scale experiments. He detected a degradation of 4 dB(A) behind a 2 m high near side barrier when reflective barrier of similar height was erected 34 m away. He also suggested that both sound absorptive barriers and tilted barriers were found to be effective in counteracting the degradation in the acoustic performance resulting from unwanted reflected paths.

1.4.6 Performance of Noise Barriers in an Urban Environment

Despite these widespread interests, there are relatively few studies that consider the shielding effect of barriers in the vicinity of tall buildings in an urban environment. Sakurai et al. [99] used a time-domain method to investigate the sound field of a façade-barrier system. They studied the transfer function and the impulse response of the system. A spark pulse was used as the noise source in their experiment. They mentioned that their theoretical model could not correctly predict the sound field in the vicinity of the back of the barrier.

Walerian et al. [57,58,114,115,116,117,118] presented a series of studies in the shielding performance of obstacles in different complex urban environments. They developed a computer program to predict the time-average sound levels in complex outdoor situations with various parameters including the road geometry, layout of the obstacles, nature of the traffic flow, etc. Predictions of the sound level distribution along building facades are also presented.

Godinho et al. [40] employed the boundary element method (BEM) to determine the shielding effects of an infinitely long barrier which was placed in front of tall building façades. In their study, different geometric models, with barriers of varying sizes, are used. They evaluated the reduction of sound pressure in the vicinity of the buildings and compared their results with a simplified method. They also performed a time-domain analysis to give better physical illustrations.

Recently, Li and Tang [74] developed an image source model for the prediction of the insertion loss of barriers that are placed in front of a tall building in high-rise cities. Comparisons of the results with indoor experimental data and wave-based boundary element formulation show reasonably good agreement over a broad frequency range.

Chapter 2 In-situ Determination of the Acoustic Impedance of a Plane Surface

2.1 Introduction

As a result of the limitations in standardized laboratory measurement methods for the determination of the acoustic impedance [6,7,54,55,56], the need of an in-situ method to obtain the acoustic impedance has emerged. Methods based on in-situ information of acoustic reflection from the surface of a specimen have been developed [2,3,4,33,51,71,72,79,85,86,87,88,108,121,122]. There is also a new standard [20] recently published for an in-situ evaluation of the reflective index of road traffic noise reducing devices. In our study, we would like to develop a complete methodology and setup for the in-situ determination of the acoustic impedance of any sound absorption material to be put on the barrier surface for enhancing noise abatement. The acoustic impedance is defined as the ratio of the complex amplitudes of sound pressure and particle velocity. It is a quantity with both magnitude and phase information. Retrieving these properties from the measurement of the reflection signals would be the main theme of the present study.

Having the advantage of high noise immunity, the technique of maximum length sequences (MLS) would serve well for the in-situ purpose. Wilms and Heinz [121] were among the first to report the use of the MLS technique to extract the direct and reflected sound. Garai [39] later conducted investigations on the limitation of frequency range and specimen size of the MLS method. Mommertz [79] suggested an improved subtraction

technique for the MLS method. These early studies form the basis of the standard BS 1798-5 [20] for the in-situ measurement of the reflective index of noise reduction device. It is also known as the ADRIENNE method.

With the MLS technique, Nocke et al [86,87,88] presented an improved methodology of impedance deduction from measurements of complex excess attenuation spectrum at near grazing angles intended for locally reacting surfaces. This methodology is frequently referred as the transfer function method and it involves two separate measurements. First, the sound pressure of the direct field without any reflection surface is measured. Second, the overall sound pressure with direct transmission and reflection from the specimen surface under investigation is measured. The ratio of the sound pressures from these two measurements forms the complex excess attenuation function. The impedance is deduced by iterative search of the value of impedance providing the best matched theoretical excess attenuation with the measured one. The Downhill Simplex method is suggested for the iteration. Taherzadeh and Attenborough [106] later found the Newton-Raphson method was also effective and more efficient in finding the impedance. More recently, Attenborough and Boulanger [13] have suggested the use of the winding number integral method described by Brazier-Smith and Scott [19] for overcoming the difficulty in picking up the correct root.

Based on the excess attenuation transfer function method from Nocke et al as mentioned before, we would like to develop a methodology and setup for in-situ determination of the acoustic properties of any sound absorption materials which will be put on the barriers' surface for improving the shielding efficiency. We would like to explore improvements on numerical deduction and experimental measurement techniques.

Comparisons of the deduced impedance with various parametric models are also presented.

2.2 Theory

Instead of the spherical wave reflection coefficient obtained from the measurements as proposed by Nocke [86,87,88], the input data for our refined method is the directly measured transfer function of the complex excess attenuation above the surface under consideration. Deduction of the surface characteristic under consideration is made by searching a theoretical value of the impedance that best fit the excess attenuation measured at each frequency. Although the input data is different, the theoretical basis of our refinement is also the classical Weyl van der Pol formula for predicting the propagation of sound above an impedance plane [27,28]. The difference in the input data provides more flexibility in choosing various acoustic theories to be applied in future.

2.2.1 Weyl van der Pol

In the case of a point source **S** located above an impedance plane, the overall sound pressure at the receiver $\mathfrak{R}$ is obtained by summation of the direct and reflected components. This is denoted as,

$$P(\mathbf{S},\mathfrak{R}) = P_0 + Q \times P_{\underline{0}} \qquad (2.1)$$

where, P_0 is the free field pressure contribution at $\mathfrak{R}$ from **S**

$P_{\underline{0}}$ is the free field pressure contribution at $\mathfrak{R}$ from ground reflected image $\mathbf{I}_{\underline{0}}$

Q is the spherical wave reflection coefficient

For the free field pressure contribution from the source and its image, they can be determined by,

$$P_0 = \frac{e^{ikR_1}}{R_1}, \tag{2.2}$$

and

$$P_{\underline{0}} = \frac{e^{ikR_2}}{R_2}, \tag{2.3}$$

where R_1 is the distance between the source **S** and receiver $\mathfrak{R}$, R_2 is the distance between the source **S** and ground reflected image source $\mathbf{I}_{\underline{0}}$ and k is the wave number. The time dependent term $e^{-i\omega t}$ is omitted.

The spherical wave reflection coefficient Q is the quantity that depends on the acoustic properties of the surface and the geometrical configuration of the source and receiver. Denoting the specific normalized impedance of the surface as Z, the spherical wave reflection coefficient can be expressed as,

$$Q(Z) = R_p + (1 - R_p) \times F(\mu) \tag{2.4}$$

In equation (2.4), the term R_p is the plane wave reflection coefficient denoted by,

$$R_p = \frac{\cos\theta - \beta}{\cos\theta + \beta}, \tag{2.5}$$

in which β is the specific normalized admittance defined as the reciprocal of the specific normalized impedance and θ is the angle of incidence of the reflected wave. The term $F(\mu)$ is commonly referred as the boundary loss factor and is given by,

$$F(\mu) = 1 + i\sqrt{\pi} \times \mu \times e^{-\mu^2} \times \operatorname{erfc}(-i \times \mu), \tag{2.6}$$

where μ is the numerical distance and erfc is the complementary error function. The numerical distance μ is commonly expressed as,

$$\mu = (\beta + \cos\theta) \times \sqrt{\frac{i}{2} \times k \times R_2} \,. \tag{2.7}$$

By defining $\tau = \sqrt{\frac{i}{2} \times k \times R_2}$ and $w(\mu) = e^{-\mu^2} \times \text{erfc}(-i \times \mu)$, the spherical wave reflection coefficient can be further simplified as,

$$Q(Z) = 1 + i \times 2 \times \tau \times \sqrt{\pi} \times \beta \times w(\mu). \tag{2.8}$$

2.2.2 Complex Excess Attenuation Transfer Function

The excess attenuation is commonly defined as the ratio of the total sound field to the direct component of the sound field. We denote the complex excess attenuation as H. With some manipulation, the transfer function H can be expressed in terms of the impedance Z as follow,

$$\begin{aligned} H(Z) &= \frac{P_0 + Q(Z) \times P_0}{P_0} \\ &= 1 + Q(Z) \times \frac{R_1}{R_2} \times e^{ik(R_2 - R_1)} \end{aligned} \,. \tag{2.9}$$

For a particular impedance of the reflecting surface and geometric relationship between the source and receiver, equation (2.9) will give the corresponding complex excess attenuation.

The determination of impedance would be an inverse problem of equation (2.9). The excess attenuation above the impedance surface is first measured. The impedance is then

deduced by searching the value of which will result the complex excess attenuation by equation (2.9) matched well with the measured value.

Mathematically, the solution searching is achieved by minimization of the function $\Gamma(Z)$ defined as,

$$\Gamma(Z) = H(Z) - H_{measured}, \tag{2.10}$$

where $H(Z)$ is the complex excess attenuation transfer function with input parameters R_1 and R_2 corresponding to the geometry in the measurement and $H_{measured}$ is the measured value. Downhill Simplex method was used by Nocke [87] and Panneton et al [89] for this minimization. Newton-Raphson method was adopted by Taherzadeh and Attenborough [106]. More recently, Attenborough and Boulanger [13] suggested the Muller method. In the following section, we report the use of the Downhill Simplex and Newton-Raphson methods adopted in our study.

2.2.3 Downhill Simplex method

The Downhill Simplex method was first used by Nocke [86,87] for the impedance deduction. It is an iterative algorithm to solve unconstrained minimization problems numerically for multidimensional variables without the use of derivatives. Details of the implementation and theory of the method have been outlined by Press [93].

For the function $\Gamma(Z)$ defined in equation (2.10), it can be considered as a two dimensional problem. The real and imaginary parts are taken as two individual parameters with equal priority. A starting guess simplex with 3 points is therefore needed. The iteration is carried out from the lowest frequency to the highest. For the first lowest

frequency, the starting simplex we selected consists of $Z_1 = 0 + 0i$, $Z_2 = 1 + 0i$, and $Z_3 = 0 + 1i$. Various operations of the minimization are subsequently carried out until a predefined tolerance or number of iterations is reached. From the adaptive algorithm suggested by Nocke [87], the final simplex resulted is then used for the minimization of the next frequency. This adaptive algorithm also solves the problem of non-uniqueness in the numerical solution.

2.2.4 Newton-Raphson method

Another method suggested for the minimization is the well known Newton-Raphson Method [106]. With this method, an improved approximation of the impedance, Z_i , towards the initial approximation, Z_0 , can be obtained from

$$Z_i = Z_0 + \delta Z = Z_0 - \frac{\Gamma(Z_0)}{\Gamma'(Z_0)}. \tag{2.11}$$

The prime in equation (2.11) denotes the differentiation with respect to the argument. By iteration, the impedance of the surface can be obtained until a desired accuracy is achieved.

The differentiation term, $\Gamma'(Z)$, of the minimization function can be expressed as follows,

$$\Gamma'(Z) = \frac{\partial \Gamma(Z)}{\partial Z} = -\frac{1}{Z^2} \times \frac{R_1}{R_2} \times e^{ik(R_2 - R_1)} \times \frac{\partial Q}{\partial \beta}. \tag{2.12}$$

The derivative term, $\frac{\partial Q}{\partial \beta}$, can be expressed as,

$$\frac{\partial Q(\beta)}{\partial \beta} = 2\tau\left[i\sqrt{\pi} \times w(z) - 2\tau\beta \times \left(1 + iz\sqrt{\pi} \times w(z)\right)\right]. \tag{2.13}$$

2.2.5 Determination of Parametric Values for Various Impedance Models

The impedance deduced from the minimization process are the actual impedance. For further analysis and study, a convenient representation of the impedance spectra would be necessary. Various models have been developed to describe the impedance with relation to the properties of the medium in the past [14].

The most commonly used impedance model is the Delany and Bazley model [34]. The model is originally intended for the fibrous absorbent materials. It is, however, found to be remarkably successful for modelling the ground effect in outdoor sound propagation. For a semi-infinite homogeneous locally reacting surface, the Delany and Bazley model expresses the impedance Z with a single parameter as follows,

$$Z = 1 + 0.0511 \times \left(\frac{\sigma_e}{f} \right)^{0.75} + i \times 0.0768 \times \left(\frac{\sigma_e}{f} \right)^{0.73}, \tag{2.14}$$

where f is the frequency in Hz and σ_e is the flow resistivity in $Pa \cdot s \cdot m^{-2}$.

For a locally reacting surface with finite thickness d above a hard-back layer, we denote the impedance as Z'. By the Delany and Bazley model,

$$Z' = Z \times \coth(-ikd), \tag{2.15}$$

where the term Z is calculated from equation (2.14).

For an extended-reaction surface, the impedance determined by the minimization gives the effective impedance at the corresponding incident angle only [88]. In order to obtain the impedance for a full range of angles, one should perform the measurements in all directions. However, this would be time consuming and inefficient. A less rigorous but more realistic alternative method is fitting the measurement data of one direction into

parametric models for extended-reaction surfaces. One of the commonly used models for this type of surface is the Pyett model [94] as reported in studies by Li et al [73] and Nicolas and Berry [84]. In the Pyett model, the effective impedance Z_e of a semi-infinite homogeneous extended-reaction surface with incident angle θ is,

$$Z_e = Z \times \frac{n}{\sqrt{n^2 - \sin^2\theta}}, \tag{2.16}$$

where n is the reflective index defined as the ratio of the wave number of the medium k to the wave number of the air k_0. We can apply the Delany-Bazley model to calculate the terms Z from equation (2.14) and n as follows,

$$n = 1 + 0.0858 \times \left(\frac{\sigma_e}{f}\right)^{0.7} + i \times 0.175 \times \left(\frac{\sigma_e}{f}\right)^{0.59}. \tag{2.17}$$

For a finite thickness d above a hard-back layer, the effective impedance $Z_e^{'}$ is,

$$Z_e^{'} = i \times \frac{n}{\sqrt{n^2 - \sin^2\theta}} \times Z \times \coth\left(k_0 \times d \times \sqrt{n^2 - \sin^2\theta}\right). \tag{2.18}$$

Apart from the above models presented, there are also other more sophisticated models available [8,9,14,78]. Due to their complexity, however, they will not be considered in the present study. Among the above models being considered, the only parameter related to the property of the medium is the flow resistivity. For the determination of the best fit value of this parameter with the impedance measured, we found the technique of the least squares fitting to be very effective and efficient.

2.3 Stability and Efficiency Analysis

To have a better understanding of the stability and efficiency of the two iteration methods, simulations have been conducted for the deduction of acoustic impedance. We use the Delany-Bazley model for a locally reacting surface. We assume an effective flow resistivity σ_e of 20000 MKS rayls/m to simulate an impedance spectrum with frequency ranging from 100 Hz to 10,000 Hz. With the geometrical configuration as shown in figure 2.1, the corresponding excess attenuation H_{cal} is obtained by equation (2.9). Random errors on the magnitude λ and phase φ are then added to the calculated excess attenuation for the simulation as follows,

$$H_{sim} = H_{cal} \times (1 + \delta \times \lambda_{\max}) \times e^{i \times \delta \times \varphi_{\max}} . \qquad (2.19)$$

δ is an arbitrary value range from -1 to +1 which is generated randomly by the computer. $\lambda_{\max}$ and $\varphi_{\max}$ are the parameters used to control the maximum value of the error in magnitude and phase of the excess attenuation respectively. To demonstrate the stability and efficiency among the two iteration methods, simulations with different degree of errors controlled by different $\lambda_{\max}$ and $\varphi_{\max}$ are carried out.

The execution of the computational codes is done by Matlab on a PC with an Intel P4 2.26 GHz processor and 1GB of memory. The running time required for each deduction is recorded and the deducted results are summarized in table 2.1. It is observed that the computational time and the deviation from the original values for both methods increase with the amount of random errors added to the data. In general, it is found that the Newton-Raphson method is faster than the Downhill Simplex method. On the other hand, parameters obtained by the Downhill Simplex method are closer to the original one.

Therefore, it is difficult to claim any one of them is superior. The two methods would be complementary with each other.

Another important observation from the numerical simulation is the importance of the phase information. The excess attenuation is a complex transfer function. In most of the presentation, only the magnitude is described and the phase is ignored. From our simulation, the phase information should be very important when using the excess attenuation for impedance deduction. Considering the simulations 03 and 13 shown in figure 2.2 and figure 2.3 respectively, a disturbance of 30% in magnitude only slightly affects the deduction while a disturbance of 30% in phase gives a large error in the deduction. The accuracy in phase would be affected largely by the accuracy in positioning. Therefore, special attention should be given to the measurements for the spatial locations of microphone and sound source.

2.4 Measurement Technique

As shown in our previous analysis, the technique for impedance deduction is strongly dependent on the measurement data. Poor quality measurement data will result in an inaccurate deduction of impedance. Due to the nature of the inverse problem, there may be no solution obtained if the inaccuracy is too large. Great care should be taken to minimize any error involved in the measurement to ensure high quality data.

2.4.1 Procedures and Methodology of the Measurement

In this section, the general procedures and methodology of the measurement are presented. Two separate measurements are required for obtaining the excess attenuation, $H_{measured}$. They are the measurements of the frequency responses between the source and receiver with and without the impedance surface. The excess attenuation, $H_{measured}$, is the ratio of these two frequency responses measured. For the frequency response with the impedance surface, we position the speaker and microphone close to the surface with a small oblique angle. For the frequency response without the impedance surface which is commonly referred to as the free field measurement, we locate the speaker and microphone far away from any surface to avoid unwanted reflections and separate them with the same distance used in the previous measurement for the convenience of subsequence data processing.

The measurement of frequency response employs a special type of test signal called a maximum-length sequence (MLS) and is chosen as the preferred alternative to the conventional white noise stimulus. The deterministic nature of the maximum-length sequence provides a vast signal-to-noise ratio which would be ideal for an in-situ application. As the measurement is on the time domain, manipulation to eliminate unwanted reflection is also possible. The equipment arrangement is shown in figure 2.4. The MLS signals are generated by the MLSSA 2000 card, transferred via the built-in DA-converter, and amplified by a B&K 2713 power amplifier. The MLS signals are then connected to a loudspeaker which emits sound for measurements. The acoustic response is recorded by a B&K 4942 microphone. The received signals are then transmitted back to the MLSSA 2000 card through the B&K 2671 preamplifier and B&K NEXUS

conditional amplifier. Typical data measured in the time domain is shown in figure 2.5. Depending on the geometrical relation, the direct and reflected signals may merge or separate with each other. The frequency response can then be obtained by applying a Fast Fourier Transform (FFT) to the selected signals. The excess attenuation, $H_{measured}$, is obtained by using the free field response as the reference signal when applying the FFT to the measurement with the impedance surface.

2.4.2 Point Source Loudspeaker

The theory of the impedance deduction is based on the sound propagation of a point source. The consistence of the sound source towards a theoretical point source in the measurement will affect the deduction results. In the following section, we will present the study in the simulation of a spherical point source from a loudspeaker and the corresponding usage in the impedance deduction.

Most commercial available loudspeakers generate sound waves from cone shaped driving units. Due to the physical shape of the vibration diaphragm, the wavefront is no longer spherical. The wavefront is further distorted due to the reflection from the case of the speaker and the interference with any available tweeter. For a typical box type speaker with size of 290mm(H)x200mm(W)x170mm(D) as shown in figure 2.6, we measured the directivity in the X-Y plane and the Y-Z plane. The measured results of the directivity pattern in various frequency bands are shown in figures 2.7 and 2.8.

From the measured directivity pattern, the acoustic power is concentrated in front of the loudspeaker. It is clear that we cannot use those box type commercial speakers for the

experimental simulation of a theoretical point source. For the study of impedance deduction and any further experimental study, we have developed a point source generator by mounting a copper pipe with l.5m length and 25mm diameter in front of a small speaker as shown in figure 2.9. The sound wave emitted from the speaker is trapped along the pipe and diffused out from the circular exit at the end. A directivity measurement has been conducted to validate the spherical properties of a point source and the results are shown in figure 2.10 and 2.11

From the measured results, we can observe that the point source loudspeaker provides much better performance than the box type loudspeaker. In the XY plane, deviation is within 5 dB for frequency bands of 250 Hz to 1000 Hz. In the YZ plane, the deviation for all direction is within 1 dB for frequency above 250Hz. Therefore, the YZ plane should be chosen for the point source simulation.

2.4.3 Time Window in Fast Fourier Transform (FFT)

The process of Fast Fourier Transform (FFT) plays an essential role in attaining the transfer functions in frequency domain from the time domain data acquired. Parameters used in FFT could affect the resulting spectrum of the transfer function. Addition of any weighting to the original signals should be avoided and, hence, rectangular windows are selected in the analysis of our study. The available range of frequency from FFT is limited by the length of the FFT window which is usually very short in duration due to the constraint of unwanted reflection afterwards. The highest sampling frequency is used in order to obtain the largest amount of data. For the MLLSSA system used, we set the sampling rate at 160 kHz. Another important parameter is the starting point of the

window. As we compared the ratio of the transfer function of two measurements, the starting time of the FFT window should be the same for the two measurements. Otherwise, the phase information would be shifted and the deduction will become difficult and unreliable due to the error introduced. By keeping the same separation distance between the source and receiver for all measurements, we can confirm the phase consistence by checking the signals of free field measurement and impedance measurement in the time domain. The signals are consistent in phase if they coincident with each other at the beginning region and an example is demonstrated in figure 2.12.

2.5 Validation of Measurement with Fiber Glass

In order to validate the method, we carried out the impedance deduction with a 25 mm thick fiber glass with density of 48 kg/m^3. The measurement is carried out inside an anechoic chamber to avoid unwanted reflection. The fiber glass is placed above a wooden board and measurements are conducted above it with different geometries. We use the measurement data to deduce the impedance with three models discussed above. Model (i) denotes the Delany-Bazley model for semi-infinite locally reacting medium as shown in equation (2.14). Model (ii) refers to the Delany-Bazley model for locally reacting medium with finite thickness above a hard-back layer as shown in equation (2.15). Model (iii) represents the Pyett model for extended reacting medium with a finite thickness above a hard-back layer as shown in equation (2.18). We only consider the data of frequency ranging from 400 Hz to 4000 Hz for the determination of the parameter. The results are summarized in table 2.2 and figures 2.13 to 2.19.

From the experimental results, it is found that different empirical models will give fitted parameters in different range. The parameters for model (i) and (ii) are close with each other while parameters for model (iii) are much smaller. It is mainly because different models are designated for medium of different nature. Model (i) and (ii) are for locally reacting surface in which the impedance is independent of angle while the model (iii) is for extended reacting surface in which the angle of propagation is a dependent factor. Therefore, parameters deduced from one model are not equivalent of others.

Another finding is that parameters deduced with deviation may be observed from the degree of matching in excess attenuation plots. Considering the second measurement shown in figure 2.14 as an example, all the three fitted excess attenuation have the first trough shifted in frequency. The shifting is probably due to phase error during the measurement and the resulted parameters do have significant difference when compared with measurement at other angles.

2.6 Conclusions

In this chapter, the study of in-situ determination of the acoustic impedance is presented. A review on the development of in-situ measurement techniques has been conducted. Based on the achievement reported by Nocke et al [86,87,88], improved methodology and experimental setup are developed for the in-situ determination. The principle of the method is based on the classical spherical wave propagation theory and numerical minimization techniques. With the use of the MLS technique, the high noise immunity of the method makes it very appropriate for in-situ condition. Numerical simulations with artificially added random errors have been conducted to explore the stability and

efficiency of various numerical minimization methods. From the simulation, the importance of the accuracy in phase is examined. For the measurement technique, improved method for point source simulation have been suggested and validated. Measurement on fibre glass with the in-situ method developed is conducted. Fitting the deduced impedance with various parametric models shows a good agreement. In conclusion, the developed method and setup for the in-situ impedance determination is found to be effective and successful. The methodology can gives the impedance of noise barrier surfaces in-situ and hence provide the essential quantity in modelling study of shielding performance in the coming chapters.

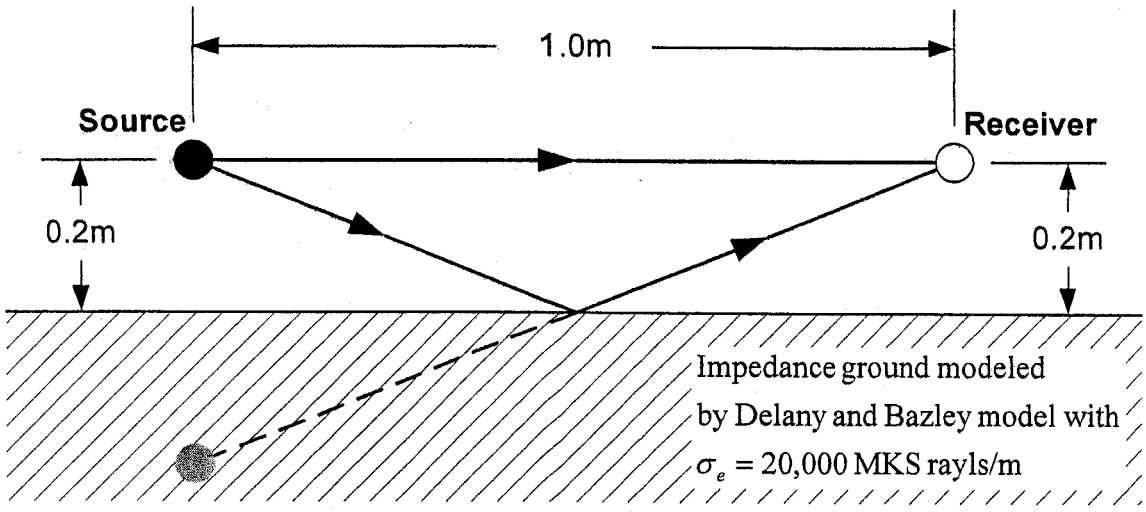

Figure 2.1 Geometrical information for the simulation.

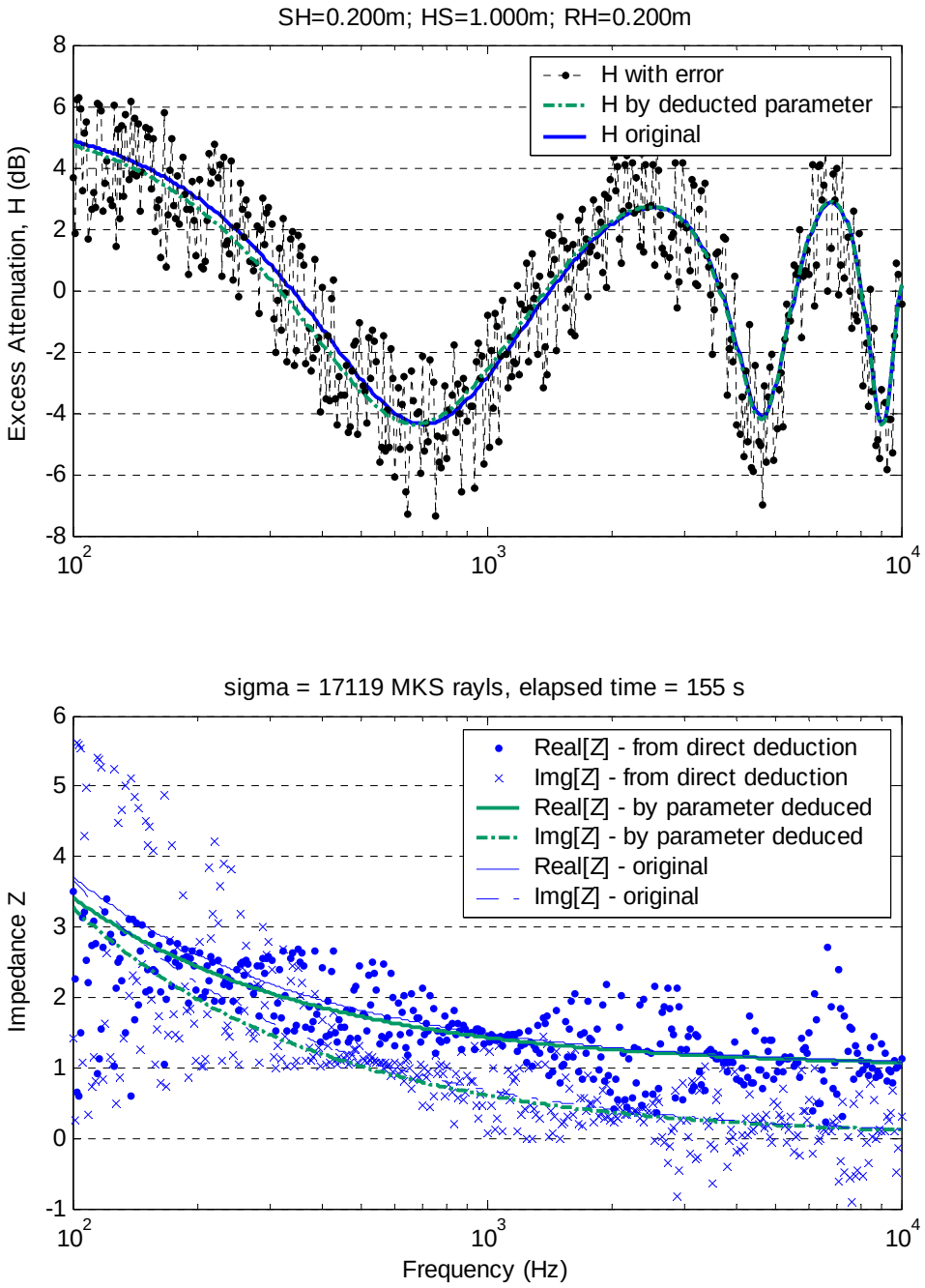

Figure 2.2 Simulation of deduction with a disturbance of 30% in magnitude added on the excess attenuation (H). In the simulation, the height of the source (SH) was 0.2m, the horizontal separation between the source and receiver (HS) was 1m, and the height of the receiver (RH) was 0.2m. The deduction elapsed time is 155s and resulted a flow resistivity of 17,119 MKS rayls/m. The original flow resistivity was 20,000 MKS rayls/m.

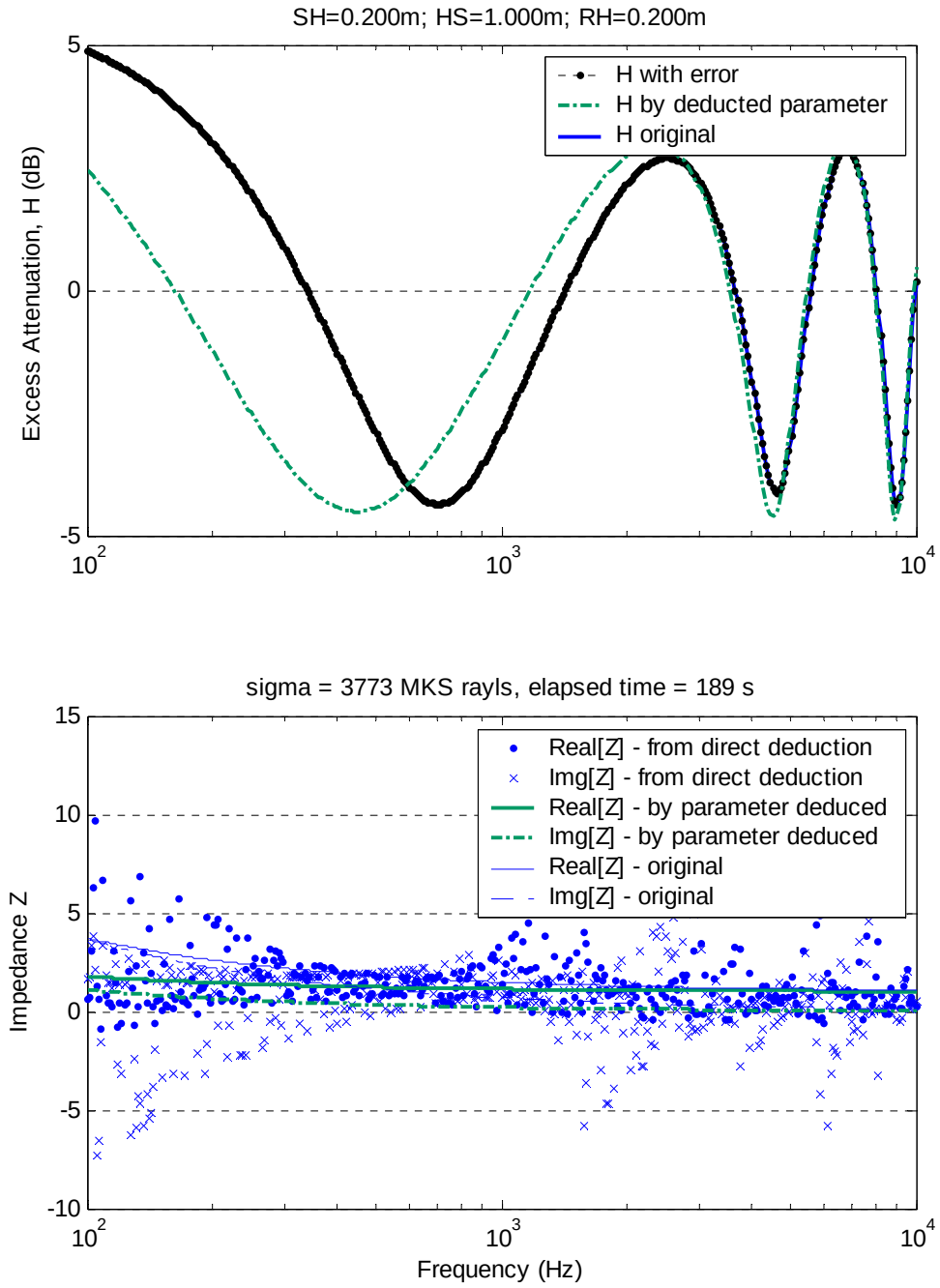

Figure 2.3 Simulation of deduction with a disturbance of 30% in phase added on the excess attenuation (H). In the simulation, the height of the source (SH) was 0.2m, the horizontal separation between the source and receiver (HS) was 1m, and the height of the receiver (RH) was 0.2m. The deduction elapsed time is 189s and resulted a flow resistivity of 3,773 MKS rayls/m. The original flow resistivity was 20,000 MKS rayls/m.

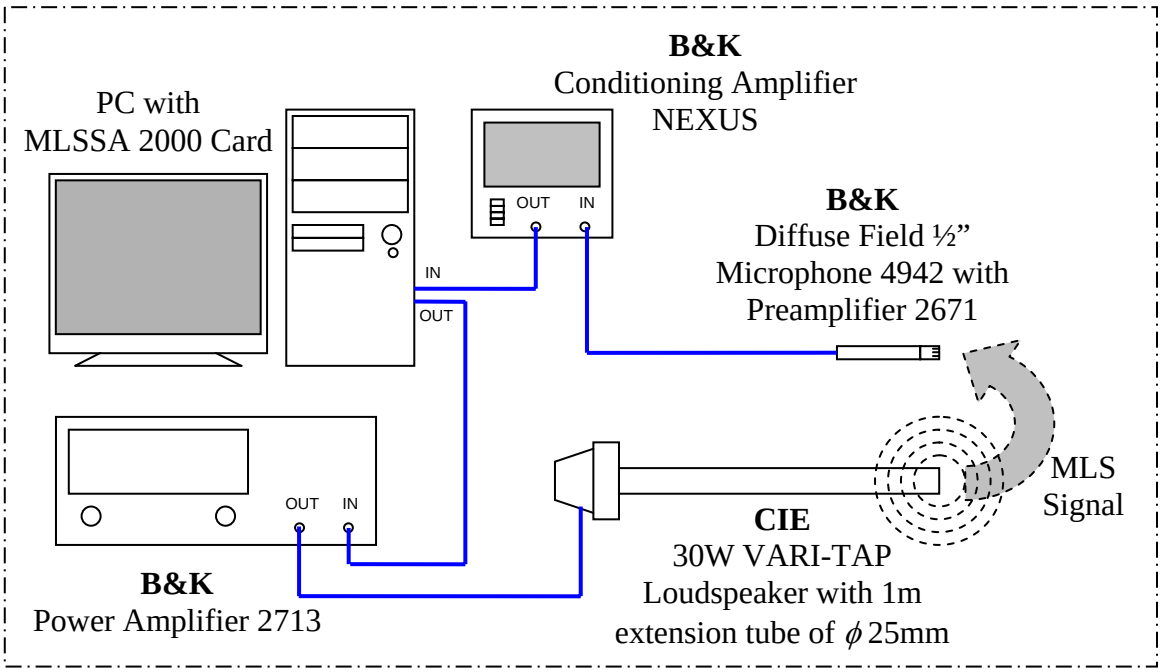

Figure 2.4 Equipment set-up for the measurement of frequency response measurement

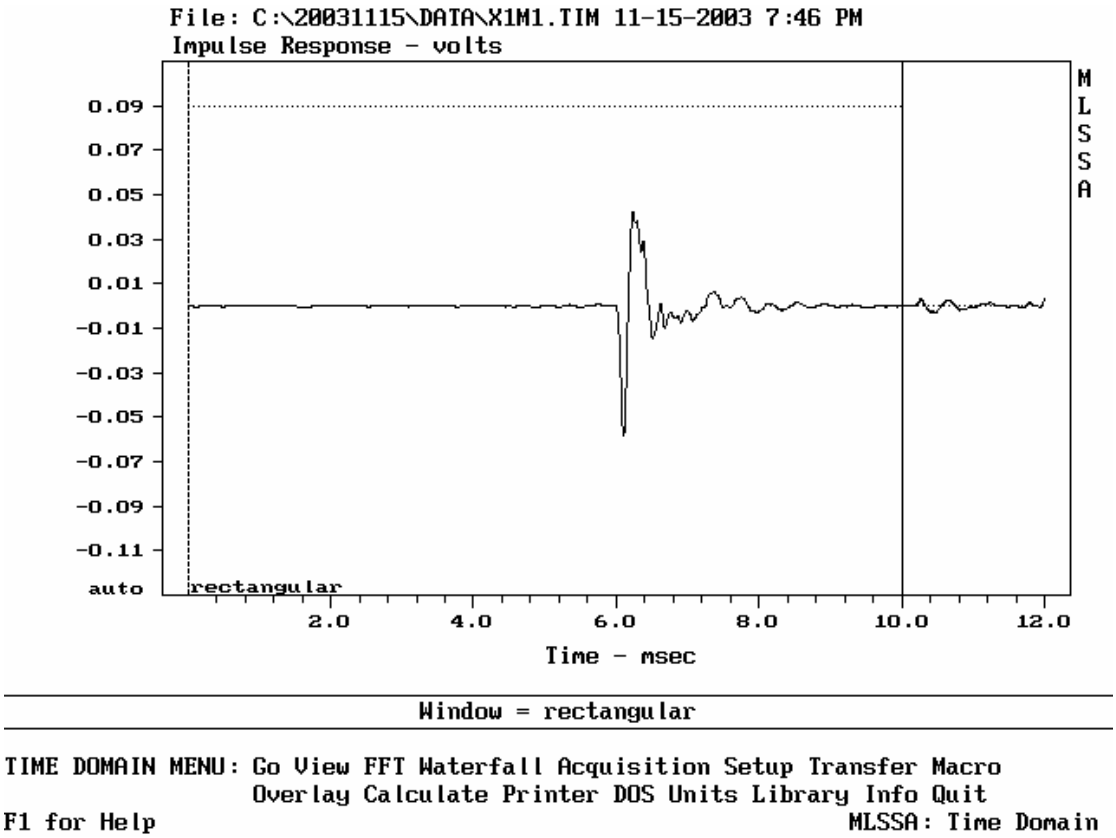

Figure 2.5 A typical MLS signal measured in time domain by MLSSA.

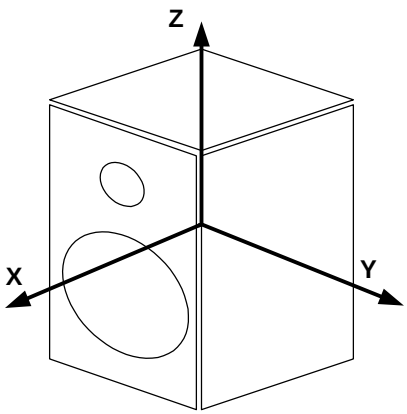

Figure 2.6 The coordinate system defined for the directivity measurement of the box type speaker. The (0,0,0) is at the geometrical center of the speaker.

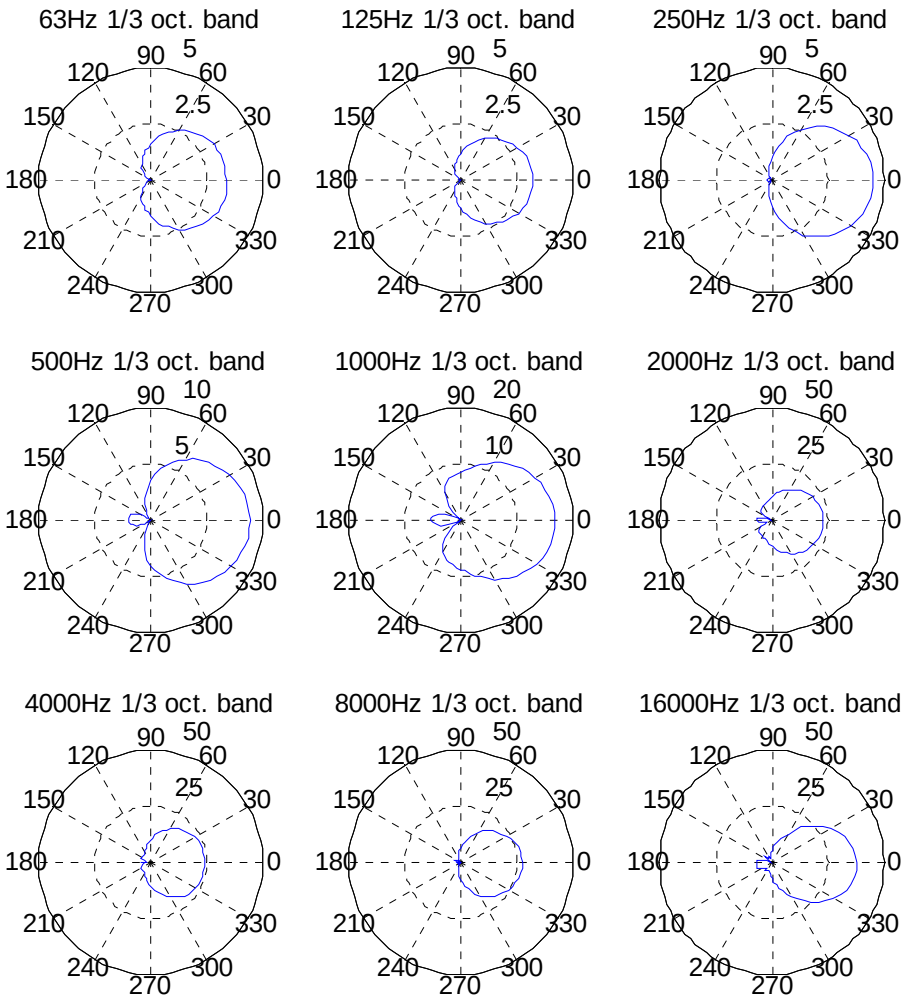

Figure 2.7 The directivity pattern of various frequency band in XY plane of a box type speaker.

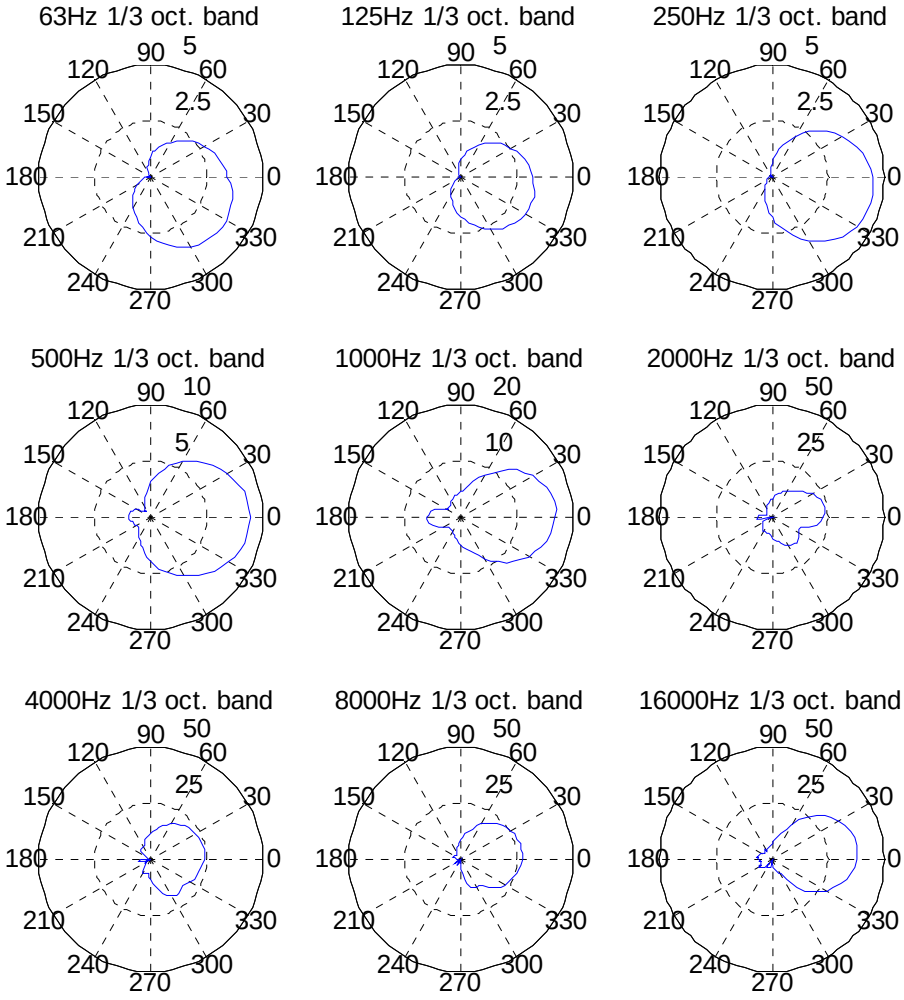

Figure 2.8 The directivity pattern of various frequency band in YZ plane of a box type speaker.

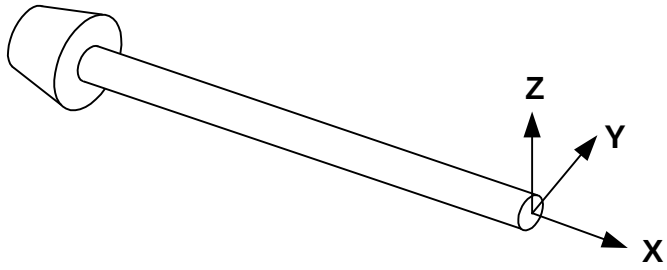

Figure 2.9 The coordinate system defined for the directivity measurement of the point source speaker. The (0,0,0) is at the center of the circular exit.

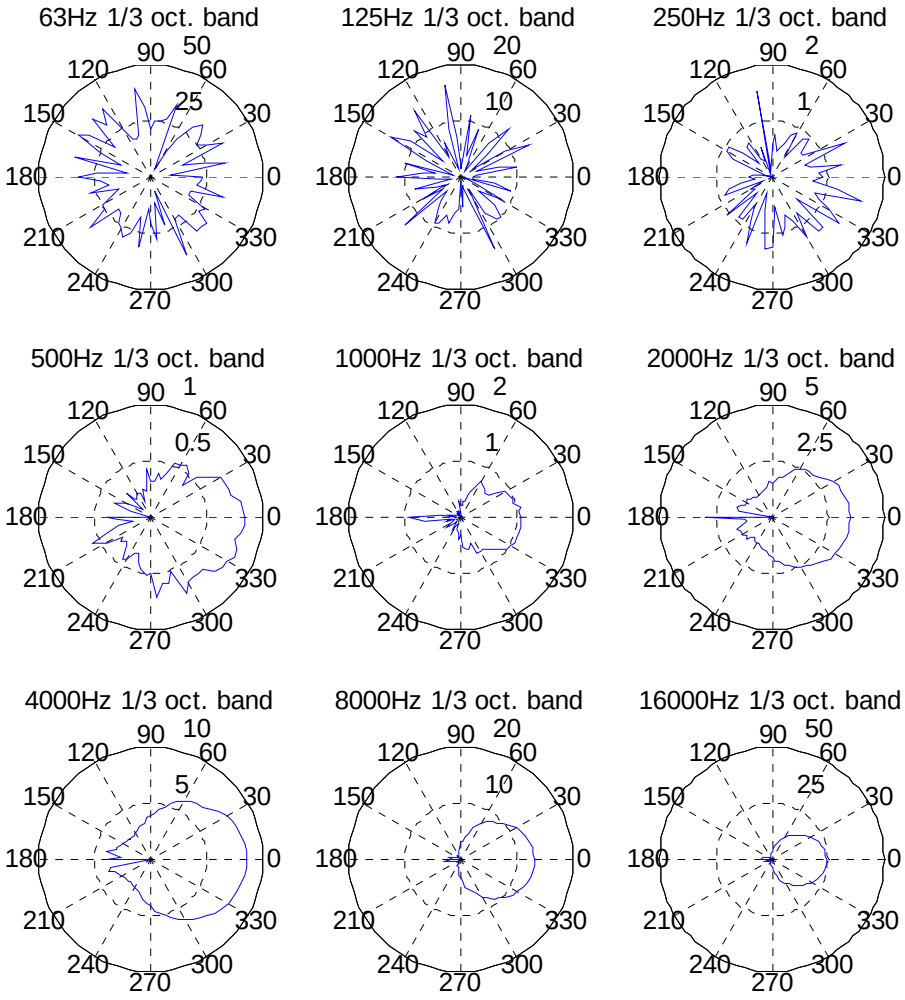

Figure 2.10 The directivity pattern of various frequency band in XY plane of the point source speaker.

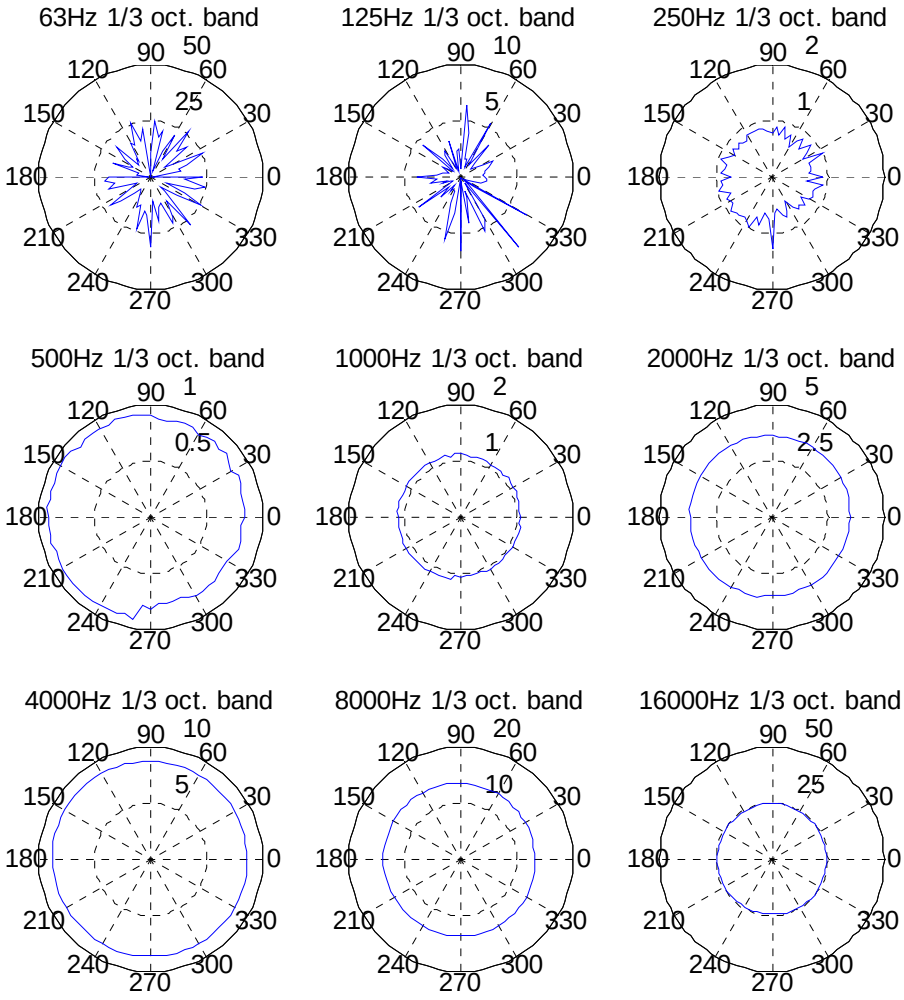

Figure 2.11 The directivity pattern of various frequency bands in YZ plane of the point source speaker.

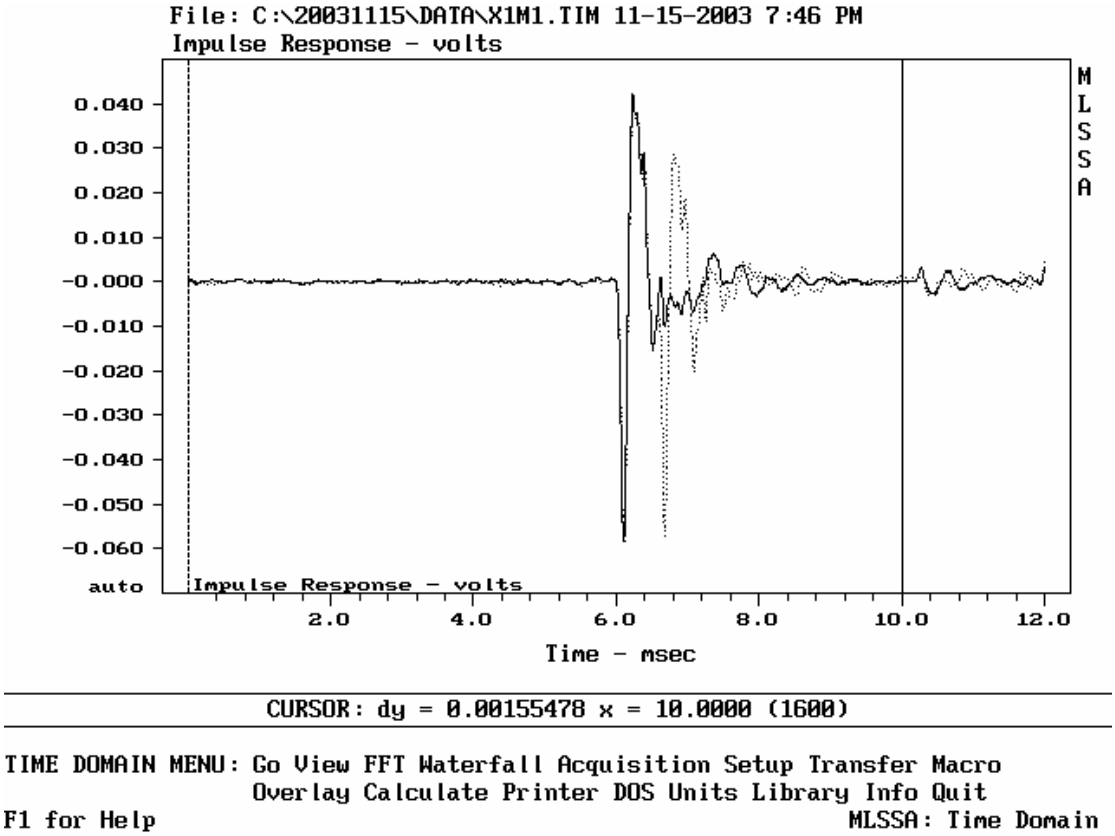

Figure 2.12 The MLS signal of free field measurement (solid line) and impedance measure (dotted line) in time domain. They are coincident with each other at the beginning.

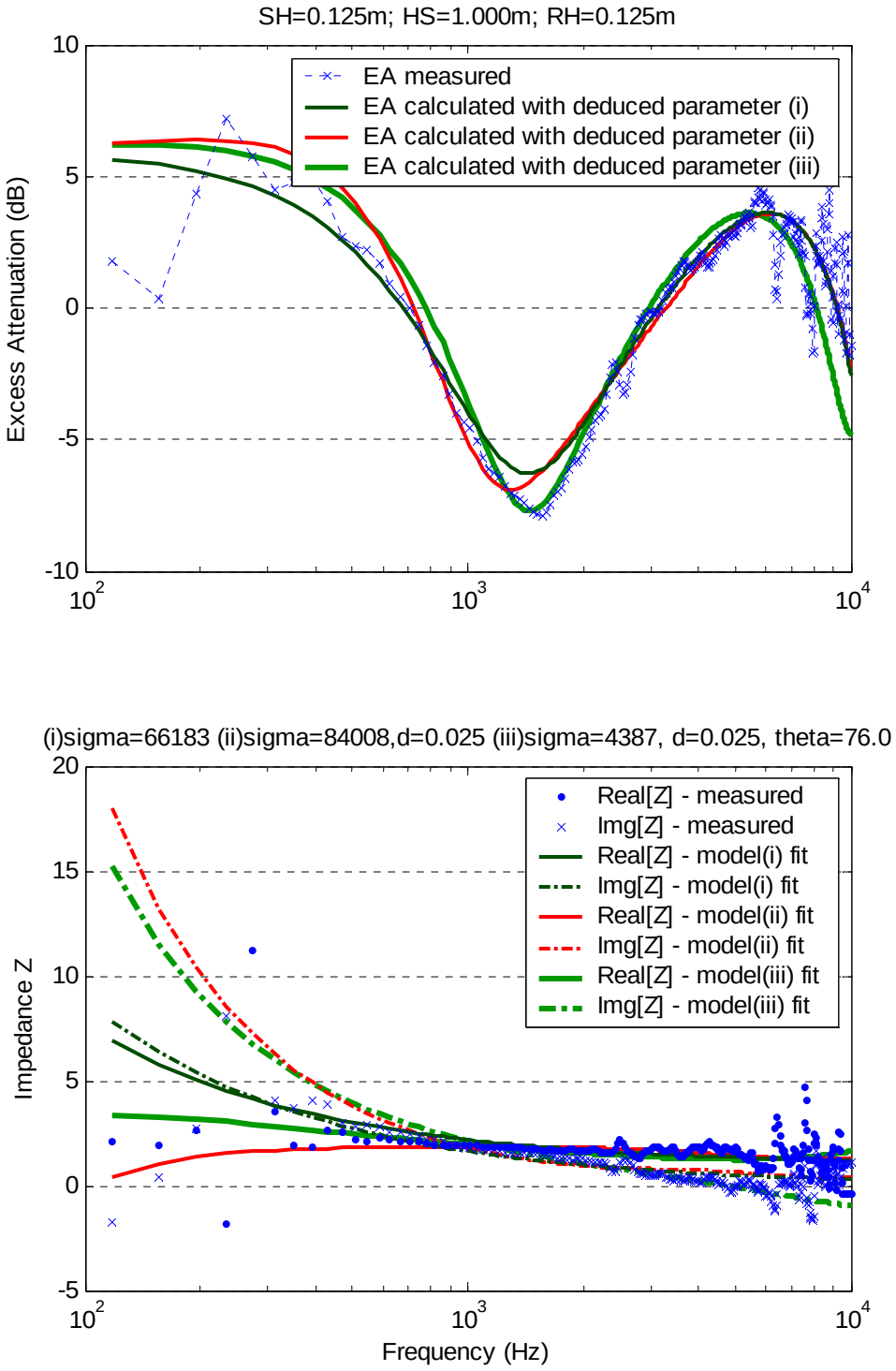

Figure 2.13 Impedance deduction and parametric fitting of measurement with incident angle of 76°. The height of the source (SH), the horizontal separation between the source and receiver (HS), and the height of the receiver (RH) were 0.125m, 1.0m, and 0.125m respectively.

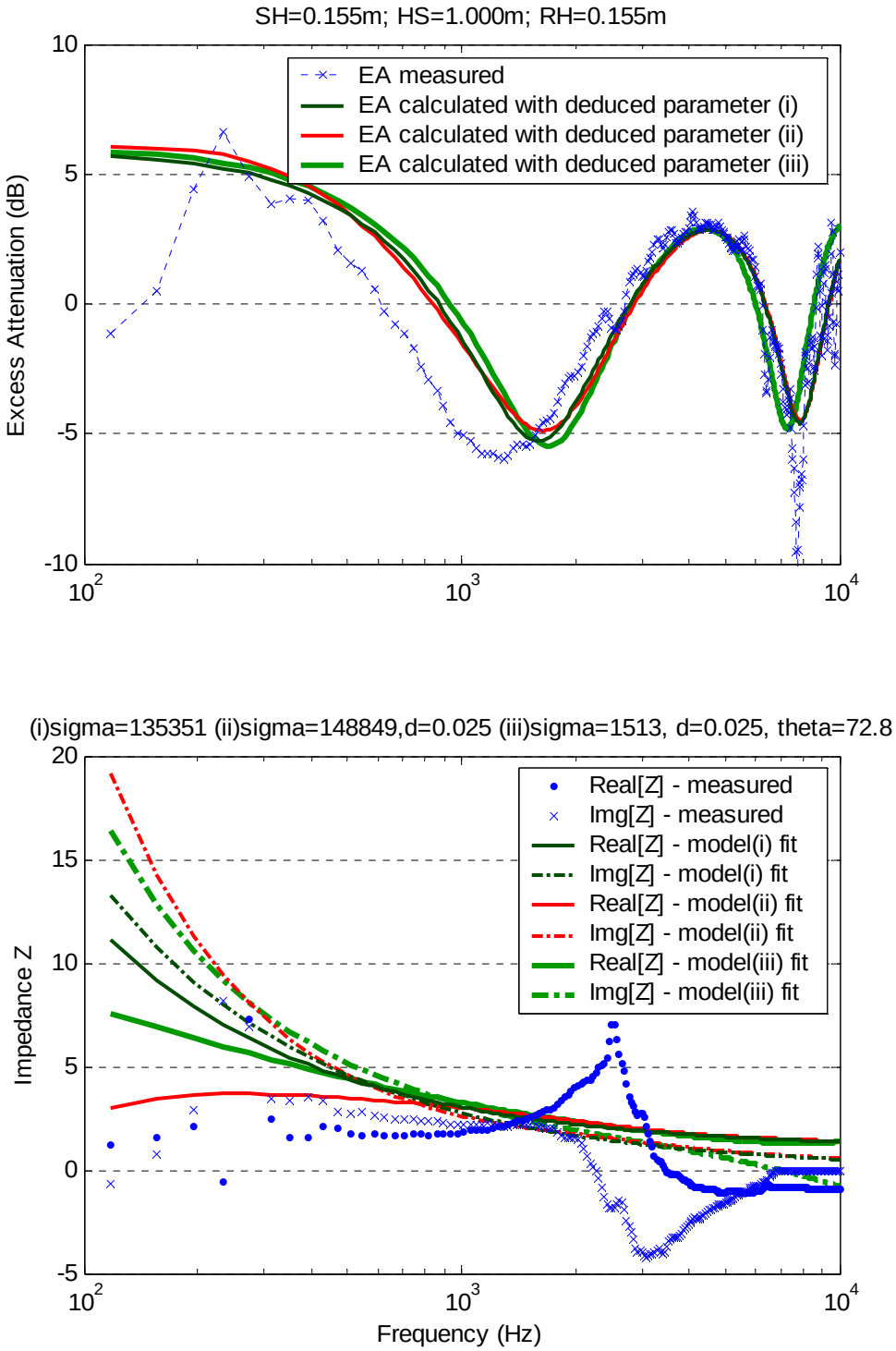

Figure 2.14 Impedance deduction and parametric fitting of measurement with incident angle of 72.8°. The height of the source (SH), the horizontal separation between the source and receiver (HS), and the height of the receiver (RH) were 0.155m, 1.0m, and 0.155m respectively.

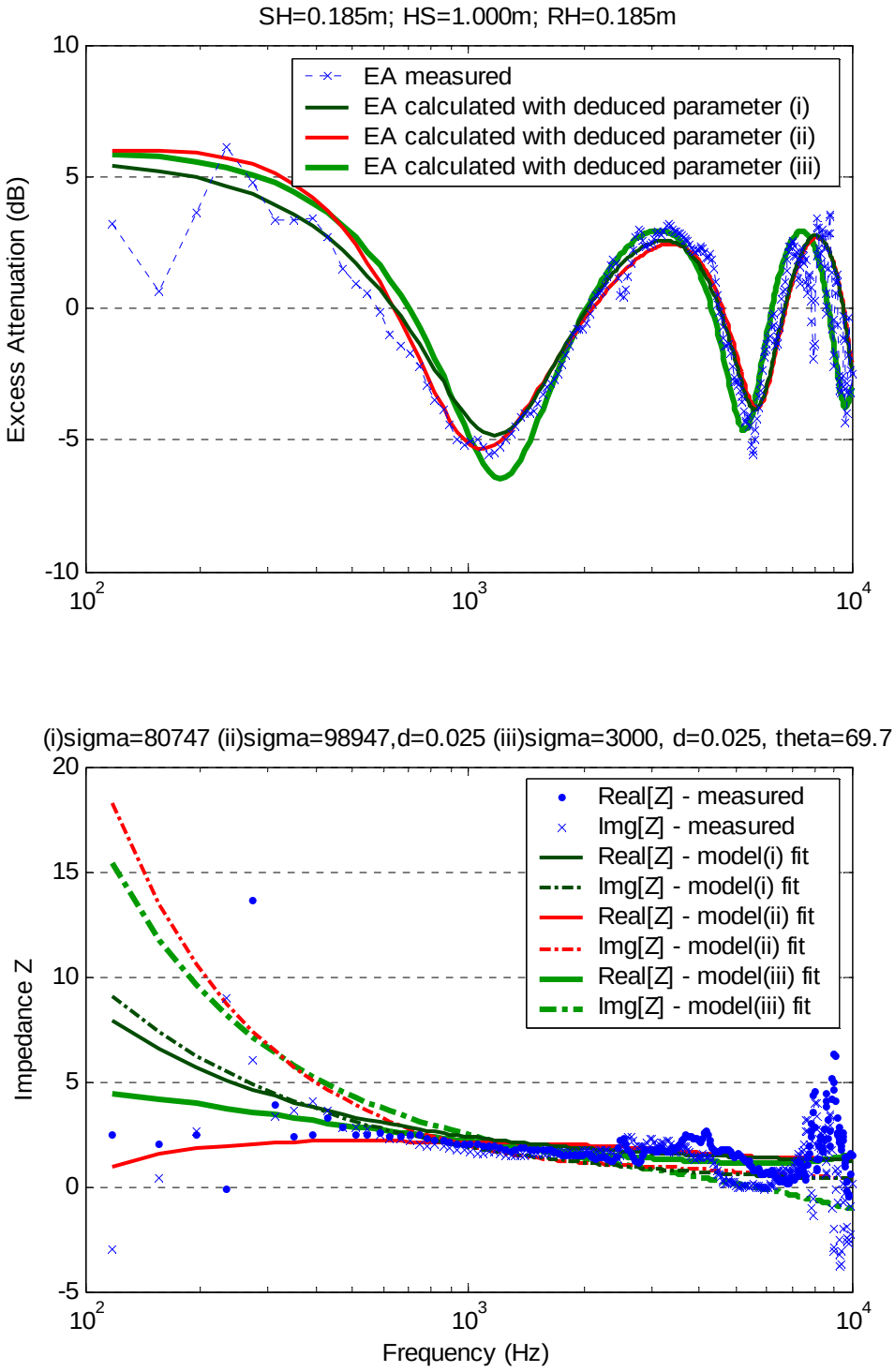

Figure 2.15 Impedance deduction and parametric fitting of measurement with incident angle of 69.7°. The height of the source (SH), the horizontal separation between the source and receiver (HS), and the height of the receiver (RH) were 0.185m, 1.0m, and 0.185m respectively.

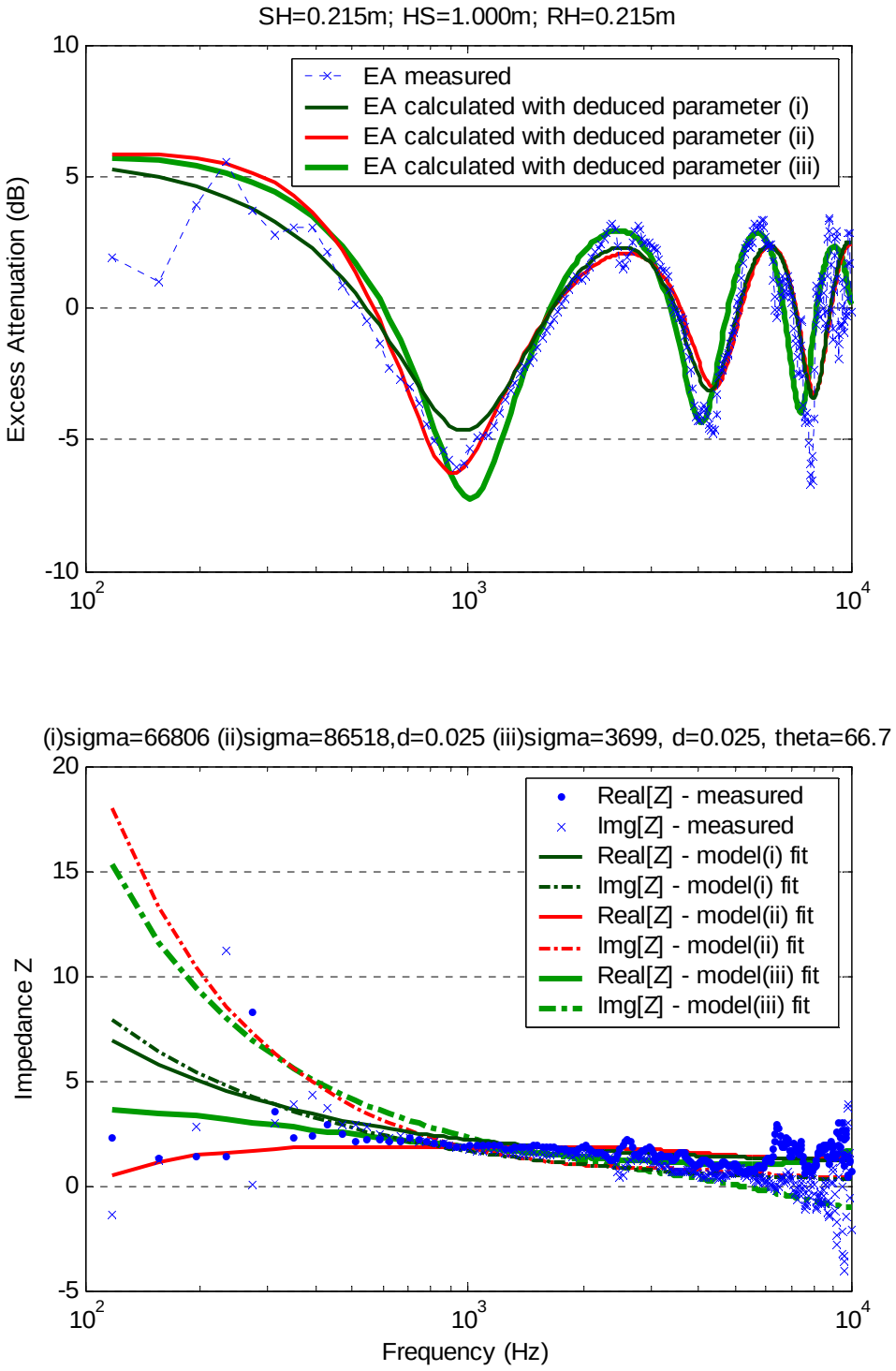

Figure 2.16 Impedance deduction and parametric fitting of measurement with incident angle of 66.7°. The height of the source (SH), the horizontal separation between the source and receiver (HS), and the height of the receiver (RH) were 0.215m, 1.0m, and 0.215m respectively.

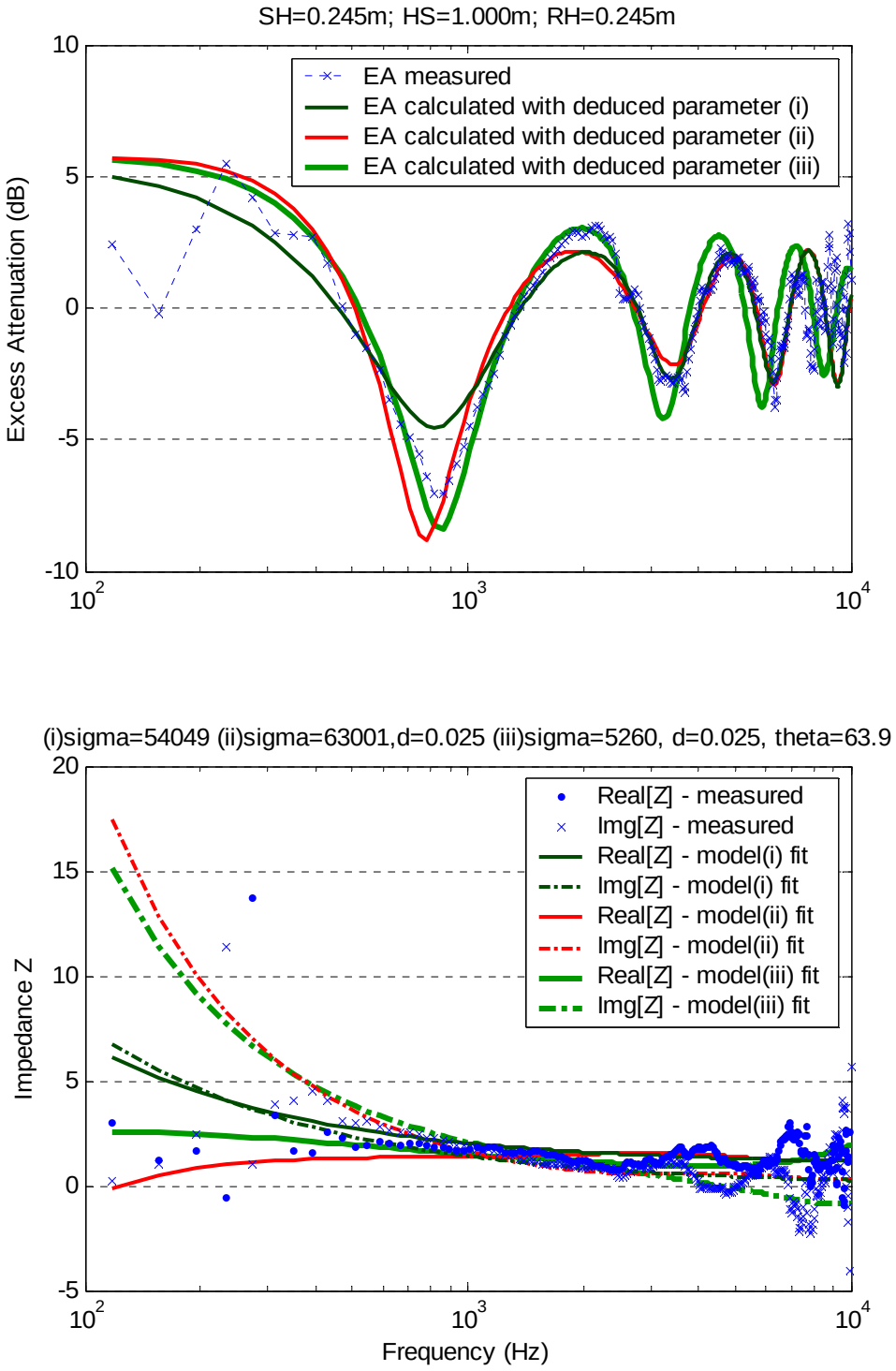

Figure 2.17 Impedance deduction and parametric fitting of measurement with incident angle of 63.9°. The height of the source (SH), the horizontal separation between the source and receiver (HS), and the height of the receiver (RH) were 0.245m, 1.0m, and 0.245m respectively.

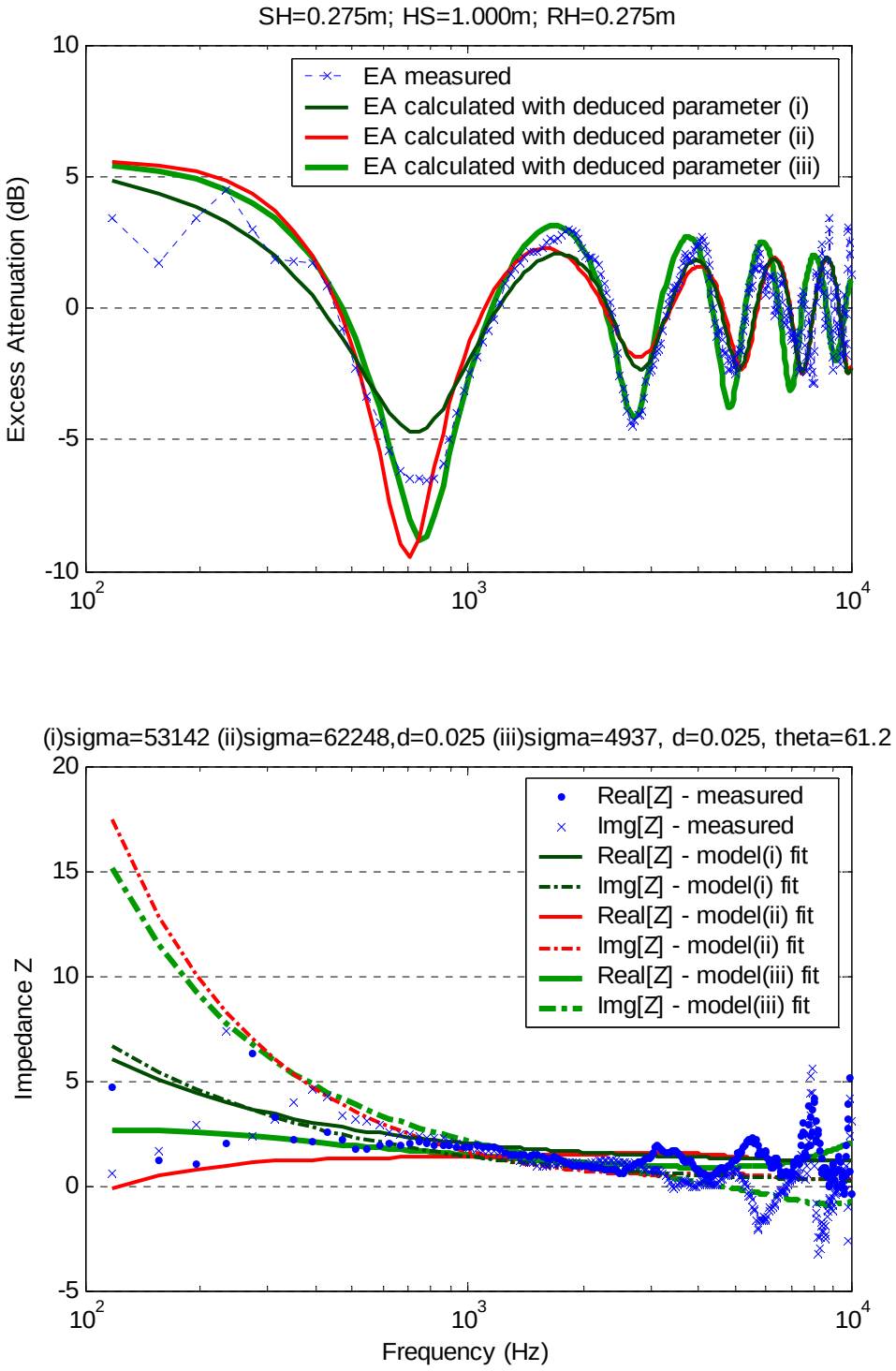

Figure 2.18 Impedance deduction and parametric fitting of measurement with incident angle of 61.2°. The height of the source (SH), the horizontal separation between the source and receiver (HS), and the height of the receiver (RH) were 0.275m, 1.0m, and 0.275m respectively.

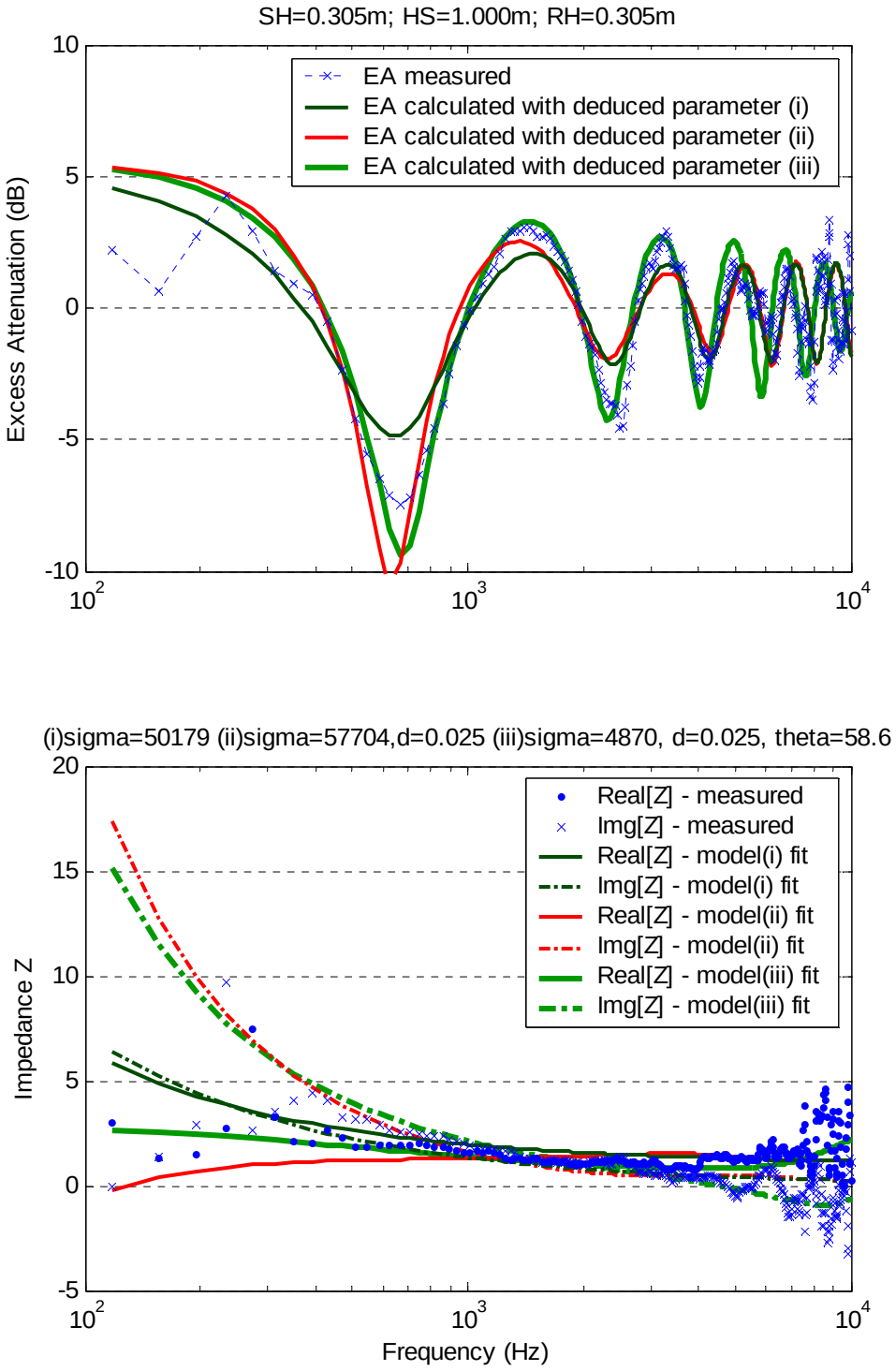

Figure 2.19 Impedance deduction and parametric fitting of measurement with incident angle of 58.6°. The height of the source (SH), the horizontal separation between the source and receiver (HS), and the height of the receiver (RH) were 0.305m, 1.0m, and 0.305m respectively.

no of simulation	λ_{max}	φ_{max}	Newton-Raphson		Downhill Simplex	
			elapsed time (s)	σ_e (MKS rayls/m)	elapsed time (s)	σ_e (MKS rayls/m)
01	0.1	0.0	14	19737	141	19737
02	0.2	0.0	15	17772	136	17772
03	0.3	0.0	15	16982	155	17119
04	0.4	0.0	18	16263	144	16359
05	0.5	0.0	12	15532	161	15580
06	0.6	0.0	5	12140	144	14688
07	0.7	0.0	21	7061	173	12313
08	0.8	0.0	5	4842	167	12181
09	0.9	0.0	15	8743	172	10210
10	1.0	0.0	8	4982	167	10481
11	0.0	0.1 x π	15	15106	158	15123
12	0.0	0.2 x π	8	8585	162	8883
13	0.0	0.3 x π	11	351	189	3773
14	0.0	0.4 x π	23	417	207	2795
15	0.0	0.5 x π	19	912	229	2447
16	0.0	0.6 x π	17	398	255	2431
17	0.0	0.7 x π	37	869	260	218
18	0.0	0.8 x π	19	11	290	137
19	0.0	0.9 x π	30	545	347	115
20	0.0	1.0 x π	39	1198	344	55
21	0.1	0.1 x π	14	15367	165	15378
22	0.2	0.2 x π	7	7317	177	7659
23	0.3	0.3 x π	15	69	205	2299
24	0.4	0.4 x π	32	857	215	2383
25	0.5	0.5 x π	14	30	269	2084
26	0.6	0.6 x π	20	773	278	1421
27	0.7	0.7 x π	39	30	309	2
28	0.8	0.8 x π	29	677	343	247
29	0.9	0.9 x π	30	48	366	20
30	1.0	1.0 x π	35	235	381	29

Table 2.1 Summary for simulations of impedance deduction with different error.

No. of measurement	Angle of incident	Effective flow resistivity deduced, σ_e (MKS rayls/m)		
		model (i)	model (ii)	model (iii)
1	76.0°	66183	84008	4387
2	72.8°	135351	148849	1513
3	69.7°	80747	98947	3000
4	66.7°	66806	86518	3699
5	63.9°	54049	63001	5260
6	61.2°	53142	62248	4937
7	58.6°	50179	57704	4870
Average		72351	85896	3952

Table 2.2 Results of impedance deduction measurements with different angles.

Chapter 3 Parallel Barriers in front of a Façade

3.1 Introduction

In recent literature on outdoor sound propagation with noise barriers, two commonly utilized methods are the image source method (ISM) and the boundary element method (BEM). Models of the ISM are based on analytical solution for predicting the diffraction and reflection of sound. In this method, image sources that make possible contributions are first determined and their contributions are calculated according to their paths of contribution. The overall sound pressure is computed by coherent summation of all the contribution from possible image sources. This coherence summation provides the consideration in the interfering phenomenon of the sound wave. For the BEM, the principle is based on the Helmholtz integration equation and the exact solution is obtained numerically. It is very suitable for the outdoor situations as only discretization on the boundary is needed. The flexibility on the boundary geometry makes the method applicable to complex situations with multiple barriers and reflecting surfaces. With the advancement of the numerical technique and computation equipment, this method is found to be promising. In current practice, however, this method is still limited by its huge requirement of computation resources.

For simple scenarios in which a single noise barrier is placed above a ground surface, there are numerous studies [52,53,56] for the shielding performance with the use of the ISM. The diffraction solution of Hadden and Pierce [42] has been utilized in most of the studies. Koers [64] later has suggested a heuristic diffraction solution of absorbing wedge

which is a modification of the Hadden and Pierce solution. Daigle et al. [31] claimed that the results from this model deviated from experimental data. However, Panneton et al. [89] have applied this heuristic model in their study of hard and absorbent parallel noise barriers and found good agreement with their experimental results. Salomons et al. [100,101] have also conducted comparison with the BEM, parabolic equation method, and experimental data. He found the Koers's solution is considerably more accurate than reported by Daigle et al. The accuracy analysis in which they conducted also concludes the ISM is well applicable in situation with multiple reflections and diffractions. More recently, Li and Tang [74] have developed an image source model for the prediction of the insertion loss of a single barrier placed in front of a tall building. Comparisons of the results with indoor experimental data and wave-based boundary element formulation show reasonably good agreement over a broad frequency range.

Success on the applications of the ISM provides us great confidence in the model development for the acoustic performance evaluation of parallel barriers placed in front of a building façade which is commonly encountered in high-rise cities. In the following sections, we report the development of the image source model presented in [63]. The hierarchy of image sources making contribution to the overall sound level and calculations of the corresponding contributions will be discussed in details. The prediction results from the image source model will be compared to the results from the wave-based boundary element formulation for validation. The effect on the shielding efficiency by mounting absorptive material on the surface of the barriers will be analyzed.

3.2 Theory

3.2.1 Geometrical configuration of the problem

In the present study, a typical scenario of a high-rise city as shown in figure 3.1 is considered in which a pair of parallel barriers is aligned with a row of tall buildings. Modeling this scenario, the tall buildings are replaced by a flat façade surface perpendicular to the ground. To facilitate the numerical analysis, a rectangular co-ordinate system is chosen where the façade surface lies on the $x = 0$ plane and the ground surface lies on the $z = 0$ plane. The origin is located on the ground surface at the bottom of the façade. A pair of barriers is placed parallel to the façade where the near-side barrier **B1** is located at a horizontal distance L from the building façade. The far-side barrier **B2** is located at a horizontal distance W from the near-side barrier. The distance W_1 and W_2 are the horizontal distances measured from the source to the near-side and far-side barriers **B1** and **B2** respectively.

In order to study the effect of sound absorbent towards the acoustic performance, we allow those reflecting surfaces with finite impedance in our model. The various surfaces are characterized by the specific surface admittance of β_{F}, β_{B11}, β_{B12} β_{B21}, β_{B22}, $\beta_{\mathrm{G1}}, \beta_{\mathrm{G2}}$, and, β_{G3} for the facade surface Γ_{F}, the outer surface of the near-side barrier Γ_{B11}, the inner surface of the near-side barrier Γ_{B12}, the inner surface of the far-side barrier Γ_{B21}, the outer surface of the far-side barrier Γ_{B22}, the ground between the building façade and the near-side barrier Γ_{G1}, the ground between both barriers Γ_{G2}, the

ground behind the far-side barrier Γ_{G3}, respectively. The various notations of the admittance are shown in figure 3.1 also.

To simplify the problem, we limit our consideration to the situation where the source denoted by **S** and receiver denoted by $\mathfrak{R}$ are located at the same vertical plane at $y = 0$. We assume that the pair of barriers and the building façades are infinitely long along the *y*-axis such that contributions from the vertical edges of the barriers and facades are ignored in our analysis. By this simplification, it becomes a two dimensional problem only. The respective coordinates of the source and receiver are given by $\mathbf{S} \equiv (x_S, 0, z_S)$ and $\mathfrak{R} \equiv (x_R, 0, z_R)$ where the subscripts S and R are used to represent the corresponding parameters for the source and receiver, respectively. In addition, we only consider the case where both barriers have the same height, *H*. The top edges of the near-side and far-side barriers are denoted by $\mathbf{E1} \equiv (L, 0, H)$ and $\mathbf{E2} \equiv (L + W, 0, H)$ respectively.

3.2.2 Principle of Image Source Method

For the image source method (ISM), the total sound pressure at a particular location is the coherence summation of all contributions from the image sources that can make contribution to that location. The main tasks are to identify all the possible image sources and calculate the corresponding contributions.

We identify the possibility of contribution of an image source by determining whether a valid transmission path can be established between the source and the receiver. The possible paths may be through direct transmission, reflection, and diffraction. They can be any combinations of reflections and diffractions with different orders. To reduce the

complexity in the determination of all possible paths, we only consider diffraction with the first order. Any further diffraction would be ignored. This assumption is justifiable because the diffracted sound field is generally much less than the direct and reflected waves. By this simplification, we can classify the contribution into two groups.

3.2.3 Calculation of Contribution

There are two groups of contribution. The first group consists of paths without any diffraction. (i.e. The image source can be observed by the receiver in straight line of sight.) The possible paths belonging to this group may be through direct transmission or reflection. We refer the image source in this group as a primary image. For a path of direct transmission, the contribution is calculated by

$$P_{direct}(\mathbf{S},\mathfrak{R}) = \begin{cases} -i \cdot H_0^{(1)}(k \cdot R) & \text{, for 2 - dimensional cylindrical wave} \\ \dfrac{e^{i \cdot k \cdot R}}{R} & \text{, for 3 - dimensional spherical wave} \end{cases}, \qquad (3.1)$$

where, $H_0^{(1)}(k \cdot R) \equiv J_n(k \cdot R) + i \cdot Y_n(k \cdot R)$ is the Hankel function of the first type

$J_n(k \cdot R)$ is a Bessel function of the first kind

$Y_n(k \cdot R)$ is a Bessel function of the second kind

R is the distance between the source $\mathbf{S}$ and receiver $\mathfrak{R}$

k is the wave number.

For a path with reflection, we calculate the contribution by multiplying a reflection factor to the direct contribution as follow,

$$P_{reflection}(\mathbf{I}_i, \mathfrak{R}) = V_i^{(n)} \cdot P_{direct}(\mathbf{I}_i, \mathfrak{R}) \qquad (3.2)$$

The factor of reflection $V_i^{(n)}$ with n order would be the multiplication of n numbers of spherical reflection coefficients as follow,

$$V_i^{(n)} = \prod_{j=1}^{n} Q_{i,j}\left(\mathbf{I}_i^{(n)}, \mathfrak{R}, \beta_j\right) \tag{3.3}$$

where, $\mathbf{I}_i^{(n)}$ denotes the i th image source with reflective order of n

β_j is the surface admittance of the j th reflection

$Q_{i,j}$ is the reflection coefficient based on admittance β_j and the distance between the image source $\mathbf{I}_i^{(n)}$ and receiver $\mathfrak{R}$. For cylindrical wave, we assume the coefficient to be the plane wave reflection coefficient. For spherical wave, we use the spherical reflection coefficient.

The second group consists of paths with diffraction. The primary image source is unobservable by the receiver directly. It is the diffraction edge that can be observed by the receiver in a straight line of sight. We refer the diffraction edge as a secondary image. There may be various orders of reflections before and after the diffraction. We denote the number of reflections before diffraction as n while the number of reflections after diffraction as q. The contribution of the k th path is determined by,

$$P_{diffraction} = V_k^{(q)} \cdot V_i^{(n)} \cdot T\left(\mathbf{I}_i^{(n)} \mid \mathbf{E}, \mathbf{E}_k^{(q)} \mid \mathfrak{R}, \boldsymbol{\beta}_{\mathrm{S}}, \boldsymbol{\beta}_{\mathrm{R}}\right) \tag{3.4.}$$

where, $V_k^{(q)}$ is the reflection factor account for the reflections before the diffraction

$V_i^{(n)}$ is the reflection factor account for the reflections after the diffraction

$T\left(\mathbf{I}_i^{(n)} \mid \mathbf{E}, \mathbf{E}_k^{(q)} \mid \mathfrak{R}, \boldsymbol{\beta}_{\mathrm{S}}, \boldsymbol{\beta}_{\mathrm{R}}\right)$ is the diffraction term

The diffraction term is the diffraction contribution of the sound pressure from a primary image source at $\mathbf{I}_i^{(n)}$, undergoing *n* number of reflections, diffracting at edge $\mathbf{E}$, and then undergoing *q* number of reflections before reaching the receiver $\mathfrak{R}$. To represent the relationship among $\mathbf{I}_i^{(n)}$ and $\mathbf{E}$ in reflection before diffraction, we use the symbol $\mathbf{I}_i^{(n)} \mid \mathbf{E}$. Similarly, we use the symbol $\mathbf{E}_k^{(q)} \mid \mathfrak{R}$ to represent the relationship among $\mathbf{E}_k^{(q)}$ and $\mathfrak{R}$ in reflection after diffraction. Symbol "|" is used instead of "," for better differentiation among $\mathbf{E}$ and $\mathbf{E}_k^{(q)}$. The term $\boldsymbol{\beta}_\mathrm{S}$ represents the specific surface admittance of barrier surface facing the source while $\boldsymbol{\beta}_\mathrm{R}$ is the specific surface admittance of barrier surface facing the receiver. This diffraction term adopts the Koers [64] modification of the Hadden and Pierce [42] solution to an absorbing wedge. With reference to figure 3.2, the computation is as follow,

$$T\left(\mathbf{I}_i^{(n)} \mid \mathbf{E}, \mathbf{E}_k^{(q)} \mid \mathfrak{R}, \boldsymbol{\beta}_\mathrm{S}, \boldsymbol{\beta}_\mathrm{R}\right) = U_1\left(\xi_1, r_{SB}, r_{RB}\right) + Q_S \cdot U_2\left(\xi_2, r_{SB}, r_{RB}\right) + Q_R \cdot U_3\left(\xi_3, r_{SB}, r_{RB}\right) + Q_S \cdot Q_R \cdot U_4\left(\xi_4, r_{SB}, r_{RB}\right) \tag{3.5}$$

where,

$$\xi_i = \begin{cases} \left|\theta_r - \theta_s\right| & \text{for } i = 1, \text{angle from source to recevier} \\ 2\pi - \theta_s - \theta_r & \text{for } i = 2, \text{angle from image source to recevier} \\ \theta_s + \theta_r & \text{for } i = 3, \text{angle from source to image recevier} \\ 2\pi - \left|\theta_r - \theta_s\right| & \text{for } i = 4, \text{angle from image source to image recevier} \end{cases}, \tag{3.6}$$

$$U\left(\xi, r_{SB}, r_{RB}\right) = -\frac{1}{\pi} A\left(\xi\right)\left(\frac{e^{ikL}}{L}\right)\int_0^\infty e^{-y} q\left(y, \xi, r_{SB}, r_{RB}\right) dy, \tag{3.7}$$

$$A\left(\xi\right) = \frac{1}{4}\left(-\xi - 3\pi\right) + \pi\delta\left(\pi - \xi\right) \text{ with } \delta\left(x\right) = \begin{cases} 1 & \text{if } x \geq 0 \\ 0 & \text{if } x < 0 \end{cases}, \tag{3.8}$$

$$q\left(y, \xi, r_{SB}, r_{RB}\right) = \frac{1}{A\left(\xi\right)}\left(1 + \frac{i}{kL + iy}\right)\left(\frac{kL}{kL + iy}\right) \times \tan^{-1}\left[\tan\left[A\left(\xi\right)\right]\tanh\left\{\sinh^{-1}\left[\frac{yL}{kr_{SB}r_{RB}}\left(\frac{i}{2} - \frac{y}{4kL}\right)\right] \Big/ 2\right\}\right], \tag{3.9}$$

and

$$L = r_{SB} + r_{RB}. \tag{3.10}$$

in which θ_s and θ_r are respectively the angular positions of the source and receiver measured from the polar plane $\theta = 0$ along the right side of the barrier surface, r_{SB} and r_{RB} are the radial distance from the source to the edge and from the edge to the receiver respectively, $Q_{\mathrm{S}} = Q\left(\mathbf{I}_i^{(n)}, \mathbf{E}, \boldsymbol{\beta}_{\mathrm{S}}\right)$ and $Q_{\mathrm{R}} = Q\left(\mathbf{E}_k^{(q)}, \mathfrak{R}, \boldsymbol{\beta}_{\mathrm{R}}\right)$ are the spherical wave reflection coefficients accounting for the absorptive surface at the source side and receiver side respectively, and the integration in the term $U\left(\xi, r_{SB}, r_{RB}\right)$ can be done by the Laguerre technique [1].

3.2.4 Image Source Model

Image sources are formed by various combinations of reflections and deflections. One of the main tasks in the image source model is to identify all the possible image sources which make contribution to the overall sound pressure at the point of consideration. The determination of the image sources is archived by checking whether the receiver is located in the illuminated zones of the image sources. The zone of illumination is obtained from geometric information of the situation. With more complexity in the geometry, the determination would be more difficult.

Due to the lengthy content and high complexity of the model, the details of the determination of the possible images sources can be found in Appendix A. In brief, the images are classified as primary and secondary sources. For the primary image sources, there is no diffraction involved. For the secondary image sources, the contribution

involves the diffraction of sound. The image sources are further classified as sub-groups based on the sequence of diffractions and reflections. The coordinates, illumination zones, and pressure contributions of each sub-group will be discussed in details in Appendix A.

3.3 Validation with Boundary Element Method

The image source model derived in the previous section provides an effective and efficient methodology to the evaluation of the acoustic performance of parallel barriers in front of a building. For validation, we compare the results from the image source model with the results from numerical techniques. As the configuration concerned is an external problem where domains are extended to infinity, boundary element method (BEM) is chosen for comparison. This method has been extensively used to study outdoor sound propagation and performance of noise barrier. For the image source model, we have implemented the calculation by compiling with Matlab code.

A realistic outdoor configuration is used in our analysis. The near-side and far-side barriers are of identical height of 2.5 m, and, they are situated at 5 m and 15 m in front of a building façade respectively. A noise source is located at 0.25 m above the ground and 7.5 m in front of the façade, i.e. 2.5 m from the near side barrier. Two cases have been considered in our analysis. The first case considers the barriers as hard. The second case considers the inner surface of both barriers as absorptive. For the absorptive surface, the impedance surfaces are modeled with the Delany and Bazley model [34] with the flow resistivity equal to 40000 MKS rayls/m. The receivers considered are located 1m away from the façade surface and with heights of 1m, 2m, 5m and 10m. In the calculation of image source model, the maximum orders of reflections are restricted to 100 for both *n*

and q in the image source model. For the implementation of the BEM, computer codes developed by the Acoustics Research Centre at the University of Hull is utilized with the permission of Dr. K M Li. For the simplicity, the elements of BEM analysis are distributed evenly in length. The lengths of each elements are shorter than 1/10 of the corresponding wavelengths to ensure to ensure a higher accuracy for the purposes of benchmarking. Meanwhile, smaller of element sizes are used for lower frequency to ensure sufficient representation of the spatial profile. Confirmed with convergence checking, the elements sizes adopted are summarized in table 3.1. Based on the available computation resources, the height of the building façade is taken as 25m for eliminating the effect of diffraction at the top of the façade surfaces.

As shown in figures 3.3 to 3.6, we compare the spectrums of insertion loss at four receiver positions calculated by the two methods. The first two locations R=(1,0,1) and R=(1,0,2) are in the shadow zone. The third location R=(1,0,5) is near the direct line of sight. The last location R=(1,0,10) is illuminated directly by the source. Those negative values of insertion loss indicate the barriers provide no noise reduction and even enhance the noise for the particular frequency. Predicted results from both methods agree very well with each other. The ISM determines the locations of peaks and troughs in frequency domain accurately. The magnitudes of those peaks and troughs among these two methods have some small differences. The results of the ISM tend to have higher fluctuations than the predictions by the BEM. In real situation, the prediction of the high peaks and low troughs are mostly unattainable. We can also observe this phenomenon in the section with experimental validation.

Having successfully completed the predictions with hard barriers, we progress to the prediction with absorptive barriers. We assume that the inner surfaces of the parallel barriers are absorptive and model the acoustic impedance with the Delany and Bazley model [34] with the flow resistivity equal to 40,000 MKS rayls/m. This degree of absorptiveness is quite high for the outdoor situation. The value is chosen for illustrative purpose. Similarly, we calculate the insertion loss at the same locations by both methods. The results are shown in figures 3.7 to 3.10 for the four positions respectively. Again, there is quite a good agreement between the two methods. To illustrate the effect on the shielding efficiency by mounting absorptive material on the surface of the barriers, we further calculate the improvement on the insertion loss due to the absorptive material. It is defined as the extra gain in insertion loss and calculated by the difference of the insertion loss of the two cases. The results of all four positions are shown in figure 3.11. Again, we should ignore those high peaks and low troughs. In general, there are observable improvements over a broad frequency range. As the improvement is highly fluctuating along the frequency axles, it is difficult to quote a qualitative value on the overall improvement. Due to the degree of absorptiveness is assumed to be much higher than reality, the actual effect of adding absorptive surface in a real life situation would be insignificant.

3.4 Validation with Experimental Measurements

Apart from comparison with numerical method as discussed previously, we further validate the prediction model with results from experimental measurements. The measurement consists of a scaled-down configuration as shown in figure 3.12. The façade and ground surfaces are made of 8.5mm thick wooden board. The height of the

facade is 2.44m which is high enough to ignore the diffraction at the top edge. The barriers consist of 3mm thick aluminum plate with height of 0.5m and length of 4.5m. They are placed 0.75m and 1.5m in front of the wooden board respectively. The source is located 1.25m in front of the façade surface and at a height of 0.125m. The receiver is placed 0.123m in front of the building façade with various heights. For modeling the absorptive surface, we attach the same 25mm thick glass fiber with density of $48\,kg/m^3$ used in the in-situ impedance determination.

The whole measurement is conducted inside an anechoic chamber of dimensions $6\text{m}\times 6\text{m}\times 6\text{m}$. The insertion loss used for comparison is obtained by measuring the transfer function with and without the barrier. The MLS system and equipment used are the same as before. Special attentions have been put on the orientation of the speaker and microphone for the modeling of spherical waves. Details on the measurement technique has been discussed earlier in Chapter 2.

Comparison of the insertion loss spectrum for the parallel barriers with hard surfaces at locations (0.123,0,0.1), (0.123,0,0.5), (0.123,0,1) and (0.123,0,1.5) are shown in figures 3.13 to 3.16 respectively. For the parallel barriers with absorptive surfaces, the comparison of the insertion loss is shown in figures 3.17 to 3.20. In the theoretical calculation, the absorptive surface is modeled with the Delany and Bazley model [34] with the flow resistivity equal to 72,351 MKS rayls/m. This value is deduced from the method discussed in Chapter 2. In addition, we have illustrated the measured and calculated improvement on the insertion loss due to the absorptive material in figure 3.21. The theoretical predictions agree quite well with the experiment results. As mentioned in

the previous section, the theoretical prediction tends to have higher peaks and lower troughs than the measured values.

3.5 Conclusions

In this chapter, we have reported the development of a computational model for the shielding performance evaluation of parallel barriers placed in front of a tall building. The model developed is based on the ISM and various classical theories of sound propagation from geometrical acoustic. The hierarchy of the image sources making contribution to the overall sound level and the calculations of the corresponding contributions are outlined in detail. This hierarchy provides an efficient implementation in searching valid source images and shortens a lot of time for calculation. Besides, the prediction model developed contains the ability in handling surface with finite acoustic impedance. This gives the possibility for the analysis of absorptive barriers and road pavement. The prediction results from our image source model are found to be consistent with the calculated results by the BEM and experimental measurement. With the accurate prediction capability and high computational efficiency, this image source model provides a valuable tool for the evaluation in the design stage and a huge contribution to urban planning.

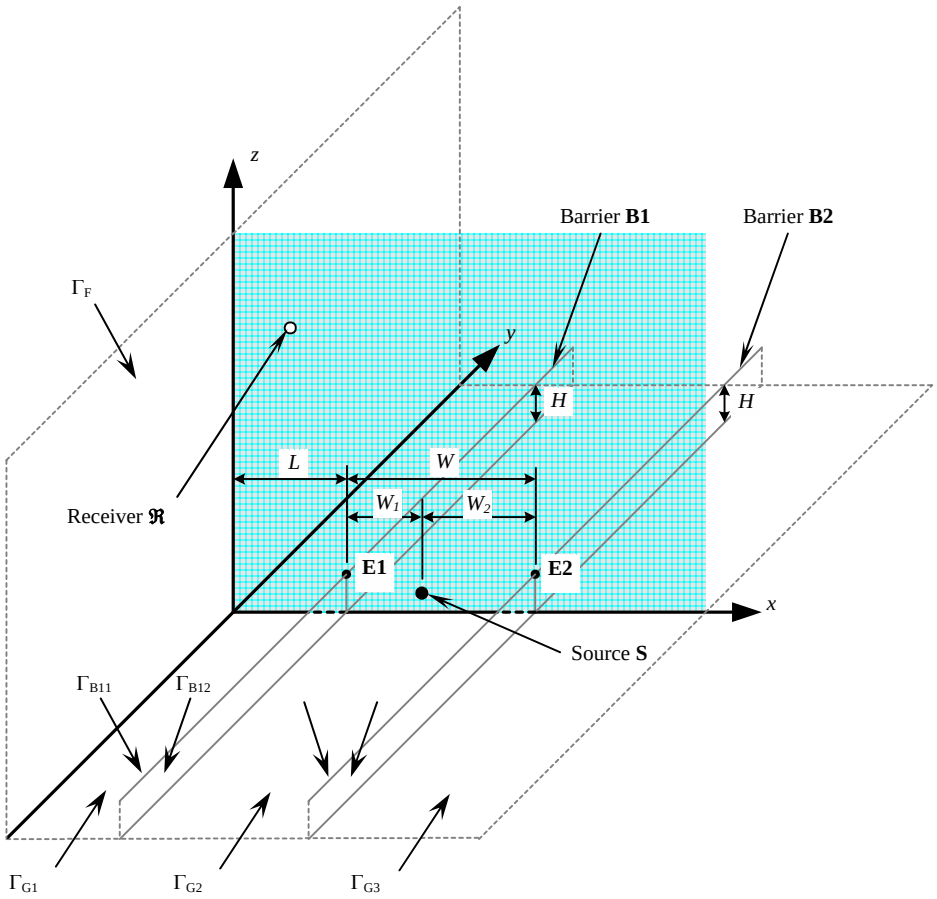

Figure 3.1 Schematic diagram of the specified problem. A source S is located at $\mathbf{I_o}\equiv(x_S, 0, z_S)$ and a receiver $\mathfrak{R}$ at $(x_R, 0, z_R)$. A pair of parallel barriers, **B1** and **B2** of height H is placed at a distance L from a façade surface Γ_F of infinite height. The barriers are separated at a distance W apart and divide the ground surface into Γ_{G1}, Γ_{G2} and Γ_{G3}.

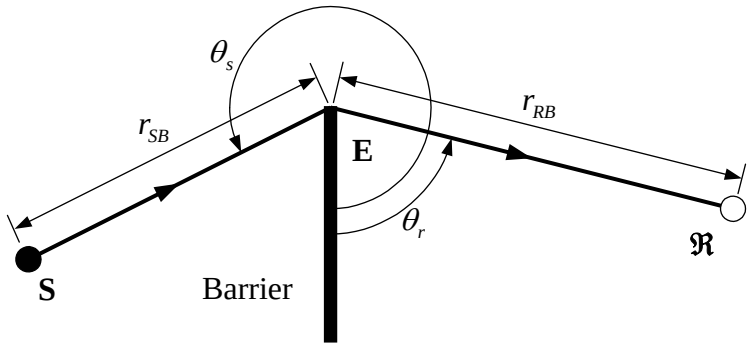

Figure 3.2 Schematic diagram of the geometrical configuration for the calculation of the diffraction component of a barrier. The distance from the source **S** to the edge **E** is denoted as r_{SB} while the distance from the edge **E** to the receiver $\mathfrak{R}$ is denoted as r_{RB}. The angle from the source **S** to the barrier surface opposite to the source **S** is denoted as θ_s. The angle from the receiver $\mathfrak{R}$ to the barrier surface opposite to the source **S** is denoted as θ_r.

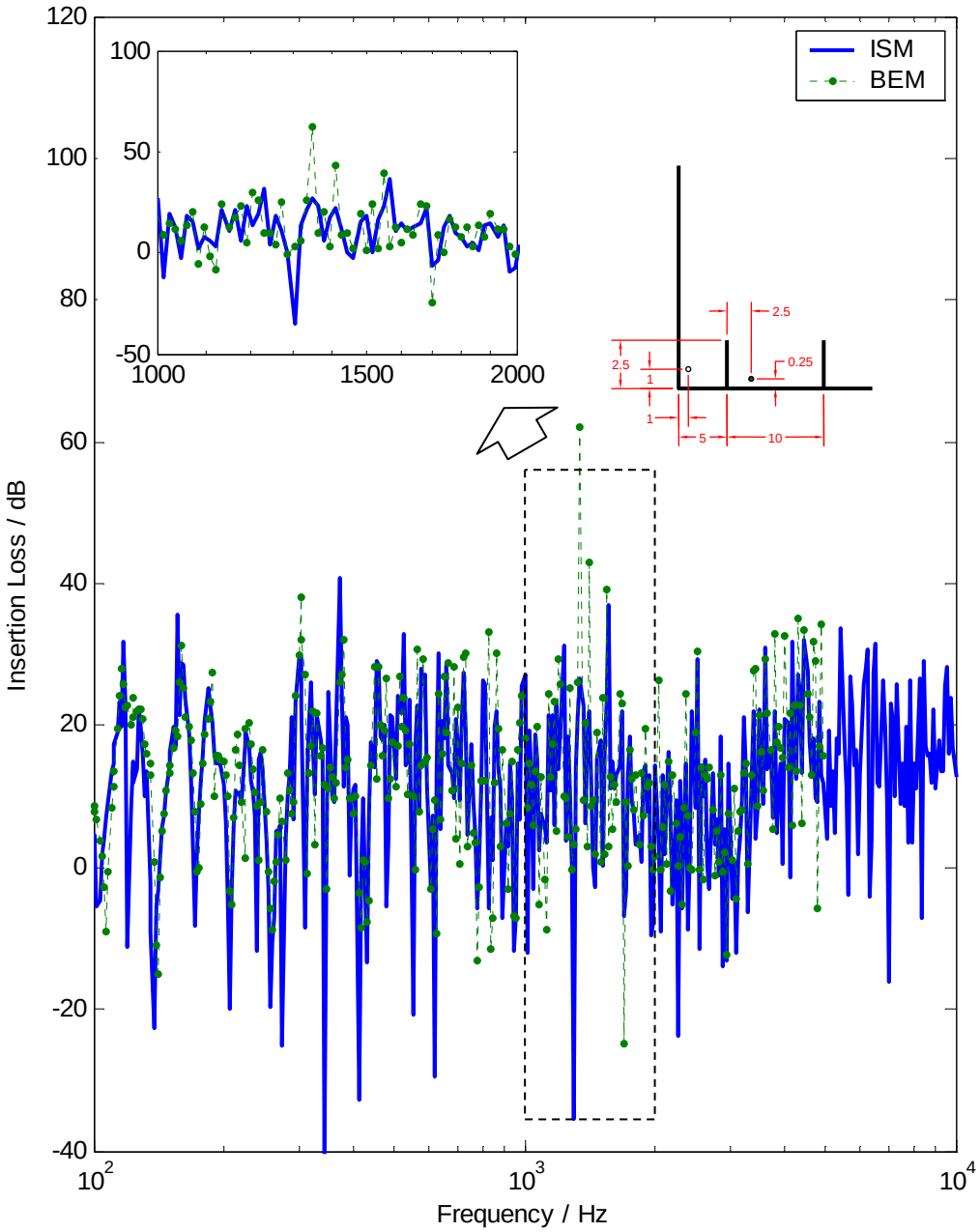

Figure 3.3 The spectrum of insertion losses (IL) at location $\mathfrak{R}$=(1,0,1) with parallel barriers having hard inner surfaces in front of a building façade. The solid line represents predictions by the image source method (ISM) and the dashed line with dots represents numerical predictions based on the boundary element method (BEM).

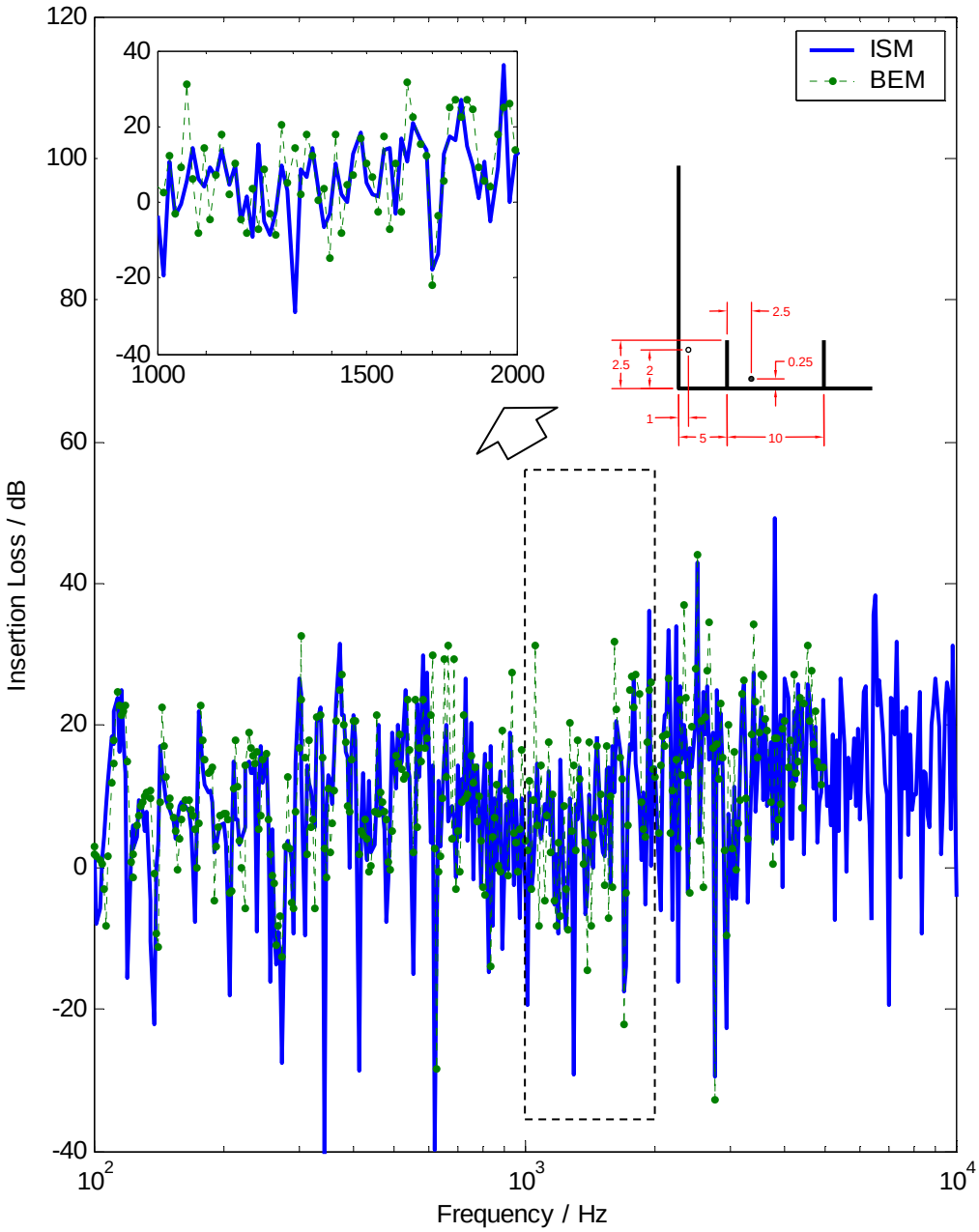

Figure 3.4 The spectrum of insertion losses (IL) at location $\mathfrak{R}$=(1,0,2) with parallel barriers having hard inner surfaces in front of a building façade. The solid line represents predictions by the image source method (ISM) and the dashed line with dots represents numerical predictions based on the boundary element method (BEM).

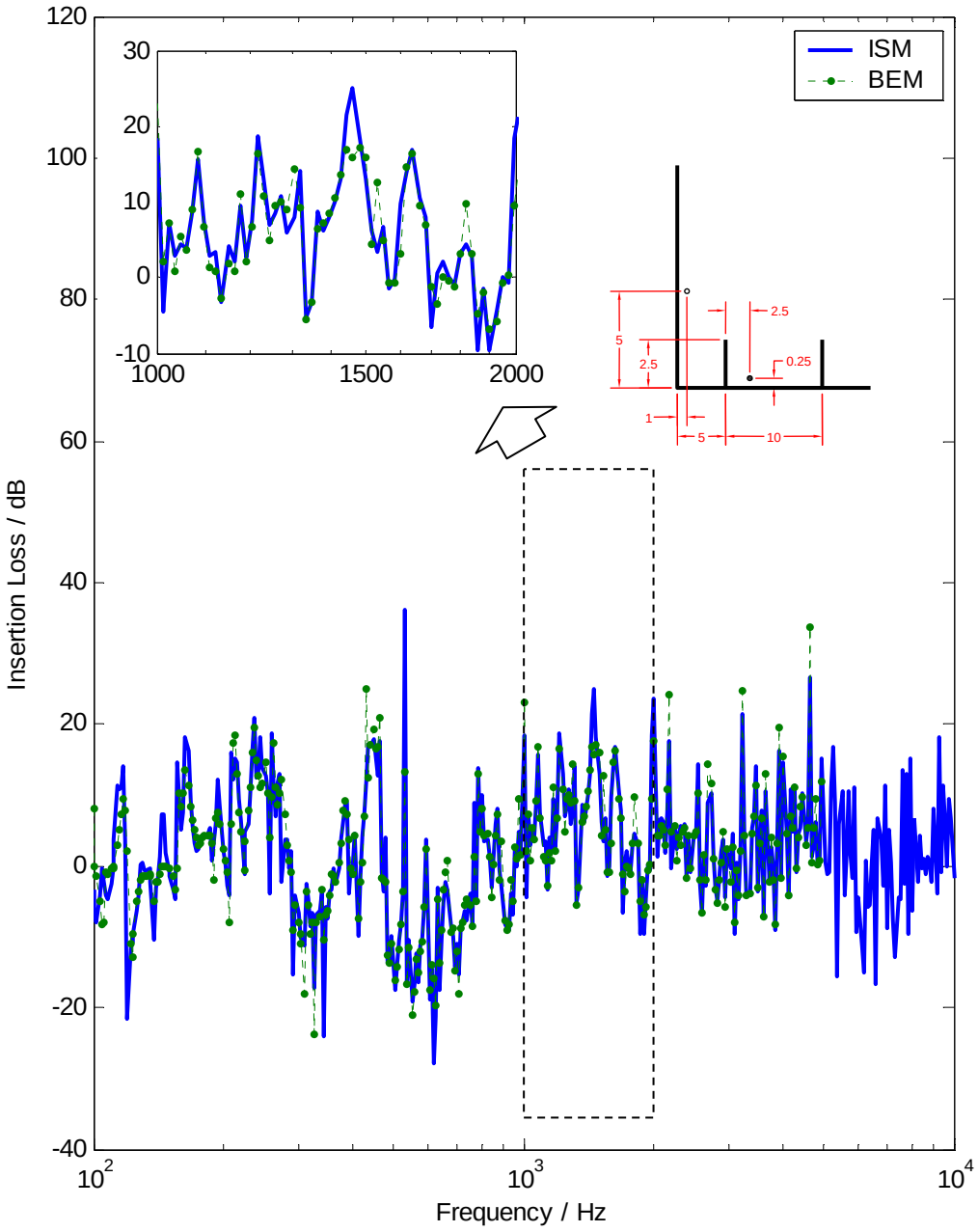

Figure 3.5 The spectrum of insertion losses (IL) at location $\mathfrak{R}$=(1,0,5) with parallel barriers having hard inner surfaces in front of a building façade. The solid line represents predictions by the image source method (ISM) and the dashed line with dots represents numerical predictions based on the boundary element method (BEM).

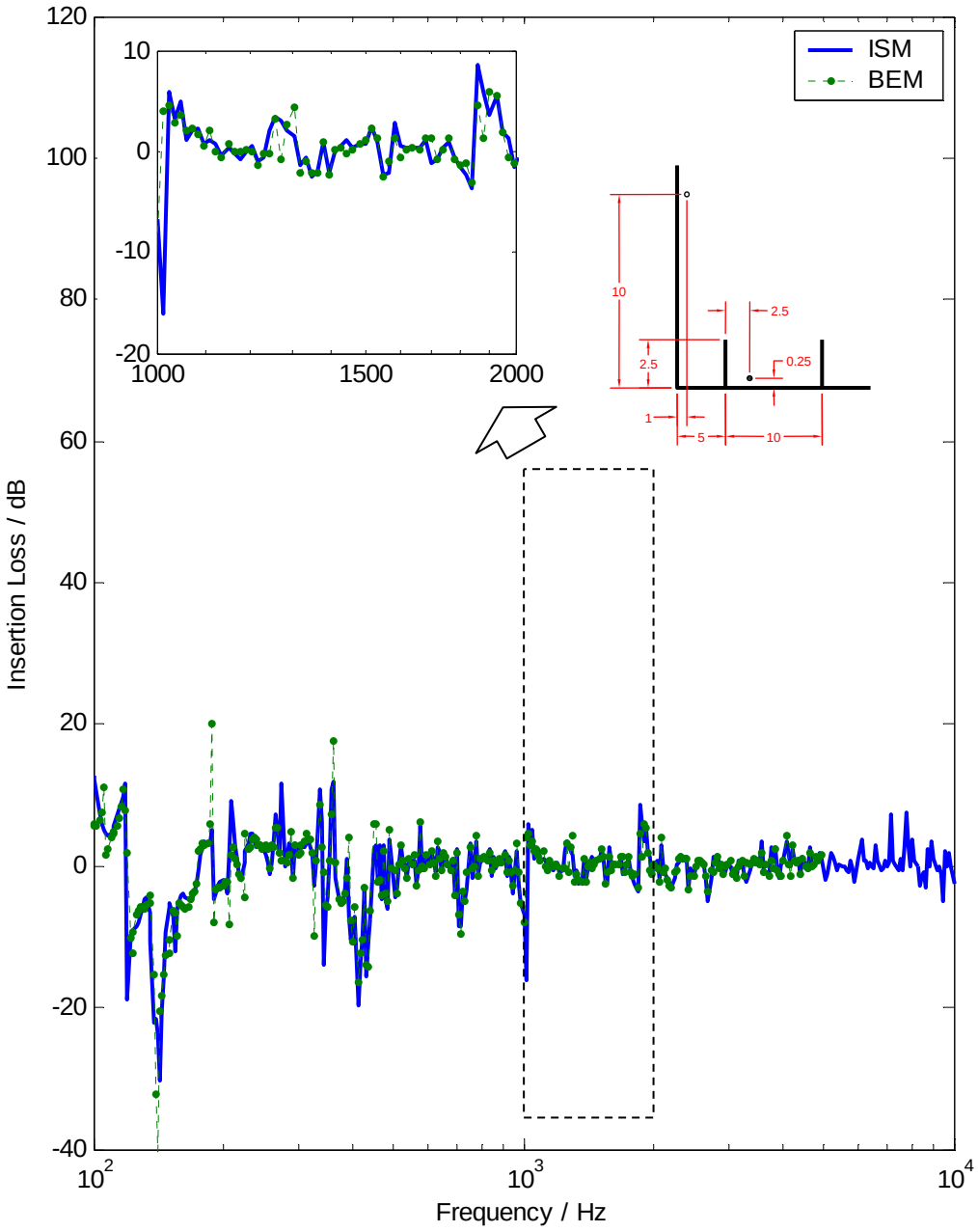

Figure 3.6 The spectrum of insertion losses (IL) at location $\mathfrak{R}$=(1,0,10) with parallel barriers having hard inner surfaces in front of a building façade. The solid line represents predictions by the image source method (ISM) and the dashed line with dots represents numerical predictions based on the boundary element method (BEM).

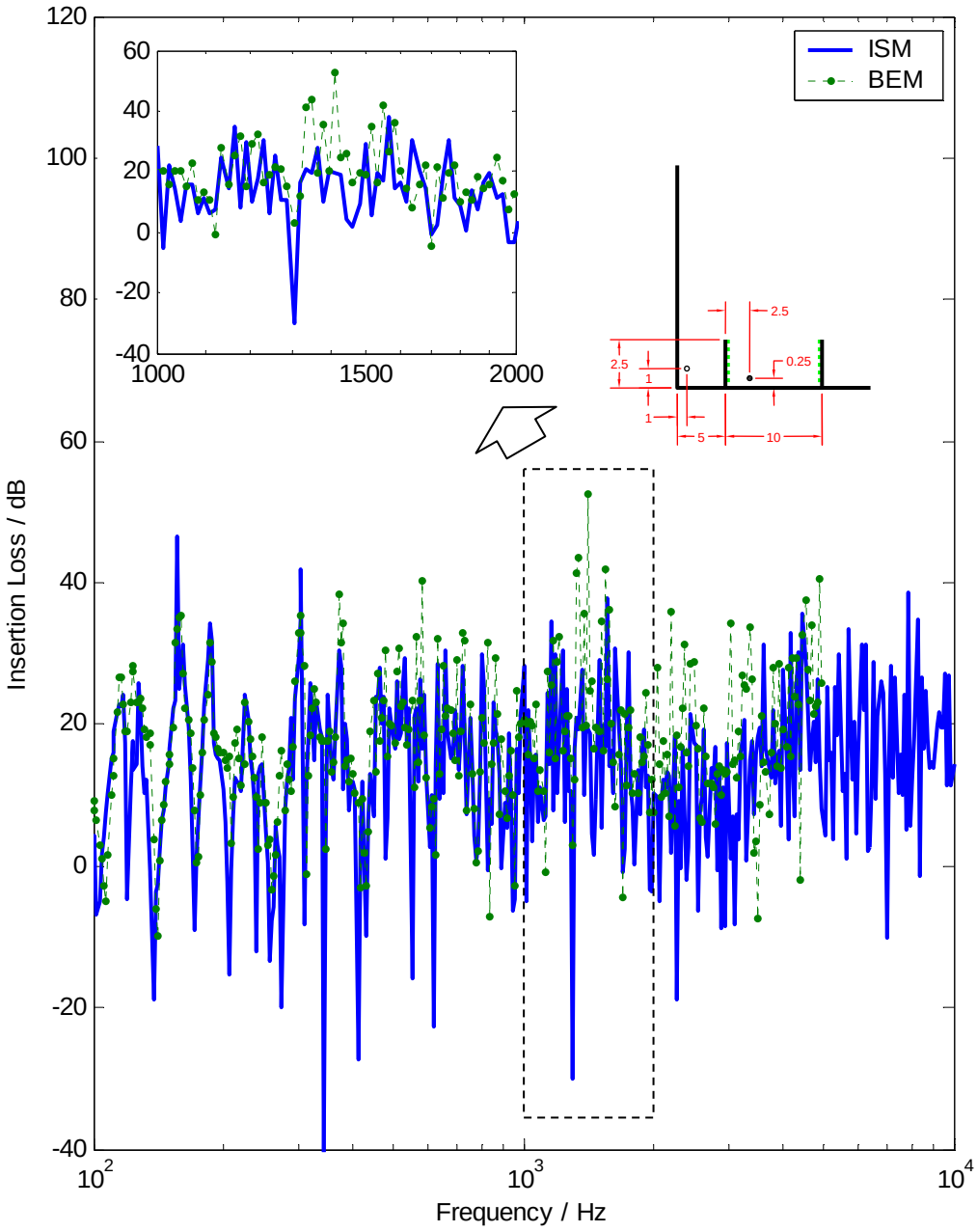

Figure 3.7 The spectrum of insertion losses (IL) at location $\mathfrak{R}$=(1,0,1) with parallel barriers having absorptive inner surfaces in front of a building façade. The impedance of the inner surface is modeled with the Delany and Bazley model with the flow resistivity equal to 40,000 MKS rayls/m. The solid line represents predictions by the image source method (ISM) and the dashed line with dots represents numerical predictions based on the boundary element method (BEM).

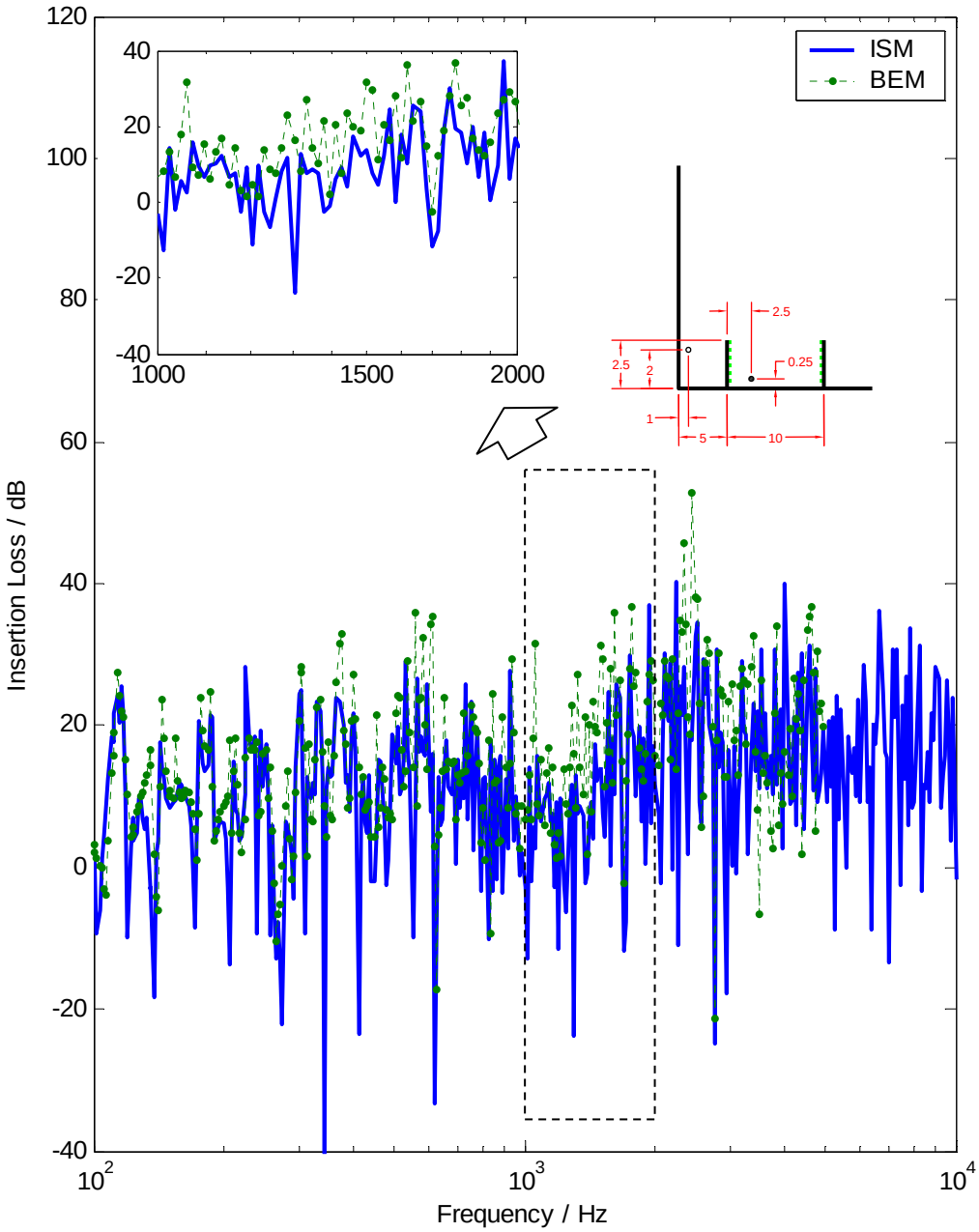

Figure 3.8 The spectrum of insertion losses (IL) at location $\mathfrak{R}$=(1,0,2) with parallel barriers having absorptive inner surfaces in front of a building façade. The impedance of the inner surface is modeled with the Delany and Bazley model with the flow resistivity equal to 40,000 MKS rayls/m. The solid line represents predictions by the image source method (ISM) and the dashed line with dots represents numerical predictions based on the boundary element method (BEM).

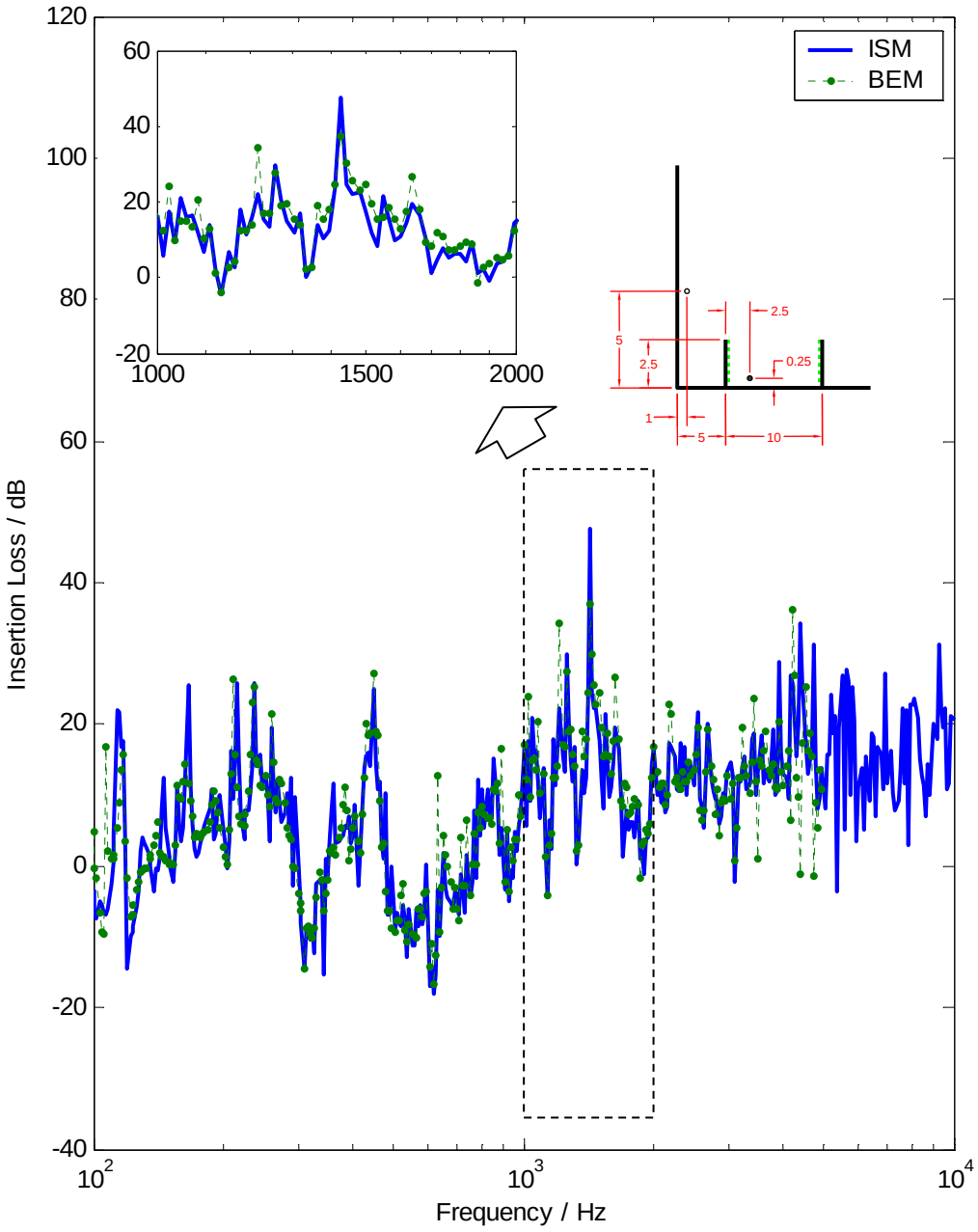

Figure 3.9 The spectrum of insertion losses (IL) at location $\mathfrak{R}$=(1,0,5) with parallel barriers having absorptive inner surfaces in front of a building façade. The impedance of the inner surface is modeled with the Delany and Bazley model with the flow resistivity equal to 40,000 MKS rayls/m. The solid line represents predictions by the image source method (ISM) and the dashed line with dots represents numerical predictions based on the boundary element method (BEM).

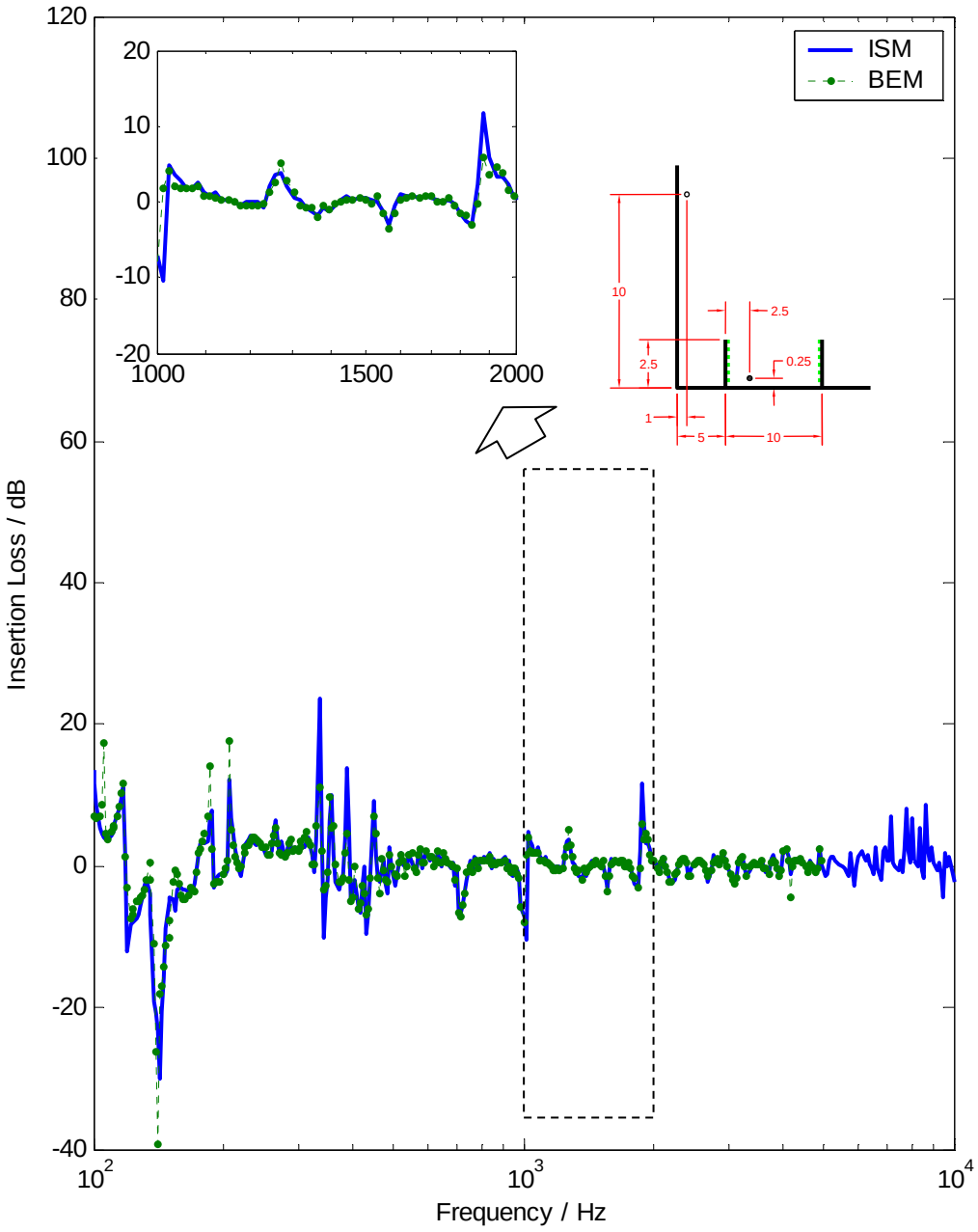

Figure 3.10 The spectrum of insertion losses (IL) at location $\mathfrak{R}$=(1,0,10) with parallel barriers having absorptive inner surfaces in front of a building façade. The impedance of the inner surface is modeled with the Delany and Bazley model with the flow resistivity equal to 40,000 MKS rayls/m. The solid line represents predictions by the image source method (ISM) and the dashed line with dots represents numerical predictions based on the boundary element method (BEM).

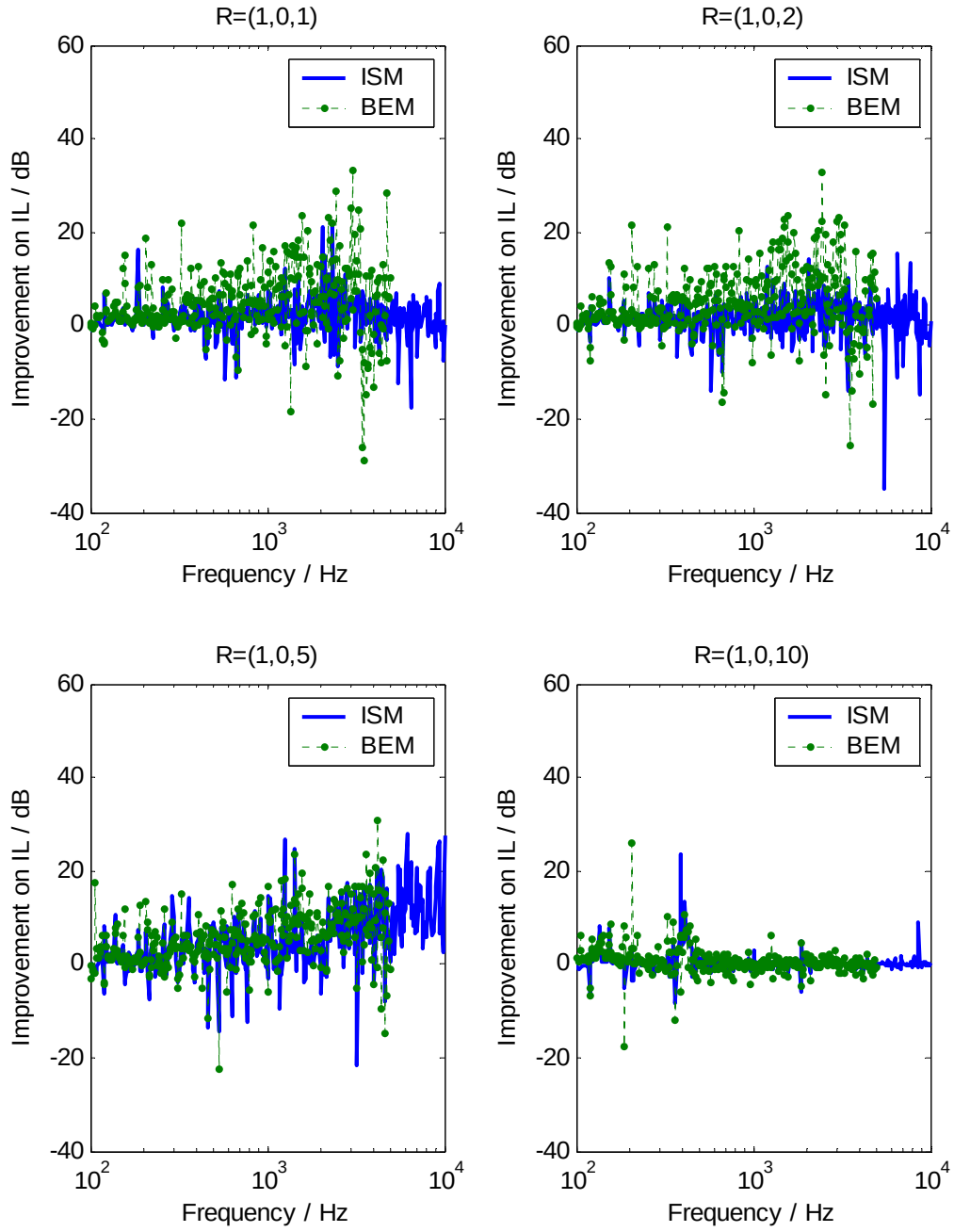

Figure 3.11 The spectrum of improvement in insertion losses (IL) at locations $\mathfrak{R}$=(1,0,1), $\mathfrak{R}$=(1,0,2), $\mathfrak{R}$=(1,0,5), and $\mathfrak{R}$=(1,0,10) with parallel barriers having absorptive inner surfaces in front of a building façade over barriers with hard surfaces. The solid line represents predictions by the image source method (ISM) and the dashed line with dots represents numerical predictions based on the boundary element method (BEM).

Figure 3.12 The experimental measurement set-up.

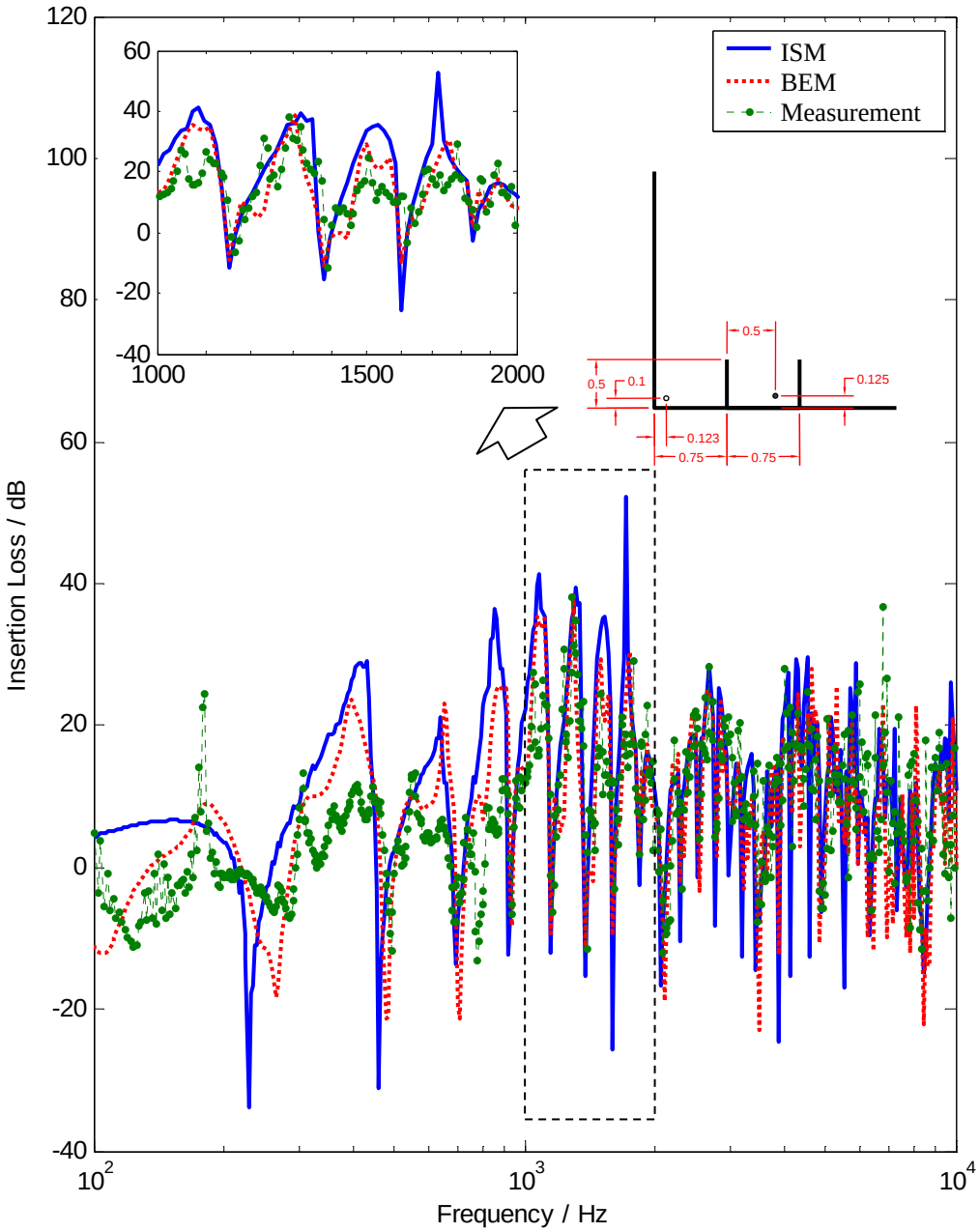

Figure 3.13 The spectrum of insertion losses (IL) at location $\Re$=(0.123,0,0.1) with parallel barriers having hard inner surfaces in front of a building façade. The solid line represents predictions by the image source method (ISM), the dashed line represents numerical predictions based on the boundary element method (BEM) and the dashed line with dots represents results from experimental measurement.

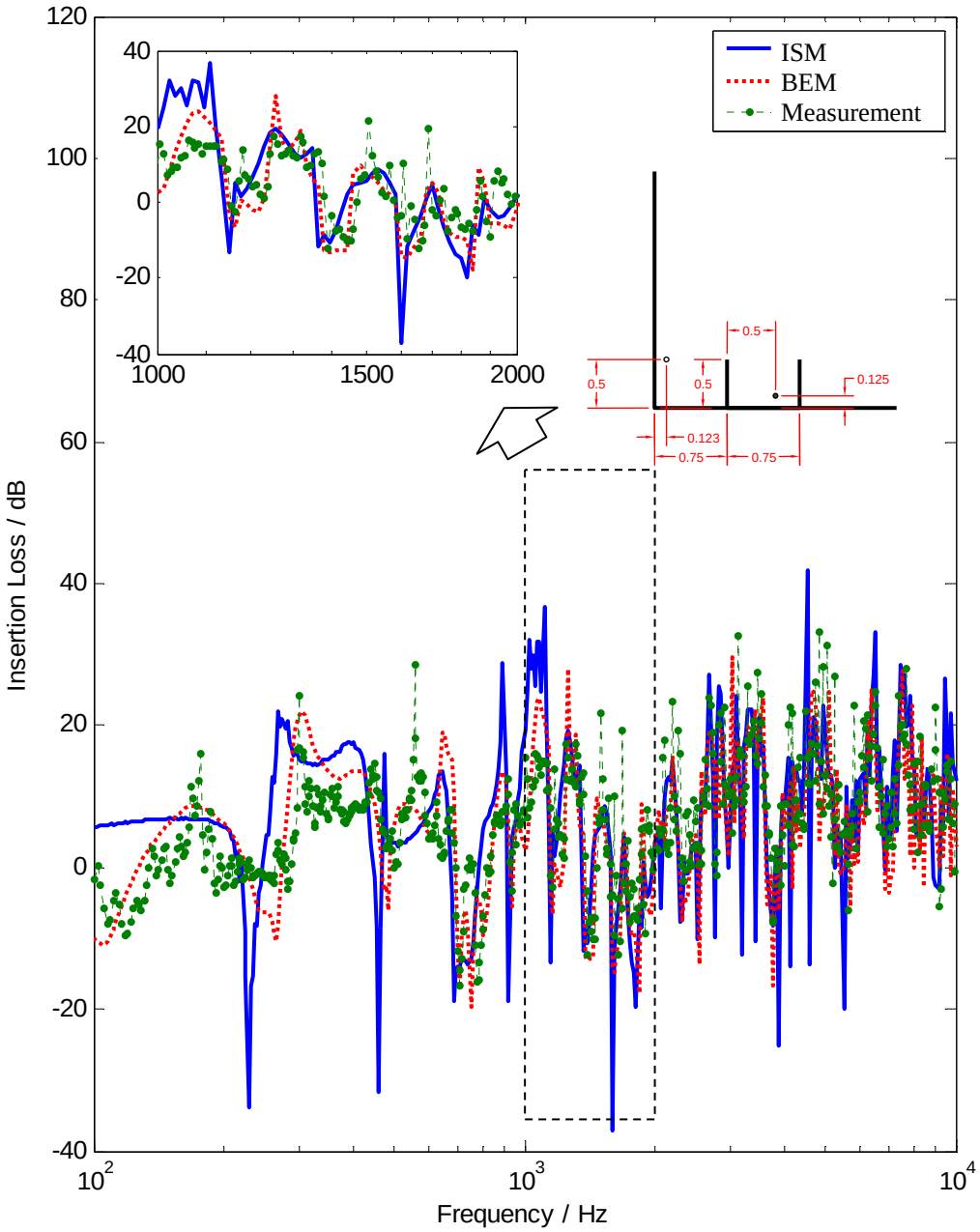

Figure 3.14 The spectrum of insertion losses (IL) at location $\Re$=(0.123,0,0.5) with parallel barriers having hard inner surfaces in front of a building façade. The solid line represents predictions by the image source method (ISM), the dashed line represents numerical predictions based on the boundary element method (BEM) and the dashed line with dots represents results from experimental measurement.

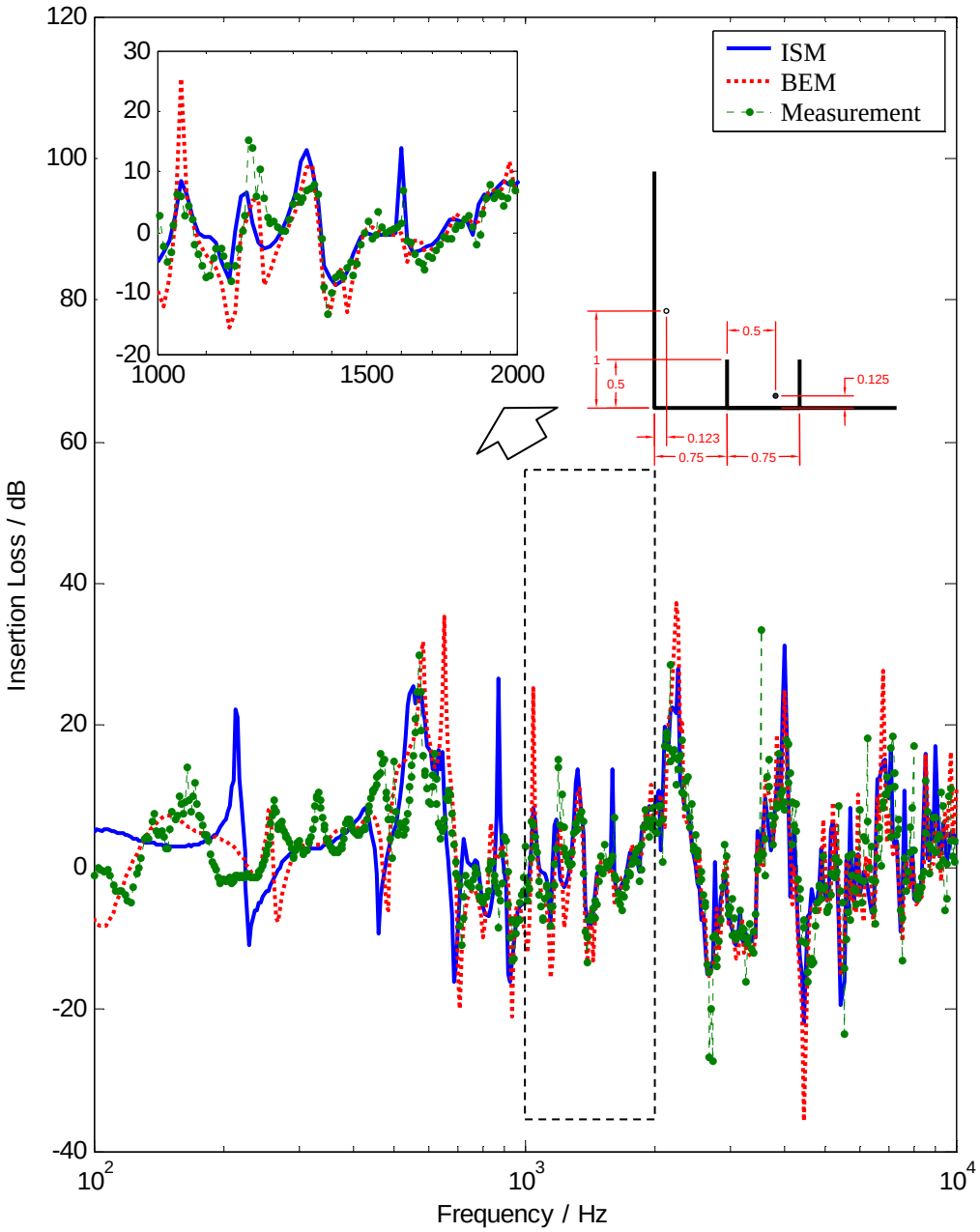

Figure 3.15 The spectrum of insertion losses (IL) at location $\Re$=(0.123,0,1) with parallel barriers having hard inner surfaces in front of a building façade. The solid line represents predictions by the image source method (ISM), the dashed line represents numerical predictions based on the boundary element method (BEM) and the dashed line with dots represents results from experimental measurement.

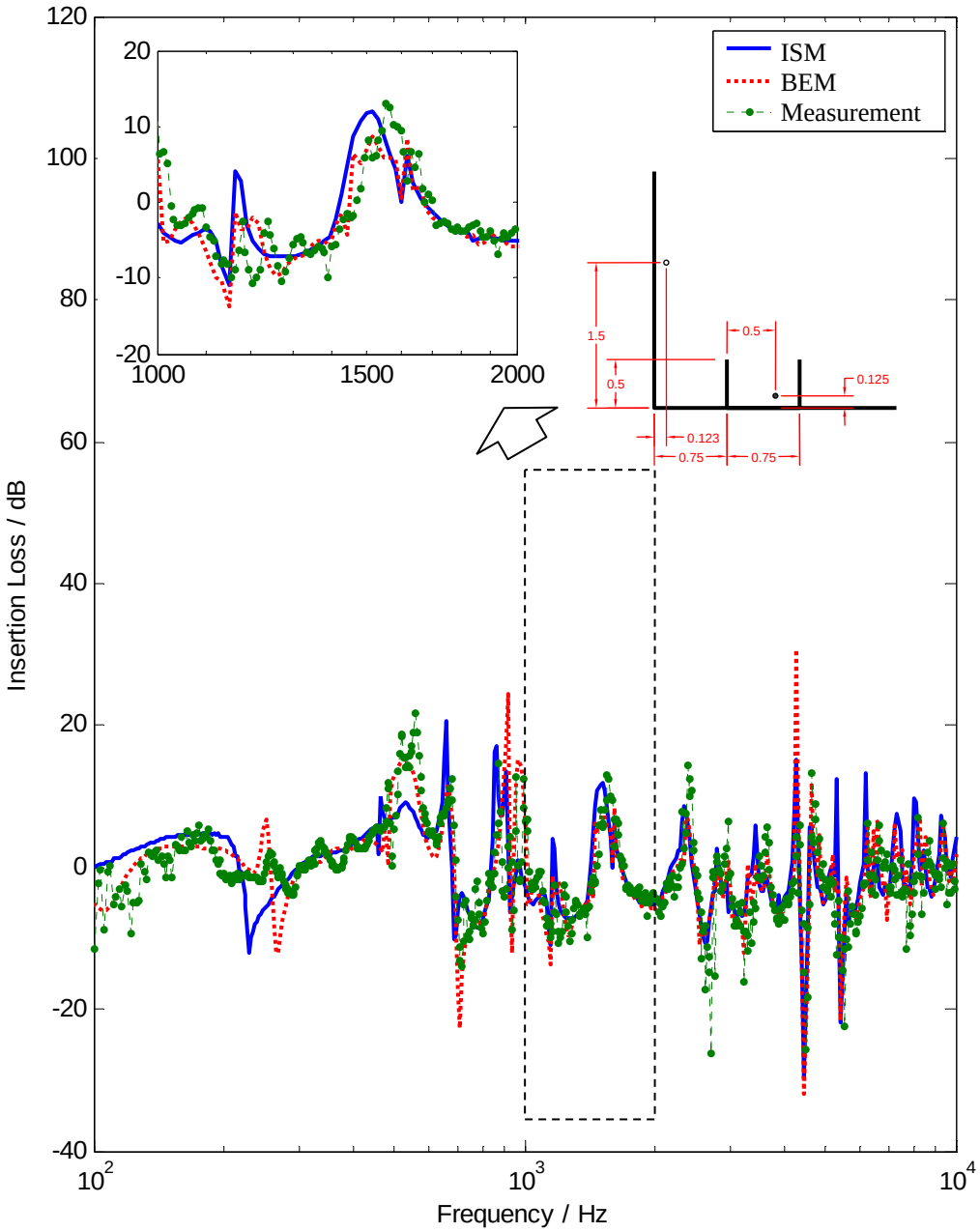

Figure 3.16 The spectrum of insertion losses (IL) at location $\Re$=(0.123,0,1.5) with parallel barriers having hard inner surfaces in front of a building façade. The solid line represents predictions by the image source method (ISM), the dashed line represents numerical predictions based on the boundary element method (BEM) and the dashed line with dots represents results from experimental measurement.

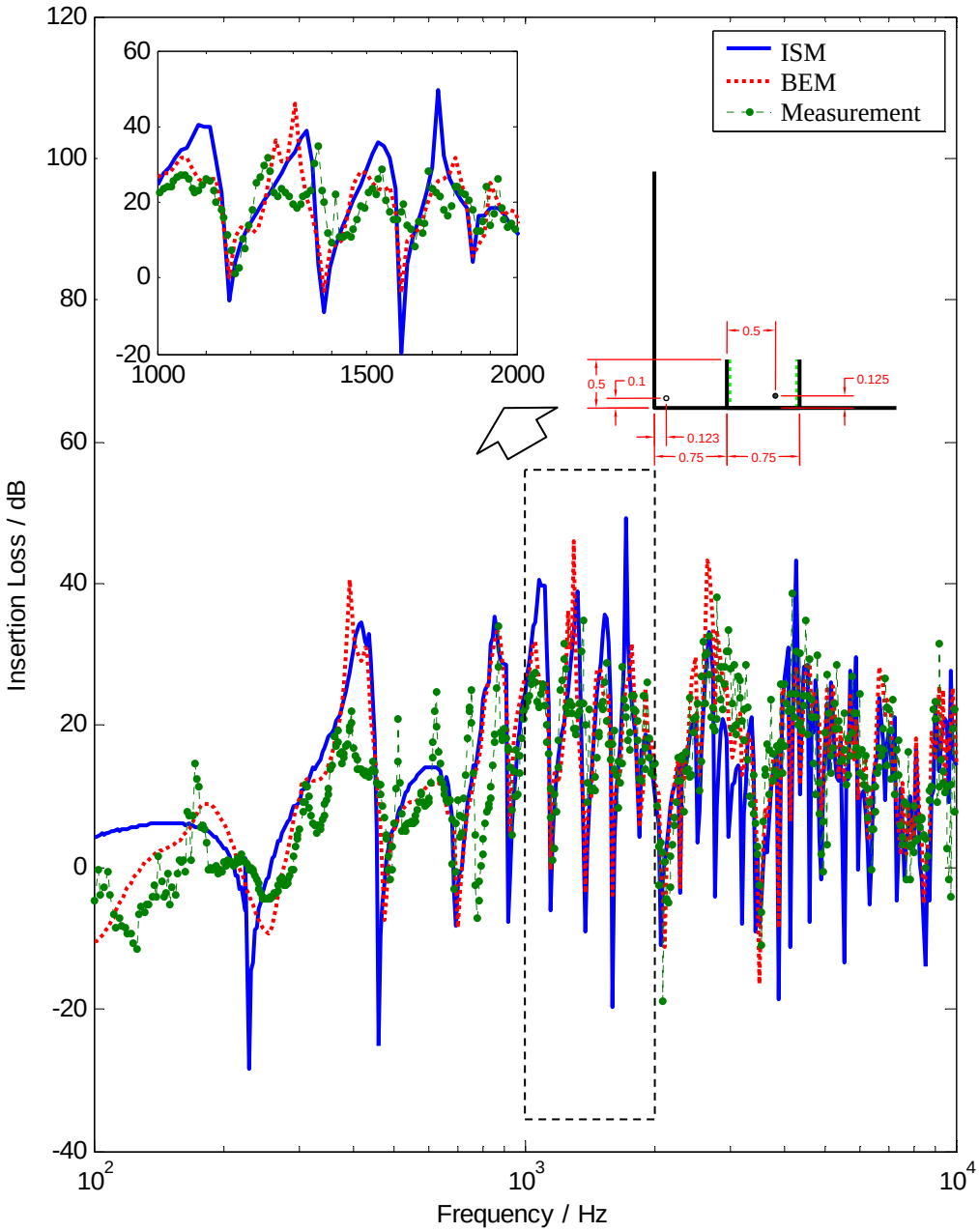

Figure 3.17 The spectrum of insertion losses (IL) at location $\Re$=(0.123,0,0.1) with parallel barriers having absorptive inner surfaces in front of a building façade. The impedance of the inner surface is modeled with the Delany and Bazley model with the flow resistivity equal to 72,351 MKS rayls/m. The solid line represents predictions by the image source method (ISM), the dashed line represents numerical predictions based on the boundary element method (BEM) and the dashed line with dots represents results from experimental measurement.

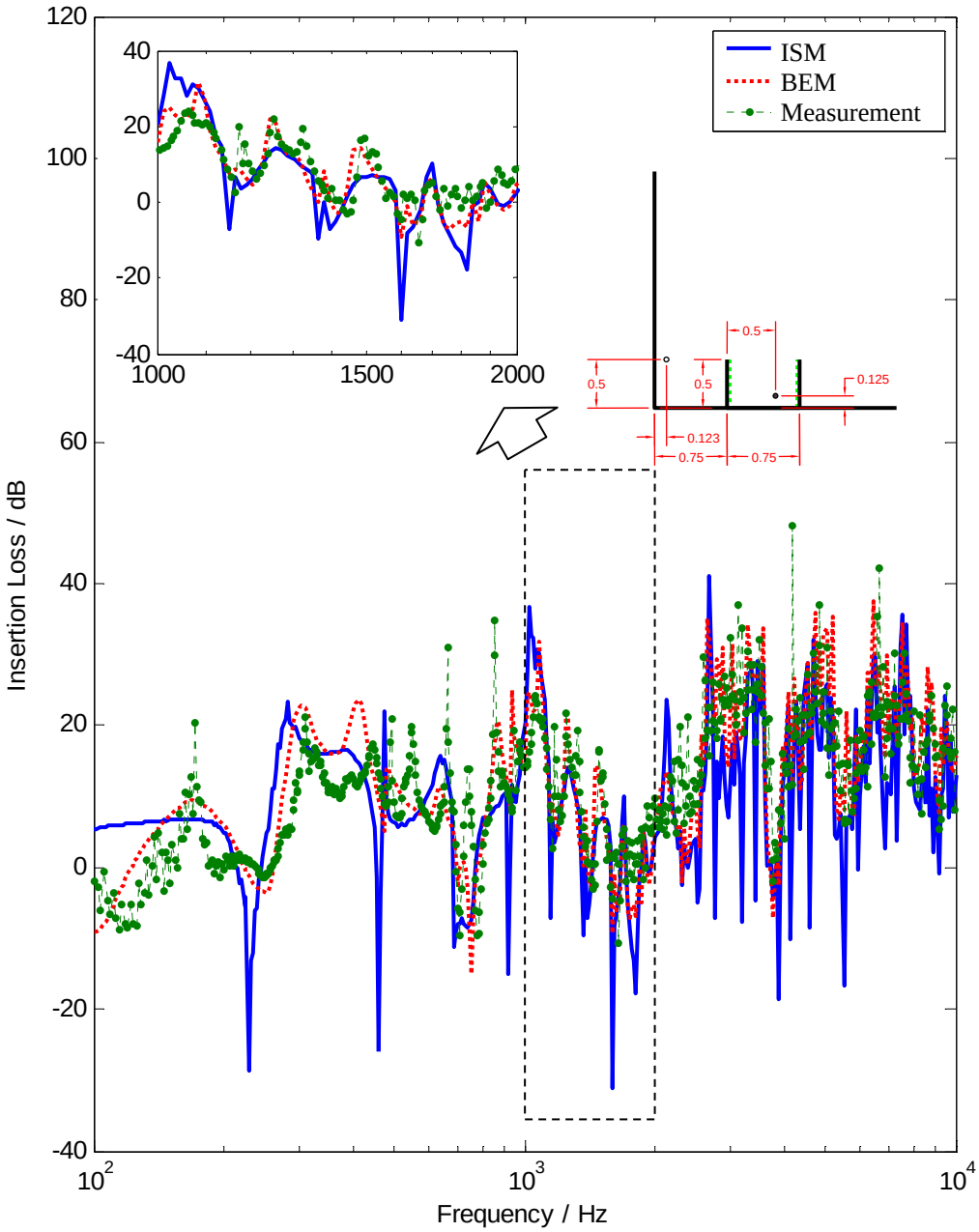

Figure 3.18 The spectrum of insertion losses (IL) at location $\Re$=(0.123,0,0.5) with parallel barriers having absorptive inner surfaces in front of a building façade. The impedance of the inner surface is modeled with the Delany and Bazley model with the flow resistivity equal to 72,351 MKS rayls/m. The solid line represents predictions by the image source method (ISM), the dashed line represents numerical predictions based on the boundary element method (BEM) and the dashed line with dots represents results from experimental measurement.

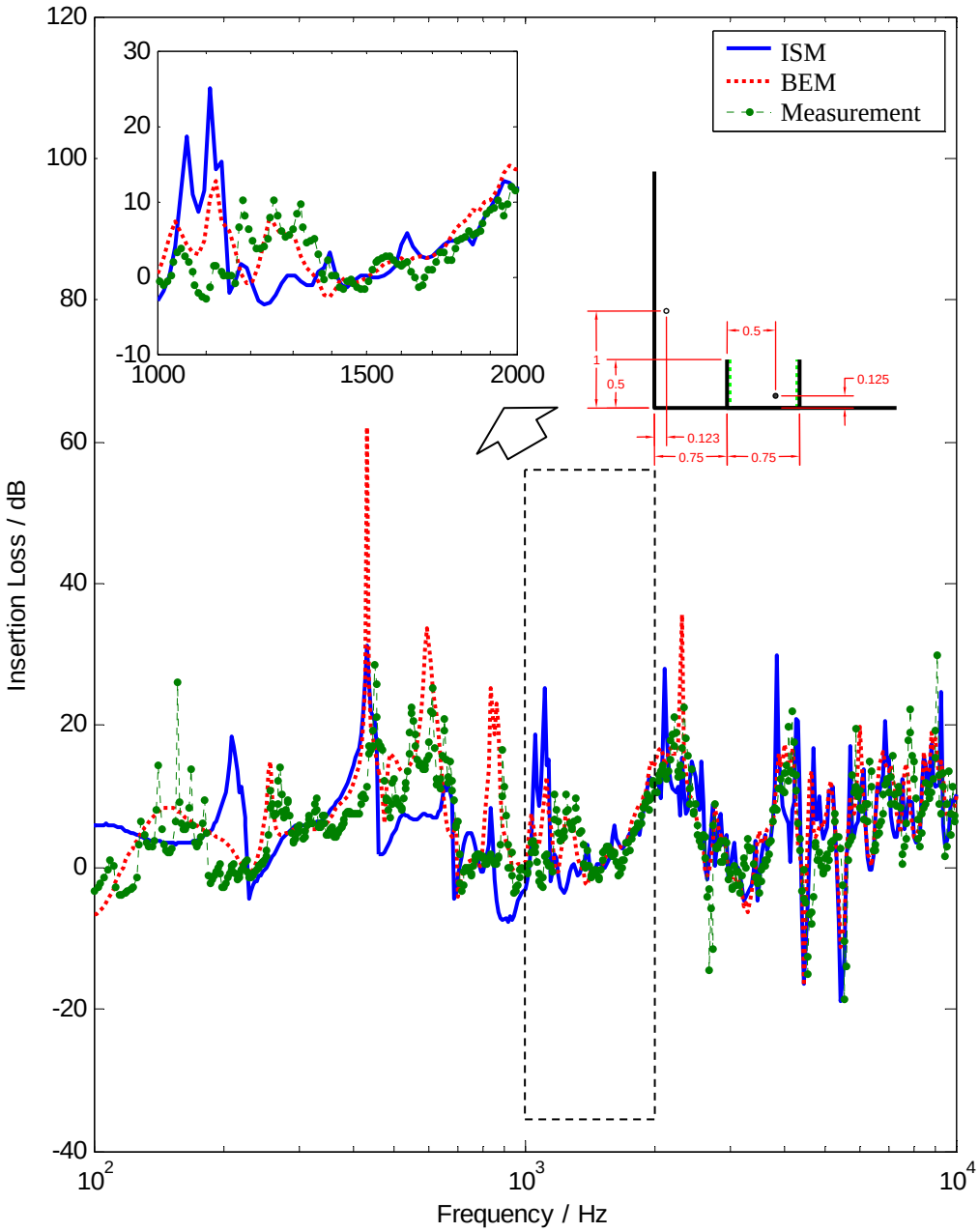

Figure 3.19 The spectrum of insertion losses (IL) at location $\Re$=(0.123,0,1.0) with parallel barriers having absorptive inner surfaces in front of a building façade. The impedance of the inner surface is modeled with the Delany and Bazley model with the flow resistivity equal to 72,351 MKS rayls/m. The solid line represents predictions by the image source method (ISM), the dashed line represents numerical predictions based on the boundary element method (BEM) and the dashed line with dots represents results from experimental measurement.

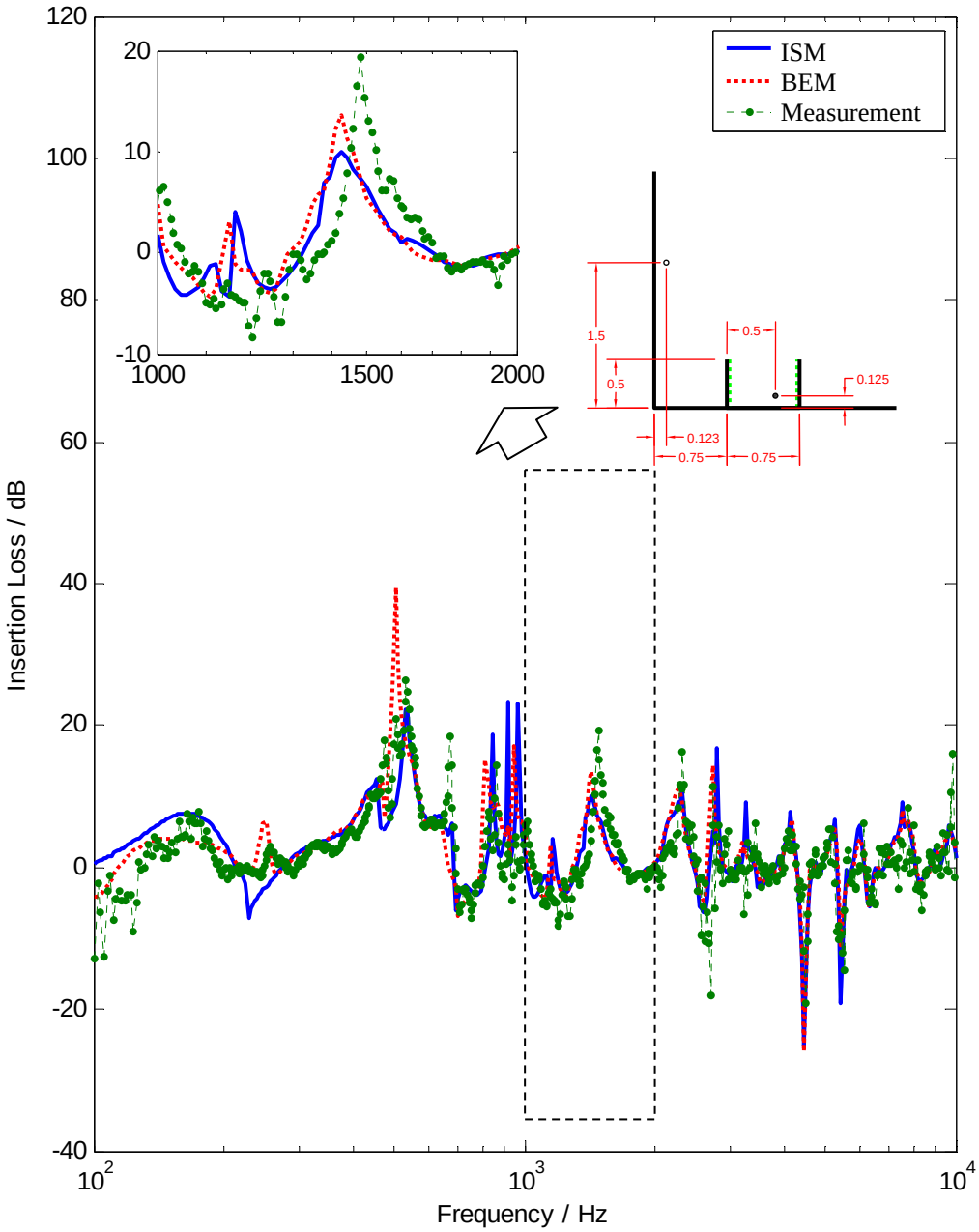

Figure 3.20 The spectrum of insertion losses (IL) at location $\Re$=(0.123,0,1.5) with parallel barriers having absorptive inner surfaces in front of a building façade. The impedance of the inner surface is modeled with the Delany and Bazley model with the flow resistivity equal to 72,351 MKS rayls/m. The solid line represents predictions by the image source method (ISM), the dashed line represents numerical predictions based on the boundary element method (BEM) and the dashed line with dots represents results from experimental measurement.

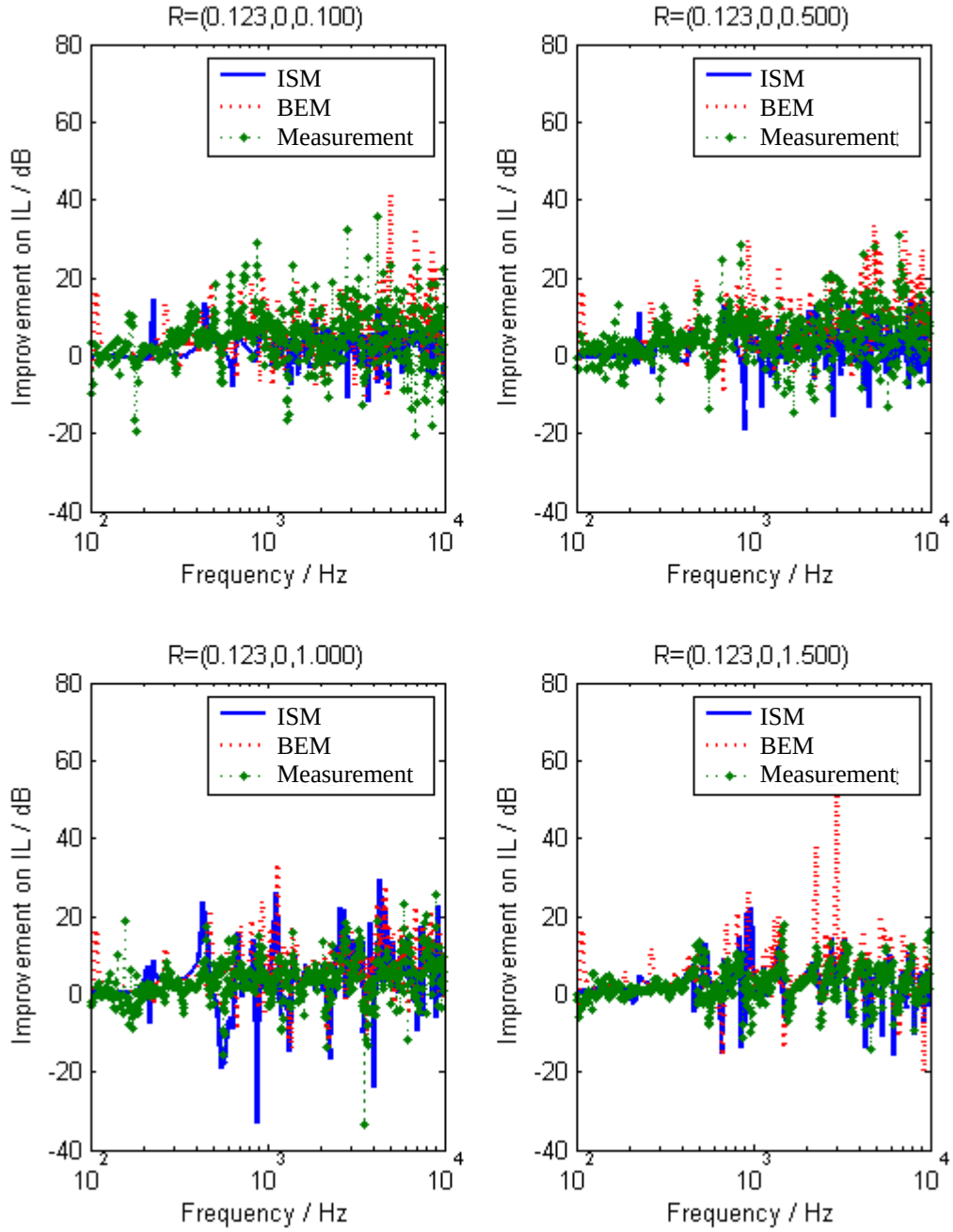

Figure 3.21 The spectrum of improvement in insertion losses (IL) at locations $\mathfrak{R}$=(0.123,0,0.1), $\mathfrak{R}$=(0.123,0,0.5), $\mathfrak{R}$=(0.123,0,1), and $\mathfrak{R}$=(0.123,0,1.5) with parallel barriers having absorptive inner surfaces in front of a building façade over barriers with hard surfaces. The solid line represents predictions by the image source method (ISM), the dashed line represents numerical predictions based on the boundary element method (BEM) and the dashed line with dots represents results from experimental measurement.

Frequency / Hz	Number of elements per wavelength
< 500	100
501 - 800	40
801 - 1000	20
>1000	10

Table 3.1 Elements size used for the implementation of the boundary element method.

Chapter 4 Parallel Barriers in a Street Canyon

4.1 Introduction

In the previous chapter, we have presented the image source model for the parallel barriers in front of a façade. The heuristic diffraction formulation for diffraction suggested by Koers [64] is found to be well applicable in conditions with multiple reflections. The sound pressure levels calculated from the image source method (ISM) are consistent with the boundary element method (BEM) and experimental results. In this chapter, we would like to extend the image source model to another commonly encountered condition in the urban environment. The situation put into consideration is commonly referred to as a street canyon. It consists of a pair of parallel barriers placed aside a road semi-enclosed by sky-rise buildings at the both sides. Study of the sound field in this spatial condition is processed with the ISM. Similar to the previous chapter, comparison with the BEM and experimental results are conducted and the acoustic performance improvement by absorptive material is analyzed.

4.2 Theory

In this study, another typical scenario of a high-rise city as shown in figure 4.1 is considered in which a pair of parallel barriers are placed inside a street canyon. The tall buildings are replaced by two flat façade surfaces Γ_{F1} and Γ_{F2} perpendicular to the ground for modeling. A rectangular co-ordinate system is chosen where the façade surface lies on the $x = 0$ plane and the ground surface lies on the $z = 0$ plane. The origin is

located on the ground surface at the bottom of the façade. We limit our consideration to the situation where the source denoted by **S** and receiver denoted by $\mathfrak{R}$ are located at the same vertical plane at $y = 0$. By this simplification, the problem becomes purely two dimensional only and we have to assume that the pair of barriers and the building façades are infinitely long along the *y*-axis such that contributions from the vertical edges of the barriers and façades are ignored in our analysis.

The coordinates of the source and receiver are given by $\mathbf{S} \equiv (x_S, 0, z_S)$ and $\mathfrak{R} \equiv (x_R, 0, z_R)$ respectively where the subscripts S and R are used to represent the corresponding parameters for the source and receiver, respectively. The separation between the two façade surfaces Γ_{F1} and Γ_{F2} is L. The barrier **B1** is located at a horizontal distance L_1 from the façade surface Γ_{F1}. The barrier **B2** is located at a horizontal distance *W* from the barrier **B1**. The distance between the barrier **B2** and the façade surface Γ_{F2} is L_2. The distance W_1 and W_2 are the horizontal distances measured from the source to the barriers **B1** and **B2** respectively. In addition, we only consider the case where both barriers have the same height, *H*. The top edges of the near-side and far-side barriers are denoted by $\mathbf{E1} \equiv (L_1, 0, H)$ and $\mathbf{E2} \equiv (L_1 + W, 0, H)$ respectively.

We consider the barrier surfaces facing the source as inner surfaces. The outer and inner surfaces of the barrier **B1** are denoted as Γ_{B11} and Γ_{B12} respectively. The inner and outer surfaces of the barrier **B2** are denoted as Γ_{B21} and Γ_{B22} respectively. The ground surface is divided into three regions. For the region between the surfaces Γ_{F1} and Γ_{B11}, the ground surface is denoted as Γ_{G1}. For the region between the surfaces Γ_{B12} and Γ_{B21}, the ground surface is denoted as Γ_{G2}. For the region between the surfaces Γ_{B22} and Γ_{F2}, the

ground surface is denoted as Γ_{G3}. Together with the façade surfaces Γ_{F1} and Γ_{F2}, there are totally nine surfaces in our consideration. The specific impedance of these nine surfaces are denoted as β_{B11}, β_{B12}, β_{B21}, β_{B22}, β_{G1}, β_{G2}, β_{G3}, β_{F1} and β_{F2}. The various notations of the admittance are also shown in figure 4.1.

The principle of the image source model used in the current chapter is same as the previous one. In brief, the overall sound pressure level at a particular location is the coherent summation of pressure contributions from the image sources that can make contribution to that location. The three basic means of contributions are the direct transmission, reflection and diffraction. The calculations of these contributions are based on the formulations reported in Chapter 3. Due to the lengthy content, the details of the image source model are described in Appendix A.

4.3 Validation with Boundary Element Method

The extension of the image source model for the condition of parallel barriers along a street canyon provided an effective evaluation tool for the shielding performance. The validation of the model is achieved by comparison of its prediction results with the results from numerical techniques. Again, BEM is chosen due to its high suitability for external problems where domains are extended to infinity. The implementation in the calculation is similar to Chapter 3.

A realistic outdoor configuration is used in our analysis. The separation of the two façade surfaces Γ_{F1} and Γ_{F2}, L, is 20m. The distance between the façade surface Γ_{F1} and the

barrier **B1**, L_1, is 5m. The distance between the façade surface Γ_{F2} and the barrier **B2**, L_2, is 5m. The two barriers are of identical height of 2.5m. A noise source is located between the two barriers and at 0.25m above the ground. The distance between the source and barrier **B1**, W_1, is 2.5m. The distance between the source and barrier **B2**, W_2, is 7.5m. Cases with hard and absorptive barrier surfaces Γ_{B12} and Γ_{B21} have been considered. For the absorptive surfaces, the acoustic impedances are modeled with the Delany and Bazley model [34] with the flow resistivity equal to 40000 MKS rayls/m. The receivers considered are located 1m away from the façade surface Γ_{F1} and with heights of 1m, 2m, 5m and 10m. The maximum orders of reflections are restricted to 100 for all n_1, n_2, q_1 and q_2 in the image source model. Similarly, we choose at least 10 elements per wavelength in implementing the BEM to ensure a higher accuracy for the benchmarking results. Details on the size of elements are summarized in table 3.1. Based on the available computational resources, the height of the building façade is taken as 25m for eliminating the effect of diffraction at the top of the façade surfaces.

As shown in figures 4.2 to 4.5, we compare the spectrums of insertion loss at four receiver positions calculated by the two methods. The first two locations $\mathfrak{R}$=(1,0,1) and $\mathfrak{R}$=(1,0,2) are in the shadow zone. The third location $\mathfrak{R}$=(1,0,5) is near the direct line of sight. The last location $\mathfrak{R}$=(1,0,10) is illuminated directly by the source. Similarly, we calculate the insertion loss at the same locations by both methods for cases with absorptive surfaces. The results are shown in figures 4.6 to 4.9 for the four positions respectively. The improvement on the insertion loss due to the absorptive material has been calculated also and the results are shown in figure 4.10.

Although the agreement between the predicted results from both methods is not as good as that observed in the previous chapter, the ISM would still provide satisfactory prediction results. In general, the ISM can determine the locations of peaks and troughs in the frequency domain as predicted by the BEM.

4.4 Validation with Experimental Measurement

Similar to Chapter 3, we have conducted the scale model measurements for the purpose of experimental validation. The measurement consists of a scaled-down configuration as shown in figure 4.11. The façade and ground surfaces are made of 8.5mm thick wooden board. The height of both façade surfaces is 2.44m which is high enough to ignore the diffraction at the top edge. The barriers consist of 3mm thick aluminum plate with height of 0.5m and length of 4.5m. They are placed 0.75m and 1.5m in front of the first façade surface respectively. The source is located 1.25m in front of the façade surface and at a height of 0.125m. The receiver is placed 0.123m in front of the first façade surface with various heights. For modeling the absorptive surface, we attach the same 25mm thick glass fiber with density of $48\,kg/m^3$ used in the in-situ impedance determination.

The whole measurement is conducted inside an anechoic chamber of dimensions $6\text{m}\times 6\text{m}\times 6\text{m}$. The insertion loss used for comparison is obtained by measuring the transfer function with and without the barriers. The MLS system and equipment used are the same as before. As mentioned previously, special attention has been put on the orientation of the speaker and microphone for the modeling of the spherical wave.

Comparison of the insertion loss spectrum for the parallel barriers with hard surfaces at locations (0.123,0,0.1), (0.123,0,0.5), (0.123,0,1) and (0.123,0,1.5) are shown in figures 4.12 to 4.15 respectively. For the parallel barriers with absorptive surfaces, the comparison of the insertion loss is shown in figures 4.16 to 4.19. In the theoretical calculation, the absorptive surface is modeled with the Delany and Bazley model [34] with the flow resistivity equal to 72,351 MKS rayls/m. This value is deduced from the method discussed in Chapter 2. In addition, we have illustrated the measured and calculated improvement on the insertion loss due to the absorptive material in figure 4.20.

In general, the theoretical predictions agree satisfactorily with the results of the experiment. Apart from the inaccuracy involved in using Hadden and Pierce's [42] formulation on diffraction in this small scale, the large number of summation involved also enlarge the error. Notwithstanding the larger discrepancy observed compared with the simpler case in the previous chapter, the image source model can predict the sound field in this much more complicated street canyon condition with reasonable accuracy.

4.5 Conclusion

In this chapter, the development of a computation model for the shielding performance evaluation of parallel barriers placed along a street canyon is reported. The model developed is an extension of the one presented in the previous chapter. It is also based on the ISM and various classical theories from geometrical acoustic. Again, the effect of acoustic absorptive surfaces is included. This gives the possibility for the analysis of absorptive barriers and road pavement. Due to the additional façade surface, the multiple reflections of sound among the surfaces are much more complicated. The consideration

of combinations involved is almost double than that of the previous chapter. Nevertheless, we can still maintain a realistic computational requirement with the effective algorithm developed for searching the possible source images. Because the higher number of summations enlarges the error intrinsically in the heuristic diffraction solution, there will be more inaccuracy involved. For the validation, it is found that the predictions are still reasonably well consistent with the calculated results by the BEM and experimental measurement over a wide range of frequencies. In conclusion, the image source model developed is also another valuable tool for the evaluation in the design stage and makes for a great contribution in urban planning due to its fairly accurate prediction capability and high computational efficiency.

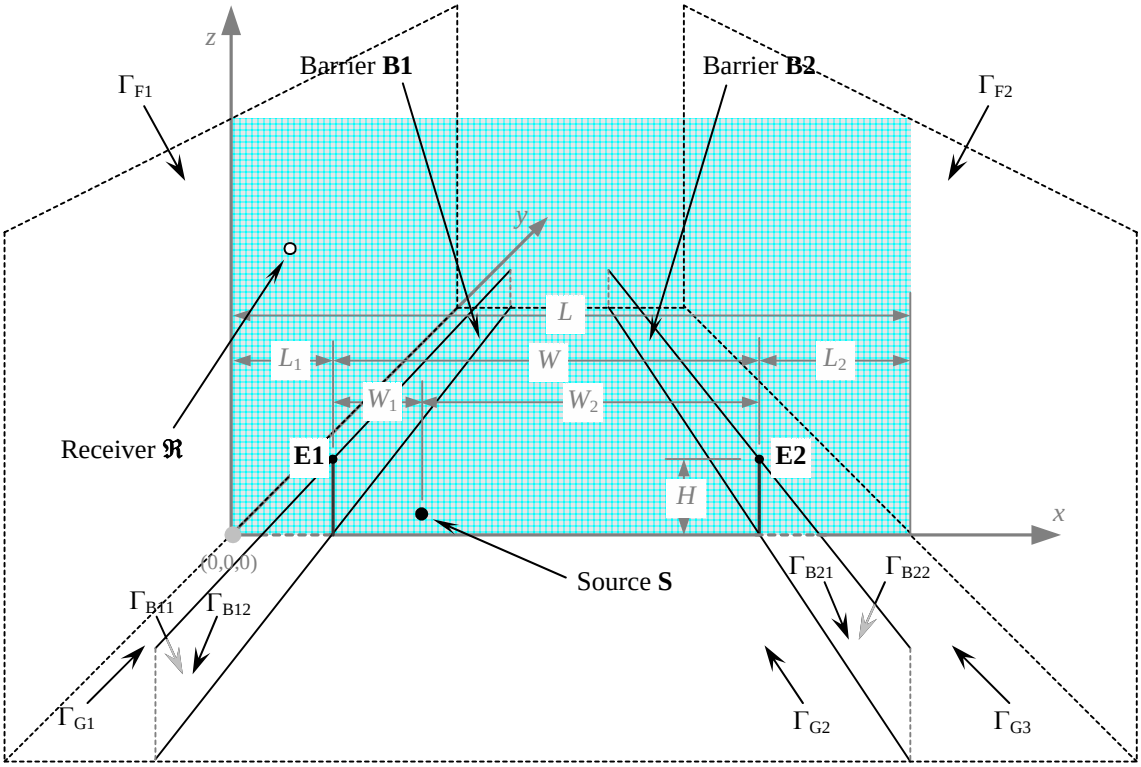

Figure 4.1 Schematic diagram of the specified problem. A source **S** is located at $\mathbf{I_o}\equiv(x_S, 0, z_S)$ and a receiver $\mathfrak{R}$ at $(x_R, 0, z_R)$. A pair of parallel barriers, **B1** and **B2**, of height H are placed inside a street canyon formed by two façade surfaces Γ_{F1} and Γ_{F2} of infinite height.

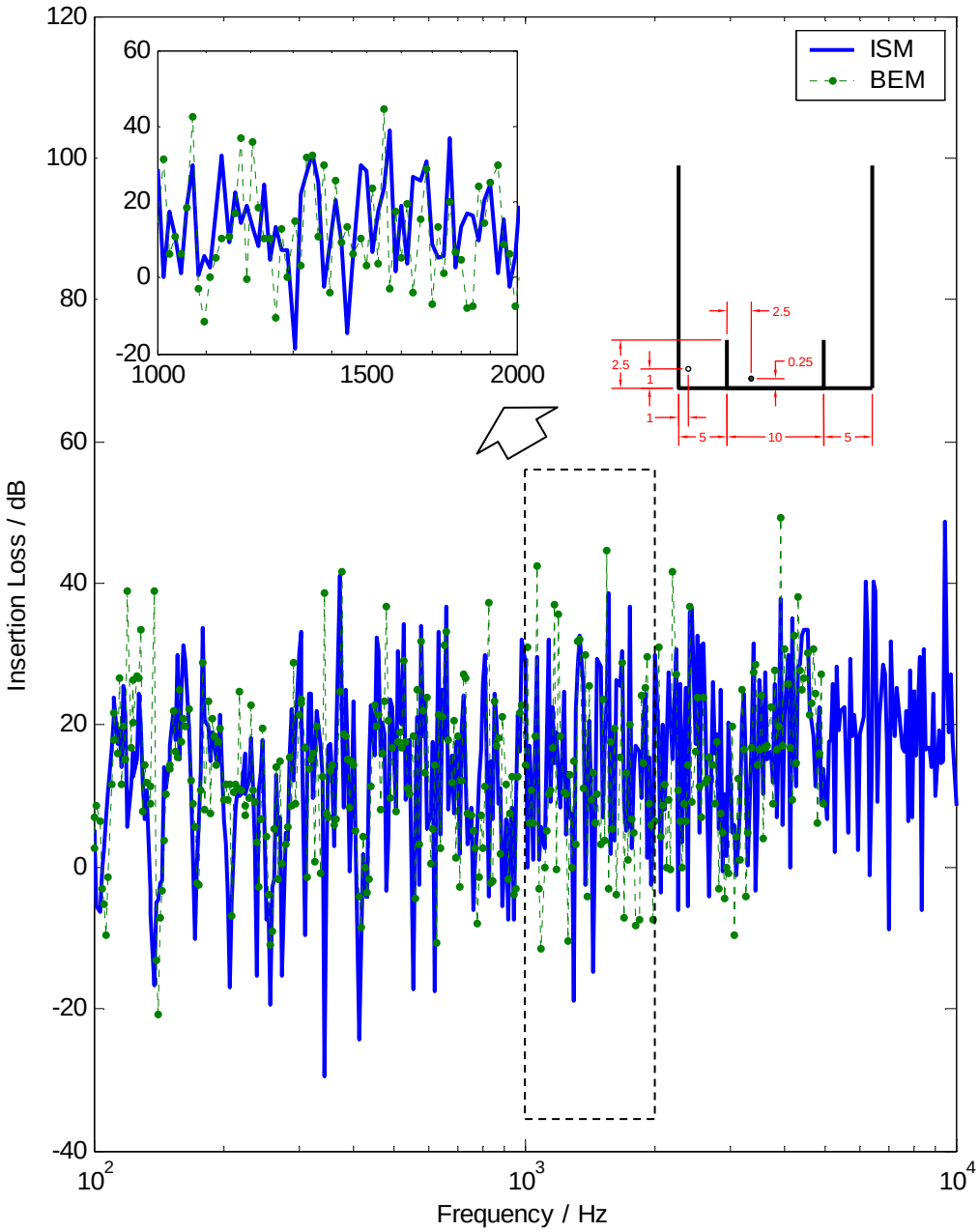

Figure 4.2 The spectrum of insertion losses (IL) at location $\mathfrak{R}$=(1,0,1) with parallel barriers having hard inner surfaces in a street canyon. The solid line represents predictions by the image source method (ISM) and the dashed line with dots represents numerical predictions based on the boundary element method (BEM).

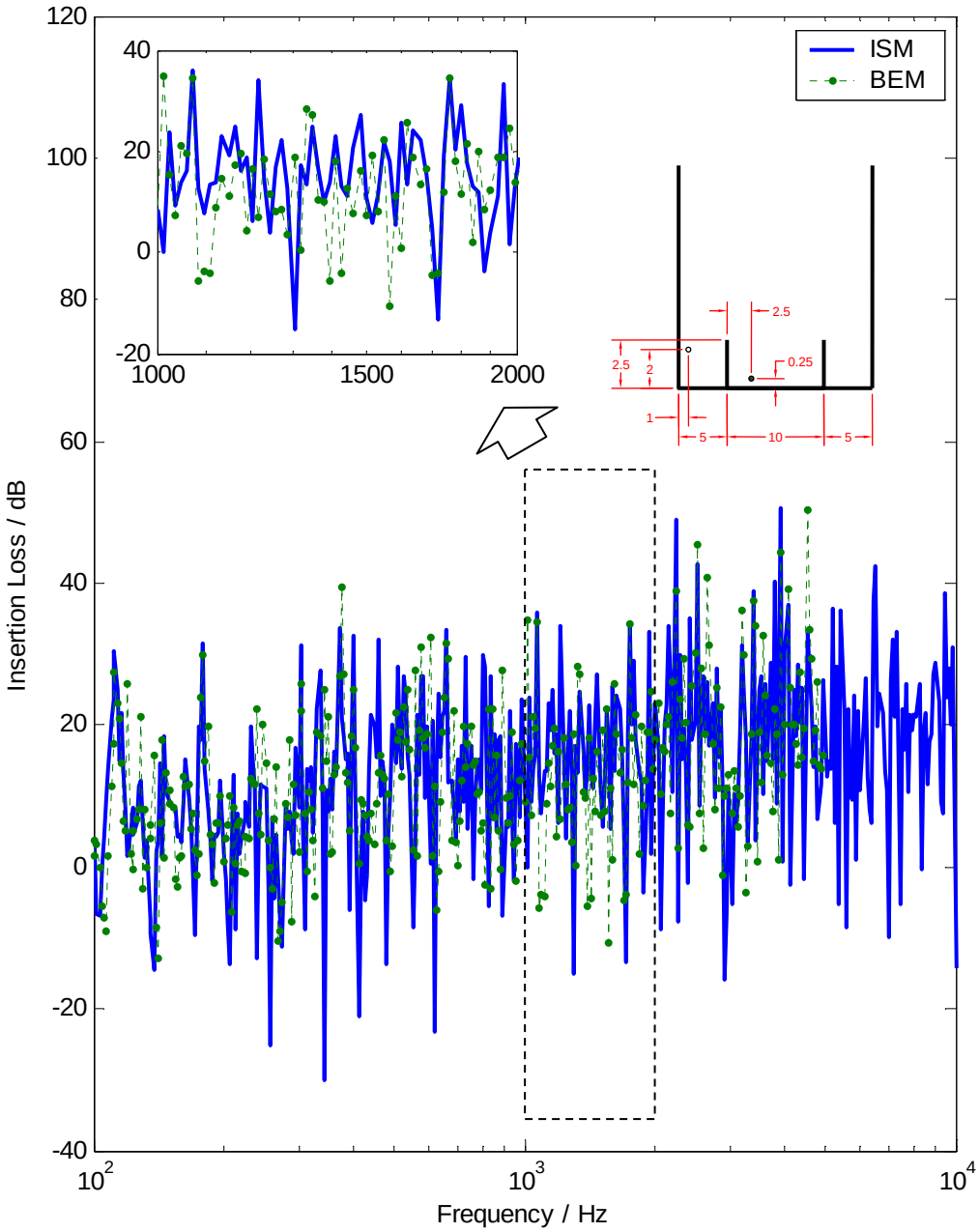

Figure 4.3 The spectrum of insertion losses (IL) at location $\mathfrak{R}$=(1,0,2) with parallel barriers having hard inner surfaces in a street canyon. The solid line represents predictions by the image source method (ISM) and the dashed line with dots represents numerical predictions based on the boundary element method (BEM).

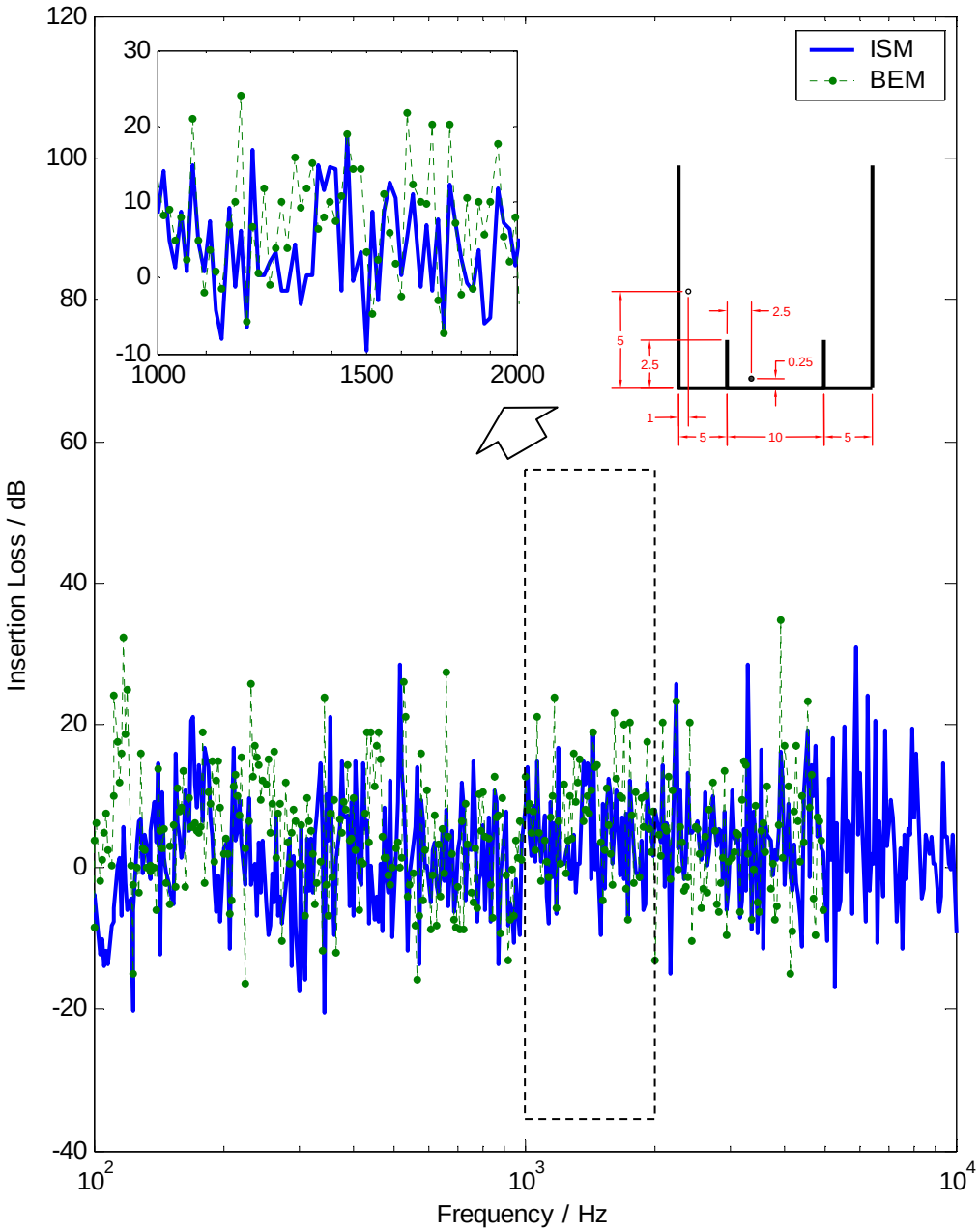

Figure 4.4 The spectrum of insertion losses (IL) at location $\mathfrak{R}$=(1,0,5) with parallel barriers having hard inner surfaces in a street canyon. The solid line represents predictions by the image source method (ISM) and the dashed line with dots represents numerical predictions based on the boundary element method (BEM).

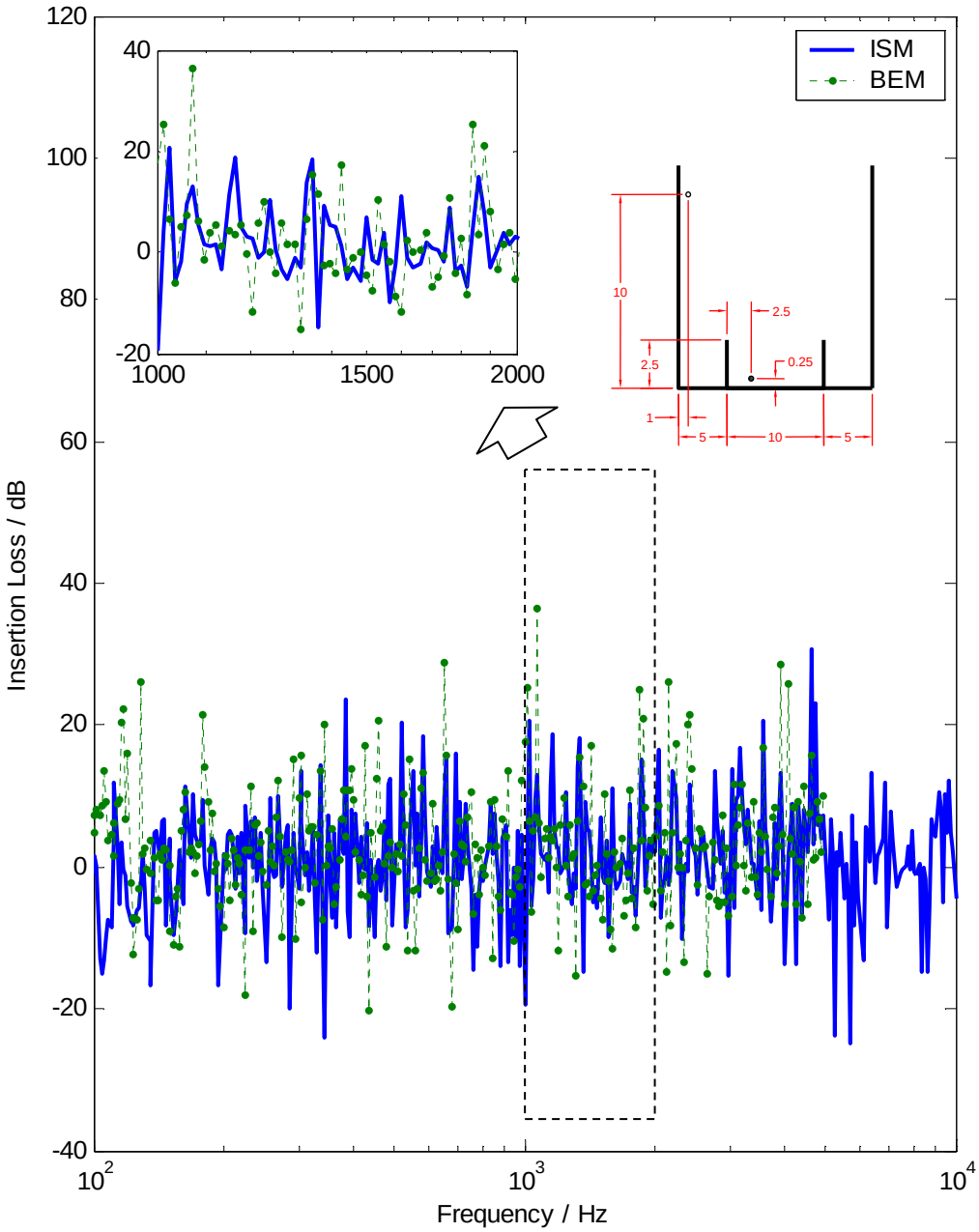

Figure 4.5 The spectrum of insertion losses (IL) at location $\mathfrak{R}$=(1,0,10) with parallel barriers having hard inner surfaces in a street canyon. The solid line represents predictions by the image source method (ISM) and the dashed line with dots represents numerical predictions based on the boundary element method (BEM).

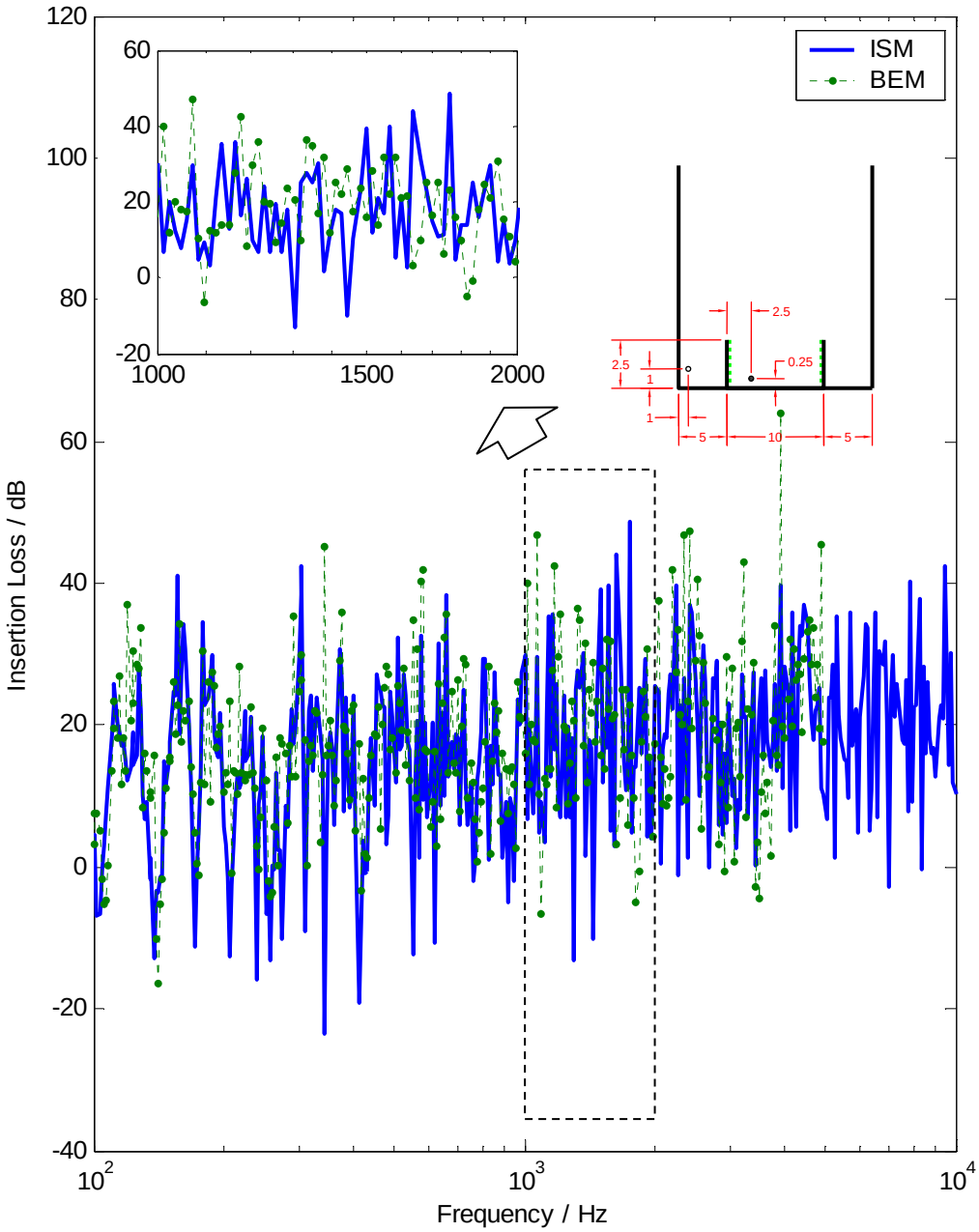

Figure 4.6 The spectrum of insertion losses (IL) at location $\mathfrak{R}$=(1,0,1) with parallel barriers having absorptive inner surfaces in a street canyon. The impedance of the inner surface is modeled with the Delany and Bazley model with the flow resistivity equal to 40,000 MKS rayls/m. The solid line represents predictions by the image source method (ISM) and the dashed line with dots represents numerical predictions based on the boundary element method (BEM).

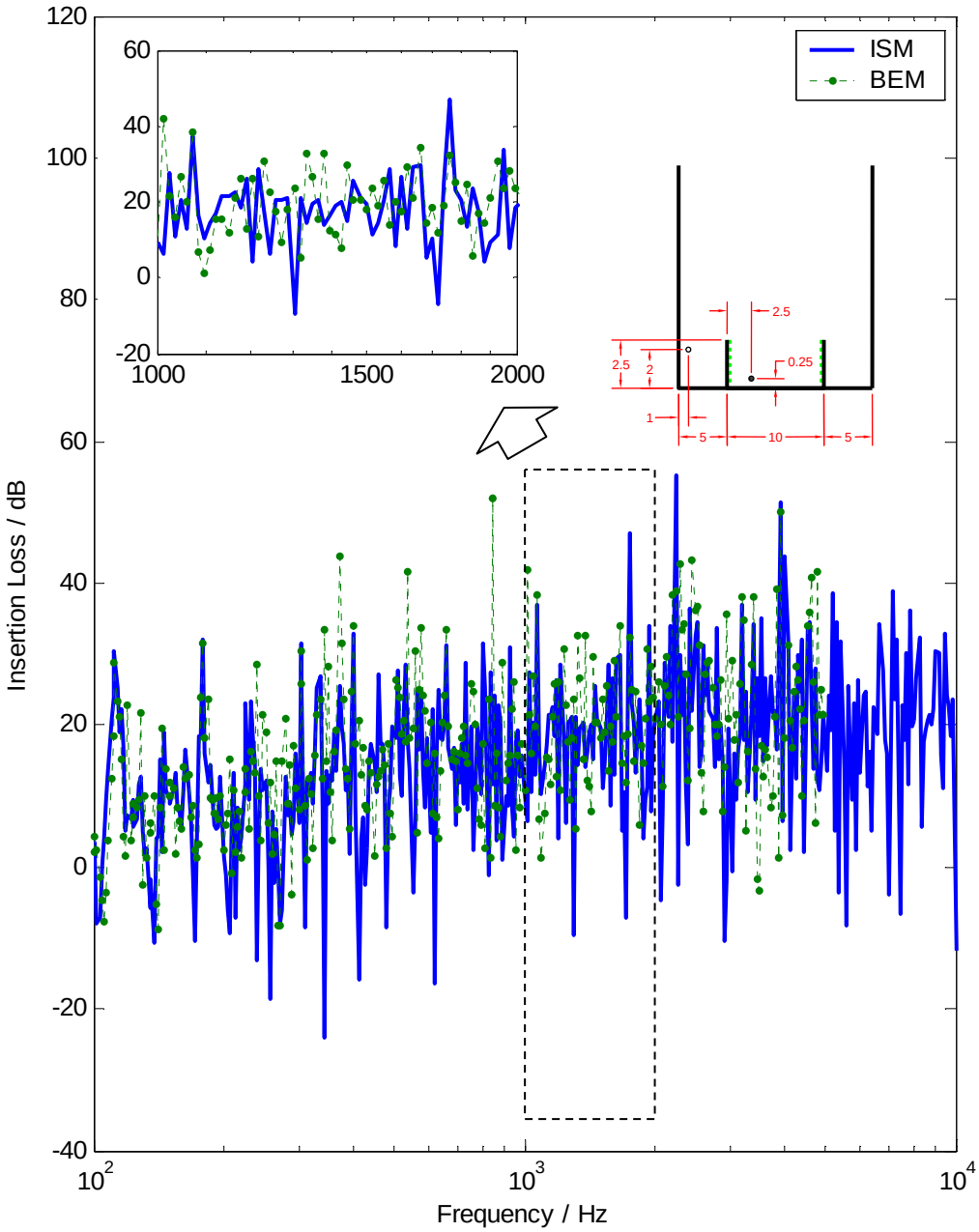

Figure 4.7 The spectrum of insertion losses (IL) at location $\mathfrak{R}$=(1,0,2) with parallel barriers having absorptive inner surfaces in a street canyon. The impedance of the inner surface is modeled with the Delany and Bazley model with the flow resistivity equal to 40,000 MKS rayls/m. The solid line represents predictions by the image source method (ISM) and the dashed line with dots represents numerical predictions based on the boundary element method (BEM).

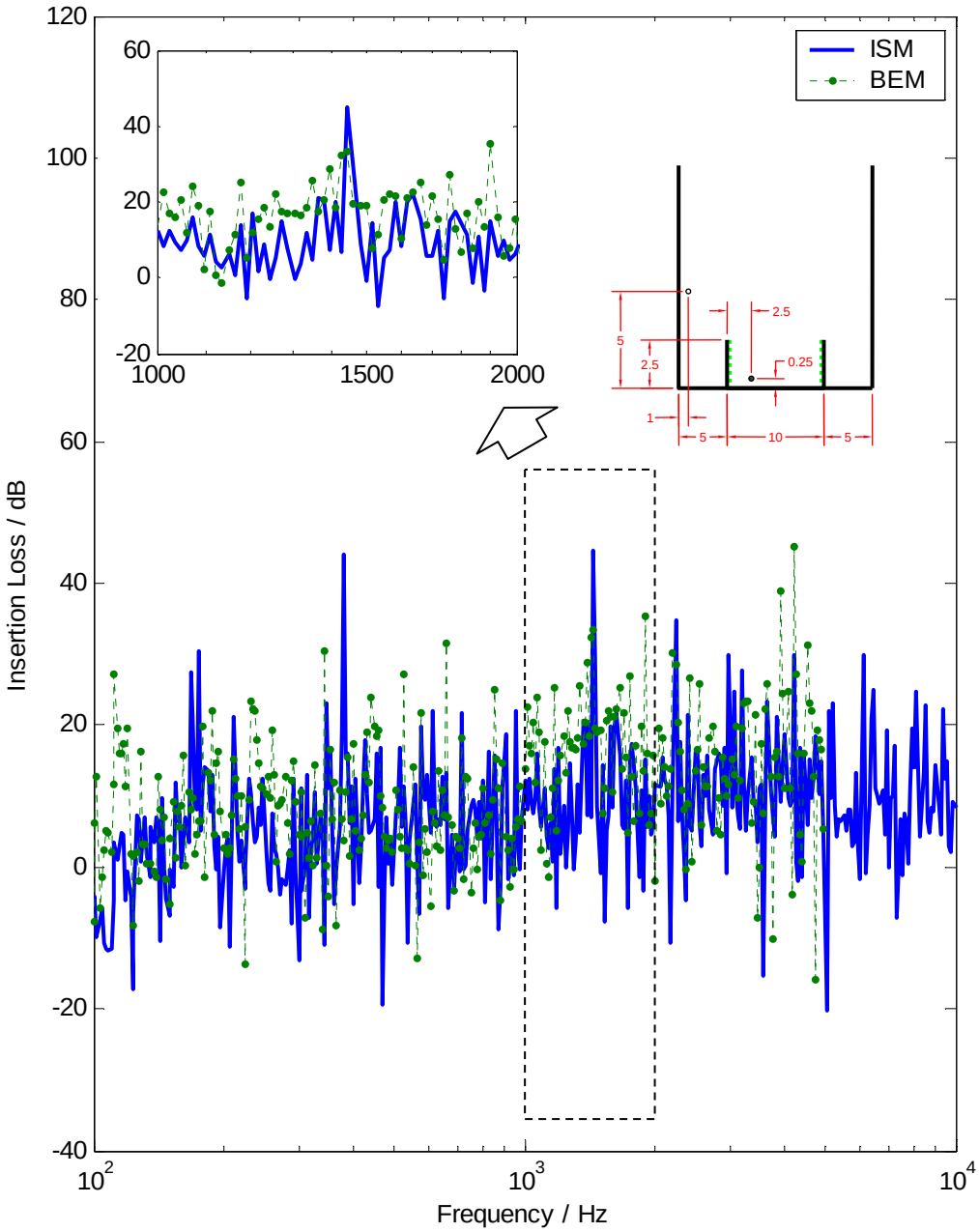

Figure 4.8 The spectrum of insertion losses (IL) at location $\mathfrak{R}$=(1,0,5) with parallel barriers having absorptive inner surfaces in a street canyon. The impedance of the inner surface is modeled with the Delany and Bazley model with the flow resistivity equal to 40,000 MKS rayls/m. The solid line represents predictions by the image source method (ISM) and the dashed line with dots represents numerical predictions based on the boundary element method (BEM).

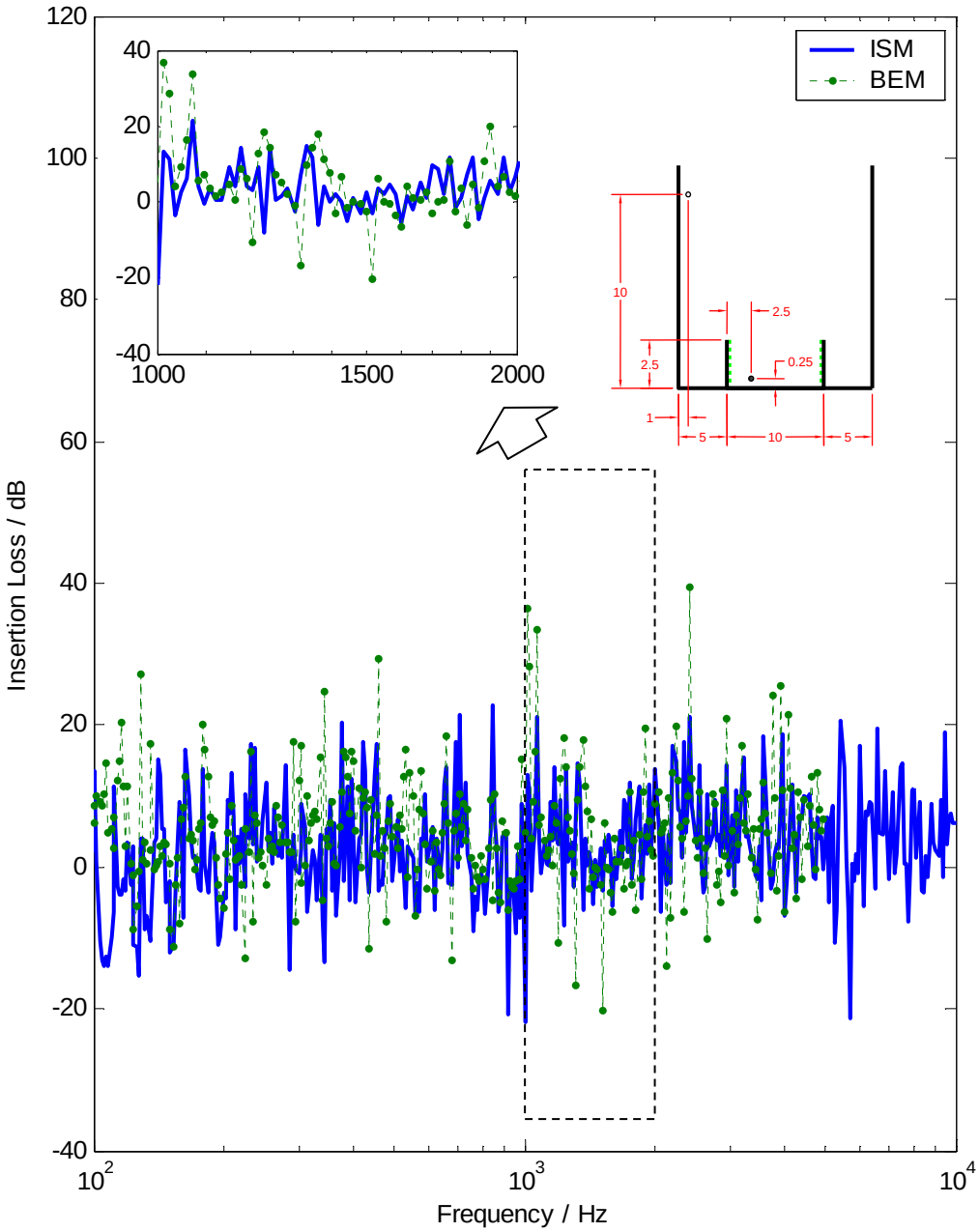

Figure 4.9 The spectrum of insertion losses (IL) at location $\mathfrak{R}$=(1,0,10) with parallel barriers having absorptive inner surfaces in a street canyon. The impedance of the inner surface is modeled with the Delany and Bazley model with the flow resistivity equal to 40,000 MKS rayls/m. The solid line represents predictions by the image source method (ISM) and the dashed line with dots represents numerical predictions based on the boundary element method (BEM).

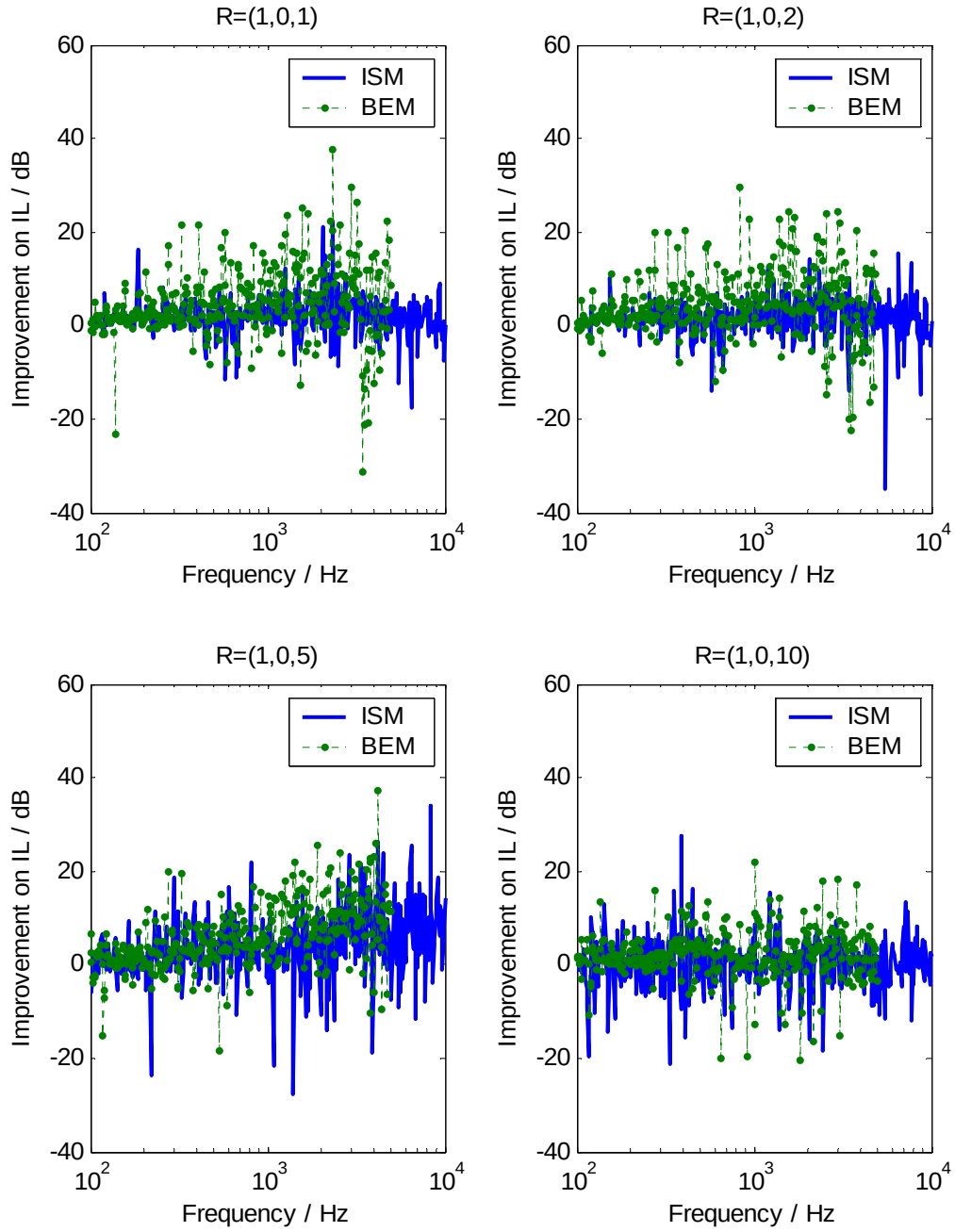

Figure 4.10 The spectrum of improvement in insertion losses (IL) at location $\mathfrak{R}$=(1,0,1), $\mathfrak{R}$=(1,0,2), $\mathfrak{R}$=(1,0,5), and $\mathfrak{R}$=(1,0,10) with parallel barriers having absorptive inner surfaces in a street canyon over barriers with hard surfaces. The solid line represents predictions by the image source method (ISM) and the dashed line with dots represents numerical predictions based on the boundary element method (BEM).

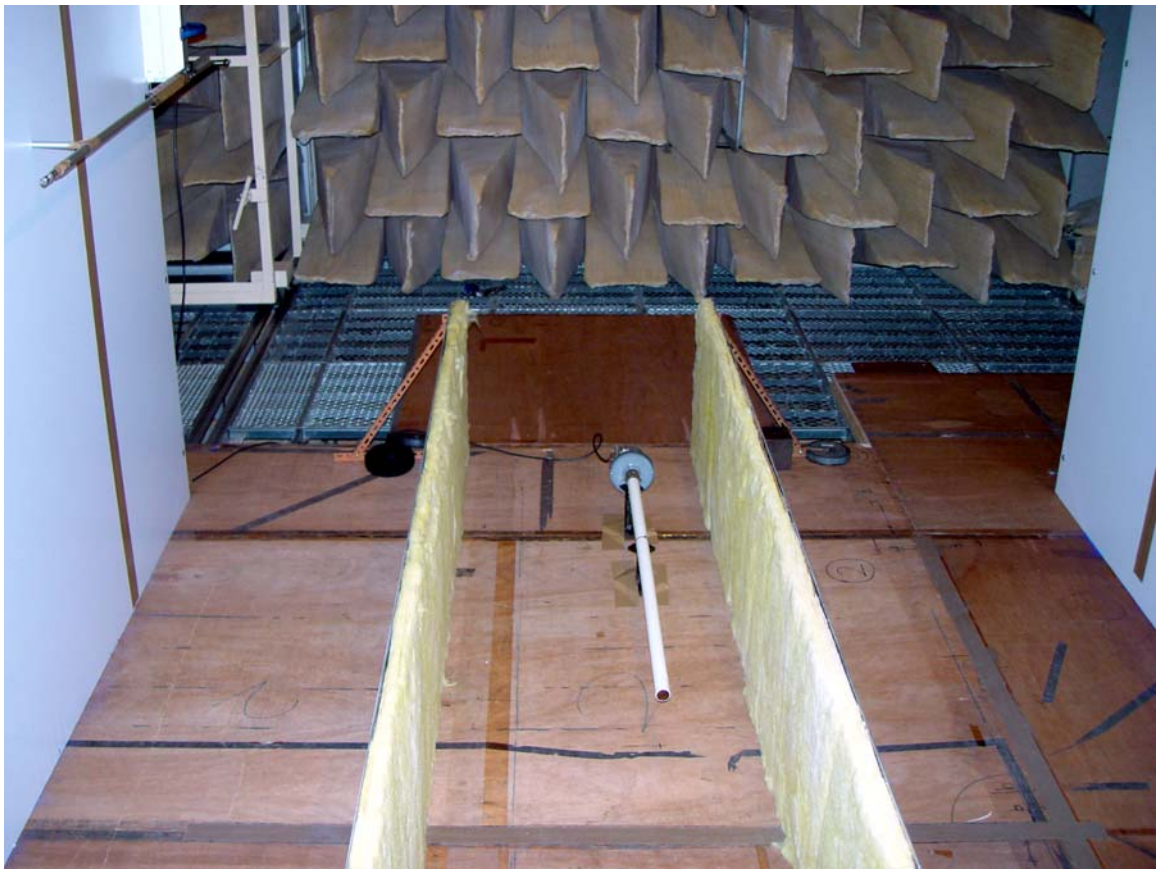

Figure 4.11 The experimental measurement set-up.

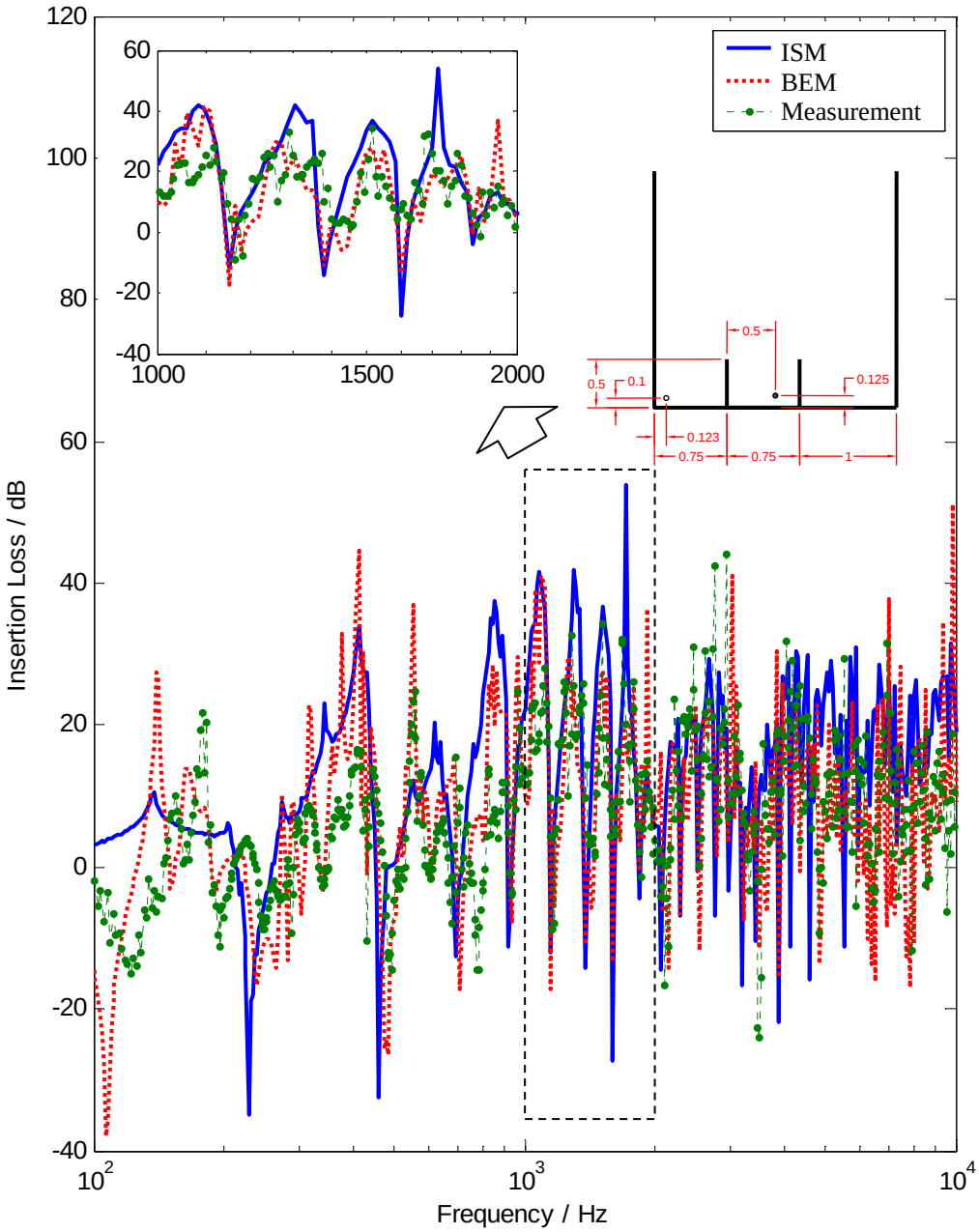

Figure 4.12 The spectrum of insertion losses (IL) at location $\mathfrak{R}$=(0.123,0,0.1) with parallel barriers having hard inner surfaces in a street canyon. The solid line represents predictions by the image source method (ISM), the dashed line represents numerical predictions based on the boundary element method (BEM) and the dashed line with dots represents results from experimental measurement.

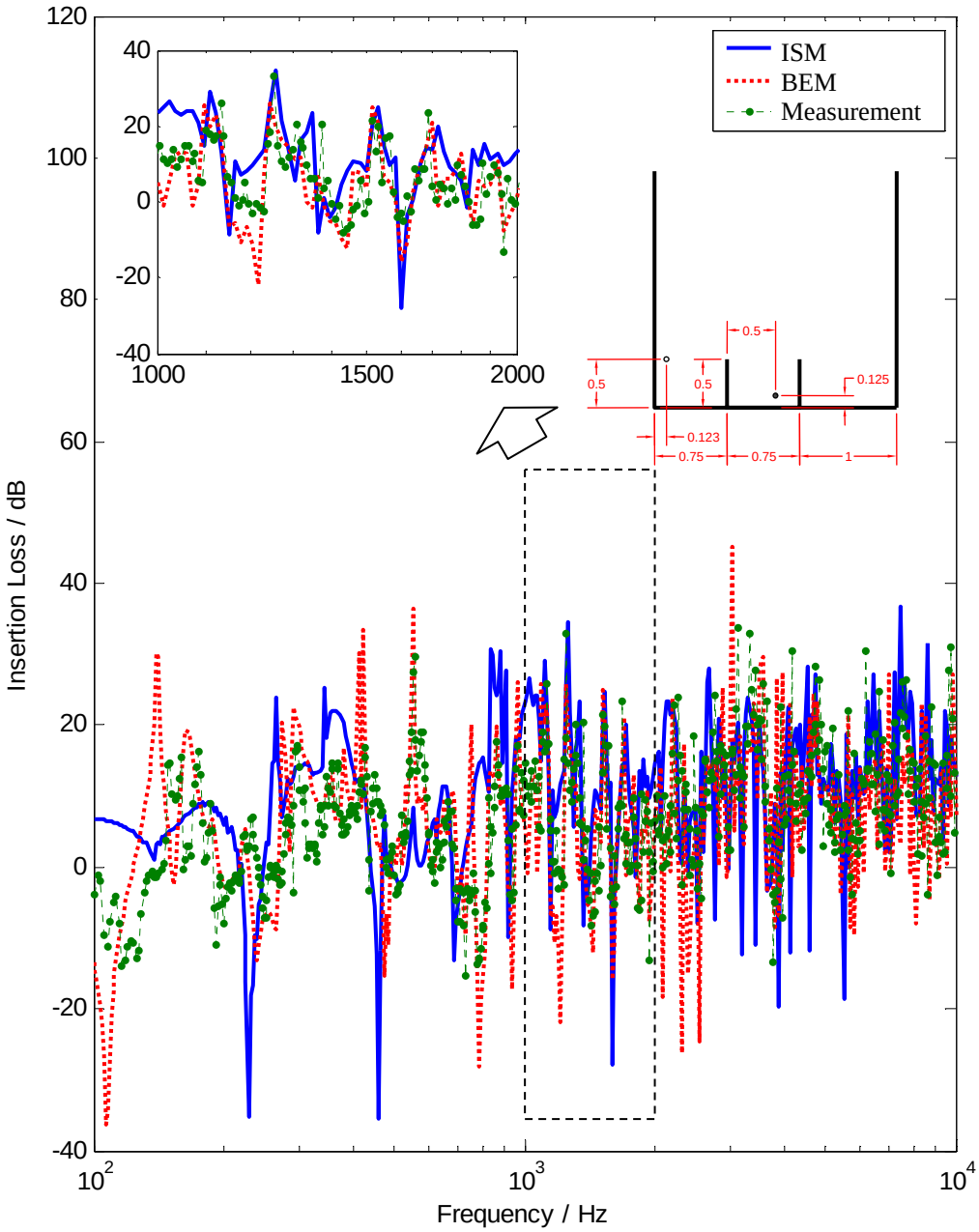

Figure 4.13 The spectrum of insertion losses (IL) at location $\mathfrak{R}$=(0.123,0,0.5) with parallel barriers having hard inner surfaces in a street canyon. The solid line represents predictions by the image source method (ISM), the dashed line represents numerical predictions based on the boundary element method (BEM) and the dashed line with dots represents results from experimental measurement.

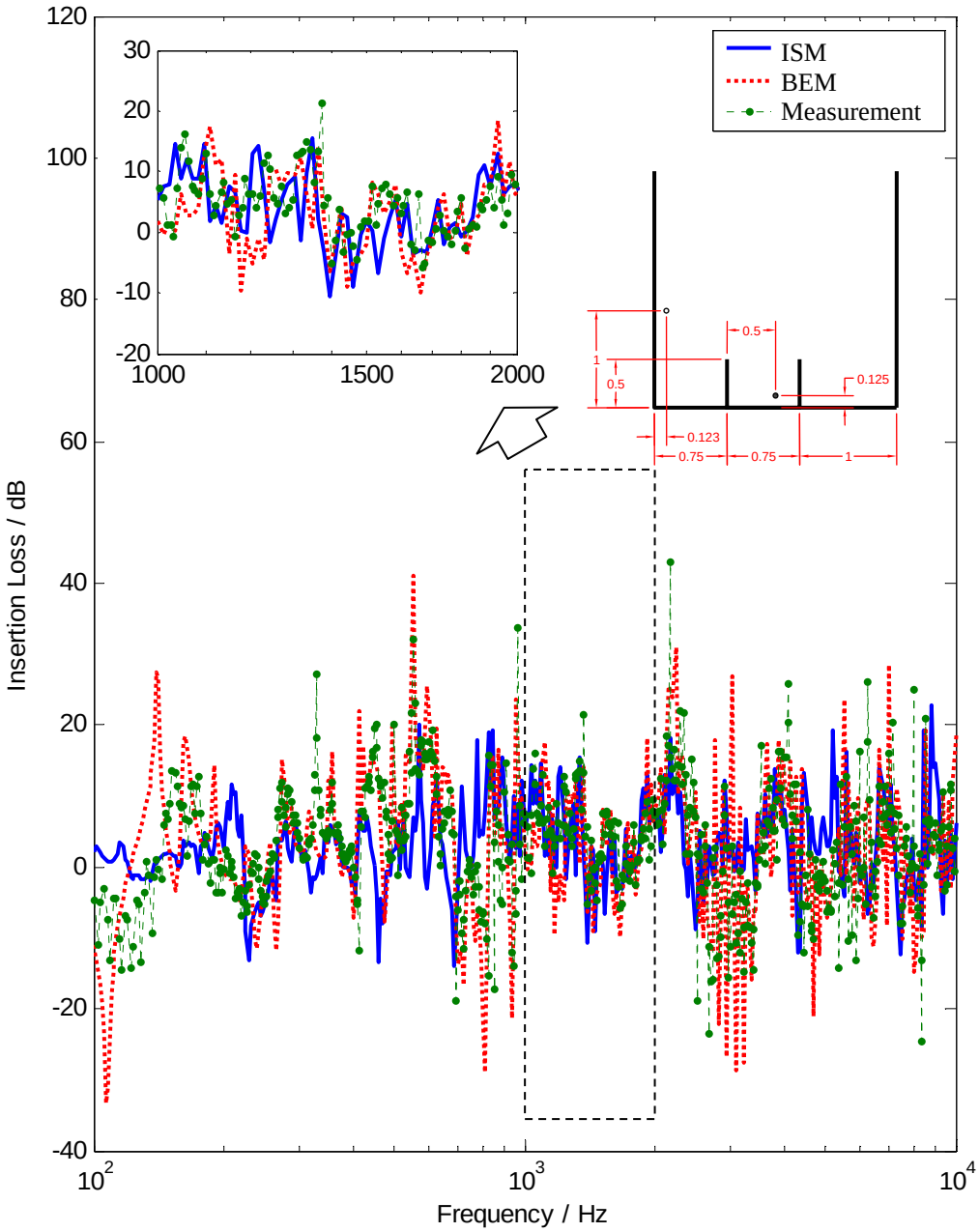

Figure 4.14 The spectrum of insertion losses (IL) at location $\mathfrak{R}$=(0.123,0,1) with parallel barriers having hard inner surfaces in a street canyon. The solid line represents predictions by the image source method (ISM), the dashed line represents numerical predictions based on the boundary element method (BEM) and the dashed line with dots represents results from experimental measurement.

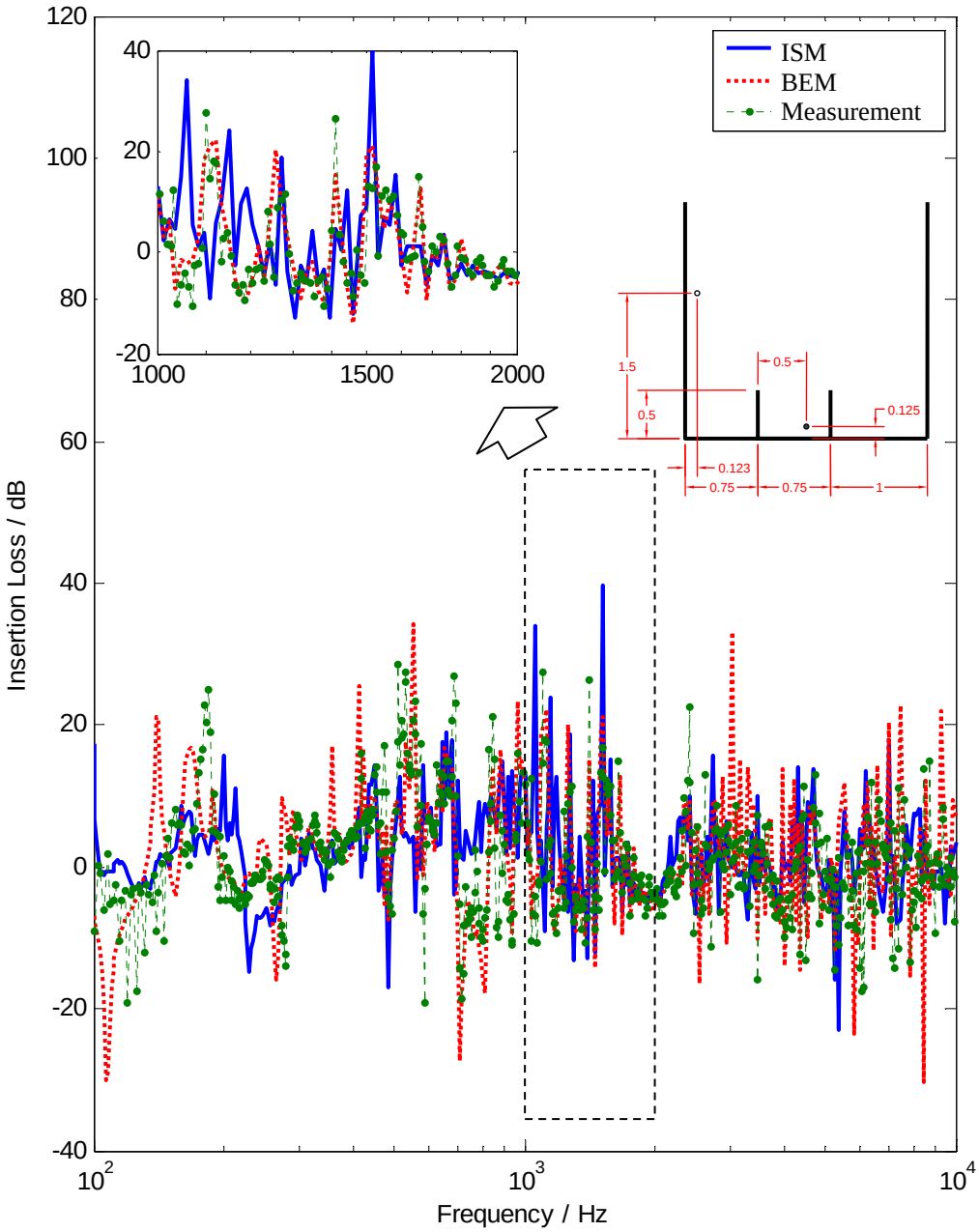

Figure 4.15 The spectrum of insertion losses (IL) at location $\mathfrak{R}$=(0.123,0,1.5) with parallel barriers having hard inner surfaces in a street canyon. The solid line represents predictions by the image source method (ISM), the dashed line represents numerical predictions based on the boundary element method (BEM) and the dashed line with dots represents results from experimental measurement.

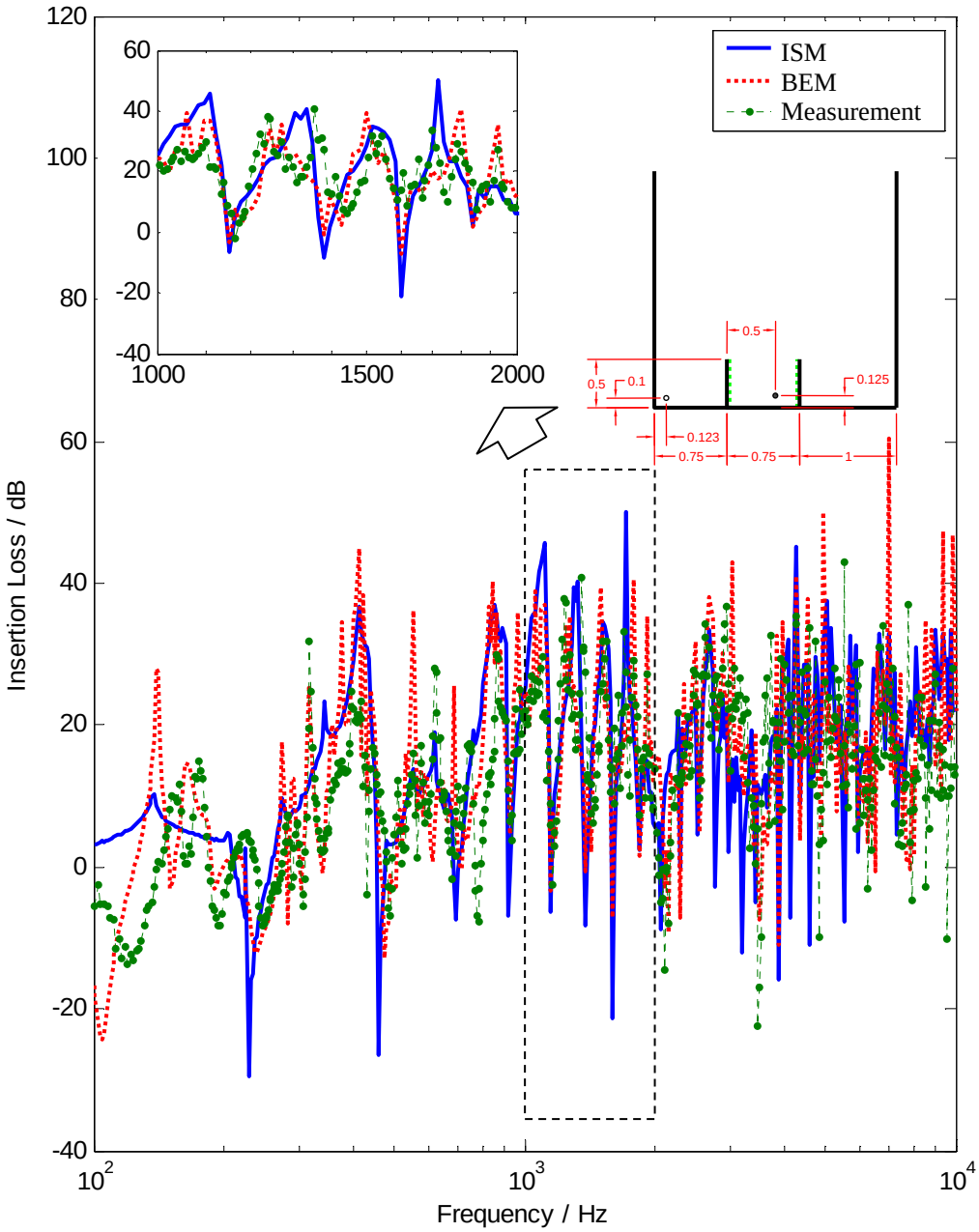

Figure 4.16 The spectrum of insertion losses (IL) at location $\mathfrak{R}$=(0.123,0,0.1) with parallel barriers having absorptive inner surfaces in a street canyon. The impedance of the inner surface is modeled with the Delany and Bazley model with the flow resistivity equal to 72,351 MKS rayls/m. The solid line represents predictions by the image source method (ISM), the dashed line represents numerical predictions based on the boundary element method (BEM) and the dashed line with dots represents results from experimental measurement.

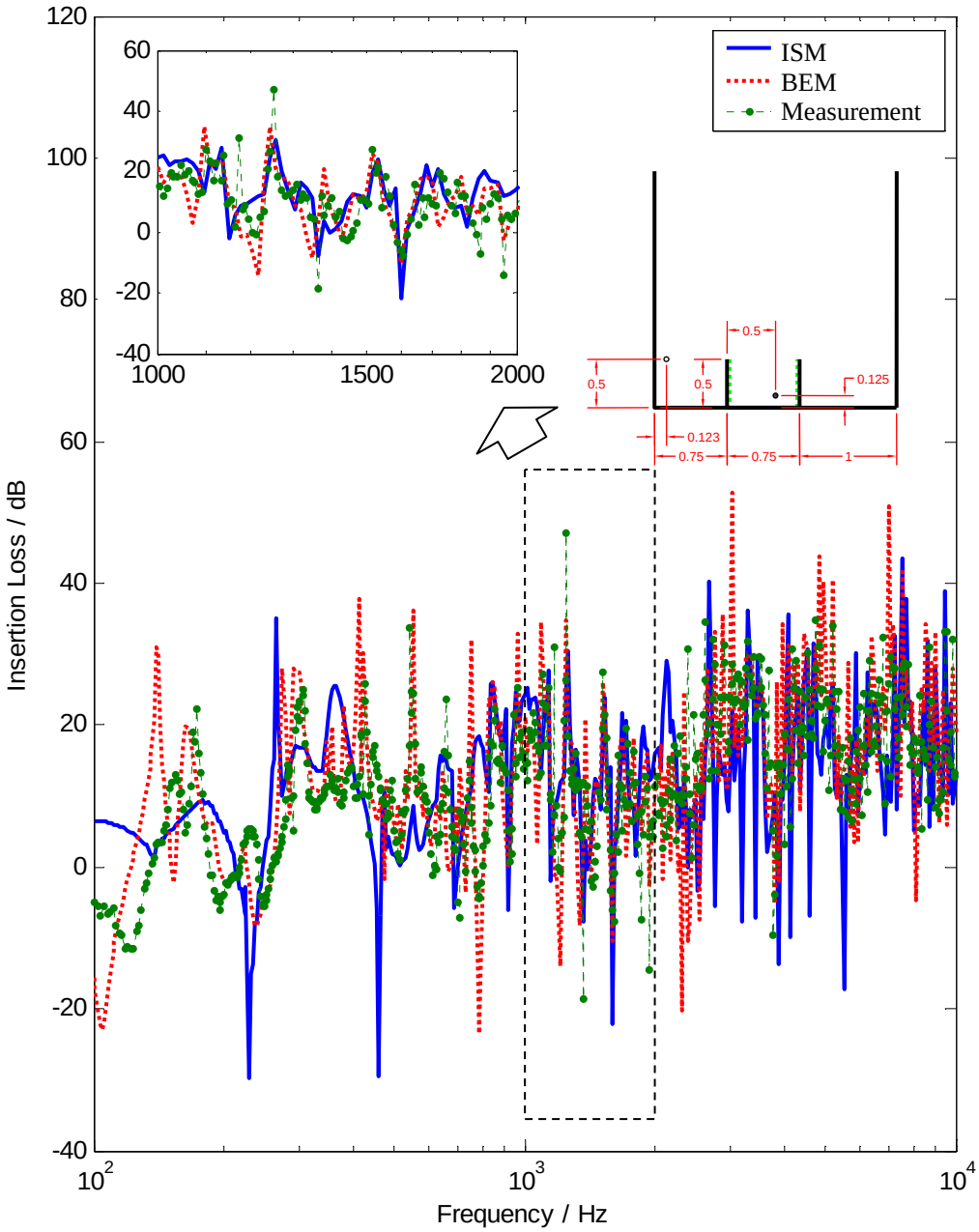

Figure 4.17 The spectrum of insertion losses (IL) at location $\mathfrak{R}$=(0.123,0,0.5) with parallel barriers having absorptive inner surfaces in a street canyon. The impedance of the inner surface is modeled with the Delany and Bazley model with the flow resistivity equal to 72,351 MKS rayls/m. The solid line represents predictions by the image source method (ISM), the dashed line represents numerical predictions based on the boundary element method (BEM) and the dashed line with dots represents results from experimental measurement.

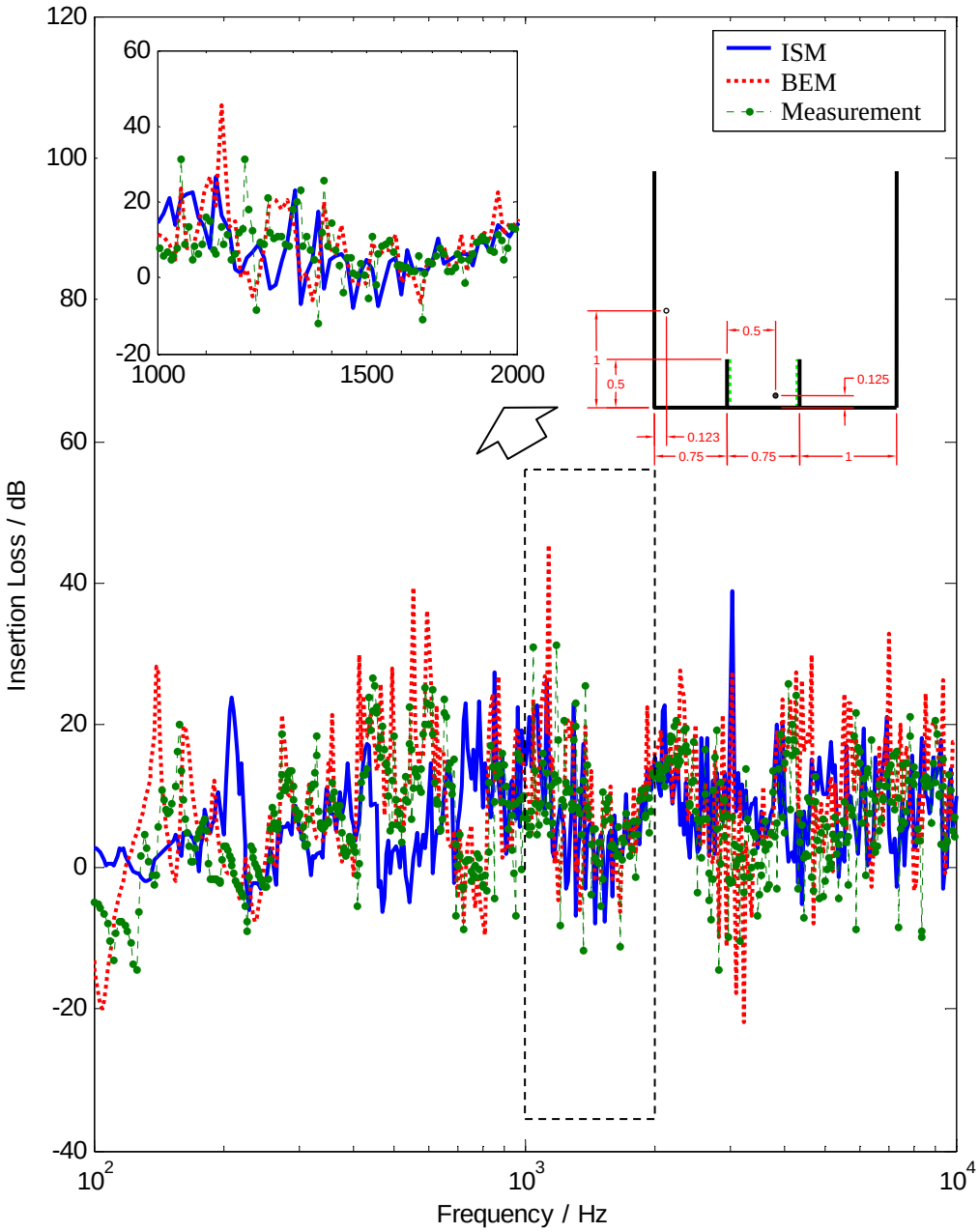

Figure 4.18 The spectrum of insertion losses (IL) at location $\mathfrak{R}$=(0.123,0,1.0) with parallel barriers having absorptive inner surfaces in a street canyon. The impedance of the inner surface is modeled with the Delany and Bazley model with the flow resistivity equal to 72,351 MKS rayls/m. The solid line represents predictions by the image source method (ISM), the dashed line represents numerical predictions based on the boundary element method (BEM) and the dashed line with dots represents results from experimental measurement.

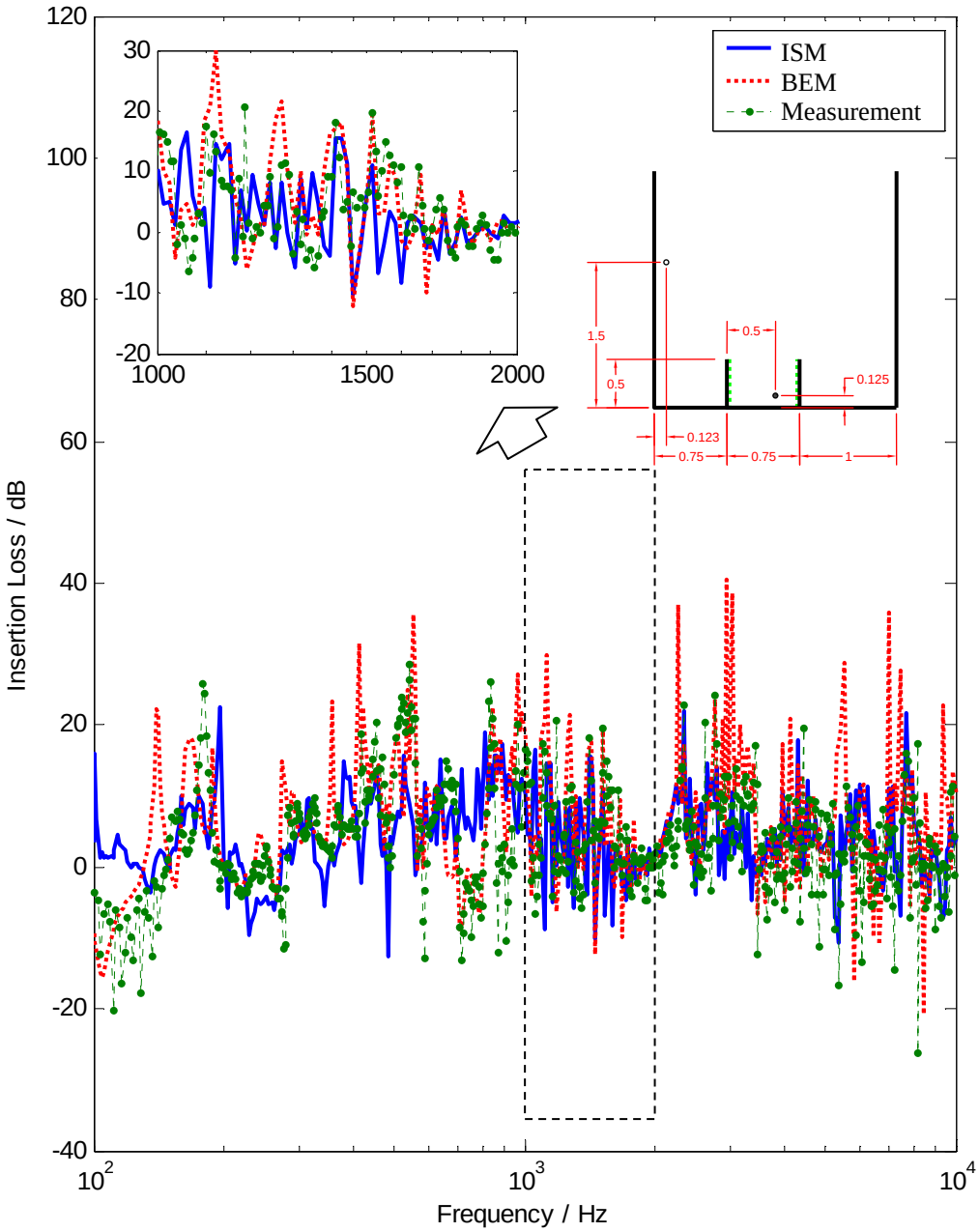

Figure 4.19 The spectrum of insertion losses (IL) at location $\mathfrak{R}$=(0.123,0,1.5) with parallel barriers having absorptive inner surfaces in a street canyon. The impedance of the inner surface is modeled with the Delany and Bazley model with the flow resistivity equal to 72,351 MKS rayls/m. The solid line represents predictions by the image source method (ISM), the dashed line represents numerical predictions based on the boundary element method (BEM) and the dashed line with dots represents results from experimental measurement.

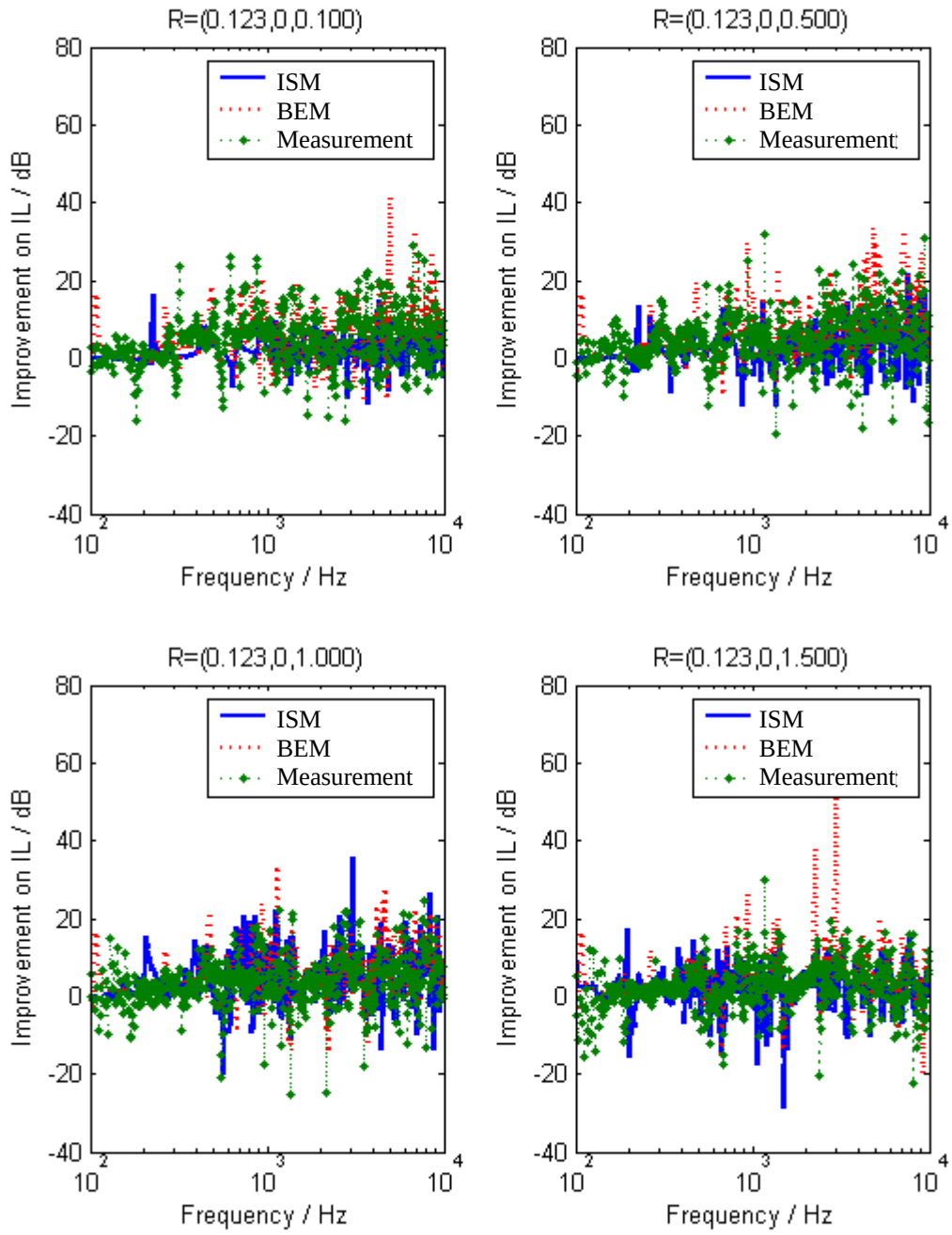

Figure 4.20 The spectrum of improvement in insertion losses (IL) at location $\mathfrak{R}$=(0.123,0,0.1), $\mathfrak{R}$=(0.123,0,0.5), $\mathfrak{R}$=(0.123,0,1), and $\mathfrak{R}$=(0.123,0,1.5) with parallel barriers having absorptive inner surfaces in a street canyon over barriers with hard surfaces. The solid line represents predictions by the image source method (ISM), the dashed line represents numerical predictions based on the boundary element method (BEM) and the dashed line with dots represents results from experimental measurement.

Chapter 5 Conclusions and Recommendations

5.1 Conclusions

The research reported in this thesis focuses on the acoustical performance evaluation of roadside barriers located in an urban environment. It aims to develop an accurate computational model for the predictions of the screening performance of roadside barriers. This can provide a quantitative justification of the construction of roadside barriers at the planning stage.

Extensive reviews on various development and research work are given in Chapter 1. The topics include outdoor sound propagation, in-situ determination of impedance, diffraction of sound wave, shielding performance of single and parallel barriers, and performance of barriers in urban environments. It is found that there are very limited studies incorporating the shielding performance of barriers in the context of a complex environment where the barriers are situated.

One of the fundamental necessities involved in the study is an accurate description of the acoustic impedances of the surfaces. In Chapter 2, an in-situ measurement methodology for acoustic impedance is developed for overcoming the shortcoming of the standardized measurement methods and traditional modelling techniques. The measurement method is based on the classical spherical wave propagation theory and numerical minimization techniques. With the improved measurement technique and minimization algorithm, the

in-situ method developed is proved to be robust and successful. It also provides an important basis for further study of noise barriers.

A common scenario for the noise mitigation of roadside barriers in urban environments is a road aligned parallel to a building façade. A prediction model of the sound field on this configuration is developed in Chapter 3. The computational model is based on the image source method and the flexibility of adopting acoustic absorptive surfaces is included in the model. Compared with those commercially available software based on the ray-tracing method, our model does not contain error due to the discrete sampling of rays. As all possible image sources can be determined in our model, the risk of getting non-convergent results is also minimized. The hierarchy of the image sources summarised provides an effective means in determination of all image sources. This gives our model a high and practical computational efficiency which is not attainable by the BEM. The image source model is validated by comparison with the BEM and experimental results. The comparison shows good agreement between the results and the accuracy of the image source model is proved.

Another typical metropolitan environment is that buildings are fully occupied along both sides of a roadway. This constitutes a street canyon in which noise is being trapped in between the buildings. Due to the effect of multiple interferences, the noise shielding performance of the parallel barriers in these situations are more complex and uncertain. In Chapter 4, the image source model is further extended for this scenario. From results of the validation, the predicted results of the image source model are found to be fairly reliable. The additional inaccuracy is mainly due to the accumulation of errors involved in the heuristic diffraction formulation during the huge numbers of summations

conducted. Nevertheless, the accuracy is still acceptable and the prediction model serves well for its purpose.

5.2 Recommendations

The effort put into this study do not limit to the shielding performance of roadside barriers. Our study forms a valuable foundation and exploration in the acoustic modeling techniques in a complex environment. Based on the experience attained through this investigation, the following topics are recommended for future study.

The overall accuracy of the image source model is strongly dependent on the accuracy of the calculation in every fundamental contribution. The heuristic diffraction formulation adopted in our study is only a high frequency approximation. When the model is applied to relatively small scale systems, the error might become significant. Furthermore, the analytic solution to the effect of finite impedance in diffraction is not yet available. A more precise understanding on this area would be very helpful.

In the current study, the quantity of insertion loss is in terms of a single frequency. It would be more useful if the insertion loss is expressed in terms of a frequency band. Due to the oscillating nature of the sound spectrum, it is possible that the interference effect of a particular frequency may dominate the whole frequency band. Meanwhile, it is also possible that the interference effect of a particular frequency is missed due to the frequency resolution in the whole spectrum. Therefore, it is worthwhile to investigate a proper representation of the insertion loss in frequency bands and a suitable selection of frequency resolution during the band conversion. This investigation also makes the

possibility to represent the shielding performance using a more meaningful A-weighted sound pressure level.

The sound sources that we adopted in our study are assumed to be spherical point sources or cylindrical line sources. In a real situation, however, there would be various directivity patterns on the sources. The difference in source strength among different angle would influence the theoretical evaluation of the acoustical performance of barriers. Further study can be processed for adopting the directivity effect on the image source model.

Appendix Image Source Modeling for Parallel Barriers

A.1 Introduction

In this section, the details of the image source models discussed in Chapter 3 and Chapter 4 are presented. The models are used for the evaluation of the shielding performance of parallel barriers located in two conditions. For the case of Chapter 3, the parallel barriers are in front of a building façade. For the case of Chapter 4, the parallel barriers are along a street canyon. The case for Chapter 3 can be considered as a simplified version of the case for Chapter 4. The image source models would provide the insertion loss of the barriers for particular positions of source and receiver and hence give an indication of the shielding performance of the barriers.

For the principle of the image source method, the total sound pressure at a particular location is the coherence summation of all contributions from the image sources that can contribute to that location. The main tasks involved are the identification of all the possible image sources and the calculation on the corresponding contribution of the image sources. We identify the possibility of contribution of an image source by determining whether a valid transmission path can be established between the source and the receiver. The possible paths may be through direct transmissions, reflections, and diffractions. They can be any combinations of reflections and diffractions with different orders. To reduce the complexity in the determination of all possible paths, we only

consider diffraction with one order. Any further diffraction would be ignored. This assumption is justifiable because the sound pressure level of the diffracted sound field is generally much less than that of the direct and reflected fields.

With the simplification of ignoring diffraction with order higher than one, the pressure contributions are categorized into two groups. The contributions without diffraction involved are considered as primary. Meanwhile, the contributions with diffraction involved are categorized as secondary. Inside these two main groups, the image sources are further classified into sub-groups based on the sequences of diffractions and reflections. Due to the additional façade surface, there would be more combinations contained in the case of the parallel barriers along a street canyon. The coordinates of the image sources are obtained by geometric relation on the reflections and diffraction. The zone of contribution would be obtained by visibility check. The pressure contributions of those image sources with successful illumination are calculated with the base of the fundamental formulations presented in Chapter 3. In the coming section, all the image source groups of the case for the parallel barriers along a street canyon would be discussed.

A.2 Primary Contribution

For image sources belonging to a primary contribution, they are observed by the receiver in a straight line of sight. The primary image sources are categorized into 14 groups.

Group 1 is the image source with contribution through direct transmission. The image source is actually at the original location of the source and is denoted by,

$$\mathbf{I}_0 \equiv \mathbf{S} = (x_S, 0, z_S). \tag{A.1}$$

The pressure contribution of $\mathbf{I}_0$ is calculated by,

$$P_{101} = P_{direct}(\mathbf{I}_0 \mid \mathfrak{R}). \tag{A.2}$$

The illuminated zone of $\mathbf{I}_0$ is illustrated in figure A.1. The lines connecting $\mathbf{I}_0$ and the illuminated receivers should have no intersection with the line from $(L_1, 0, 0)$ to $(L_1, 0, H)$ and the line from $(L_1 + W, 0, 0)$ to $(L_1 + W, 0, H)$.

Group 2 is the image source with one time ground reflection. The image source is denoted as,

$$\mathbf{I}_{\underline{0}} = (x_S, 0, -z_S). \tag{A.3}$$

The underline in the subscript indicates ground reflection. The pressure contribution of $\mathbf{I}_{\underline{0}}$ is calculated by,

$$P_{102} = V_{102}(\mathbf{I}_{\underline{0}} \mid \mathfrak{R}) \cdot P_{direct}(\mathbf{I}_{\underline{0}} \mid \mathfrak{R}), \tag{A.4}$$

where the reflection factor $V_{102}(\mathbf{I} \mid \mathfrak{R})$ accounts for the ground reflection as follows,

$$V_{102}(\mathbf{I} \mid \mathfrak{R}) = Q(\mathbf{I}, \mathfrak{R}, \beta_{G2}). \tag{A.5}$$

The illuminated Zone of $\mathbf{I}_{\underline{0}}$ is illustrated in figure A.2. The lines connecting $\mathbf{I}_{\underline{0}}$ and the illuminated receivers should have no intersection with the line from $(L_1, 0, -H)$ to $(L_1, 0, H)$ and the line from $(L_1 + W, 0, -H)$ to $(L_1 + W, 0, H)$.

Group 3 comprises of the image sources formed by multiple reflections between the two parallel barriers and lastly reflected by the surface Γ_{B12}. They are denoted as,

$$\mathbf{I}_{B1}^{(n_1)} \equiv (x_{S\text{-}B1}^{(n_1)}, 0, z_S), \tag{A.6}$$

where $n_1 = 1,2,3,\cdots$. The subscript B1 indicates that they are located behind the barrier B1 and the superscript n_1 in bracket denotes the total number, or sometimes known as the order, of reflections from the barrier surfaces. For odd order image sources $\mathbf{I}_{\mathrm{B1}}^{(2m_1+1)}$, where $m_1 = 0,1,2,\ldots$, they are reflected m_1+1 times by the barrier surface Γ_{B12} and m_1 times by the barrier surface Γ_{B21}. For even order image sources $\mathbf{I}_{\mathrm{B1}}^{(2m_1)}$, where $m_1 = 1,2,3,\ldots$, they are reflected m_1 times by both barrier surfaces Γ_{B12} and Γ_{B21}. It is straightforward to determine The x-coordinate $x_{\mathrm{S\text{-}B1}}^{(n_1)}$ of the image source is calculated as,

$$x_{\mathrm{S\text{-}B1}}^{(n_1)} = \begin{cases} L_1 - W_1 - W\cdot(n_1-1) & \text{for } n_1 = 1,3,5,\ldots \\ L_1 - W_2 - W\cdot(n_1-1) & \text{for } n_1 = 2,4,6,\ldots \end{cases} \tag{A.7}$$

The contribution of $\mathbf{I}_{\mathrm{B1}}^{(n_1)}$ is calculated by,

$$P_{103}^{(n_1)} = V_{103}^{(n_1)}\left(\mathbf{I}_{\mathrm{B1}}^{(n_1)} \mid \mathfrak{R}\right)\cdot P_{direct}\left(\mathbf{I}_{\mathrm{B1}}^{(n_1)} \mid \mathfrak{R}\right). \tag{A.8}$$

The factor $V_{103}^{(n_1)}\left(\mathbf{I} \mid \mathfrak{R}\right)$, which accounts for the effects of the multiple reflections between the surfaces Γ_{B12} and Γ_{B21}, is given by,

$$V_{103}^{(n_1)}\left(\mathbf{I} \mid \mathfrak{R}\right) = \begin{cases} \left[Q\left(\mathbf{I},\mathfrak{R},\beta_{\mathrm{B12}}\right)\right]^{m+1}\cdot\left[Q\left(\mathbf{I},\mathfrak{R},\beta_{\mathrm{B21}}\right)\right]^{m_1} & \text{for } n_1 = 2m_1+1 \\ \left[Q\left(\mathbf{I},\mathfrak{R},\beta_{\mathrm{B12}}\right)\cdot Q\left(\mathbf{I},\mathfrak{R},\beta_{\mathrm{B21}}\right)\right]^{m_1} & \text{for } n_1 = 2m_1 \end{cases}. \tag{A.9}$$

The illuminated zone of $\mathbf{I}_{\mathrm{B1}}^{(n_1)}$ is illustrated in figure A.3. The lines connecting $\mathbf{I}_{\mathrm{B1}}^{(n_1)}$ and the illuminated receivers should have an intersection with the line from $(L_1, 0, 0)$ to $(L_1, 0, H)$ and have no intersection with the line from $(L_1+W, 0, 0)$ to $(L_1+W, 0, H)$.

Group 4 contains the ground reflected image sources formed by multiple reflections between the surfaces Γ_{B12} and Γ_{B21} and lastly reflected by the surface Γ_{B12}. They are

similar to the image sources in group 3 but involve one more reflection with the ground surface Γ_{G2}. They are denoted as,

$$\mathbf{I}_{\underline{B1}}^{(n_1)} \equiv \left(x_{S\text{-}B1}^{(n_1)}, 0, -z_S\right), \tag{A.10}$$

where $n_1 = 1,2,3,\cdots$. The subscript $\underline{B1}$ indicates that they are located behind the barrier B1 and the underline in the subscript indicates the ground reflection. The superscript n_1 in bracket denotes the total number of reflections from the barrier surfaces. For odd order image sources $\mathbf{I}_{\underline{B1}}^{(2m_1+1)}$, where $m_1 = 0,1,2,\ldots$, they are reflected once by the ground surface Γ_{G2}, m_1+1 times by the barrier surface Γ_{B12} and m_1 times by the barrier surface Γ_{B21}. For even order image sources $\mathbf{I}_{B1}^{(2m_1)}$, where $m_1 = 1,2,3,\ldots$, they are reflected once by the ground surface Γ_{G2} and m_1 times by both barrier surfaces Γ_{B12} and Γ_{B21}. The x-coordinate of the image source $x_{S\text{-}B1}^{(n_1)}$ is calculated by equation A.7. The contribution of $\mathbf{I}_{\underline{B1}}^{(n_1)}$ is calculated by,

$$P_{104}^{(n_1)} = V_{104}^{(n_1)}\left(\mathbf{I}_{\underline{B1}}^{(n_1)} \mid \mathfrak{R}\right) \cdot P_{direct}\left(\mathbf{I}_{\underline{B1}}^{(n_1)} \mid \mathfrak{R}\right). \tag{A.11}$$

The factor $V_{104}^{(n_1)}\left(\mathbf{I} \mid \mathfrak{R}\right)$, which accounts for the effects of the multiple reflections between the surfaces Γ_{G2}, Γ_{B12} and Γ_{B21}, is given by,

$$V_{104}^{(n_1)}\left(\mathbf{I} \mid \mathfrak{R}\right) = \begin{cases} Q\left(\mathbf{I}, \mathfrak{R}, \beta_{G2}\right) \cdot \left[Q\left(\mathbf{I}, \mathfrak{R}, \beta_{B12}\right)\right]^{m_1+1} \cdot \left[Q\left(\mathbf{I}, \mathfrak{R}, \beta_{B21}\right)\right]^{m_1} & \text{for } n_1 = 2m_1+1 \\ Q\left(\mathbf{I}, \mathfrak{R}, \beta_{G2}\right) \cdot \left[Q\left(\mathbf{I}, \mathfrak{R}, \beta_{B12}\right) \cdot Q\left(\mathbf{I}, \mathfrak{R}, \beta_{B21}\right)\right]^{m_1} & \text{for } n_1 = 2m_1 \end{cases}. \tag{A.12}$$

The illuminated zone of $\mathbf{I}_{\underline{B1}}^{(n_1)}$ is illustrated in figure A.4. The lines connecting $\mathbf{I}_{\underline{B1}}^{(n_1)}$ and the illuminated receivers should have no intersection with the line from $\left(L_1, 0, -H\right)$ to $\left(L_1, 0, H\right)$ and have an intersection with the line from $\left(L_1+W, 0, -H\right)$ to $\left(L_1+W, 0, H\right)$.

Group 5 consists of image sources formed by multiple reflections between the surfaces Γ_{B12} and Γ_{B21} and lastly reflected by the surface Γ_{B21}. They are denoted as,

$$\mathbf{I}_{B2}^{(n_1)} \equiv \left(x_{S\text{-}B2}^{(n_1)}, 0, z_S\right), \tag{A.13}$$

where $n_1 = 1,2,3,\cdots$. The subscript B2 indicates that they are located behind the barrier B2 and the superscript n_1 in bracket denotes the total number of reflections from the barrier surfaces. For odd order image sources $\mathbf{I}_{B2}^{(2m_1+1)}$, where $m_1 = 0,1,2,\ldots$, they are reflected m_1 times by the barrier surface Γ_{B12} and m_1+1 times by the barrier surface Γ_{B21}. For even order image sources $\mathbf{I}_{B2}^{(2m_1)}$, where $m_1 = 1,2,3,\ldots$, they are reflected m_1 times by both barrier surfaces Γ_{B12} and Γ_{B21}. The x-coordinate $x_{S\text{-}B2}^{(n_1)}$ of the image source is calculated by,

$$x_{S\text{-}B2}^{(n_1)} = \begin{cases} L_1 + W_2 + W \cdot (n_1) & \text{for } n_1 = 1,3,5,\ldots \\ L_1 + W_1 + W \cdot (n_1) & \text{for } n_1 = 2,4,6,\ldots \end{cases}. \tag{A.14}$$

The pressure contribution of $\mathbf{I}_{B2}^{(n_1)}$ is calculated by,

$$P_{105}^{(n_1)} = V_{105}^{(n_1)}\left(\mathbf{I}_{B2}^{(n_1)} \mid \mathfrak{R}\right) \cdot P_{direct}\left(\mathbf{I}_{B2}^{(n_1)} \mid \mathfrak{R}\right). \tag{A.15}$$

The factor $V_{105}^{(n_1)}\left(\mathbf{I} \mid \mathfrak{R}\right)$, which accounts for the effects of the multiple reflections between the surfaces Γ_{B12} and Γ_{B21}, is given by,

$$V_{105}^{(n_1)}\left(\mathbf{I} \mid \mathfrak{R}\right) = \begin{cases} \left[Q\left(\mathbf{I}, \mathfrak{R}, \beta_{B12}\right)\right]^m \cdot \left[Q\left(\mathbf{I}, \mathfrak{R}, \beta_{B21}\right)\right]^{m_1+1} & \text{for } n_1 = 2m_1 + 1 \\ \left[Q\left(\mathbf{I}, \mathfrak{R}, \beta_{B12}\right) \cdot Q\left(\mathbf{I}, \mathfrak{R}, \beta_{B21}\right)\right]^{m_1} & \text{for } n_1 = 2m_1 \end{cases}. \tag{A.16}$$

The illuminated zone of $\mathbf{I}_{B2}^{(n_1)}$ is illustrated in figure A.5. The lines connecting $\mathbf{I}_{B2}^{(n_1)}$ and the illuminated receivers should have no intersection with the line from $(L_1, 0, 0)$ to $(L_1, 0, H)$ and have an intersection with the line from $(L_1 + W, 0, 0)$ to $(L_1 + W, 0, H)$.

Group 6 contains the ground reflected image sources formed by multiple reflections between the surfaces Γ_{B12} and Γ_{B21} and lastly reflected by the surface Γ_{B21}. They are denoted as,

$$\mathbf{I}_{\underline{B2}}^{(n_1)} \equiv \left(x_{S\text{-}B2}^{(n_1)}, 0, -z_S\right), \tag{A.17}$$

where $n_1 = 1,2,3,\cdots$. The subscript $\underline{B2}$ indicates that they are located behind the barrier $B2$ and the underline in the subscript indicates the ground reflection. The superscript n_1 in bracket denotes the total number of reflections from the barrier surfaces. For odd order image sources $\mathbf{I}_{\underline{B2}}^{(2m_1+1)}$, where $m_1 = 0,1,2,\ldots$, they are reflected once by the ground surface Γ_{G2}, m_1 times by the barrier surface Γ_{B12} and m_1+1 times by the barrier surface Γ_{B21}. For even order image sources $\mathbf{I}_{\underline{B2}}^{(2m_1)}$, where $m_1 = 1,2,3,\ldots$, they are reflected once by the ground surface Γ_{G2} and m_1 times by both barrier surfaces Γ_{B12} and Γ_{B21}. The x-coordinate $x_{S\text{-}B2}^{(n_1)}$ of the image source is calculated by equation A.14. The pressure contribution of $\mathbf{I}_{\underline{B2}}^{(n_1)}$ is calculated by,

$$P_{106}^{(n_1)} = V_{106}^{(n_1)}\left(\mathbf{I}_{\underline{B2}}^{(n_1)} \mid \mathfrak{R}\right) \cdot P_{direct}\left(\mathbf{I}_{\underline{B2}}^{(n_1)} \mid \mathfrak{R}\right). \tag{A.18}$$

The factor $V_{106}^{(n_1)}\left(\mathbf{I} \mid \mathfrak{R}\right)$, which accounts for the effects of the multiple reflections between the surfaces Γ_{B12} and Γ_{B21}, is given by,

$$V_{106}^{(n_1)}\left(\mathbf{I} \mid \mathfrak{R}\right) = \begin{cases} Q\left(\mathbf{I}, \mathfrak{R}, \beta_{G2}\right) \cdot \left[Q\left(\mathbf{I}, \mathfrak{R}, \beta_{B12}\right)\right]^{m_1} \cdot \left[Q\left(\mathbf{I}, \mathfrak{R}, \beta_{B21}\right)\right]^{m_1+1} & \text{for } n_1 = 2m_1 + 1 \\ Q\left(\mathbf{I}, \mathfrak{R}, \beta_{G2}\right) \cdot \left[Q\left(\mathbf{I}, \mathfrak{R}, \beta_{B12}\right) \cdot Q\left(\mathbf{I}, \mathfrak{R}, \beta_{B21}\right)\right]^{m_1} & \text{for } n_1 = 2m_1 \end{cases} \tag{A.19}$$

The illuminated zone of $\mathbf{I}_{\underline{B2}}^{(n_1)}$ is illustrated in figure A.6. The lines connecting $\mathbf{I}_{\underline{B2}}^{(n_1)}$ and the illuminated receivers should have no intersection with the line from $\left(L_1, 0, -H\right)$ to $\left(L_1, 0, H\right)$ and have an intersection with the line from $\left(L_1 + W, 0, -H\right)$ to $\left(L_1 + W, 0, H\right)$.

Group 7 comprises of the image sources formed by multiple reflections between the two façade surfaces Γ_{F1} and Γ_{F2} and lastly reflected by the surface Γ_{F1}. They are denoted as,

$$\mathbf{I}_{F1}^{(n_2)} \equiv \left(x_{S\text{-}F1}^{(n_2)}, 0, z_S\right), \tag{A.20}$$

where $n_2 = 1,2,3,\cdots$. The subscript F1 indicates that they are located behind the façade surface Γ_{F1} and the superscript n_2 in bracket denotes the total number of reflections from the façade surfaces Γ_{F1} and Γ_{F2}. For odd order image sources $\mathbf{I}_{F1}^{(2m_2+1)}$, where $m_2 = 0,1,2,\ldots$, they are reflected m_2+1 times by the façade surface Γ_{F1} and m_2 times by the façade surface Γ_{F2}. For even order image sources $\mathbf{I}_{F1}^{(2m_2)}$, where $m_2 = 1,2,3,\ldots$, they are reflected m_2 times by both the façade surfaces Γ_{F1} and Γ_{F2}.The x-coordinate $x_{S\text{-}F1}^{(n_2)}$ of the image source is determined by,

$$x_{S\text{-}F1}^{(n_2)} = \begin{cases} -L_1 - W_1 - L\cdot(n_2 - 1) & \text{for } n_2 = 1,3,5,\ldots \\ -L_2 - W_2 - L\cdot(n_2 - 1) & \text{for } n_2 = 2,4,6,\ldots \end{cases} \tag{A.21}$$

The contribution of $\mathbf{I}_{F1}^{(n_2)}$ is calculated by,

$$P_{107}^{(n_2)} = V_{107}^{(n_2)}\left(\mathbf{I}_{F1}^{(n_2)} \mid \mathfrak{R}\right)\cdot P_{direct}\left(\mathbf{I}_{F1}^{(n_2)} \mid \mathfrak{R}\right). \tag{A.22}$$

The factor $V_{107}^{(n_2)}\left(\mathbf{I} \mid \mathfrak{R}\right)$, which accounts for the effects of the multiple reflections between the surfaces Γ_{F1} and Γ_{F2}, is given by,

$$V_{107}^{(n_2)}\left(\mathbf{I} \mid \mathfrak{R}\right) = \begin{cases} \left[Q\left(\mathbf{I}, \mathfrak{R}, \beta_{F1}\right)\right]^{m_2+1}\cdot\left[Q\left(\mathbf{I}, \mathfrak{R}, \beta_{F2}\right)\right]^{m_2} & \text{for } n_2 = 2m_2 + 1 \\ \left[Q\left(\mathbf{I}, \mathfrak{R}, \beta_{F1}\right)\cdot Q\left(\mathbf{I}, \mathfrak{R}, \beta_{F2}\right)\right]^{m_2} & \text{for } n_2 = 2m_2 \end{cases}. \tag{A.23}$$

The illuminated zone of $\mathbf{I}_{F1}^{(n_2)}$ is illustrated in figure A.7. For image sources $\mathbf{I}_{F1}^{(n_2)}$ with odd n_2, the lines connecting $\mathbf{I}_{F1}^{(n_2)}$ and the illuminated receivers should have no intersection with the line from $\left(x_{E1\text{-}F1\text{-}F2}^{(n_2)}, 0, 0\right)$ to $\left(x_{E1\text{-}F1\text{-}F2}^{(n_2)}, 0, H\right)$. The x-coordinate $x_{E1\text{-}F1\text{-}F2}^{(n_2)}$ is given by,

$$x_{E1\text{-}F1\text{-}F2}^{(n_2)} = \begin{cases} -L_1 + L\cdot(n_2 - 1) & \text{for } n_2 = 1, 3, 5,\ldots \\ L_1 + L\cdot(n_2) & \text{for } n_2 = 2, 4, 6,\cdots \end{cases}. \tag{A.24}$$

For image sources $\mathbf{I}_{\mathrm{F1}}^{(n_2)}$ with even n_2, the lines connecting $\mathbf{I}_{\mathrm{F1}}^{(n_2)}$ and the illuminated receivers should have no intersection with the line from $\left(x_{\mathrm{E2\text{-}F2\text{-}F1}}^{(n_2)}, 0, 0\right)$ to $\left(x_{\mathrm{E2\text{-}F2\text{-}F1}}^{(n_2)}, 0, H\right)$. The x-coordinate $x_{\mathrm{E2\text{-}F2\text{-}F1}}^{(n_2)}$ is given by,

$$x_{\mathrm{E2\text{-}F2\text{-}F1}}^{(n_2)} = \begin{cases} L_2 + L\cdot(n_2) & \text{for } n_2 = 1, 3, 5, \ldots \\ -L_2 - L\cdot(n_2 - 1) & \text{for } n_2 = 2, 4, 6, \cdots \end{cases}. \tag{A.25}$$

Group 8 contains the ground reflected image sources formed by multiple reflections between the two façade surfaces Γ_{F1} and Γ_{F2} and lastly reflected by the surface Γ_{F1}. They are denoted as,

$$\mathbf{I}_{\underline{\mathrm{F1}}}^{(n_2)} \equiv \left(x_{\mathrm{S\text{-}F1}}^{(n_2)}, 0, -z_{\mathrm{S}}\right), \tag{A.26}$$

where $n_2 = 1,2,3,\cdots$. The subscript $\underline{\mathrm{F1}}$ indicates that they are located behind the façade surface Γ_{F1} and the underline in the subscript indicates the ground reflection. The superscript n_2 in bracket denotes the total number of reflections from the façade surfaces Γ_{F1} and Γ_{F2}. For odd order image sources $\mathbf{I}_{\underline{\mathrm{F1}}}^{(2m_2+1)}$, where $m_2 = 0,1,2,\ldots$, they are reflected once by the ground surface Γ_{G2}, m_2+1 times by the façade surface Γ_{F1} and m_2 times by the façade surface Γ_{F2}. For even order image sources $\mathbf{I}_{\underline{\mathrm{F1}}}^{(2m_2)}$, where $m_2 = 1,2,3,\ldots$, they are reflected once by the ground surface Γ_{G2} and m_2 times by both the façade surfaces Γ_{F1} and Γ_{F2}.The x-coordinate $x_{\mathrm{S\text{-}F1}}^{(n_2)}$ of the image source is determined by equation A.21. The contribution of $\mathbf{I}_{\underline{\mathrm{F1}}}^{(n_2)}$ is calculated by,

$$P_{108}^{(n_2)} = V_{108}^{(n_2)}\left(\mathbf{I}_{\underline{\mathrm{F1}}}^{(n_2)} \mid \mathfrak{R}\right)\cdot P_{direct}\left(\mathbf{I}_{\underline{\mathrm{F1}}}^{(n_2)} \mid \mathfrak{R}\right). \tag{A.27}$$

The factor $V_{108}^{(n_2)}\left(\mathbf{I} \mid \mathfrak{R}\right)$, which accounts for the effects of the multiple reflections between the surfaces Γ_{G2}, Γ_{F1} and Γ_{F2}, is given by,

$$V_{108}^{(n_2)}(\mathbf{I}\,|\,\mathfrak{R}) = \begin{cases} Q(\mathbf{I},\mathfrak{R},\beta_{G2})\cdot\left[Q(\mathbf{I},\mathfrak{R},\beta_{F1})\right]^{m_2+1}\cdot\left[Q(\mathbf{I},\mathfrak{R},\beta_{F2})\right]^{m_2} & \text{for } n_2 = 2m_2+1 \\ Q(\mathbf{I},\mathfrak{R},\beta_{G2})\cdot\left[Q(\mathbf{I},\mathfrak{R},\beta_{F1})\cdot Q(\mathbf{I},\mathfrak{R},\beta_{F2})\right]^{m_2} & \text{for } n_2 = 2m_2 \end{cases}. \qquad \text{(A.28)}$$

The illuminated zone of $\mathbf{I}_{\underline{F1}}^{(n_2)}$ is illustrated in figure A.8. For image sources $\mathbf{I}_{\underline{F1}}^{(n_2)}$ with odd order n_2, the lines connecting $\mathbf{I}_{\underline{F1}}^{(n_2)}$ and the illuminated receivers should have no intersection with the line from $\left(x_{\text{E1-F1-F2}}^{(n_2)}, 0, -H\right)$ to $\left(x_{\text{E1-F1-F2}}^{(n_2)}, 0, H\right)$. The x-coordinate $x_{\text{E1-F1-F2}}^{(n_2)}$ is given by equation A.24. For image sources $\mathbf{I}_{\underline{F1}}^{(n_2)}$ with even order n_2, the lines connecting $\mathbf{I}_{\underline{F1}}^{(n_2)}$ and the illuminated receivers should have no intersection with the line from $\left(x_{\text{E2-F2-F1}}^{(n_2)}, 0, -H\right)$ to $\left(x_{\text{E2-F2-F1}}^{(n_2)}, 0, H\right)$. The x-coordinate $x_{\text{E2-F2-F1}}^{(n_2)}$ is given by equation A.25.

Group 9 comprises of the image sources formed by multiple reflections between the two façade surfaces Γ_{F1} and Γ_{F2} and lastly reflected by the surface Γ_{F2}. They are denoted as,

$$\mathbf{I}_{F2}^{(n_2)} \equiv \left(x_{\text{S-F2}}^{(n_2)}, 0, z_S\right), \qquad \text{(A.29)}$$

where $n_2 = 1,2,3,\cdots$. The subscript F2 indicates that they are located behind the façade surface Γ_{F2} and the superscript n_2 in bracket denotes the total number of reflections from the façade surfaces Γ_{F1} and Γ_{F2}. For odd order image sources $\mathbf{I}_{F2}^{(2m_2+1)}$, where $m_2 = 0,1,2,\ldots$, they are reflected m_2 times by the façade surface Γ_{F1} and m_2+1 times by the façade surface Γ_{F2}. For even order image sources $\mathbf{I}_{F2}^{(2m_2)}$, where $m_2 = 1,2,3,\ldots$, they are reflected m_2 times by both the façade surfaces Γ_{F1} and Γ_{F2}. The x-coordinate $x_{\text{S-F2}}^{(n_2)}$ of the image source is determined by,

$$x_{\text{S-F2}}^{(n_2)} = \begin{cases} L_2 + W_2 + L\cdot(n_2) & \text{for } n_2 = 1,3,5,\ldots \\ L_1 + W_1 + L\cdot(n_2) & \text{for } n_2 = 2,4,6,\ldots \end{cases} \qquad \text{(A.30)}$$

The contribution of $\mathbf{I}_{\mathrm{F2}}^{(n_2)}$ is calculated by,

$$P_{109}^{(n_2)} = V_{109}^{(n_2)}\left(\mathbf{I}_{\mathrm{F2}}^{(n_2)} \mid \mathfrak{R}\right) \cdot P_{direct}\left(\mathbf{I}_{\mathrm{F2}}^{(n_2)} \mid \mathfrak{R}\right). \tag{A.31}$$

The factor $V_{109}^{(n_2)}\left(\mathbf{I} \mid \mathfrak{R}\right)$, which accounts for the effects of the multiple reflections between the surfaces Γ_{F1} and Γ_{F2}, is given by,

$$V_{109}^{(n_2)}\left(\mathbf{I} \mid \mathfrak{R}\right) = \begin{cases} \left[Q\left(\mathbf{I}, \mathfrak{R}, \beta_{\mathrm{F1}}\right)\right]^{m} \cdot \left[Q\left(\mathbf{I}, \mathfrak{R}, \beta_{\mathrm{F2}}\right)\right]^{m_2+1} & \text{for } n_2 = 2m_2 + 1 \\ \left[Q\left(\mathbf{I}, \mathfrak{R}, \beta_{\mathrm{F1}}\right) \cdot Q\left(\mathbf{I}, \mathfrak{R}, \beta_{\mathrm{F2}}\right)\right]^{m_2} & \text{for } n_2 = 2m_2 \end{cases}. \tag{A.32}$$

The illuminated zone of $\mathbf{I}_{\mathrm{F2}}^{(n_2)}$ is illustrated in figure A.9. For image sources $\mathbf{I}_{\mathrm{F2}}^{(n_2)}$ with odd order n_2, the lines connecting $\mathbf{I}_{\mathrm{F2}}^{(n_2)}$ and the illuminated receivers should have no intersection with the line from $\left(x_{\mathrm{E2\text{-}F2\text{-}F1}}^{(n_2)}, 0, 0\right)$ to $\left(x_{\mathrm{E2\text{-}F2\text{-}F1}}^{(n_2)}, 0, H\right)$. The x-coordinate $x_{\mathrm{E2\text{-}F2\text{-}F1}}^{(n_2)}$ is given by equation A.25. For image sources $\mathbf{I}_{\mathrm{F2}}^{(n_2)}$ with even order n_2, the lines connecting $\mathbf{I}_{\mathrm{F2}}^{(n_2)}$ and the illuminated receivers should have no intersection with the line from $\left(x_{\mathrm{E1\text{-}F1\text{-}F2}}^{(n_2)}, 0, 0\right)$ to $\left(x_{\mathrm{E1\text{-}F1\text{-}F2}}^{(n_2)}, 0, H\right)$. The x-coordinate $x_{\mathrm{E1\text{-}F1\text{-}F2}}^{(n_2)}$ is given by equation A.24.

Group 10 contains the ground reflected image sources formed by multiple reflections between the two façade surfaces Γ_{F1} and Γ_{F2} and lastly reflected by the surface Γ_{F2}. They are denoted as,

$$\mathbf{I}_{\underline{\mathrm{F2}}}^{(n_2)} \equiv \left(x_{\mathrm{S\text{-}F2}}^{(n_2)}, 0, -z_{\mathrm{S}}\right), \tag{A.33}$$

where $n_2 = 1,2,3,\cdots$. The subscript $\underline{\mathrm{F2}}$ indicates that they are located behind the façade surface Γ_{F2} and the underline in the subscript indicates the ground reflection. The superscript n_2 in bracket denotes the total number of reflections from the façade surfaces Γ_{F1} and Γ_{F2}. For odd order image sources $\mathbf{I}_{\underline{\mathrm{F2}}}^{(2m_2+1)}$, where $m_2 = 0,1,2,\ldots$, they are reflected

once by the ground surface Γ_{G2}, m_2 times by the façade surface Γ_{F1} and m_2+1 times by the façade surface Γ_{F2}. For even order image sources $\mathbf{I}_{\underline{F2}}^{(2m_2)}$, where $m_2 = 1,2,3,\ldots$, they are reflected once by the ground surface Γ_{G2} and m_2 times by both the façade surfaces Γ_{F1} and Γ_{F2}. The x-coordinate $x_{S\text{-}F2}^{(n_2)}$ of the image source is determined by equation A.30. The contribution of $\mathbf{I}_{\underline{F2}}^{(n_1)}$ is calculated by,

$$P_{110}^{(n_2)} = V_{110}^{(n_2)}\left(\mathbf{I}_{\underline{F2}}^{(n_2)} \mid \mathfrak{R}\right) \cdot P_{direct}\left(\mathbf{I}_{\underline{F2}}^{(n_2)} \mid \mathfrak{R}\right). \tag{A.34}$$

The factor $V_{110}^{(n_2)}\left(\mathbf{I} \mid \mathfrak{R}\right)$, which accounts for the effects of the multiple reflections between the surfaces Γ_{G2}, Γ_{F1} and Γ_{F2}, is given by,

$$V_{110}^{(n_2)}\left(\mathbf{I} \mid \mathfrak{R}\right) = \begin{cases} Q\left(\mathbf{I}, \mathfrak{R}, \beta_{G2}\right) \cdot \left[Q\left(\mathbf{I}, \mathfrak{R}, \beta_{F1}\right)\right]^{m_2} \cdot \left[Q\left(\mathbf{I}, \mathfrak{R}, \beta_{F2}\right)\right]^{m_2+1} & \text{for } n_2 = 2m_2 + 1 \\ Q\left(\mathbf{I}, \mathfrak{R}, \beta_{G2}\right) \cdot \left[Q\left(\mathbf{I}, \mathfrak{R}, \beta_{F1}\right) \cdot Q\left(\mathbf{I}, \mathfrak{R}, \beta_{F2}\right)\right]^{m_2} & \text{for } n_2 = 2m_2 \end{cases}. \tag{A.35}$$

The illuminated zone of $\mathbf{I}_{\underline{F2}}^{(n_1)}$ is illustrated in figure A.10. For image sources $\mathbf{I}_{\underline{F2}}^{(n_1)}$ with odd order n_2, the lines connecting $\mathbf{I}_{\underline{F2}}^{(n_1)}$ and the illuminated receivers should have no intersection with the line from $\left(x_{E2\text{-}F2\text{-}F1}^{(n_2)}, 0, -H\right)$ to $\left(x_{E2\text{-}F2\text{-}F1}^{(n_2)}, 0, H\right)$. The x-coordinate $x_{E2\text{-}F2\text{-}F1}^{(n_2)}$ is given by equation A.25. For image sources $\mathbf{I}_{\underline{F2}}^{(n_1)}$ with even order n_2, the lines connecting $\mathbf{I}_{\underline{F2}}^{(n_1)}$ and the illuminated receivers should have no intersection with the line from $\left(x_{E1\text{-}F1\text{-}F2}^{(n_2)}, 0, -H\right)$ to $\left(x_{E1\text{-}F1\text{-}F2}^{(n_2)}, 0, H\right)$. The x-coordinate $x_{E1\text{-}F1\text{-}F2}^{(n_2)}$ is given by equation A.24.

Group 11 consists of image sources formed by multiple reflections between the surfaces Γ_{F1} and Γ_{F2} of the image sources $\mathbf{I}_{B1}^{(n_1)}$. They are denoted as,

$$\mathbf{I}_{B1\text{-}F2\text{-}F1}^{(n_1,n_2)} \equiv \left(x_{S\text{-}B1\text{-}F2\text{-}F1}^{(n_1,n_2)}, 0, z_S\right), \tag{A.36}$$

where $n_1 = 1,2,3,\cdots$ and $n_2 = 1,2,3,\cdots$. The subscript B1 - F2 - F1 indicates the multiple reflections involved. After the last reflection by Γ_{B12} among the n_1 times multiple reflections between Γ_{B12} and Γ_{B21}, there would be n_2 times multiple reflections between surfaces Γ_{F1} and Γ_{F2} . For odd n_2 , the image sources $\mathbf{I}_{\text{B1-F2-F1}}^{(n_1,2m_2+1)}$, where $m_2 = 0,1,2,\ldots$, are reflected m_2 times by the surface Γ_{F1} and m_2+1 times by the surface Γ_{F2} . For even n_2 , the image sources $\mathbf{I}_{\text{B1-F2-F1}}^{(n_1,2m_2)}$, where $m_2 = 1,2,3,\ldots$, they are reflected m_2 times by both surfaces Γ_{F1} and Γ_{F2} . The x-coordinate $x_{\text{S-B1-F2-F1}}^{(n_1,n_2)}$ of the image source is calculated by,

$$x_{\text{S-B1-F2-F1}}^{(n_1,n_2)} = \begin{cases} -x_{\text{S-B1}}^{(n_1)} + L\cdot(n_2+1) & \text{for } n_2 = 1,3,5,\ldots \\ x_{\text{S-B1}}^{(n_1)} + L\cdot(n_2) & \text{for } n_2 = 2,4,6,\ldots \end{cases}. \tag{A.37}$$

The pressure contribution of $\mathbf{I}_{\text{B1-F2-F1}}^{(n_1,n_2)}$ is calculated by,

$$P_{111}^{(n_1,n_2)} = V_{111}^{(n_1,n_2)}\left(\mathbf{I}_{\text{B1-F2-F1}}^{(n_1,n_2)} \mid \mathfrak{R}\right)\cdot P_{direct}\left(\mathbf{I}_{\text{B1-F2-F1}}^{(n_1,n_2)} \mid \mathfrak{R}\right). \tag{A.38}$$

The factor $V_{111}^{(n_1,n_2)}(\mathbf{I} \mid \mathfrak{R})$, which accounts for the effects of the multiple reflections between the surfaces Γ_{B12}, Γ_{B21}, Γ_{F1} and Γ_{F2} is given by,

$$V_{111}^{(n_1,n_2)}(\mathbf{I} \mid \mathfrak{R}) = \begin{cases} V_{103}^{(n_1)}(\mathbf{I} \mid \mathfrak{R})\cdot\left[Q(\mathbf{I},\mathfrak{R},\beta_{F1})\right]^{m_2}\cdot\left[Q(\mathbf{I},\mathfrak{R},\beta_{F2})\right]^{m_2+1} & \text{for } n_2 = 2m_2+1 \\ V_{103}^{(n_1)}(\mathbf{I} \mid \mathfrak{R})\cdot\left[Q(\mathbf{I},\mathfrak{R},\beta_{F1})\cdot Q(\mathbf{I},\mathfrak{R},\beta_{F2})\right]^{m_2} & \text{for } n_2 = 2m_2 \end{cases}. \tag{A.39}$$

The illuminated zone of $\mathbf{I}_{\text{B1-F2-F1}}^{(n_1,n_2)}$ is illustrated in figure A.11. The lines connecting $\mathbf{I}_{\text{B1-F2-F1}}^{(n_1,n_2)}$ and the illuminated receivers should have an intersection with the line from $\left(x_{\text{E1-F2-F1}}^{(n_2)}, 0, 0\right)$ to $\left(x_{\text{E1-F2-F1}}^{(n_2)}, 0, H\right)$ and have no intersection with the line from $\left(x_{\text{E2-F2-F1}}^{(n_2)}, 0, 0\right)$ to $\left(x_{\text{E2-F2-F1}}^{(n_2)}, 0, H\right)$. The x-coordinate $x_{\text{E1-F2-F1}}^{(n_2)}$ can be calculated by,

$$x_{\text{E1-F2-F1}}^{(n_2)} = \begin{cases} L_2 + W + L\cdot(n_2) & \text{for } n_2 = 1,3,5,\ldots \\ -L_2 - W - L\cdot(n_2-1) & \text{for } n_2 = 2,4,6,\ldots \end{cases}. \tag{A.40}$$

Meanwhile, the x-coordinate $x_{\text{E2-F2-F1}}^{(n_2)}$ can be calculated by equation A.25.

Group 12 consists of image sources formed by multiple reflections between the surfaces Γ_{F1} and Γ_{F2} of the image sources $\mathbf{I}_{\underline{B1}}^{(n_1)}$. They are denoted as,

$$\mathbf{I}_{\underline{\text{B1-F2-F1}}}^{(n_1,n_2)} \equiv \left(x_{\text{S-B1-F2-F1}}^{(n_1,n_2)}, 0, -z_S\right), \tag{A.41}$$

where $n_1 = 1,2,3,\cdots$ and $n_2 = 1,2,3,\cdots$. The subscript $\underline{\text{B1-F2-F1}}$ indicates the multiple reflections involved and the underline in the subscript indicates the ground reflection. After the last reflection by the surface Γ_{B12} among the n_1 times multiple reflections between the surfaces Γ_{B12} and Γ_{B21}, there would be n_2 times multiple reflections between the surfaces Γ_{F1} and Γ_{F2}. For odd n_2, the image sources $\mathbf{I}_{\underline{\text{B1-F2-F1}}}^{(n_1,2m_2+1)}$, where $m_2 = 0,1,2,\ldots$, are reflected m_2 times by the surface Γ_{F1} and m_2+1 times by the surface Γ_{F2}. For even n_2, the image sources $\mathbf{I}_{\underline{\text{B1-F2-F1}}}^{(n_1,2m_2)}$, where $m_2 = 1,2,3,\ldots$, they are reflected m_2 times by both surfaces Γ_{F1} and Γ_{F2}. The x-coordinate $x_{\text{S-B1-F2-F1}}^{(n_1,n_2)}$ of the image source is calculated by equation A.37. The pressure contribution of $\mathbf{I}_{\underline{\text{B1-F2-F1}}}^{(n_1,n_2)}$ is calculated by,

$$P_{112}^{(n_1,n_2)} = V_{112}^{(n_1,n_2)}\left(\mathbf{I}_{\underline{\text{B1-F2-F1}}}^{(n_1,n_2)} \mid \mathfrak{R}\right) \cdot P_{direct}\left(\mathbf{I}_{\underline{\text{B1-F2-F1}}}^{(n_1,n_2)} \mid \mathfrak{R}\right). \tag{A.42}$$

The factor $V_{112}^{(n_1,n_2)}\left(\mathbf{I} \mid \mathfrak{R}\right)$, which accounts for the effects of the multiple reflections between the surfaces Γ_{B12}, Γ_{B21}, Γ_{G2}, Γ_{F1} and Γ_{F2} is given by,

$$V_{112}^{(n_1,n_2)}\left(\mathbf{I} \mid \mathfrak{R}\right) = \begin{cases} V_{104}^{(n_1)}\left(\mathbf{I} \mid \mathfrak{R}\right) \cdot \left[Q\left(\mathbf{I}, \mathfrak{R}, \beta_{F1}\right)\right]^{m_2} \cdot \left[Q\left(\mathbf{I}, \mathfrak{R}, \beta_{F2}\right)\right]^{m_2+1} & \text{for } n_2 = 2m_2 + 1 \\ V_{104}^{(n_1)}\left(\mathbf{I} \mid \mathfrak{R}\right) \cdot \left[Q\left(\mathbf{I}, \mathfrak{R}, \beta_{F1}\right) \cdot Q\left(\mathbf{I}, \mathfrak{R}, \beta_{F2}\right)\right]^{m_2} & \text{for } n_2 = 2m_2 \end{cases}. \tag{A.43}$$

The illuminated zone of $\mathbf{I}_{\underline{\text{B1-F2-F1}}}^{(n_1,n_2)}$ is illustrated in figure A.11. The lines connecting $\mathbf{I}_{\underline{\text{B1-F2-F1}}}^{(n_1,n_2)}$ and the illuminated receivers should have an intersection with the line from $\left(x_{\text{E1-F2-F1}}^{(n_2)}, 0, -H\right)$ to $\left(x_{\text{E1-F2-F1}}^{(n_2)}, 0, H\right)$ and have no intersection with the line from

$\left(x_{\text{E2-F2-F1}}^{(n_2)}, 0, -H\right)$ to $\left(x_{\text{E2-F2-F1}}^{(n_2)}, 0, H\right)$. The x-coordinate $x_{\text{E1-F2-F1}}^{(n_2)}$ and $x_{\text{E2-F2-F1}}^{(n_2)}$ can be calculated by equations A.40 and A.25 respectively.

Group 13 consists of image sources formed by multiple reflections between the surfaces Γ_{F1} and Γ_{F2} of the image sources $\mathbf{I}_{\text{B2}}^{(n_1)}$. They are denoted as,

$$\mathbf{I}_{\text{B2-F1-F2}}^{(n_1,n_2)} \equiv \left(x_{\text{S-B2-F1-F2}}^{(n_1,n_2)}, 0, z_{\text{S}}\right), \tag{A.44}$$

where $n_1 = 1,2,3,\cdots$ and $n_2 = 1,2,3,\cdots$. The subscript B2-F1-F2 indicates the multiple reflections involved. After the last reflection by the surface Γ_{B21} among the n_1 times multiple reflections between the surfaces Γ_{B12} and Γ_{B21}, there would be n_2 times multiple reflections between the surfaces Γ_{F1} and Γ_{F2}. For odd n_2, the image sources $\mathbf{I}_{\text{B2-F1-F2}}^{(n_1,2m_2+1)}$, where $m_2 = 0,1,2,\ldots$, are reflected m_2+1 times by the surface Γ_{F1} and m_2 times by the surface Γ_{F2}. For even n_2, the image sources $\mathbf{I}_{\text{B2-F1-F2}}^{(n_1,2m_2)}$, where $m_2 = 1,2,3,\ldots$, they are reflected m_2 times by both surfaces Γ_{F1} and Γ_{F2}. The x-coordinate $x_{\text{S-B2-F1-F2}}^{(n_1,n_2)}$ of the image source is calculated by,

$$x_{\text{S-B2-F1-F2}}^{(n_1,n_2)} = \begin{cases} -x_{\text{S-B2}}^{(n_1)} - L\cdot(n_2-1) & \text{for } n_2 = 1,3,5,\ldots \\ x_{\text{S-B2}}^{(n_1)} + L\cdot(n_2) & \text{for } n_2 = 2,4,6,\ldots \end{cases}. \tag{A.45}$$

The pressure contribution of $\mathbf{I}_{\text{B2-F1-F2}}^{(n_1,n_2)}$ is calculated by,

$$P_{113}^{(n_1,n_2)} = V_{113}^{(n_1,n_2)}\left(\mathbf{I}_{\text{B2-F1-F2}}^{(n_1,n_2)} \mid \mathfrak{R}\right)\cdot P_{direct}\left(\mathbf{I}_{\text{B2-F1-F2}}^{(n_1,n_2)} \mid \mathfrak{R}\right). \tag{A.46}$$

The factor $V_{113}^{(n_1,n_2)}\left(\mathbf{I} \mid \mathfrak{R}\right)$, which accounts for the effects of the multiple reflections between the surfaces Γ_{B12}, Γ_{B21}, Γ_{F1} and Γ_{F2} is given by,

$$V_{113}^{(n_1,n_2)}\left(\mathbf{I} \mid \mathfrak{R}\right) = \begin{cases} V_{105}^{(n_1)}\left(\mathbf{I} \mid \mathfrak{R}\right)\cdot\left[Q\left(\mathbf{I},\mathfrak{R},\beta_{\text{F1}}\right)\right]^{m_2+1}\cdot\left[Q\left(\mathbf{I},\mathfrak{R},\beta_{\text{F2}}\right)\right]^{m_2} & \text{for } n_2 = 2m_2+1 \\ V_{105}^{(n_1)}\left(\mathbf{I} \mid \mathfrak{R}\right)\cdot\left[Q\left(\mathbf{I},\mathfrak{R},\beta_{\text{F1}}\right)\cdot Q\left(\mathbf{I},\mathfrak{R},\beta_{\text{F2}}\right)\right]^{m_2} & \text{for } n_2 = 2m_2 \end{cases}. \tag{A.47}$$

The illuminated zone of $\mathbf{I}_{\text{B2-F1-F2}}^{(n_1,n_2)}$ is illustrated in figure A.13. The lines connecting $\mathbf{I}_{\text{B2-F1-F2}}^{(n_1,n_2)}$ and the illuminated receivers should have no intersection with the line from $\left(x_{\text{E1-F1-F2}}^{(n_2)}, 0, 0\right)$ to $\left(x_{\text{E1-F1-F2}}^{(n_2)}, 0, H\right)$ and have an intersection with the line from $\left(x_{\text{E2-F1-F2}}^{(n_2)}, 0, 0\right)$ to $\left(x_{\text{E2-F1-F2}}^{(n_2)}, 0, H\right)$. The x-coordinate $x_{\text{E1-F1-F2}}^{(n_2)}$ can be calculated by equation A.24.

Meanwhile, the x-coordinate $x_{\text{E2-F1-F2}}^{(n_2)}$ can be calculated by,

$$x_{\text{E2-F1-F2}}^{(n_2)} = \begin{cases} -L_1 - W - L\cdot(n_2 - 1) & \text{for } n_2 = 1,3,5,\ldots \\ L_1 + W + L\cdot(n_2) & \text{for } n_2 = 2,4,6,\ldots \end{cases}. \tag{A.48}$$

Group 14 consists of image sources formed by multiple reflections between the surfaces Γ_{F1} and Γ_{F2} of the image sources $\mathbf{I}_{\underline{\text{B2}}}^{(n_1)}$. They are denoted as,

$$\mathbf{I}_{\underline{\text{B2-F1-F2}}}^{(n_1,n_2)} \equiv \left(x_{\text{S-B2-F1-F2}}^{(n_1,n_2)}, 0, -z_{\text{S}}\right), \tag{A.49}$$

where $n_1 = 1,2,3,\cdots$ and $n_2 = 1,2,3,\cdots$. The subscript $\underline{\text{B2-F1-F2}}$ indicates the multiple reflections involved and the underline in the subscript indicates the ground reflection. After the last reflection by the surface Γ_{B21} among the n_1 times multiple reflections between the surfaces Γ_{B12} and Γ_{B21}, there would be n_2 times multiple reflections between the surfaces Γ_{F1} and Γ_{F2}. For odd n_2, the image sources $\mathbf{I}_{\underline{\text{B2-F1-F2}}}^{(n_1,2m_2+1)}$, where $m_2 = 0,1,2,\ldots$, are reflected m_2+1 times by the surface Γ_{F1} and m_2 times by the surface Γ_{F2}. For even n_2, the image sources $\mathbf{I}_{\underline{\text{B2-F1-F2}}}^{(n_1,2m_2)}$, where $m_2 = 1,2,3,\ldots$, they are reflected m_2 times by both façade surfaces Γ_{F1} and Γ_{F2}. The x-coordinate $x_{\text{S-B2-F1-F2}}^{(n_1,n_2)}$ of the image source is calculated by equation A.45. The pressure contribution of $\mathbf{I}_{\underline{\text{B2-F1-F2}}}^{(n_1,n_2)}$ is calculated by,

$$P_{114}^{(n_1,n_2)} = V_{114}^{(n_1,n_2)}\left(\mathbf{I}_{\underline{\text{B2-F1-F2}}}^{(n_2)} \mid \mathfrak{R}\right)\cdot P_{direct}\left(\mathbf{I}_{\underline{\text{B2-F1-F2}}}^{(n_2)} \mid \mathfrak{R}\right). \tag{A.50}$$

The factor $V_{114}^{(n_1,n_2)}(\mathbf{I}\,|\,\mathfrak{R})$, which accounts for the effects of the multiple reflections between the surfaces Γ_{B12}, Γ_{B21}, Γ_{G2}, Γ_{F1} and Γ_{F2} is given by,

$$V_{114}^{(n_1,n_2)}(\mathbf{I}\,|\,\mathfrak{R}) = \begin{cases} V_{106}^{(n_1)}(\mathbf{I}\,|\,\mathfrak{R}) \cdot \left[Q(\mathbf{I},\mathfrak{R},\beta_{F1})\right]^{m_2+1} \cdot \left[Q(\mathbf{I},\mathfrak{R},\beta_{F2})\right]^{m_2} & \text{for } n_2 = 2m_2+1 \\ V_{106}^{(n_1)}(\mathbf{I}\,|\,\mathfrak{R}) \cdot \left[Q(\mathbf{I},\mathfrak{R},\beta_{F1}) \cdot Q(\mathbf{I},\mathfrak{R},\beta_{F2})\right]^{m_2} & \text{for } n_2 = 2m_2 \end{cases} . \quad \text{(A.51)}$$

The illuminated zone of $\mathbf{I}_{\underline{\text{B2-F1-F2}}}^{(n_1,n_2)}$ is illustrated in figure A.14. The lines connecting $\mathbf{I}_{\underline{\text{B2-F1-F2}}}^{(n_1,n_2)}$ and the illuminated receivers should have no intersection with the line from $\left(x_{\text{E1-F1-F2}}^{(n_2)}, 0, -H\right)$ to $\left(x_{\text{E1-F1-F2}}^{(n_2)}, 0, H\right)$ and have an intersection with the line from $\left(x_{\text{E2-F1-F2}}^{(n_2)}, 0, -H\right)$ to $\left(x_{\text{E2-F1-F2}}^{(n_2)}, 0, H\right)$. The x-coordinate $x_{\text{E1-F1-F2}}^{(n_2)}$ and $x_{\text{E2-F1-F2}}^{(n_2)}$ can be calculated by equations A.24 and A.48 respectively.

A.3 Secondary Contribution from Edge of Diffraction E1

In the previous section, we have discussed in details the formation and calculation with primary contributions. We now change our concentration to the secondary contributions. As mentioned before, the secondary image sources are not observed by the receiver in straight line of sight in the transmission paths with secondary contributions. The sound wave is transmitted to the receiver with diffraction involved. The edges of diffraction are considered as the secondary sources which form series of images due to reflection afterwards. In this section, we first concentrate on the diffraction at the edge **E1**. The primary image sources $\mathbf{I}_0$, $\mathbf{I}_{\underline{0}}$, $\left\{\mathbf{I}_{\mathrm{B2}}^{(1)},\mathbf{I}_{\mathrm{B2}}^{(2)},\cdots,\mathbf{I}_{\mathrm{B2}}^{(\infty)}\right\}$ and $\left\{\mathbf{I}_{\underline{\mathrm{B2}}}^{(1)},\mathbf{I}_{\underline{\mathrm{B2}}}^{(2)},\cdots,\mathbf{I}_{\underline{\mathrm{B2}}}^{(\infty)}\right\}$ can contribute the pressure with diffraction at **E1**. For the convenience in the upcoming explanation, we represent them into two series $\left\{\mathbf{I}_{\mathrm{B2}}^{(n)}\right\}$ and $\left\{\mathbf{I}_{\underline{\mathrm{B2}}}^{(n)}\right\}$, where n = 0,1,2, … , in which $\mathbf{I}_{\mathrm{B2}}^{(0)}=\mathbf{I}_0$ and $\mathbf{I}_{\underline{\mathrm{B2}}}^{(0)}=\mathbf{I}_{\underline{0}}$. Similar to the primary image sources, we categorize the contribution of the secondary image sources of **E1** into 13 groups based on various combinations of reflections.

Group 1 is the image source of **E1** with contribution through direct transmission. The image source is actually at the original location of the edge **E1** and is denoted by,

$$\mathbf{E1}_0 \equiv \mathbf{E1} = \left(L_1, 0, H\right). \tag{A.52}$$

The pressure contribution of $\mathbf{E1}_0$ is calculated by,

$$P_{2101}=\sum_{n_1=0}^{\infty}\left[\begin{array}{l} V_{105}^{(n_1)}\left(\mathbf{I}_{\mathrm{B2}}^{(n_1)}\,|\,\mathbf{E1}\right)\cdot T\left(\mathbf{I}_{\mathrm{B2}}^{(n_1)}\,|\,\mathbf{E1},\mathbf{E1}_0\,|\,\mathfrak{R},\beta_{\mathrm{B12}},\boldsymbol{\beta}_{\mathrm{R}}\right) \\ +V_{106}^{(n_1)}\left(\mathbf{I}_{\mathrm{B2}}^{(n_1)}\,|\,\mathbf{E1}\right)\cdot T\left(\mathbf{I}_{\underline{\mathrm{B2}}}^{(n_1)}\,|\,\mathbf{E1},\mathbf{E1}_0\,|\,\mathfrak{R},\beta_{\mathrm{B12}},\boldsymbol{\beta}_{\mathrm{R}}\right)\end{array}\right], \tag{A.53}$$

where the term $\boldsymbol{\beta}_{\mathrm{R}}$ used for calculation of diffraction is dependent on the location of the receivers as follows,

$$\boldsymbol{\beta}_{\mathrm{R}} = \begin{cases} \beta_{\mathrm{B21}} & \text{if } x_{\mathrm{R}} \le L_1 \\ & \\ \beta_{\mathrm{B22}} & \text{if } x_{\mathrm{R}} > L_1 \end{cases}. \tag{A.54}$$

The illuminated zone of $\mathbf{E1}_0$ is illustrated in figure A.15. The lines connecting $\mathbf{E1}_0$ and the illuminated receivers should have no intersection with the line from $(L_1+W, 0, 0)$ to $(L_1+W, 0, H)$.

Group 2 is the image source with one ground reflection and is denoted as,

$$\mathbf{E1}_{\underline{0}} \equiv (L_1, 0, -H). \tag{A.55}$$

The underline in the subscript indicates ground reflection. The pressure contribution of $\mathbf{E1}_{\underline{0}}$ is calculated by,

$$P_{2102} = \sum_{n_1=0}^{\infty} \left[\begin{array}{l} V_{105}^{(n_1)}\left(\mathbf{I}_{\mathrm{B2}}^{(n_1)} \mid \mathbf{E1}\right) \cdot V_{2102}\left(\mathbf{E1}_{\underline{0}} \mid \mathfrak{R}\right) \cdot T\left(\mathbf{I}_{\mathrm{B2}}^{(n_1)} \mid \mathbf{E1}, \mathbf{E1}_{\underline{0}} \mid \mathfrak{R}, \beta_{\mathrm{B12}}, \boldsymbol{\beta}_{\mathrm{R}}\right) \\ + V_{106}^{(n_1)}\left(\mathbf{I}_{\underline{\mathrm{B2}}}^{(n_1)} \mid \mathbf{E1}\right) \cdot V_{2102}\left(\mathbf{E1}_{\underline{0}} \mid \mathfrak{R}\right) \cdot T\left(\mathbf{I}_{\underline{\mathrm{B2}}}^{(n_1)} \mid \mathbf{E1}, \mathbf{E1}_{\underline{0}} \mid \mathfrak{R}, \beta_{\mathrm{B12}}, \boldsymbol{\beta}_{\mathrm{R}}\right) \end{array} \right], \tag{A.56}$$

where the term $\boldsymbol{\beta}_{\mathrm{R}}$ is calculated using equation (A.54) and the reflection factor $V_{2102}(\mathbf{I} \mid \mathfrak{R})$ accounts for the ground reflection as follows,

$$V_{2102}(\mathbf{I} \mid \mathfrak{R}) = Q(\mathbf{I}, \mathfrak{R}, \boldsymbol{\beta}_{\mathrm{G}}). \tag{A.57}$$

Again, the term $\boldsymbol{\beta}_{\mathrm{G}}$ is dependent on the location of the receiver and can be expressed as,

$$\boldsymbol{\beta}_{\mathrm{G}} = \begin{cases} \beta_{\mathrm{G1}} & \text{if } x_{\mathrm{R}} \le L_1 \\ & \\ \beta_{\mathrm{G2}} & \text{if } x_{\mathrm{R}} > L_1 \end{cases}. \tag{A.58}$$

The illuminated Zone of $\mathbf{E1}_{\underline{0}}$ is illustrated in figure A.17. The lines connecting $\mathbf{I}_{\underline{0}}$ and the illuminated receivers should have no intersection with the line from $(L_1+W, 0, -H)$ to $(L_1+W, 0, H)$.

Group 3 comprises of the image sources formed by multiple reflections between the surfaces Γ_{F1} and Γ_{B11}. They are denoted as,

$$\mathbf{E1}_{\text{F1-B11}}^{(q_1)} \equiv \left(x_{\text{E1-F1-B11}}^{(q_1)}, 0, H\right), \tag{A.59}$$

where $q_1 = 1,2,3,\cdots$. The subscript F1-B11 indicates the surfaces of reflections involved and the superscript q_1 in bracket denotes the total number of reflections from the surfaces Γ_{F1} and Γ_{B11}. For odd order image sources $\mathbf{E1}_{\text{F1-B11}}^{(2p_1+1)}$, where $p_1 = 0,1,2,\ldots$, they are reflected p_1+1 times by the façade surface Γ_{F1} and p_1 times by the barrier surface Γ_{B11}. For even order image sources $\mathbf{E1}_{\text{F1-B11}}^{(2p_1)}$, where $p_1 = 1,2,3,\ldots$, they are reflected p_1 times by both surfaces Γ_{F1} and Γ_{B11}. The x-coordinate $x_{\text{E1-F1-B11}}^{(q_1)}$ of the image source is determined as,

$$x_{\text{E1-F1-B11}}^{(q_1)} = \begin{cases} -q_1 \times L_1 & \text{for } q_1 = 3, 5, 7, \ldots \\ (q_1+1) \times L_1 & \text{for } q_1 = 2, 4, 6, \cdots \end{cases} \tag{A.60}$$

The contribution of $\mathbf{E1}_{\text{F1-B11}}^{(q_1)}$ is calculated by,

$$P_{2103}^{(q_1)} = \sum_{n_1=0}^{\infty} \left[\begin{array}{l} V_{105}^{(n_1)}\left(\mathbf{I}_{\text{B2}}^{(n_1)} \mid \mathbf{E1}\right) \cdot V_{2103}^{(q_1)}\left(\mathbf{E1}_{\text{F1-B11}}^{(q_1)} \mid \mathfrak{R}\right) \cdot T\left(\mathbf{I}_{\text{B2}}^{(n_1)} \mid \mathbf{E1}, \mathbf{E1}_{\text{F1-B11}}^{(q_1)} \mid \mathfrak{R}, \beta_{\text{B12}}, \beta_{\text{B11}}\right) \\ + V_{106}^{(n_1)}\left(\mathbf{I}_{\text{B2}}^{(n_1)} \mid \mathbf{E1}\right) \cdot V_{2103}^{(q_1)}\left(\mathbf{E1}_{\text{F1-B11}}^{(q_1)} \mid \mathfrak{R}\right) \cdot T\left(\underline{\mathbf{I}_{\text{B2}}^{(n_1)}} \mid \mathbf{E1}, \mathbf{E1}_{\text{F1-B11}}^{(q_1)} \mid \mathfrak{R}, \beta_{\text{B12}}, \beta_{\text{B11}}\right) \end{array} \right]. \tag{A.61}$$

The factor $V_{2103}^{(q_1)}\left(\mathbf{I} \mid \mathfrak{R}\right)$, which accounts for the effects of the multiple reflections between the surfaces Γ_{F1} and Γ_{B11}, is given by,

$$V_{2103}^{(q_1)}\left(\mathbf{I} \mid \mathfrak{R}\right) = \begin{cases} \left[Q\left(\mathbf{I}, \mathfrak{R}, \beta_{\text{F1}}\right)\right]^{p_1+1} \cdot \left[Q\left(\mathbf{I}, \mathfrak{R}, \beta_{\text{B11}}\right)\right]^{p_1} & \text{for } q_1 = 2p_1 + 1 \\ \left[Q\left(\mathbf{I}, \mathfrak{R}, \beta_{\text{F1}}\right) \cdot Q\left(\mathbf{I}, \mathfrak{R}, \beta_{\text{B11}}\right)\right]^{p_1} & \text{for } q_1 = 2p_1 \end{cases}. \tag{A.62}$$

The illuminated zone of $\mathbf{E1}_{\text{F1-B11}}^{(q_1)}$ is illustrated in figure A.17. Receivers having a height lower than H and located between the façade surface Γ_{F1} and the barrier B1 should be illuminated by all $\mathbf{E1}_{\text{F1-B11}}^{(q_1)}$. Especially for $\mathbf{E1}_{\text{F1-B11}}^{(1)}$, receivers located higher than H are also illuminated.

Group 4 contains the ground reflected image sources formed by multiple reflections between the surfaces Γ_{F1} and Γ_{B11}. They are similar to the image sources in group 3 but involve a one additional reflection with the ground surface Γ_{G1}. They are denoted as,

$$\mathbf{E1}_{\underline{\text{F1-B11}}}^{(q_1)} \equiv \left(x_{\text{F1-B11}}^{(q_1)}, 0, -H\right), \tag{A.63}$$

where $q_1 = 1,2,3,\cdots$. The subscript $\underline{\text{F1-B11}}$ indicates the surfaces of reflections involved and the underline in the subscript indicates the ground reflection. The superscript q_1 in bracket denotes the total number of reflections from the surfaces Γ_{F1} and Γ_{B11}. For odd order image sources $\mathbf{E1}_{\underline{\text{F1-B11}}}^{(2p_1+1)}$, where $p_1 = 0,1,2,\ldots$, they are reflected once by the ground surface Γ_{G1}, p_1+1 times by the façade surface Γ_{F1} and p_1 times by the barrier surface Γ_{B11}. For even order image sources $\mathbf{E1}_{\text{F1-B11}}^{(2p_1)}$, where $p_1 = 1,2,3,\ldots$, they are reflected once by the ground surface Γ_{G1} and p_1 times by both surfaces Γ_{F1} and Γ_{B11}. The x-coordinate $x_{\text{E1-F1-B11}}^{(q_1)}$ of the image source is determined by equation A.60. The contribution of $\mathbf{E1}_{\underline{\text{F1-B11}}}^{(q_1)}$ is calculated by,

$$P_{2104}^{(q_1)} = \sum_{n_1=0}^{\infty}\left[\begin{array}{l} V_{105}^{(n_1)}\left(\mathbf{I}_{\text{B2}}^{(n_1)} \mid \mathbf{E1}\right)\cdot V_{2104}^{(q_1)}\left(\mathbf{E1}_{\underline{\text{F1-B11}}}^{(q_1)} \mid \mathfrak{R}\right)\cdot T\left(\mathbf{I}_{\text{B2}}^{(n_1)} \mid \mathbf{E1}, \mathbf{E1}_{\underline{\text{F1-B11}}}^{(q_1)} \mid \mathfrak{R}, \beta_{\text{B12}}, \beta_{\text{B11}}\right) \\ + V_{106}^{(n_1)}\left(\mathbf{I}_{\underline{\text{B2}}}^{(n_1)} \mid \mathbf{E1}\right)\cdot V_{2104}^{(q_1)}\left(\mathbf{E1}_{\underline{\text{F1-B11}}}^{(q_1)} \mid \mathfrak{R}\right)\cdot T\left(\mathbf{I}_{\underline{\text{B2}}}^{(n_1)} \mid \mathbf{E1}, \mathbf{E1}_{\underline{\text{F1-B11}}}^{(q_1)} \mid \mathfrak{R}, \beta_{\text{B12}}, \beta_{\text{B11}}\right) \end{array}\right]. \tag{A.64}$$

The factor $V_{2104}^{(q_1)}\left(\mathbf{I} \mid \mathfrak{R}\right)$, which accounts for the effects of the multiple reflections between the surfaces Γ_{G1}, Γ_{F1} and Γ_{B11}, is given by,

$$V_{2104}^{(q_1)}\left(\mathbf{I} \mid \mathfrak{R}\right) = \begin{cases} Q\left(\mathbf{I}, \mathfrak{R}, \beta_{\text{G1}}\right)\cdot\left[Q\left(\mathbf{I}, \mathfrak{R}, \beta_{\text{F1}}\right)\right]^{p_1+1}\cdot\left[Q\left(\mathbf{I}, \mathfrak{R}, \beta_{\text{B11}}\right)\right]^{p_1} & \text{for } q_1 = 2p_1+1 \\ Q\left(\mathbf{I}, \mathfrak{R}, \beta_{\text{G1}}\right)\cdot\left[Q\left(\mathbf{I}, \mathfrak{R}, \beta_{\text{F1}}\right)\cdot Q\left(\mathbf{I}, \mathfrak{R}, \beta_{\text{B11}}\right)\right]^{p_1} & \text{for } q_1 = 2p_1 \end{cases}. \tag{A.65}$$

The illuminated zone of $\mathbf{E1}_{\underline{\text{F1-B11}}}^{(q_1)}$ is illustrated in figure A.18. For image sources $\mathbf{E1}_{\underline{\text{F1-B11}}}^{(q_1)}$ with odd order q_1, the lines connecting the illuminated receivers with $\mathbf{E1}_{\underline{\text{F1-B11}}}^{(q_1)}$ should

have an intersection with the line from $(-L_1, 0, -H)$ to $(-L_1, 0, H)$ and have no intersection with the line from $(L_1, 0, -H)$ to $(L_1, 0, H)$. For the $\mathbf{E1}^{(q_1)}_{\underline{\text{F1-B11}}}$ with even q_1, the lines connecting the illuminated receivers with $\mathbf{E1}^{(q_1)}_{\underline{\text{F1-B11}}}$ should have an intersection with the line from $(L_1, 0, -H)$ to $(L_1, 0, H)$.

Group 5 comprises of the image sources formed by multiple reflections between the barrier surfaces Γ_{B12} and Γ_{B21}. They are denoted as,

$$\mathbf{E1}^{(q_1)}_{\text{B21-B12}} \equiv \left(x^{(q_1)}_{\text{E1-B21-B12}}, 0, H\right), \tag{A.66}$$

where $q_1 = 1, 2, 3, \cdots$. The subscript B21-B12 indicates the surfaces of reflections involved and the superscript q_1 in bracket denotes the total number of reflections from the surfaces Γ_{B12} and Γ_{B21}. For odd order image sources $\mathbf{E1}^{(2p_1+1)}_{\text{B21-B12}}$, where $p_1 = 0, 1, 2, \ldots$, they are reflected p_1 times by the surface Γ_{B12} and p_1+1 times by the surface Γ_{B21}. For even order image sources $\mathbf{E1}^{(2p_1)}_{\text{B21-B12}}$, where $p_1 = 1, 2, 3, \ldots$, they are reflected p_1 times by both surfaces Γ_{B12} and Γ_{B21} . The x-coordinate $x^{(q_1)}_{\text{E1-B21-B12}}$ of the image source is determined as,

$$x^{(q_1)}_{\text{E1-B21-B12}} = \begin{cases} L_1 + (q_1 + 1)\cdot W & \text{for } q_1 = 1, 3, 5, \ldots \\ L_1 - q_1 \cdot W & \text{for } q_1 = 2, 4, 6, \cdots \end{cases}. \tag{A.67}$$

The contribution of $\mathbf{E1}^{(q_1)}_{\text{B21-B12}}$ is calculated by,

$$P^{(q_1)}_{2105} = \sum_{n_1=0}^{\infty} \left[\begin{array}{l} V^{(n_1)}_{105}\left(\mathbf{I}^{(n_1)}_{\text{B2}} \mid \mathbf{E1}\right) \cdot V^{(q_1)}_{2105}\left(\mathbf{E1}^{(q_1)}_{\text{B21-B12}} \mid \mathfrak{R}\right) \cdot T\left(\mathbf{I}^{(n_1)}_{\text{B2}} \mid \mathbf{E1}, \mathbf{E1}^{(q_1)}_{\text{B21-B12}} \mid \mathfrak{R}, \beta_{\text{B12}}, \beta_{\text{B12}}\right) \\ + V^{(n_1)}_{106}\left(\mathbf{I}^{(n_1)}_{\underline{\text{B2}}} \mid \mathbf{E1}\right) \cdot V^{(q_1)}_{2105}\left(\mathbf{E1}^{(q_1)}_{\text{B21-B12}} \mid \mathfrak{R}\right) \cdot T\left(\mathbf{I}^{(n_1)}_{\underline{\text{B2}}} \mid \mathbf{E1}, \mathbf{E1}^{(q_1)}_{\text{B21-B12}} \mid \mathfrak{R}, \beta_{\text{B12}}, \beta_{\text{B12}}\right) \end{array} \right]. \tag{A.68}$$

The factor $V^{(q_1)}_{2105}\left(\mathbf{I} \mid \mathfrak{R}\right)$, which accounts for the effects of the multiple reflections between the surfaces Γ_{B12} and Γ_{B21}, is given by,

$$V_{2105}^{(q_1)}(\mathbf{I}\,|\,\mathfrak{R}) = \begin{cases} \left[Q(\mathbf{I},\mathfrak{R},\beta_{\mathrm{B21}})\right]^{p_1+1}\cdot\left[Q(\mathbf{I},\mathfrak{R},\beta_{\mathrm{B12}})\right]^{p_1} & \text{for } q_1 = 2p_1+1 \\ \left[Q(\mathbf{I},\mathfrak{R},\beta_{\mathrm{B21}})\cdot Q(\mathbf{I},\mathfrak{R},\beta_{\mathrm{B12}})\right]^{p_1} & \text{for } q_1 = 2p_1 \end{cases}. \tag{A.69}$$

The illuminated zone of $\mathbf{E1}_{\mathrm{B21\text{-}B12}}^{(q_1)}$ is illustrated in figure A.19. The illuminated receiver should be located between the two barriers **B1** and **B2** and have a height lower than H.

Group 6 contains the ground reflected image sources formed by multiple reflections between the surfaces Γ_{B12} and Γ_{B21}. They are similar to the image sources in group 5 but involve an additonal reflection with the ground surface Γ_{G2}. They are denoted as,

$$\mathbf{E1}_{\underline{\mathrm{B21\text{-}B12}}}^{(q_1)} \equiv \left(x_{\mathrm{B21\text{-}B12}}^{(q_1)}, 0, -H\right), \tag{A.70}$$

where $q_1 = 1,2,3,\cdots$. The subscript $\underline{\mathrm{B21\text{-}B12}}$ indicates the surfaces of reflections involved and the underline in the subscript indicates the ground reflection from the surfaces Γ_{B12} and Γ_{B21}. The superscript q_1 in bracket denotes the total number of reflections. For odd order image sources $\mathbf{E1}_{\underline{\mathrm{B21\text{-}B12}}}^{(2p_1+1)}$, where $p_1 = 0,1,2,\ldots$, they are reflected once by the surface Γ_{G2}, p_1 times by the surface Γ_{B12} and p_1+1 times by the surface Γ_{B21}. For even order image sources $\mathbf{E1}_{\underline{\mathrm{B21\text{-}B12}}}^{(2p_1)}$, where $p_1 = 1,2,3,\ldots$, they are reflected once by the surface Γ_{G2} and p_1 times by both surfaces Γ_{B12} and Γ_{B21}. The x-coordinate $x_{\mathrm{E1\text{-}B21\text{-}B12}}^{(q_1)}$ of the image source is determined by equation A.67. The contribution of $\mathbf{E1}_{\underline{\mathrm{B21\text{-}B12}}}^{(q_1)}$ is calculated by,

$$P_{2106}^{(q_1)} = \sum_{n_1=0}^{\infty}\left[\begin{array}{l} V_{105}^{(n_1)}\left(\mathbf{I}_{\mathrm{B2}}^{(n_1)}\,|\,\mathbf{E1}\right)\cdot V_{2106}^{(q_1)}\left(\mathbf{E1}_{\underline{\mathrm{B21\text{-}B12}}}^{(q_1)}\,|\,\mathfrak{R}\right)\cdot T\left(\mathbf{I}_{\mathrm{B2}}^{(n_1)}\,|\,\mathbf{E1},\mathbf{E1}_{\underline{\mathrm{B21\text{-}B12}}}^{(q_1)}\,|\,\mathfrak{R},\beta_{\mathrm{B12}},\beta_{\mathrm{B12}}\right) \\ +V_{106}^{(n_1)}\left(\mathbf{I}_{\underline{\mathrm{B2}}}^{(n_1)}\,|\,\mathbf{E1}\right)\cdot V_{2106}^{(q_1)}\left(\mathbf{E1}_{\underline{\mathrm{B21\text{-}B12}}}^{(q_1)}\,|\,\mathfrak{R}\right)\cdot T\left(\mathbf{I}_{\underline{\mathrm{B2}}}^{(n_1)}\,|\,\mathbf{E1},\mathbf{E1}_{\underline{\mathrm{B21\text{-}B12}}}^{(q_1)}\,|\,\mathfrak{R},\beta_{\mathrm{B12}},\beta_{\mathrm{B12}}\right) \end{array}\right]. \tag{A.71}$$

The factor $V_{2106}^{(q_1)}(\mathbf{I}\,|\,\mathfrak{R})$, which accounts for the effects of the multiple reflections between the surfaces Γ_{G2}, Γ_{B12} and Γ_{B21}, is given by,

$$V_{2106}^{(q_1)}(\mathbf{I}\,|\,\mathfrak{R}) = \begin{cases} Q(\mathbf{I},\mathfrak{R},\beta_{G2})\cdot\left[Q(\mathbf{I},\mathfrak{R},\beta_{B21})\right]^{p_1+1}\cdot\left[Q(\mathbf{I},\mathfrak{R},\beta_{B12})\right]^{p_1} & \text{for } q_1 = 2p_1+1 \\ Q(\mathbf{I},\mathfrak{R},\beta_{G2})\cdot\left[Q(\mathbf{I},\mathfrak{R},\beta_{B21})\cdot Q(\mathbf{I},\mathfrak{R},\beta_{B12})\right]^{p_1} & \text{for } q_1 = 2p_1 \end{cases}. \tag{A.72}$$

The illuminated zone of $\mathbf{E1}_{\underline{\text{B21-B12}}}^{(q_1)}$ is illustrated in figure A.20. For the $\mathbf{E1}_{\underline{\text{B21-B12}}}^{(q_1)}$ with odd q_1, the lines connecting the illuminated receivers with $\mathbf{E1}_{\underline{\text{B21-B12}}}^{(q_1)}$ should have no intersection with the line from $(L_1,0,-H)$ to $(L_1,0,H)$ and have an intersection with the line from $(L_1+W,0,-H)$ to $(L_1+W,0,H)$. For the $\mathbf{E1}_{\underline{\text{B21-B12}}}^{(q_1)}$ with even q_1, the lines connecting the illuminated receivers with $\mathbf{E1}_{\underline{\text{B21-B12}}}^{(q_1)}$ should have an intersection with the line from $(L_1,0,-H)$ to $(L_1,0,H)$ and have no intersection with the line from $(L_1+W,0,-H)$ to $(L_1+W,0,H)$.

Group 7 comprises of the image sources formed by multiple reflections between the surfaces Γ_{F1} and Γ_{F2}. They are denoted as,

$$\mathbf{E1}_{\text{F1-F2}}^{(q_2)} \equiv \left(x_{\text{E1-F1-F2}}^{(q_2)},0,H\right), \tag{A.73}$$

where $q_2 = 2,3,4,\cdots$. The subscript F1-F2 indicates the surfaces of reflections involved and the superscript q_2 in bracket denotes the total number of reflections from the surfaces Γ_{F1} and Γ_{F2}. The starting number of reflection is 2 to avoid duplication with $\mathbf{E1}_{\text{F1-B11}}^{(1)}$. For odd order image sources $\mathbf{E1}_{\text{F1-F2}}^{(2p_2+1)}$, where $p_2 = 1,2,3,\ldots$, they are reflected p_2+1 times by the façade surface Γ_{F1} and p_2 times by the surface Γ_{F2}. For even order image sources $\mathbf{E1}_{\text{F1-F2}}^{(2p_2)}$, where $p_2 = 1,2,3,\ldots$, they are reflected p_2 times by both surfaces

Γ_{F1} and Γ_{F2}. The x-coordinate $x_{E1\text{-}F1\text{-}F2}^{(q_2)}$ of the image source can be determined by equation A.24. The contribution of $\mathbf{E1}_{F1\text{-}F2}^{(q_2)}$ is calculated by,

$$P_{2107}^{(q_2)} = \sum_{n_1=0}^{\infty} \left[\begin{array}{l} V_{105}^{(n_1)}\left(\mathbf{I}_{B2}^{(n_1)} \mid \mathbf{E1}\right) \cdot V_{2107}^{(q_2)}\left(\mathbf{E1}_{F1\text{-}F2}^{(q_2)} \mid \mathfrak{R}\right) \cdot T\left(\mathbf{I}_{B2}^{(n_1)} \mid \mathbf{E1}, \mathbf{E1}_{F1\text{-}F2}^{(q_2)} \mid \mathfrak{R}, \beta_{B12}, \beta_{B11}\right) \\ + V_{106}^{(n_1)}\left(\mathbf{I}_{\underline{B2}}^{(n_1)} \mid \mathbf{E1}\right) \cdot V_{2107}^{(q_2)}\left(\mathbf{E1}_{F1\text{-}F2}^{(q_2)} \mid \mathfrak{R}\right) \cdot T\left(\mathbf{I}_{\underline{B2}}^{(n_1)} \mid \mathbf{E1}, \mathbf{E1}_{F1\text{-}F2}^{(q_2)} \mid \mathfrak{R}, \beta_{B12}, \beta_{B11}\right) \end{array} \right]. \quad \text{(A.74)}$$

The factor $V_{2107}^{(q_2)}\left(\mathbf{I} \mid \mathfrak{R}\right)$, which accounts for the effects of the multiple reflections between the surfaces Γ_{F1} and Γ_{F2}, is given by,

$$V_{2107}^{(q_2)}\left(\mathbf{I} \mid \mathfrak{R}\right) = \begin{cases} \left[Q\left(\mathbf{I}, \mathfrak{R}, \beta_{F1}\right)\right]^{p_2+1} \cdot \left[Q\left(\mathbf{I}, \mathfrak{R}, \beta_{F2}\right)\right]^{p_2} & \text{for } q_2 = 2p_2 + 1 \\ \left[Q\left(\mathbf{I}, \mathfrak{R}, \beta_{F1}\right) \cdot Q\left(\mathbf{I}, \mathfrak{R}, \beta_{F2}\right)\right]^{p_2} & \text{for } q_2 = 2p_2 \end{cases}. \quad \text{(A.75)}$$

The illuminated zone of $\mathbf{E1}_{F1\text{-}F2}^{(q_2)}$ is illustrated in figure A.21. The illuminated receiver should have a height higher than H.

Group 8 contains the ground reflected image sources formed by multiple reflections between the surfaces Γ_{F1} and Γ_{F2}. They are similar to the image sources in group 7 but involve an additional reflection with the ground surface Γ_{G1}. They are denoted as,

$$\mathbf{E1}_{\underline{F1-F2}}^{(q_2)} \equiv \left(x_{E1\text{-}F1\text{-}F2}^{(q_2)}, 0, -H\right), \quad \text{(A.76)}$$

where $q_2 = 2,3,4,\cdots$. The subscript $\underline{F1\text{-}F2}$ indicates the surfaces of reflections involved and the underline in the subscript indicates the ground reflection. The superscript q_2 in bracket denotes the total number of reflections from the surfaces Γ_{F1} and Γ_{F2}. Again, the starting number of reflection is 2 to avoid duplication with $\mathbf{E1}_{\underline{F1\text{-}B11}}^{(1)}$. For odd order image sources $\mathbf{E1}_{\underline{F1\text{-}F2}}^{(2p_2+1)}$, where $p_2 = 1,2,3,\ldots$, they are reflected once by the ground surface Γ_{G1}, p_2+1 times by the façade surface Γ_{F1} and p_2 times by the façade surface Γ_{F2}. For even order image sources $\mathbf{E1}_{\underline{F1\text{-}F2}}^{(2p_2)}$, where $p_2 = 1,2,3,\ldots$, they are reflected

once by the ground surface Γ_{G1} and p_2 times by both surfaces Γ_{F1} and Γ_{F2}. The x-coordinate $x_{E1\text{-}F1\text{-}F2}^{(q_2)}$ of the image source is determined by equation A.24. The contribution of $\mathbf{E1}_{\underline{F1\text{-}F2}}^{(q_2)}$ is calculated by,

$$P_{2108}^{(q_2)} = \sum_{n_1=0}^{\infty}\left[\begin{array}{l} V_{105}^{(n_1)}\left(\mathbf{I}_{B2}^{(n_1)} \mid \mathbf{E1}\right)\cdot V_{2108}^{(q_2)}\left(\mathbf{E1}_{\underline{F1\text{-}F2}}^{(q_2)} \mid \mathfrak{R}\right)\cdot T\left(\mathbf{I}_{B2}^{(n_1)} \mid \mathbf{E1}, \mathbf{E1}_{\underline{F1\text{-}F2}}^{(q_2)} \mid \mathfrak{R}, \beta_{B12}, \beta_{B11}\right) \\ +V_{106}^{(n_1)}\left(\mathbf{I}_{\underline{B2}}^{(n_1)} \mid \mathbf{E1}\right)\cdot V_{2108}^{(q_2)}\left(\mathbf{E1}_{\underline{F1\text{-}F2}}^{(q_2)} \mid \mathfrak{R}\right)\cdot T\left(\mathbf{I}_{\underline{B2}}^{(n_1)} \mid \mathbf{E1}, \mathbf{E1}_{\underline{F1\text{-}F2}}^{(q_2)} \mid \mathfrak{R}, \beta_{B12}, \beta_{B11}\right) \end{array}\right]. \quad \text{(A.77)}$$

The factor $V_{2108}^{(q_2)}\left(\mathbf{I} \mid \mathfrak{R}\right)$, which accounts for the effects of the multiple reflections between the surfaces Γ_{G1}, Γ_{F1} and Γ_{B2}, is given by,

$$V_{2108}^{(q_2)}\left(\mathbf{I} \mid \mathfrak{R}\right) = \begin{cases} Q\left(\mathbf{I}, \mathfrak{R}, \beta_{G1}\right)\cdot\left[Q\left(\mathbf{I}, \mathfrak{R}, \beta_{F1}\right)\right]^{p_2+1}\cdot\left[Q\left(\mathbf{I}, \mathfrak{R}, \beta_{F2}\right)\right]^{p_2} & \text{for } q_2 = 2p_2+1 \\ Q\left(\mathbf{I}, \mathfrak{R}, \beta_{G1}\right)\cdot\left[Q\left(\mathbf{I}, \mathfrak{R}, \beta_{F1}\right)\cdot Q\left(\mathbf{I}, \mathfrak{R}, \beta_{F2}\right)\right]^{p_2} & \text{for } q_2 = 2p_2 \end{cases}. \quad \text{(A.78)}$$

The illuminated zone of $\mathbf{E1}_{\underline{F1\text{-}F2}}^{(q_2)}$ is illustrated in figure A.22. The lines connecting the illuminated receivers with $\mathbf{E1}_{\underline{F1\text{-}F2}}^{(q_2)}$ should have no intersection with the line from $\left(x_{E1\text{-}F2\text{-}F1}^{(q_2-1)}, 0, -H\right)$ to $\left(x_{E1\text{-}F2\text{-}F1}^{(q_2-1)}, 0, H\right)$. The x-coordinate $x_{E1\text{-}F2\text{-}F1}^{(q_2)}$ is calculated by equation A.40.

Group 9 comprises of the image sources formed by multiple reflections between the surfaces Γ_{F1} and Γ_{F2}. They are denoted as,

$$\mathbf{E1}_{F2\text{-}F1}^{(q_2)} \equiv \left(x_{E1\text{-}F2\text{-}F1}^{(q_2)}, 0, H\right), \quad \text{(A.79)}$$

where $q_2 = 1,2,3,\cdots$. The subscript F1-F2 indicates the surfaces of reflections involved and the superscript q_2 in bracket denotes the total number of reflections from the surfaces Γ_{F1} and Γ_{F2}. For odd order image sources $\mathbf{E1}_{F2\text{-}F1}^{(2p_2+1)}$, where $p_2 = 0,1,2,\ldots$, they are reflected p_2 times by the façade surface Γ_{F1} and p_2+1 times by the surface Γ_{F2}. For even order image sources $\mathbf{E1}_{F2\text{-}F1}^{(2p_2)}$, where $p_1 = 1,2,3,\ldots$, they are reflected p_2 times by both

surfaces Γ_{F1} and Γ_{F2}. The x-coordinate $x_{E1\text{-}F2\text{-}F1}^{(q_2)}$ of the image source is determined by equation A.40.

The contribution of $\mathbf{E1}_{F2\text{-}F1}^{(q_2)}$ is calculated by,

$$P_{2109}^{(q_2)} = \sum_{n_1=0}^{\infty}\left[\begin{array}{l} V_{105}^{(n_1)}\left(\mathbf{I}_{B2}^{(n_1)} \mid \mathbf{E1}\right)\cdot V_{2109}^{(q_2)}\left(\mathbf{E1}_{F2\text{-}F1}^{(q_2)} \mid \mathfrak{R}\right)\cdot T\left(\mathbf{I}_{B2}^{(n_1)} \mid \mathbf{E1}, \mathbf{E1}_{F2\text{-}F1}^{(q_2)} \mid \mathfrak{R}, \beta_{B12}, \beta_{B12}\right) \\ +V_{106}^{(n_1)}\left(\mathbf{I}_{\underline{B2}}^{(n_1)} \mid \mathbf{E1}\right)\cdot V_{2109}^{(q_2)}\left(\mathbf{E1}_{F2\text{-}F1}^{(q_2)} \mid \mathfrak{R}\right)\cdot T\left(\mathbf{I}_{\underline{B2}}^{(n_1)} \mid \mathbf{E1}, \mathbf{E1}_{F2\text{-}F1}^{(q_2)} \mid \mathfrak{R}, \beta_{B12}, \beta_{B12}\right) \end{array}\right]. \quad \text{(A.80)}$$

The factor $V_{2109}^{(q_2)}\left(\mathbf{I} \mid \mathfrak{R}\right)$, which accounts for the effects of the multiple reflections between the surfaces Γ_{F1} and Γ_{F2}, is given by,

$$V_{2109}^{(q_2)}\left(\mathbf{I} \mid \mathfrak{R}\right) = \begin{cases} \left[Q\left(\mathbf{I}, \mathfrak{R}, \beta_{F1}\right)\right]^{p_2}\cdot\left[Q\left(\mathbf{I}, \mathfrak{R}, \beta_{F2}\right)\right]^{p_2+1} & \text{for } q_2 = 2p_2+1 \\ \left[Q\left(\mathbf{I}, \mathfrak{R}, \beta_{F1}\right)\cdot Q\left(\mathbf{I}, \mathfrak{R}, \beta_{F2}\right)\right]^{p_2} & \text{for } q_2 = 2p_2 \end{cases}. \quad \text{(A.81)}$$

The illuminated zone of $\mathbf{E1}_{F2\text{-}F1}^{(q_2)}$ is illustrated in figure A.23. The illuminated receiver should have a height higher than H.

Group 10 contains the ground reflected image sources formed by multiple reflections between the surfaces Γ_{F1} and Γ_{F2}. They are similar to the image sources in group 9 but involve an additional reflection with the ground surface Γ_{G2}. They are denoted as,

$$\mathbf{E1}_{\underline{F2\text{-}F1}}^{(q_2)} \equiv \left(x_{E1\text{-}F2\text{-}F1}^{(q_2)}, 0, -H\right), \quad \text{(A.82)}$$

where $q_2 = 1,2,3,\cdots$. The subscript $\underline{F2\text{-}F1}$ indicates the surfaces of reflections involved and the underline in the subscript indicates the ground reflection. The superscript q_2 in bracket denotes the total number of reflections from the surfaces Γ_{F1} and Γ_{F2}. For odd order image sources $\mathbf{E1}_{\underline{F2\text{-}F1}}^{(2p_2+1)}$, where $p_2 = 0,1,2,\ldots$, they are reflected once by the ground surface Γ_{G2}, p_2 times by the façade surface Γ_{F1} and p_2+1 times by the barrier surface Γ_{F2}. For even order image sources $\mathbf{E1}_{\underline{F2\text{-}F1}}^{(2p_2)}$, where $p_2 = 1,2,3,\ldots$, they are reflected once

by the ground surface Γ_{G2} and p_2 times by both surfaces Γ_{F1} and Γ_{F2}. The x-coordinate $x_{\text{E1-F2-F1}}^{(q_2)}$ of the image source is determined by equation A.40. The contribution of $\mathbf{E1}_{\underline{\text{F2-F1}}}^{(q_2)}$ is calculated by,

$$P_{2110}^{(q_2)} = \sum_{n_1=0}^{\infty} \left[\begin{array}{l} V_{105}^{(n_1)}\left(\mathbf{I}_{\text{B2}}^{(n_1)} \mid \mathbf{E1}\right) \cdot V_{2110}^{(q_2)}\left(\mathbf{E1}_{\underline{\text{F2-F1}}}^{(q_2)} \mid \mathfrak{R}\right) \cdot T\left(\mathbf{I}_{\text{B2}}^{(n_1)} \mid \mathbf{E1}, \mathbf{E1}_{\underline{\text{F2-F1}}}^{(q_2)} \mid \mathfrak{R}, \beta_{\text{B12}}, \beta_{\text{B12}}\right) \\ + V_{106}^{(n_1)}\left(\mathbf{I}_{\underline{\text{B2}}}^{(n_1)} \mid \mathbf{E1}\right) \cdot V_{2110}^{(q_2)}\left(\mathbf{E1}_{\underline{\text{F2-F1}}}^{(q_2)} \mid \mathfrak{R}\right) \cdot T\left(\mathbf{I}_{\underline{\text{B2}}}^{(n_1)} \mid \mathbf{E1}, \mathbf{E1}_{\underline{\text{F2-F1}}}^{(q_2)} \mid \mathfrak{R}, \beta_{\text{B12}}, \beta_{\text{B12}}\right) \end{array} \right]. \quad \text{(A.83)}$$

The factor $V_{2110}^{(q_2)}\left(\mathbf{I} \mid \mathfrak{R}\right)$, which accounts for the effects of the multiple reflections between the surfaces Γ_{G3}, Γ_{F1} and Γ_{B2}, is given by,

$$V_{2110}^{(q_2)}\left(\mathbf{I} \mid \mathfrak{R}\right) = \begin{cases} Q\left(\mathbf{I}, \mathfrak{R}, \beta_{\text{G2}}\right) \cdot \left[Q\left(\mathbf{I}, \mathfrak{R}, \beta_{\text{F1}}\right)\right]^{p_2} \cdot \left[Q\left(\mathbf{I}, \mathfrak{R}, \beta_{\text{F2}}\right)\right]^{p_2+1} & \text{for } q_2 = 2p_2 + 1 \\ Q\left(\mathbf{I}, \mathfrak{R}, \beta_{\text{G2}}\right) \cdot \left[Q\left(\mathbf{I}, \mathfrak{R}, \beta_{\text{F1}}\right) \cdot Q\left(\mathbf{I}, \mathfrak{R}, \beta_{\text{F2}}\right)\right]^{p_2} & \text{for } q_2 = 2p_2 \end{cases}. \quad \text{(A.84)}$$

The illuminated zone of $\mathbf{E1}_{\underline{\text{F2-F1}}}^{(q_2)}$ is illustrated in figure A.24. The lines connecting the illuminated receivers with $\mathbf{E1}_{\underline{\text{F2-F1}}}^{(q_2)}$ should have no intersection with the line from $\left(x_{\text{E2-F2-F1}}^{(q_2)}, 0, -H\right)$ to $\left(x_{\text{E2-F2-F1}}^{(q_2)}, 0, H\right)$ and. The x-coordinate $x_{\text{E2-F2-F1}}^{(q_2)}$ is calculated by equation A.25.

Group 11 consists of image sources formed by multiple reflections between the surfaces Γ_{F1} and Γ_{F2} of the image sources $\mathbf{E1}_{\underline{\text{B21-B12}}}^{(q_1)}$ with odd q_1. They are denoted as,

$$\mathbf{E1}_{\underline{\text{B21-B12-F1-F2}}}^{(q_1,q_2)} \equiv \left(x_{\text{E1-B21-B12-F1-F2}}^{(q_1,q_2)}, 0, -H\right), \quad \text{(A.85)}$$

where $q_1 = 1,3,5,\cdots$ and $q_2 = 1,2,3,\cdots$. The subscript $\underline{\text{B21-B12-F1-F2}}$ indicates the surfaces of reflections involved and the underline in the subscript indicates the ground reflection. After the last reflection by Γ_{B21} among the q_1 times multiple reflections between the surfaces Γ_{B12} and Γ_{B21}, there would be q_2 times multiple reflections between the surfaces Γ_{F1} and Γ_{F2}. For odd q_2, the image sources $\mathbf{E1}_{\underline{\text{B21-B12-F1-F2}}}^{(q_1,2p_2+1)}$, where

$p_2 = 0,1,2,\ldots$, are reflected p_2+1 times by the surface Γ_{F1} and p_2 times by the surface Γ_{F2}. For even q_2, the image sources $\mathbf{E1}^{(q_1,2p_2)}_{\underline{\text{B21-B12-F1-F2}}}$, where $p_2 = 1,2,3,\ldots$, they are reflected p_2 times by both surfaces Γ_{F1} and Γ_{F2}. The x-coordinate $x^{(q_1,q_2)}_{\text{E1-B21-B12-F1-F2}}$ of the image source is calculated by,

$$x^{(q_1,q_2)}_{\text{E1-B21-B12-F1-F2}} = \begin{cases} -x^{(q_1)}_{\text{E1-B21-B12}} - (q_2-1)\cdot L & \text{for } q_2 = 1,3,5,\ldots \\ x^{(q_1)}_{\text{E1-B21-B12}} + (q_2)\cdot L & \text{for } q_2 = 2,4,6,\cdots \end{cases}. \tag{A.86}$$

The pressure contribution of $\mathbf{E1}^{(q_1,q_2)}_{\underline{\text{B21-B12-F1-F2}}}$ is calculated by,

$$P^{(q_1,q_2)}_{2111} = \sum_{n_1=0}^{\infty} \begin{bmatrix} V^{(n_1)}_{105}\left(\mathbf{I}^{(n_1)}_{\text{B2}} \mid \mathbf{E1}\right)\cdot V^{(q_1,q_2)}_{2111}\left(\mathbf{E1}^{(q_1,q_2)}_{\underline{\text{B21-B12-F1-F2}}} \mid \mathfrak{R}\right) \\ \cdot T\left(\mathbf{I}^{(n_1)}_{\text{B2}} \mid \mathbf{E1}, \mathbf{E1}^{(q_1,q_2)}_{\underline{\text{B21-B12-F1-F2}}} \mid \mathfrak{R}, \beta_{\text{B12}}, \beta_{\text{B12}}\right) \\ + V^{(n_1)}_{106}\left(\mathbf{I}^{(n_1)}_{\underline{\text{B2}}} \mid \mathbf{E1}\right)\cdot V^{(q_1,q_2)}_{2111}\left(\mathbf{E1}^{(q_1,q_2)}_{\underline{\text{B21-B12-F1-F2}}} \mid \mathfrak{R}\right) \\ \cdot T\left(\mathbf{I}^{(n_1)}_{\underline{\text{B2}}} \mid \mathbf{E1}, \mathbf{E1}^{(q_1,q_2)}_{\underline{\text{B21-B12-F1-F2}}} \mid \mathfrak{R}, \beta_{\text{B12}}, \beta_{\text{B12}}\right) \end{bmatrix}. \tag{A.87}$$

The factor $V^{(q_1,q_2)}_{2111}(\mathbf{I} \mid \mathfrak{R})$, which accounts for the effects of the multiple reflections between the surfaces Γ_{G2}, Γ_{B12}, Γ_{B21}, Γ_{F1} and Γ_{F2} is given by,

$$V^{(q_1,q_2)}_{2111}(\mathbf{I} \mid \mathfrak{R}) = \begin{cases} V^{(q_1)}_{106}(\mathbf{I} \mid \mathfrak{R})\cdot\left[Q(\mathbf{I}, \mathfrak{R}, \beta_{\text{F1}})\right]^{p_2}\cdot\left[Q(\mathbf{I}, \mathfrak{R}, \beta_{\text{F2}})\right]^{p_2+1} \\ \qquad\qquad \text{for } q_1 = 2p_1+1 \text{ and } q_2 = 2p_2+1 \\ V^{(q_1)}_{106}(\mathbf{I} \mid \mathfrak{R})\cdot\left[Q(\mathbf{I}, \mathfrak{R}, \beta_{\text{F1}})\cdot Q(\mathbf{I}, \mathfrak{R}, \beta_{\text{F2}})\right]^{p_2} \\ \qquad\qquad \text{for } q_1 = 2p_1+1 \text{ and } q_2 = 2p_2 \end{cases}. \tag{A.88}$$

The illuminated zone of $\mathbf{E1}^{(q_1,q_2)}_{\underline{\text{B21-B12-F1-F2}}}$ is illustrated in figure A.25. The lines connecting the illuminated receivers with $\mathbf{E1}^{(q_1,q_2)}_{\underline{\text{B21-B12-F1-F2}}}$ should have no intersection with the line from $\left(x^{(q_2)}_{\text{E1-F1-F2}}, 0, -H\right)$ to $\left(x^{(q_2)}_{\text{E1-F1-F2}}, 0, H\right)$ and have an intersection with the line from $\left(x^{(q_2)}_{\text{E2-F1-F2}}, 0, -H\right)$ to $\left(x^{(q_2)}_{\text{E2-F1-F2}}, 0, H\right)$. The x-coordinate $x^{(q_2)}_{\text{E1-F1-F2}}$ can be calculated by equation A.24 while the x-coordinate $x^{(q_2)}_{\text{E2-F1-F2}}$ can be calculated by equation A.48.

Group 12 consists of image sources formed by multiple reflections between the surfaces Γ_{F1} and Γ_{F2} of the image sources $\mathbf{E1}^{(q_1)}_{\underline{\text{B21-B12}}}$ with even q_1. They are denoted as,

$$\mathbf{E1}^{(q_1,q_2)}_{\underline{\text{B21-B12-F2-F1}}} \equiv \left(x^{(q_1,q_2)}_{\text{E1-B21-B12-F2-F1}}, 0, -H\right), \tag{A.89}$$

where $q_1 = 2,4,6,\cdots$ and $q_2 = 1,2,3,\cdots$. The subscript $\underline{\text{B21-B12-F2-F1}}$ indicates the surfaces of reflections involved and the underline in the subscript indicates the ground reflection. After the last reflection by Γ_{B12} among the q_1 times multiple reflections between the surfaces Γ_{B12} and Γ_{B21}, there would be q_2 times multiple reflections between the surfaces Γ_{F1} and Γ_{F2}. For odd q_2, the image sources $\mathbf{E1}^{(q_1,2p_2+1)}_{\underline{\text{B21-B12-F2-F1}}}$, where $p_2 = 0,1,2,\ldots$, are reflected p_2 times by the surface Γ_{F1} and p_2+1 times by the surface Γ_{F2}. For even q_2, the image sources $\mathbf{E1}^{(q_1,2p_2)}_{\underline{\text{B21-B12-F2-F1}}}$, where $p_2 = 1,2,3,\ldots$, they are reflected p_2 times by both surfaces Γ_{F1} and Γ_{F2}. The x-coordinate $x^{(q_1,q_2)}_{\text{E1-B21-B12-F2-F1}}$ of the image source is calculated by,

$$x^{(q_1,q_2)}_{\text{E1-B21-B12-F2-F1}} = \begin{cases} -x^{(q_1)}_{\text{E1-B21-B12}} + (q_2+1)\cdot L & \text{for } q_2 = 1, 3, 5, \ldots \\ x^{(q_1)}_{\text{E1-B21-B12}} - (q_2)\cdot L & \text{for } q_2 = 2, 4, 6, \cdots \end{cases}. \tag{A.90}$$

The pressure contribution of $\mathbf{E1}^{(q_1,q_2)}_{\underline{\text{B21-B12-F2-F1}}}$ is calculated by,

$$P^{(q_1,q_2)}_{2112} = \sum_{n_1=0}^{\infty} \begin{bmatrix} V^{(n_1)}_{105}\left(\mathbf{I}^{(n_1)}_{\text{B2}} \mid \mathbf{E1}\right)\cdot V^{(q_1,q_2)}_{2112}\left(\mathbf{E1}^{(q_1,q_2)}_{\underline{\text{B21-B12-F2-F1}}} \mid \mathfrak{R}\right) \\ \cdot T\left(\mathbf{I}^{(n_1)}_{\text{B2}} \mid \mathbf{E1}, \mathbf{E1}^{(q_1,q_2)}_{\underline{\text{B21-B12-F2-F1}}} \mid \mathfrak{R}, \beta_{\text{B12}}, \beta_{\text{B12}}\right) \\ + V^{(n_1)}_{106}\left(\mathbf{I}^{(n_1)}_{\underline{\text{B2}}} \mid \mathbf{E1}\right)\cdot V^{(q_1,q_2)}_{2112}\left(\mathbf{E1}^{(q_1,q_2)}_{\underline{\text{B21-B12-F2-F1}}} \mid \mathfrak{R}\right) \\ \cdot T\left(\mathbf{I}^{(n_1)}_{\underline{\text{B2}}} \mid \mathbf{E1}, \mathbf{E1}^{(q_1,q_2)}_{\underline{\text{B21-B12-F2-F1}}} \mid \mathfrak{R}, \beta_{\text{B12}}, \beta_{\text{B12}}\right) \end{bmatrix}. \tag{A.91}$$

The factor $V^{(q_1,q_2)}_{2112}(\mathbf{I} \mid \mathfrak{R})$, which accounts for the effects of the multiple reflections between the surfaces Γ_{G2}, Γ_{B12}, Γ_{B21}, Γ_{F1} and Γ_{F2} is given by,

$$V_{2112}^{(q_1,q_2)}(\mathbf{I}\,|\,\mathfrak{R})=\begin{cases} V_{106}^{(q_1)}(\mathbf{I}\,|\,\mathfrak{R})\cdot\left[Q(\mathbf{I},\mathfrak{R},\beta_{\mathrm{F1}})\right]^{p_2+1}\cdot\left[Q(\mathbf{I},\mathfrak{R},\beta_{\mathrm{F2}})\right]^{p_2} \\ \qquad\qquad \text{for } q_1=2p_1 \text{ and } q_2=2p_2+1 \\ V_{106}^{(q_1)}(\mathbf{I}\,|\,\mathfrak{R})\cdot\left[Q(\mathbf{I},\mathfrak{R},\beta_{\mathrm{F1}})\cdot Q(\mathbf{I},\mathfrak{R},\beta_{\mathrm{F2}})\right]^{p_2} \\ \qquad\qquad \text{for } q_1=2p_1 \text{ and } q_2=2p_2 \end{cases}. \tag{A.92}$$

The illuminated zone of $\mathbf{E1}_{\underline{\text{B21-B12-F2-F1}}}^{(q_1,q_2)}$ is illustrated in figure A.26. The lines connecting the illuminated receivers with $\mathbf{E1}_{\underline{\text{B21-B12-F2-F1}}}^{(q_1,q_2)}$ should have an intersection with the line from $\left(x_{\text{E1-F2-F1}}^{(q_2)},0,-H\right)$ to $\left(x_{\text{E1-F2-F1}}^{(q_2)},0,H\right)$ and have no intersection with the line from $\left(x_{\text{E2-F2-F1}}^{(q_2)},0,-H\right)$ to $\left(x_{\text{E2-F2-F1}}^{(q_2)},0,H\right)$. The x-coordinate $x_{\text{E1-F2-F1}}^{(q_2)}$ can be calculated by equation A.40 while the x-coordinate $x_{\text{E2-F2-F1}}^{(q_2)}$ can be calculated by equation A.25.

Group 13 consists of image sources formed by multiple reflections between the surfaces Γ_{F1} and Γ_{F2} of the image sources $\mathbf{E1}_{\underline{\text{F1-B11}}}^{(q_1)}$ with odd q_1. They are denoted as,

$$\mathbf{E1}_{\underline{\text{F1-B11-F2-F1}}}^{(q_1,q_2)}\equiv\left(x_{\text{E1-F1-B11-F2-F1}}^{(q_1,q_2)},0,-H\right), \tag{A.93}$$

where $q_1=3,5,7,\cdots$ and $q_2=1,2,3,\cdots$. The subscript $\underline{\text{F1-B11-F2-F1}}$ indicates the surfaces of reflections involved and the underline in the subscript indicates the ground reflection. The order of reflections q_1 is starts from 3 as the image sources $\mathbf{E1}_{\underline{\text{F1-B11-F2-F1}}}^{(1,q_2)}$ are already considered as $\mathbf{E1}_{\text{F1-F2}}^{(q_2+1)}$ already. After the last reflection by Γ_{F1} among the q_1 times multiple reflections between Γ_{F1} and Γ_{B11}, there would be q_2 times multiple reflections between Γ_{F1} and Γ_{F2}. For odd q_2, the image sources $\mathbf{E1}_{\underline{\text{F1-B11-F2-F1}}}^{(q_1,2p_2+1)}$, where $p_2=0,1,2,\ldots$, are reflected p_2 times by the surface Γ_{F1} and p_2+1 times by the surface Γ_{F2}. For even q_2, the image sources $\mathbf{E1}_{\underline{\text{F1-B11-F2-F1}}}^{(q_1,2p_2)}$, where $p_2=1,2,3,\ldots$, they are reflected p_2

times by both surfaces Γ_{F1} and Γ_{F2}. The x-coordinate $x_{\text{E1-F1-B11-F2-F1}}^{(q_1,q_2)}$ of the image source is given by,

$$x_{\text{E1-F1-B11-F2-F1}}^{(q_1,q_2)} = \begin{cases} -x_{\text{E1-F1-B11}}^{(q_1)} + (q_2+1)\cdot L & \text{for } q_2 = 1,3,5,\ldots \\ x_{\text{E1-F1-B11}}^{(q_1)} - (q_2)\cdot L & \text{for } q_2 = 2,4,6,\cdots \end{cases}. \tag{A.94}$$

The pressure contribution of $\mathbf{E1}_{\underline{\text{F1-B11-F2-F1}}}^{(q_1,q_2)}$ is calculated by,

$$P_{2113}^{(q_1,q_2)} = \sum_{n_1=0}^{\infty} \begin{bmatrix} V_{105}^{(n_1)}\left(\mathbf{I}_{\text{B2}}^{(n_1)} \mid \mathbf{E1}\right)\cdot V_{2113}^{(q_1,q_2)}\left(\mathbf{E1}_{\underline{\text{F1-B11-F2-F1}}}^{(q_1,q_2)} \mid \mathfrak{R}\right) \\ \cdot T\left(\mathbf{I}_{\text{B2}}^{(n_1)} \mid \mathbf{E1}, \mathbf{E1}_{\underline{\text{F1-B11-F2-F1}}}^{(q_1,q_2)} \mid \mathfrak{R}, \beta_{\text{B12}}, \beta_{\text{B12}}\right) \\ + V_{106}^{(n_1)}\left(\mathbf{I}_{\underline{\text{B2}}}^{(n_1)} \mid \mathbf{E1}\right)\cdot V_{2113}^{(q_1,q_2)}\left(\mathbf{E1}_{\underline{\text{F1-B11-F2-F1}}}^{(q_1,q_2)} \mid \mathfrak{R}\right) \\ \cdot T\left(\mathbf{I}_{\underline{\text{B2}}}^{(n_1)} \mid \mathbf{E1}, \mathbf{E1}_{\underline{\text{F1-B11-F2-F1}}}^{(q_1,q_2)} \mid \mathfrak{R}, \beta_{\text{B12}}, \beta_{\text{B12}}\right) \end{bmatrix}. \tag{A.95}$$

The factor $V_{2113}^{(q_1,q_2)}(\mathbf{I} \mid \mathfrak{R})$, which accounts for the effects of the multiple reflections between the surfaces Γ_{G2}, Γ_{B12}, Γ_{B21}, Γ_{F1} and Γ_{F2} is given by,

$$V_{2113}^{(q_1,q_2)}(\mathbf{I} \mid \mathfrak{R}) = \begin{cases} Q(\mathbf{I},\mathfrak{R},\beta_{\text{G1}})\cdot\left[Q(\mathbf{I},\mathfrak{R},\beta_{\text{B11}})\right]^{p_2}\cdot\left[Q(\mathbf{I},\mathfrak{R},\beta_{\text{F1}})\right]^{p_1+p_2+1}\cdot\left[Q(\mathbf{I},\mathfrak{R},\beta_{\text{F2}})\right]^{p_2} \\ \qquad\qquad \text{for } q_1 = 2p_1+1 \text{ and } q_2 = 2p_2+1 \\ Q(\mathbf{I},\mathfrak{R},\beta_{\text{G1}})\cdot\left[Q(\mathbf{I},\mathfrak{R},\beta_{\text{B11}})\right]^{p_2}\cdot\left[Q(\mathbf{I},\mathfrak{R},\beta_{\text{F1}})\right]^{p_1+p_2}\cdot\left[Q(\mathbf{I},\mathfrak{R},\beta_{\text{F2}})\right]^{p_2} \\ \qquad\qquad \text{for } q_1 = 2p_1+1 \text{ and } q_2 = 2p_2 \end{cases}. \tag{A.96}$$

The illuminated zone of $\mathbf{E1}_{\underline{\text{F1-B11-F2-F1}}}^{(q_1,q_2)}$ is illustrated in figure A.27. The lines connecting the illuminated receivers with $\mathbf{E1}_{\underline{\text{F1-B11-F2-F1}}}^{(q_1,q_2)}$ should have no intersection with the line from $\left(x_{\text{E1-F2-F1}}^{(q_2)},0,-H\right)$ to $\left(x_{\text{E1-F2-F1}}^{(q_2)},0,H\right)$ and have an intersection with the line from $\left(x_{\text{E1-F1-F2}}^{(q_2+1)},0,-H\right)$ to $\left(x_{\text{E1-F1-F2}}^{(q_2+1)},0,H\right)$. The x-coordinate $x_{\text{E1-F2-F1}}^{(q_2)}$ can be calculated by equation A.40 while the x-coordinate $x_{\text{E1-F1-F2}}^{(q_2)}$ can be calculated by equation A.24.

A.4 Secondary Contribution from Edge of Diffraction E2

In section A.3, we have discussed in details the secondary contribution of the diffraction at the edge **E1**. In this section, we put our attention to the diffraction at the edge **E2**. The primary image sources that can contribute to the pressure with diffraction at **E2** are $\mathbf{I}_0$, $\mathbf{I}_{\underline{0}}$, $\left\{\mathbf{I}_{\mathrm{B1}}^{(1)}, \mathbf{I}_{\mathrm{B1}}^{(2)}, \cdots, \mathbf{I}_{\mathrm{B1}}^{(\infty)}\right\}$ and $\left\{\mathbf{I}_{\underline{\mathrm{B1}}}^{(1)}, \mathbf{I}_{\underline{\mathrm{B1}}}^{(2)}, \cdots, \mathbf{I}_{\underline{\mathrm{B1}}}^{(\infty)}\right\}$. Similar to the diffraction at **E1**, we represent these primary image sources into two series $\left\{\mathbf{I}_{\mathrm{B1}}^{(n)}\right\}$ and $\left\{\mathbf{I}_{\underline{\mathrm{B1}}}^{(n)}\right\}$, where n = 0,1,2, … ,. The image sources $\mathbf{I}_0$ and $\mathbf{I}_{\underline{0}}$ are represented by $\mathbf{I}_{\mathrm{B1}}^{(0)}$ and $\mathbf{I}_{\underline{\mathrm{B1}}}^{(0)}$ respectively. Similar to our previous analysis, we categorize the contribution of the secondary image sources of **E2** into 13 groups based on various combinations of reflections.

Group 1 is the image source of **E2** with contribution through direct transmission. The image source is actually at the original location of the edge **E2** and is denoted by,

$$\mathbf{E2}_0 \equiv \mathbf{E2} = \left(L_1 + W, 0, H\right). \tag{A.97}$$

The pressure contribution of $\mathbf{E2}_0$ is calculated by,

$$P_{2201} = \sum_{n_1=0}^{\infty}\left[\begin{array}{l} V_{103}^{(n_1)}\left(\mathbf{I}_{\mathrm{B1}}^{(n_1)} \mid \mathbf{E2}\right)\cdot T\left(\mathbf{I}_{\mathrm{B1}}^{(n_1)} \mid \mathbf{E2}, \mathbf{E2}_0 \mid \mathfrak{R}, \beta_{\mathrm{B21}}, \boldsymbol{\beta}_{\mathrm{R}}\right) \\ +V_{104}^{(n_1)}\left(\mathbf{I}_{\mathrm{B1}}^{(n_1)} \mid \mathbf{E2}\right)\cdot T\left(\mathbf{I}_{\underline{\mathrm{B1}}}^{(n_1)} \mid \mathbf{E2}, \mathbf{E2}_0 \mid \mathfrak{R}, \beta_{\mathrm{B21}}, \boldsymbol{\beta}_{\mathrm{R}}\right) \end{array}\right], \tag{A.98}$$

where the term $\boldsymbol{\beta}_{\mathrm{R}}$ used for the calculation of diffraction is dependent on the location of the receivers as follows,

$$\boldsymbol{\beta}_{\mathrm{R}} = \begin{cases} \beta_{\mathrm{B21}} & \text{if } x_{\mathrm{R}} \le L_1 + W \\ \\ \beta_{\mathrm{B22}} & \text{if } x_{\mathrm{R}} > L_1 + W \end{cases}. \tag{A.99}$$

The illuminated zone of $\mathbf{E2}_0$ is illustrated in figure A.28. The lines connecting $\mathbf{E2}_0$ and the illuminated receivers should have no intersection with the line from $(L_1, 0, 0)$ to $(L_1, 0, H)$.

Group 2 is the image source with one ground reflection and it is denoted as,

$$\mathbf{E2}_{\underline{0}} \equiv (L_1 + W, 0, -H). \tag{A.100}$$

The underline in the subscript indicates ground reflection. The pressure contribution of $\mathbf{E2}_{\underline{0}}$ is calculated by,

$$P_{2202} = \sum_{n_1=0}^{\infty} \left[\begin{array}{l} V_{103}^{(n_1)}\left(\mathbf{I}_{\mathrm{B1}}^{(n_1)} \mid \mathbf{E2}\right) \cdot V_{2202}\left(\mathbf{E2}_{\underline{0}} \mid \mathfrak{R}\right) \cdot T\left(\mathbf{I}_{\mathrm{B1}}^{(n_1)} \mid \mathbf{E2}, \mathbf{E2}_{\underline{0}} \mid \mathfrak{R}, \beta_{\mathrm{B12}}, \boldsymbol{\beta}_{\mathrm{R}}\right) \\ + V_{104}^{(n_1)}\left(\mathbf{I}_{\underline{\mathrm{B1}}}^{(n_1)} \mid \mathbf{E2}\right) \cdot V_{2202}\left(\mathbf{E2}_{\underline{0}} \mid \mathfrak{R}\right) \cdot T\left(\mathbf{I}_{\underline{\mathrm{B1}}}^{(n_1)} \mid \mathbf{E2}, \mathbf{E2}_{\underline{0}} \mid \mathfrak{R}, \beta_{\mathrm{B12}}, \boldsymbol{\beta}_{\mathrm{R}}\right) \end{array} \right], \tag{A.101}$$

where the term $\boldsymbol{\beta}_{\mathrm{R}}$ is calculated by equation (A.99) and the reflection factor $V_{2202}(\mathbf{I} \mid \mathfrak{R})$ accounts for the ground reflection as follows,

$$V_{2202}(\mathbf{I} \mid \mathfrak{R}) = Q(\mathbf{I}, \mathfrak{R}, \boldsymbol{\beta}_{\mathrm{G}}). \tag{A.102}$$

Again, the term $\boldsymbol{\beta}_{\mathrm{G}}$ is dependent on the location of the receiver and can be expressed as,

$$\boldsymbol{\beta}_{\mathrm{G}} = \begin{cases} \beta_{\mathrm{G2}} & \text{if } x_{\mathrm{R}} \le L_1 + W \\ \\ \beta_{\mathrm{G3}} & \text{if } x_{\mathrm{R}} > L_1 + W \end{cases}. \tag{A.103}$$

The illuminated Zone of $\mathbf{E2}_{\underline{0}}$ is illustrated in figure A.29. The lines connecting $\mathbf{E2}_{\underline{0}}$ and the illuminated receivers should have no intersection with the line from $(L_1, 0, -H)$ to $(L_1, 0, H)$.

Group 3 comprises of the image sources formed by multiple reflections between the surfaces Γ_{F2} and Γ_{B22}. They are denoted as,

$$\mathbf{E2}_{\mathrm{F2\text{-}B22}}^{(q_1)} \equiv \left(x_{\mathrm{E2\text{-}F2\text{-}B22}}^{(q_1)}, 0, H\right), \tag{A.104}$$

where $q_1 = 1,2,3,\cdots$. The subscript F2 - B22 indicates the surfaces of reflections involved and the superscript q_1 in bracket denotes the total number of reflections from the surfaces Γ_{F2} and Γ_{B22}. For odd order image sources $\mathbf{E2}^{(2p_1+1)}_{\mathrm{F2\text{-}B22}}$, where $p_1 = 0,1,2,\ldots$, they are reflected p_1+1 times by the façade surface Γ_{F2} and p_1 times by the barrier surface Γ_{B22}. For even order image sources $\mathbf{E2}^{(2p_1)}_{\mathrm{F2\text{-}B22}}$, where $p_1 = 1,2,3,\ldots$, they are reflected p_1 times by both surfaces Γ_{F2} and Γ_{B22}. The x-coordinate $x^{(q_1)}_{\mathrm{E2\text{-}F2\text{-}B22}}$ of the image source is determined as,

$$x^{(q_1)}_{\mathrm{E2\text{-}F2\text{-}B22}} = \begin{cases} L_1 + W + (q_1+1)\times L_2 & \text{for } q_1 = 1, 3, 5, \ldots \\ L_1 + W - q_1 \times L_2 & \text{for } q_1 = 2, 4, 6, \cdots \end{cases} \tag{A.105}$$

The contribution of $\mathbf{E2}^{(q_1)}_{\mathrm{F2\text{-}B22}}$ is calculated by,

$$P^{(q_1)}_{2203} = \sum_{n_1=0}^{\infty} \left[\begin{array}{l} V^{(n_1)}_{103}\left(\mathbf{I}^{(n_1)}_{\mathrm{B1}} \mid \mathbf{E2}\right) \cdot V^{(q_1)}_{2203}\left(\mathbf{E2}^{(q_1)}_{\mathrm{F2\text{-}B22}} \mid \mathfrak{R}\right) \cdot T\left(\mathbf{I}^{(n_1)}_{\mathrm{B1}} \mid \mathbf{E2}, \mathbf{E2}^{(q_1)}_{\mathrm{F2\text{-}B22}} \mid \mathfrak{R}, \beta_{\mathrm{B21}}, \beta_{\mathrm{B22}}\right) \\ + V^{(n_1)}_{104}\left(\mathbf{I}^{(n_1)}_{\mathrm{B1}} \mid \mathbf{E2}\right) \cdot V^{(q_1)}_{2203}\left(\mathbf{E2}^{(q_1)}_{\mathrm{F2\text{-}B22}} \mid \mathfrak{R}\right) \cdot T\left(\mathbf{I}^{(n_1)}_{\underline{\mathrm{B1}}} \mid \mathbf{E2}, \mathbf{E2}^{(q_1)}_{\mathrm{F2\text{-}B22}} \mid \mathfrak{R}, \beta_{\mathrm{B21}}, \beta_{\mathrm{B22}}\right) \end{array} \right]. \tag{A.106}$$

The factor $V^{(q_1)}_{2203}\left(\mathbf{I} \mid \mathfrak{R}\right)$, which accounts for the effects of the multiple reflections between the surfaces Γ_{F2} and Γ_{B22}, is given by,

$$V^{(q_1)}_{2203}\left(\mathbf{I} \mid \mathfrak{R}\right) = \begin{cases} \left[Q\left(\mathbf{I}, \mathfrak{R}, \beta_{\mathrm{F2}}\right)\right]^{p_1+1} \cdot \left[Q\left(\mathbf{I}, \mathfrak{R}, \beta_{\mathrm{B22}}\right)\right]^{p_1} & \text{for } q_1 = 2p_1 + 1 \\ \left[Q\left(\mathbf{I}, \mathfrak{R}, \beta_{\mathrm{F2}}\right) \cdot Q\left(\mathbf{I}, \mathfrak{R}, \beta_{\mathrm{B22}}\right)\right]^{p_1} & \text{for } q_1 = 2p_1 \end{cases}. \tag{A.107}$$

The illuminated zone of $\mathbf{E2}^{(q_1)}_{\mathrm{F2\text{-}B22}}$ is illustrated in figure A.30. Receivers having a height lower than H and located between the façade surface Γ_{F2} and the barrier **B2** should be illuminated by all $\mathbf{E2}^{(q_1)}_{\mathrm{F2\text{-}B22}}$. Especially for $\mathbf{E2}^{(1)}_{\mathrm{F2\text{-}B22}}$, receivers located higher than H are also illuminated.

Group 4 contains the ground reflected image sources formed by multiple reflections between the surfaces Γ_{F2} and Γ_{B22}. They are similar to the image sources in group 3 but involve an additional reflection with the ground surface Γ_{G3}. They are denoted as,

$$\mathbf{E2}_{\underline{\text{F2-B22}}}^{(q_1)} \equiv \left(x_{\text{F2-B22}}^{(q_1)}, 0, -H\right), \tag{A.108}$$

where $q_1 = 1,2,3,\cdots$. The subscript $\underline{\text{F2-B22}}$ indicates the surfaces of reflections involved and the underline in the subscript indicates the ground reflection. The superscript q_1 in bracket denotes the total number of reflections from the surfaces Γ_{F2} and Γ_{B22}. For odd order image sources $\mathbf{E2}_{\underline{\text{F2-B22}}}^{(2p_1+1)}$, where $p_1 = 0,1,2,\ldots$, they are reflected once by the ground surface Γ_{G3}, p_1+1 times by the façade surface Γ_{F2} and p_1 times by the barrier surface Γ_{B22}. For even order image sources $\mathbf{E2}_{\underline{\text{F2-B22}}}^{(2p_1)}$, where $p_1 = 1,2,3,\ldots$, they are reflected once by the ground surface Γ_{G3} and p_1 times by both surfaces Γ_{F2} and Γ_{B22}. The x-coordinate $x_{\text{E2-F2-B22}}^{(q_1)}$ of the image source is determined by equation A.105. The contribution of $\mathbf{E2}_{\underline{\text{F2-B22}}}^{(q_1)}$ is calculated by,

$$P_{2204}^{(q_1)} = \sum_{n_1=0}^{\infty}\left[\begin{array}{l} V_{103}^{(n_1)}\left(\mathbf{I}_{\text{B1}}^{(n_1)} \mid \mathbf{E2}\right)\cdot V_{2104}^{(q_1)}\left(\mathbf{E2}_{\underline{\text{F2-B22}}}^{(q_1)} \mid \mathfrak{R}\right)\cdot T\left(\mathbf{I}_{\text{B1}}^{(n_1)} \mid \mathbf{E2}, \mathbf{E2}_{\underline{\text{F2-B22}}}^{(q_1)} \mid \mathfrak{R}, \beta_{\text{B21}}, \beta_{\text{B22}}\right) \\ + V_{104}^{(n_1)}\left(\mathbf{I}_{\underline{\text{B1}}}^{(n_1)} \mid \mathbf{E2}\right)\cdot V_{2104}^{(q_1)}\left(\mathbf{E2}_{\underline{\text{F2-B22}}}^{(q_1)} \mid \mathfrak{R}\right)\cdot T\left(\mathbf{I}_{\underline{\text{B1}}}^{(n_1)} \mid \mathbf{E2}, \mathbf{E2}_{\underline{\text{F2-B22}}}^{(q_1)} \mid \mathfrak{R}, \beta_{\text{B21}}, \beta_{\text{B22}}\right) \end{array}\right]. \tag{A.109}$$

The factor $V_{2204}^{(q_1)}\left(\mathbf{I} \mid \mathfrak{R}\right)$, which accounts for the effects of the multiple reflections between the surfaces Γ_{G1}, Γ_{F2} and Γ_{B22}, is given by,

$$V_{2204}^{(q_1)}\left(\mathbf{I} \mid \mathfrak{R}\right) = \begin{cases} Q\left(\mathbf{I}, \mathfrak{R}, \beta_{\text{G3}}\right)\cdot\left[Q\left(\mathbf{I}, \mathfrak{R}, \beta_{\text{F2}}\right)\right]^{p_1+1}\cdot\left[Q\left(\mathbf{I}, \mathfrak{R}, \beta_{\text{B22}}\right)\right]^{p_1} & \text{for } q_1 = 2p_1+1 \\ Q\left(\mathbf{I}, \mathfrak{R}, \beta_{\text{G3}}\right)\cdot\left[Q\left(\mathbf{I}, \mathfrak{R}, \beta_{\text{F2}}\right)\cdot Q\left(\mathbf{I}, \mathfrak{R}, \beta_{\text{B22}}\right)\right]^{p_1} & \text{for } q_1 = 2p_1 \end{cases}. \tag{A.110}$$

The illuminated zone of $\mathbf{E2}^{(q_1)}_{\underline{\text{F2-B22}}}$ is illustrated in figure A.31. For image sources $\mathbf{E2}^{(q_1)}_{\underline{\text{F2-B22}}}$ with odd order q_1, the lines connecting the illuminated receivers with $\mathbf{E2}^{(q_1)}_{\underline{\text{F2-B22}}}$ should have an intersection with the line from $(L+L_2, 0, -H)$ to $(L+L_2, 0, H)$ and have no intersection with the line from $(L_1+W, 0, -H)$ to $(L_1+W, 0, H)$. For the $\mathbf{E2}^{(q_1)}_{\underline{\text{F2-B22}}}$ with even q_1, the lines connecting the illuminated receivers with $\mathbf{E2}^{(q_1)}_{\underline{\text{F2-B22}}}$ should have an intersection with the line from $(L_1+W, 0, -H)$ to $(L_1+W, 0, H)$.

Group 5 comprises of the image sources formed by multiple reflections between the barrier surfaces Γ_{B12} and Γ_{B21}. They are denoted as,

$$\mathbf{E2}^{(q_1)}_{\text{B12-B21}} \equiv \left(x^{(q_1)}_{\text{E2-B12-B21}}, 0, H\right), \tag{A.111}$$

where $q_1 = 1,2,3,\cdots$. The subscript B12-B21 indicates the surfaces of reflections involved and the superscript q_1 in bracket denotes the total number of reflections from the surfaces Γ_{B12} and Γ_{B21}. For odd order image sources $\mathbf{E2}^{(2q_1+1)}_{\text{B12-B21}}$, where $p_1 = 0,1,2,\ldots$, they are reflected p_1+1 times by the surface Γ_{B12} and p_1 times by the surface Γ_{B21}. For even order image sources $\mathbf{E2}^{(2q_1)}_{\text{B12-B21}}$, where $p_1 = 1,2,3,\ldots$, they are reflected p_1 times by both surfaces Γ_{B12} and Γ_{B21}. The x-coordinate $x^{(q_1)}_{\text{E2-B12-B21}}$ of the image source is determined as,

$$x^{(q_1)}_{\text{E2-B12-B21}} = \begin{cases} L_1 - q_1 \cdot W & \text{for } q_1 = 1, 3, 5, \ldots \\ L_1 + (q_1+1)\cdot W & \text{for } q_1 = 2, 4, 6, \cdots \end{cases}. \tag{A.112}$$

The contribution of $\mathbf{E2}^{(q_1)}_{\text{B12-B21}}$ is calculated by,

$$P^{(q_1)}_{2205} = \sum_{n_1=0}^{\infty} \left[\begin{array}{l} V^{(n_1)}_{103}\left(\mathbf{I}^{(n_1)}_{\text{B1}} \mid \mathbf{E2}\right) \cdot V^{(q_1)}_{2205}\left(\mathbf{E2}^{(q_1)}_{\text{B12-B21}} \mid \mathfrak{R}\right) \cdot T\left(\mathbf{I}^{(n_1)}_{\text{B1}} \mid \mathbf{E2}, \mathbf{E2}^{(q_1)}_{\text{B12-B21}} \mid \mathfrak{R}, \beta_{\text{B21}}, \beta_{\text{B21}}\right) \\ + V^{(n_1)}_{104}\left(\mathbf{I}^{(n_1)}_{\underline{\text{B1}}} \mid \mathbf{E2}\right) \cdot V^{(q_1)}_{2205}\left(\mathbf{E2}^{(q_1)}_{\text{B12-B21}} \mid \mathfrak{R}\right) \cdot T\left(\mathbf{I}^{(n_1)}_{\underline{\text{B1}}} \mid \mathbf{E2}, \mathbf{E2}^{(q_1)}_{\text{B12-B21}} \mid \mathfrak{R}, \beta_{\text{B21}}, \beta_{\text{B21}}\right) \end{array} \right]. \tag{A.113}$$

The factor $V_{2205}^{(q_1)}(\mathbf{I}\,|\,\mathfrak{R})$, which accounts for the effects of the multiple reflections between the surfaces Γ_{B12} and Γ_{B21}, is given by,

$$V_{2205}^{(q_1)}(\mathbf{I}\,|\,\mathfrak{R}) = \begin{cases} \left[Q(\mathbf{I},\mathfrak{R},\beta_{\mathrm{B12}})\right]^{p_1+1}\cdot\left[Q(\mathbf{I},\mathfrak{R},\beta_{\mathrm{B21}})\right]^{p_1} & \text{for } q_1 = 2p_1+1 \\ \left[Q(\mathbf{I},\mathfrak{R},\beta_{\mathrm{B12}})\cdot Q(\mathbf{I},\mathfrak{R},\beta_{\mathrm{B21}})\right]^{p_1} & \text{for } q_1 = 2p_1 \end{cases}. \qquad \text{(A.114)}$$

The illuminated zone of $\mathbf{E2}_{\mathrm{B12\text{-}B21}}^{(q_1)}$ is illustrated in figure A.32. The illuminated receivers should be located between the two barriers **B1** and **B2** and have a height lower than H.

Group 6 contains the ground reflected image sources formed by multiple reflections between the surfaces Γ_{B12} and Γ_{B21}. They are similar to the image sources in group 5 but involve an additional reflection with the ground surface Γ_{G2}. They are denoted as,

$$\mathbf{E2}_{\underline{\mathrm{B12\text{-}B21}}}^{(q_1)} \equiv \left(x_{\mathrm{E2\text{-}B12\text{-}B21}}^{(q_1)}, 0, -H\right), \qquad \text{(A.115)}$$

where $q_1 = 1,2,3,\cdots$. The subscript $\underline{\mathrm{B12\text{-}B21}}$ indicates the surfaces of reflections involved and the underline in the subscript indicates the ground reflection. The superscript q_1 in bracket denotes the total number of reflections from the surfaces Γ_{B12} and Γ_{B21}. For odd order image sources $\mathbf{E2}_{\underline{\mathrm{B12\text{-}B21}}}^{(2p_1+1)}$, where $p_1 = 0,1,2,\ldots$, they are reflected once by the surface Γ_{G2}, p_1+1 times by the surface Γ_{B12} and p_1 times by the surface Γ_{B21}. For even order image sources $\mathbf{E2}_{\underline{\mathrm{B12\text{-}B21}}}^{(2p_1)}$, where $p_1 = 1,2,3,\ldots$, they are reflected once by the surface Γ_{G2} and p_1 times by both surfaces Γ_{B12} and Γ_{B21}. The x-coordinate $x_{\mathrm{E2\text{-}B12\text{-}B21}}^{(q_1)}$ of the image source is determined by equation A.112. The contribution of $\mathbf{E2}_{\underline{\mathrm{B12\text{-}B21}}}^{(q_1)}$ is calculated by,

$$P_{2206}^{(q_1)} = \sum_{n_1=0}^{\infty} \begin{bmatrix} V_{103}^{(n_1)}\left(\mathbf{I}_{\mathrm{B1}}^{(n_1)} \mid \mathbf{E2}\right) \cdot V_{2206}^{(q_1)}\left(\mathbf{E2}_{\underline{\mathrm{B12\text{-}B21}}}^{(q_1)} \mid \mathfrak{R}\right) \cdot T\left(\mathbf{I}_{\mathrm{B1}}^{(n_1)} \mid \mathbf{E2}, \mathbf{E2}_{\underline{\mathrm{B12\text{-}B21}}}^{(q_1)} \mid \mathfrak{R}, \beta_{\mathrm{B21}}, \beta_{\mathrm{B21}}\right) \\ + V_{104}^{(n_1)}\left(\mathbf{I}_{\underline{\mathrm{B1}}}^{(n_1)} \mid \mathbf{E2}\right) \cdot V_{2206}^{(q_1)}\left(\mathbf{E2}_{\underline{\mathrm{B12\text{-}B21}}}^{(q_1)} \mid \mathfrak{R}\right) \cdot T\left(\mathbf{I}_{\underline{\mathrm{B1}}}^{(n_1)} \mid \mathbf{E2}, \mathbf{E2}_{\underline{\mathrm{B12\text{-}B21}}}^{(q_1)} \mid \mathfrak{R}, \beta_{\mathrm{B21}}, \beta_{\mathrm{B21}}\right) \end{bmatrix}. \tag{A.116}$$

The factor $V_{2206}^{(q_1)}(\mathbf{I} \mid \mathfrak{R})$, which accounts for the effects of the multiple reflections between the surfaces Γ_{G2}, Γ_{B12} and Γ_{B21}, is given by,

$$V_{2206}^{(q_1)}(\mathbf{I} \mid \mathfrak{R}) = \begin{cases} Q(\mathbf{I}, \mathfrak{R}, \beta_{\mathrm{G2}}) \cdot \left[Q(\mathbf{I}, \mathfrak{R}, \beta_{\mathrm{B12}})\right]^{p_1+1} \cdot \left[Q(\mathbf{I}, \mathfrak{R}, \beta_{\mathrm{B21}})\right]^{p_1} & \text{for } q_1 = 2p_1 + 1 \\ Q(\mathbf{I}, \mathfrak{R}, \beta_{\mathrm{G2}}) \cdot \left[Q(\mathbf{I}, \mathfrak{R}, \beta_{\mathrm{B12}}) \cdot Q(\mathbf{I}, \mathfrak{R}, \beta_{\mathrm{B21}})\right]^{p_1} & \text{for } q_1 = 2p_1 \end{cases}. \tag{A.117}$$

The illuminated zone of $\mathbf{E2}_{\underline{\mathrm{B12\text{-}B21}}}^{(q_1)}$ is illustrated in figure A.33. For the $\mathbf{E2}_{\underline{\mathrm{B12\text{-}B21}}}^{(q_1)}$ with odd q_1, the lines connecting the illuminated receivers with $\mathbf{E2}_{\underline{\mathrm{B12\text{-}B21}}}^{(q_1)}$ should have an intersection with the line from $(L_1, 0, -H)$ to $(L_1, 0, H)$ and have no intersection with the line from $(L_1 + W, 0, -H)$ to $(L_1 + W, 0, H)$. For the $\mathbf{E2}_{\underline{\mathrm{B12\text{-}B21}}}^{(q_1)}$ with even q_1, the lines connecting the illuminated receivers with $\mathbf{E2}_{\underline{\mathrm{B12\text{-}B21}}}^{(q_1)}$ should have no intersection with the line from $(L_1, 0, -H)$ to $(L_1, 0, H)$ and have an intersection with the line from $(L_1 + W, 0, -H)$ to $(L_1 + W, 0, H)$.

Group 7 comprises of the image sources formed by multiple reflections between the surfaces Γ_{F1} and Γ_{F2}. They are denoted as,

$$\mathbf{E2}_{\mathrm{F1\text{-}F2}}^{(q_2)} \equiv \left(x_{\mathrm{E2\text{-}F1\text{-}F2}}^{(q_2)}, 0, H\right), \tag{A.118}$$

where $q_2 = 1, 2, 3, \cdots$. The subscript F1-F2 indicates the surfaces of reflections involved and the superscript q_2 in bracket denotes the total number of reflections from the surfaces Γ_{F1} and Γ_{F2}. For odd order image sources $\mathbf{E2}_{\mathrm{F1\text{-}F2}}^{(2p_2+1)}$, where $p_2 = 0, 1, 2, \ldots$, they are

reflected p_2+1 times by the surface Γ_{F1} and p_2 times by the surface Γ_{F2}. For even order image sources $\mathbf{E2}_{\text{F1-F2}}^{(2p_2)}$, where $p_2=1,2,3,\ldots$, they are reflected p_2 times by both surfaces Γ_{F1} and Γ_{F2}. The x-coordinate $x_{\text{E2-F1-F2}}^{(q_2)}$ of the image source can be determined by equation A.48. The contribution of $\mathbf{E2}_{\text{F1-F2}}^{(q_2)}$ is calculated by,

$$P_{2207}^{(q_2)}=\sum_{n_1=0}^{\infty}\left[\begin{array}{l}V_{103}^{(n_1)}\left(\mathbf{I}_{\text{B1}}^{(n_1)}\,|\,\mathbf{E2}\right)\cdot V_{2207}^{(q_2)}\left(\mathbf{E2}_{\text{F1-F2}}^{(q_2)}\,|\,\mathfrak{R}\right)\cdot T\left(\mathbf{I}_{\text{B1}}^{(n_1)}\,|\,\mathbf{E2},\mathbf{E2}_{\text{F1-F2}}^{(q_2)}\,|\,\mathfrak{R},\beta_{\text{B21}},\beta_{\text{B21}}\right)\\ +V_{104}^{(n_1)}\left(\mathbf{I}_{\underline{\text{B1}}}^{(n_1)}\,|\,\mathbf{E2}\right)\cdot V_{2207}^{(q_2)}\left(\mathbf{E2}_{\text{F1-F2}}^{(q_2)}\,|\,\mathfrak{R}\right)\cdot T\left(\mathbf{I}_{\underline{\text{B1}}}^{(n_1)}\,|\,\mathbf{E2},\mathbf{E2}_{\text{F1-F2}}^{(q_2)}\,|\,\mathfrak{R},\beta_{\text{B21}},\beta_{\text{B21}}\right)\end{array}\right]. \tag{A.119}$$

The factor $V_{2207}^{(q_2)}\left(\mathbf{I}\,|\,\mathfrak{R}\right)$, which accounts for the effects of the multiple reflections between the surfaces Γ_{F1} and Γ_{F2}, is given by,

$$V_{2207}^{(q_2)}\left(\mathbf{I}\,|\,\mathfrak{R}\right)=\begin{cases}\left[Q\left(\mathbf{I},\mathfrak{R},\beta_{\text{F1}}\right)\right]^{p_2+1}\cdot\left[Q\left(\mathbf{I},\mathfrak{R},\beta_{\text{F2}}\right)\right]^{p_2} & \text{for } q_2=2p_2+1\\ \left[Q\left(\mathbf{I},\mathfrak{R},\beta_{\text{F1}}\right)\cdot Q\left(\mathbf{I},\mathfrak{R},\beta_{\text{F2}}\right)\right]^{p_2} & \text{for } q_2=2p_2\end{cases}. \tag{A.120}$$

The illuminated zone of $\mathbf{E2}_{\text{F1-F2}}^{(q_2)}$ is illustrated in figure A.34. The illuminated receivers should have a height higher than H.

Group 8 contains the ground reflected image sources formed by multiple reflections between the surfaces Γ_{F1} and Γ_{F2}. They are similar to the image sources in group 7 but involve an additional reflection with the ground surface Γ_{G2}. They are denoted as,

$$\mathbf{E2}_{\underline{\text{F1–F2}}}^{(q_2)}\equiv\left(x_{\text{E2-F1-F2}}^{(q_2)},0,-H\right), \tag{A.121}$$

where $q_2=2,3,4,\cdots$. The subscript $\underline{\text{F1-F2}}$ indicates the surfaces of reflections involved and the underline in the subscript indicates the ground reflection. The superscript q_2 in bracket denotes the total number of reflections from the surfaces Γ_{F1} and Γ_{F2}. For odd order image sources $\mathbf{E2}_{\underline{\text{F1–F2}}}^{(2p_2+1)}$, where $p_2=0,1,2,\ldots$, they are reflected

once by the ground surface Γ_{G2}, p_2+1 times by the surface Γ_{F1} and p_2 times by the surface Γ_{F2}. For even order image sources $\mathbf{E2}_{\underline{\text{F1–F2}}}^{(2p_2)}$, where $p_2 = 1,2,3,\ldots$, they are reflected once by the ground surface Γ_{G2} and p_2 times by both surfaces Γ_{F1} and Γ_{F2}. The x-coordinate $x_{\text{E2-F1-F2}}^{(q_2)}$ of the image source is determined by equation A.48. The contribution of $\mathbf{E2}_{\underline{\text{F1–F2}}}^{(q_2)}$ is calculated by,

$$P_{2208}^{(q_2)} = \sum_{n_1=0}^{\infty}\left[\begin{array}{l} V_{103}^{(n_1)}\left(\mathbf{I}_{\text{B1}}^{(n_1)} \mid \mathbf{E2}\right)\cdot V_{2208}^{(q_2)}\left(\mathbf{E2}_{\underline{\text{F1-F2}}}^{(q_2)} \mid \mathfrak{R}\right)\cdot T\left(\mathbf{I}_{\text{B1}}^{(n_1)} \mid \mathbf{E2}, \mathbf{E2}_{\underline{\text{F1-F2}}}^{(q_2)} \mid \mathfrak{R}, \beta_{\text{B21}}, \beta_{\text{B21}}\right) \\ + V_{104}^{(n_1)}\left(\mathbf{I}_{\underline{\text{B1}}}^{(n_1)} \mid \mathbf{E2}\right)\cdot V_{2208}^{(q_2)}\left(\mathbf{E2}_{\underline{\text{F1-F2}}}^{(q_2)} \mid \mathfrak{R}\right)\cdot T\left(\mathbf{I}_{\underline{\text{B1}}}^{(n_1)} \mid \mathbf{E2}, \mathbf{E2}_{\underline{\text{F1-F2}}}^{(q_2)} \mid \mathfrak{R}, \beta_{\text{B21}}, \beta_{\text{B21}}\right) \end{array}\right]. \tag{A.122}$$

The factor $V_{2208}^{(q_2)}\left(\mathbf{I} \mid \mathfrak{R}\right)$, which accounts for the effects of the multiple reflections between the surfaces Γ_{G2}, Γ_{F1} and Γ_{B2}, is given by,

$$V_{2208}^{(q_2)}\left(\mathbf{I} \mid \mathfrak{R}\right) = \begin{cases} Q\left(\mathbf{I}, \mathfrak{R}, \beta_{\text{G2}}\right)\cdot\left[Q\left(\mathbf{I}, \mathfrak{R}, \beta_{\text{F1}}\right)\right]^{p_2+1}\cdot\left[Q\left(\mathbf{I}, \mathfrak{R}, \beta_{\text{F2}}\right)\right]^{p_2} & \text{for } q_2 = 2p_2+1 \\ Q\left(\mathbf{I}, \mathfrak{R}, \beta_{\text{G2}}\right)\cdot\left[Q\left(\mathbf{I}, \mathfrak{R}, \beta_{\text{F1}}\right)\cdot Q\left(\mathbf{I}, \mathfrak{R}, \beta_{\text{F2}}\right)\right]^{p_2} & \text{for } q_2 = 2p_2 \end{cases}. \tag{A.123}$$

The illuminated zone of $\mathbf{E2}_{\underline{\text{F1–F2}}}^{(q_2)}$ is illustrated in figure A.35. The lines connecting the illuminated receivers with $\mathbf{E2}_{\underline{\text{F1–F2}}}^{(q_2)}$ should have no intersection with the line from $\left(x_{\text{E1-F1-F2}}^{(q_2)}, 0, -H\right)$ to $\left(x_{\text{E1-F1-F2}}^{(q_2)}, 0, H\right)$. The x-coordinate $x_{\text{E1-F1-F2}}^{(q_2)}$ is calculated by equation A.24.

Group 9 comprises of the image sources formed by multiple reflections between the surfaces Γ_{F1} and Γ_{F2}. They are denoted as,

$$\mathbf{E2}_{\text{F2-F1}}^{(q_2)} \equiv \left(x_{\text{E2-F2-F1}}^{(q_2)}, 0, H\right), \tag{A.124}$$

where $q_2 = 2,3,4,\cdots$. The subscript F2-F1 indicates the surfaces of reflections involved and the superscript q_2 in bracket denotes the total number of reflections from the surfaces Γ_{F1} and Γ_{F2} . The starting number of reflection is 2 to avoid duplication with image source $\mathbf{E2}^{(1)}_{\text{F2-B22}}$. For odd order image sources $\mathbf{E2}^{(2p_2+1)}_{\text{F2-F1}}$, where $p_2 = 0,1,2,\ldots$, they are reflected p_2 times by the façade surface Γ_{F1} and p_2+1 times by the façade surface Γ_{F2} . For even order image sources $\mathbf{E2}^{(2p_2)}_{\text{F2-F1}}$, where $p_1 = 1,2,3,\ldots$, they are reflected p_2 times by both façade surfaces Γ_{F1} and Γ_{F2} . The x-coordinate $x^{(q_2)}_{\text{E2-F2-F1}}$ of the image source is determined by equation A.25.

The contribution of $\mathbf{E2}^{(q_2)}_{\text{F2-F1}}$ is calculated by,

$$P^{(q_2)}_{2209} = \sum_{n_1=0}^{\infty}\left[\begin{array}{l} V^{(n_1)}_{103}\left(\mathbf{I}^{(n_1)}_{\text{B1}} \mid \mathbf{E2}\right)\cdot V^{(q_2)}_{2209}\left(\mathbf{E2}^{(q_2)}_{\text{F2-F1}} \mid \mathfrak{R}\right)\cdot T\left(\mathbf{I}^{(n_1)}_{\text{B1}} \mid \mathbf{E2}, \mathbf{E2}^{(q_2)}_{\text{F2-F1}} \mid \mathfrak{R}, \beta_{\text{B21}}, \beta_{\text{B22}}\right) \\ + V^{(n_1)}_{104}\left(\mathbf{I}^{(n_1)}_{\underline{\text{B1}}} \mid \mathbf{E2}\right)\cdot V^{(q_2)}_{2209}\left(\mathbf{E2}^{(q_2)}_{\text{F2-F1}} \mid \mathfrak{R}\right)\cdot T\left(\mathbf{I}^{(n_1)}_{\underline{\text{B1}}} \mid \mathbf{E2}, \mathbf{E2}^{(q_2)}_{\text{F2-F1}} \mid \mathfrak{R}, \beta_{\text{B21}}, \beta_{\text{B22}}\right) \end{array}\right]. \tag{A.125}$$

The factor $V^{(q_2)}_{2209}\left(\mathbf{I} \mid \mathfrak{R}\right)$, which accounts for the effects of the multiple reflections between the surfaces Γ_{F1} and Γ_{F2} , is given by,

$$V^{(q_2)}_{2209}\left(\mathbf{I} \mid \mathfrak{R}\right) = \begin{cases} \left[Q\left(\mathbf{I}, \mathfrak{R}, \beta_{\text{F1}}\right)\right]^{p_2} \cdot \left[Q\left(\mathbf{I}, \mathfrak{R}, \beta_{\text{F2}}\right)\right]^{p_2+1} & \text{for } q_2 = 2p_2+1 \\ \left[Q\left(\mathbf{I}, \mathfrak{R}, \beta_{\text{F1}}\right)\cdot Q\left(\mathbf{I}, \mathfrak{R}, \beta_{\text{F2}}\right)\right]^{p_2} & \text{for } q_2 = 2p_2 \end{cases}. \tag{A.126}$$

The illuminated zone of $\mathbf{E2}^{(q_2)}_{\text{F2-F1}}$ is illustrated in figure A.36. The illuminated receiver should have a height higher than H .

Group 10 contains the ground reflected image sources formed by multiple reflections between the surfaces Γ_{F1} and Γ_{F2} . They are similar to the image sources in group 9 but involve an additional reflection with the ground surface Γ_{G3}. They are denoted as,

$$\mathbf{E2}_{\underline{\text{F2-F1}}}^{(q_2)} \equiv \left(x_{\text{E2-F2-F1}}^{(q_2)}, 0, -H\right), \tag{A.127}$$

where $q_2 = 2,3,4,\cdots$. The subscript $\underline{\text{F2-F1}}$ indicates the surfaces of reflections involved and the underline in the subscript indicates the ground reflection. The superscript q_2 in bracket denotes the total number of reflections from the surfaces Γ_{F1} and Γ_{F2}. Again, the starting number of reflection is 2 to avoid duplication with the image source $\mathbf{E2}_{\underline{\text{F2-B22}}}^{(1)}$. For odd order image sources $\mathbf{E2}_{\underline{\text{F2-F1}}}^{(2p_2+1)}$, where $p_2 = 0,1,2,\ldots$, they are reflected once by the ground surface Γ_{G3}, p_2 times by the façade surface Γ_{F1} and p_2+1 times by the façade surface Γ_{F2}. For even order image sources $\mathbf{E2}_{\underline{\text{F2-F1}}}^{(2p_2)}$, where $p_2 = 1,2,3,\ldots$, they are reflected once by the ground surface Γ_{G3} and p_2 times by both façade surfaces Γ_{F1} and Γ_{F2}. The x-coordinate $x_{\text{E2-F2-F1}}^{(q_2)}$ of the image source is determined by equation A.25. The contribution of $\mathbf{E2}_{\underline{\text{F2-F1}}}^{(q_2)}$ is calculated by,

$$P_{2210}^{(q_2)} = \sum_{n_1=0}^{\infty}\left[\begin{array}{l} V_{103}^{(n_1)}\left(\mathbf{I}_{\text{B1}}^{(n_1)} \mid \mathbf{E2}\right)\cdot V_{2110}^{(q_2)}\left(\mathbf{E2}_{\underline{\text{F2-F1}}}^{(q_2)} \mid \mathfrak{R}\right)\cdot T\left(\mathbf{I}_{\text{B1}}^{(n_1)} \mid \mathbf{E2}, \mathbf{E2}_{\underline{\text{F2-F1}}}^{(q_2)} \mid \mathfrak{R}, \beta_{\text{B21}}, \beta_{\text{B22}}\right) \\ + V_{104}^{(n_1)}\left(\mathbf{I}_{\underline{\text{B1}}}^{(n_1)} \mid \mathbf{E2}\right)\cdot V_{2110}^{(q_2)}\left(\mathbf{E2}_{\underline{\text{F2-F1}}}^{(q_2)} \mid \mathfrak{R}\right)\cdot T\left(\mathbf{I}_{\underline{\text{B1}}}^{(n_1)} \mid \mathbf{E2}, \mathbf{E2}_{\underline{\text{F2-F1}}}^{(q_2)} \mid \mathfrak{R}, \beta_{\text{B21}}, \beta_{\text{B22}}\right) \end{array}\right]. \tag{A.128}$$

The factor $V_{2210}^{(q_2)}\left(\mathbf{I} \mid \mathfrak{R}\right)$, which accounts for the effects of the multiple reflections between the surfaces Γ_{G3}, Γ_{F1} and Γ_{B2}, is given by,

$$V_{2210}^{(q_2)}\left(\mathbf{I} \mid \mathfrak{R}\right) = \begin{cases} Q\left(\mathbf{I}, \mathfrak{R}, \beta_{\text{G3}}\right)\cdot\left[Q\left(\mathbf{I}, \mathfrak{R}, \beta_{\text{F1}}\right)\right]^{p_2}\cdot\left[Q\left(\mathbf{I}, \mathfrak{R}, \beta_{\text{F2}}\right)\right]^{p_2+1} & \text{for } q_2 = 2p_2+1 \\ Q\left(\mathbf{I}, \mathfrak{R}, \beta_{\text{G3}}\right)\cdot\left[Q\left(\mathbf{I}, \mathfrak{R}, \beta_{\text{F1}}\right)\cdot Q\left(\mathbf{I}, \mathfrak{R}, \beta_{\text{F2}}\right)\right]^{p_2} & \text{for } q_2 = 2p_2 \end{cases}. \tag{A.129}$$

The illuminated zone of $\mathbf{E2}_{\underline{\text{F2-F1}}}^{(q_2)}$ is illustrated in figure A.37. The lines connecting the illuminated receivers with $\mathbf{E2}_{\underline{\text{F2-F1}}}^{(q_2)}$ should have no intersection with the line connecting

$\left(x_{\text{E2-F1-F2}}^{(q_2-1)},0,-H\right)$ and $\left(x_{\text{E2-F1-F2}}^{(q_2-1)},0,H\right)$. The x-coordinate $x_{\text{E2-F1-F2}}^{(q_2)}$ is calculated by equation A.48.

Group 11 consists of image sources formed by multiple reflections between the surfaces Γ_{F1} and Γ_{F2} of the image sources $\mathbf{E2}_{\underline{\text{B12-B21}}}^{(q_1)}$ with even q_1. They are denoted as,

$$\mathbf{E2}_{\underline{\text{B12-B21-F1-F2}}}^{(q_1,q_2)} \equiv \left(x_{\text{E2-B12-B21-F1-F2}}^{(q_1,q_2)},0,-H\right), \tag{A.130}$$

where $q_1 = 2,4,6,\cdots$ and $q_2 = 1,2,3,\cdots$. The subscript $\underline{\text{B12-B21-F1-F2}}$ indicates the surfaces of reflections involved and the underline in the subscript indicates the ground reflection. After the last reflection by Γ_{B21} among the q_1 times multiple reflections between the surfaces Γ_{B12} and Γ_{B21}, there would be q_2 times multiple reflections between the surfaces Γ_{F1} and Γ_{F2}. For odd q_2, the image sources $\mathbf{E2}_{\underline{\text{B12-B21-F1-F2}}}^{(q_1,2p_2+1)}$, where $p_2 = 0,1,2,\ldots$, are reflected p_2+1 times by the surface Γ_{F1} and p_2 times by the surface Γ_{F2}. For even q_2, the image sources $\mathbf{E2}_{\underline{\text{B12-B21-F1-F2}}}^{(q_1,2p_2)}$, where $p_2 = 1,2,3,\ldots$, they are reflected p_2 times by both surfaces Γ_{F1} and Γ_{F2}. The x-coordinate $x_{\text{E2-B12-B21-F1-F2}}^{(q_1,q_2)}$ of the image source is calculated by,

$$x_{\text{E2-B12-B21-F1-F2}}^{(q_1,q_2)} = \begin{cases} -x_{\text{E2-B12-B21}}^{(q_1)} - (q_2-1)\cdot L & \text{for } q_2 = 1,3,5,\ldots \\ x_{\text{E2-B12-B21}}^{(q_1)} + (q_2)\cdot L & \text{for } q_2 = 2,4,6,\cdots \end{cases}. \tag{A.131}$$

The pressure contribution of $\mathbf{E2}_{\underline{\text{B12-B21-F1-F2}}}^{(q_1,q_2)}$ is calculated by,

$$P_{2211}^{(q_1,q_2)} = \sum_{n_1=0}^{\infty} \begin{bmatrix} V_{103}^{(n_1)}\left(\mathbf{I}_{\text{B1}}^{(n_1)} \mid \mathbf{E2}\right)\cdot V_{2211}^{(q_1,q_2)}\left(\mathbf{E2}_{\underline{\text{B12-B21-F1-F2}}}^{(q_1,q_2)} \mid \mathfrak{R}\right) \\ \cdot T\left(\mathbf{I}_{\text{B1}}^{(n_1)} \mid \mathbf{E2}, \mathbf{E2}_{\underline{\text{B12-B21-F1-F2}}}^{(q_1,q_2)} \mid \mathfrak{R}, \beta_{\text{B21}}, \beta_{\text{B21}}\right) \\ + V_{104}^{(n_1)}\left(\mathbf{I}_{\underline{\text{B1}}}^{(n_1)} \mid \mathbf{E2}\right)\cdot V_{2211}^{(q_1,q_2)}\left(\mathbf{E2}_{\underline{\text{B12-B21-F1-F2}}}^{(q_1,q_2)} \mid \mathfrak{R}\right) \\ \cdot T\left(\mathbf{I}_{\underline{\text{B1}}}^{(n_1)} \mid \mathbf{E2}, \mathbf{E2}_{\underline{\text{B12-B21-F1-F2}}}^{(q_1,q_2)} \mid \mathfrak{R}, \beta_{\text{B21}}, \beta_{\text{B21}}\right) \end{bmatrix}. \tag{A.132}$$

The factor $V_{2211}^{(q_1,q_2)}\left(\mathbf{I} \mid \mathfrak{R}\right)$, which accounts for the effects of the multiple reflections between the surfaces Γ_{G2}, Γ_{B12}, Γ_{B21}, Γ_{F1} and Γ_{F2} is given by,

$$V_{2211}^{(q_1,q_2)}(\mathbf{I}\,|\,\mathfrak{R})=\begin{cases} V_{104}^{(q_1)}(\mathbf{I}\,|\,\mathfrak{R})\cdot\left[Q(\mathbf{I},\mathfrak{R},\beta_{\mathrm{F1}})\right]^{p_2}\cdot\left[Q(\mathbf{I},\mathfrak{R},\beta_{\mathrm{F2}})\right]^{p_2+1} \\ \qquad\qquad\qquad\qquad\qquad\qquad \text{for } q_1=2p_1 \text{ and } q_2=2p_2+1 \\ V_{104}^{(q_1)}(\mathbf{I}\,|\,\mathfrak{R})\cdot\left[Q(\mathbf{I},\mathfrak{R},\beta_{\mathrm{F1}})\cdot Q(\mathbf{I},\mathfrak{R},\beta_{\mathrm{F2}})\right]^{p_2} \\ \qquad\qquad\qquad\qquad\qquad\qquad \text{for } q_1=2p_1 \text{ and } q_2=2p_2 \end{cases}. \tag{A.133}$$

The illuminated zone of $\mathbf{E2}_{\underline{\text{B12-B21-F1-F2}}}^{(q_1,q_2)}$ is illustrated in figure A.38. The lines connecting the illuminated receivers with $\mathbf{E2}_{\underline{\text{B12-B21-F1-F2}}}^{(q_1,q_2)}$ should have no intersection with the line from $\left(x_{\text{E1-F1-F2}}^{(q_2)},0,-H\right)$ to $\left(x_{\text{E1-F1-F2}}^{(q_2)},0,H\right)$ and have an intersection with the line from $\left(x_{\text{E2-F1-F2}}^{(q_2)},0,-H\right)$ to $\left(x_{\text{E2-F1-F2}}^{(q_2)},0,H\right)$. The x-coordinate $x_{\text{E1-F1-F2}}^{(q_2)}$ can be calculated by equation A.24 while the x-coordinate $x_{\text{E2-F1-F2}}^{(q_2)}$ can be calculated by equation A.48.

Group 12 consists of image sources formed by multiple reflections between the surfaces Γ_{F1} and Γ_{F2} of the image sources $\mathbf{E2}_{\underline{\text{B12-B21}}}^{(q_1)}$ with odd q_1. They are denoted as,

$$\mathbf{E2}_{\underline{\text{B12-B21-F2-F1}}}^{(q_1,q_2)}\equiv\left(x_{\text{E2-B12-B21-F2-F1}}^{(q_1,q_2)},0,-H\right), \tag{A.134}$$

where $q_1=1,3,5,\cdots$ and $q_2=1,2,3,\cdots$. The subscript $\underline{\text{B12-B21-F2-F1}}$ indicates the surfaces of reflections involved and the underline in the subscript indicates the ground reflection. After the last reflection by Γ_{B12} among the q_1 times multiple reflections between the surfaces Γ_{B12} and Γ_{B21}, there would be q_2 times multiple reflections between the surfaces Γ_{F1} and Γ_{F2}. For odd q_2, the image sources $\mathbf{E2}_{\underline{\text{B12-B21-F2-F1}}}^{(q_1,2p_2+1)}$, where $p_2=0,1,2,\ldots$, are reflected p_2 times by the surface Γ_{F1} and p_2+1 times by the surface Γ_{F2}. For even q_2, the image sources $\mathbf{E2}_{\underline{\text{B12-B21-F2-F1}}}^{(q_1,2p_2)}$, where $p_2=1,2,3,\ldots$, they are reflected p_2 times by both surfaces Γ_{F1} and Γ_{F2}. The x-coordinate $x_{\text{E1-B21-B12-F2-F1}}^{(q_1,q_2)}$ of the image source is calculated by,

$$x_{\text{E2-B12-B21-F2-F1}}^{(q_1,q_2)} = \begin{cases} -x_{\text{E2-B12-B21}}^{(q_1)} + (q_2+1)\cdot L & \text{for } q_2 = 1,3,5,\ldots \\ x_{\text{E2-B12-B21}}^{(q_1)} - (q_2)\cdot L & \text{for } q_2 = 2,4,6,\cdots \end{cases}. \tag{A.135}$$

The pressure contribution of $\mathbf{E2}_{\underline{\text{B12-B21-F2-F1}}}^{(q_1,q_2)}$ is calculated by,

$$P_{2212}^{(q_1,q_2)} = \sum_{n_1=0}^{\infty} \begin{bmatrix} V_{103}^{(n_1)}\left(\mathbf{I}_{\text{B1}}^{(n_1)} \mid \mathbf{E2}\right)\cdot V_{2212}^{(q_1,q_2)}\left(\mathbf{E2}_{\underline{\text{B12-B21-F2-F1}}}^{(q_1,q_2)} \mid \mathfrak{R}\right) \\ \cdot T\left(\mathbf{I}_{\text{B1}}^{(n_1)} \mid \mathbf{E2}, \mathbf{E2}_{\underline{\text{B12-B21-F2-F1}}}^{(q_1,q_2)} \mid \mathfrak{R}, \beta_{\text{B21}}, \beta_{\text{B21}}\right) \\ + V_{104}^{(n_1)}\left(\mathbf{I}_{\underline{\text{B1}}}^{(n_1)} \mid \mathbf{E2}\right)\cdot V2\left(\mathbf{E2}_{\underline{\text{B12-B21-F2-F1}}}^{(q_1,q_2)} \mid \mathfrak{R}\right) \\ \cdot T\left(\mathbf{I}_{\underline{\text{B1}}}^{(n_1)} \mid \mathbf{E2}, \mathbf{E2}_{\underline{\text{B12-B21-F2-F1}}}^{(q_1,q_2)} \mid \mathfrak{R}, \beta_{\text{B21}}, \beta_{\text{B21}}\right) \end{bmatrix}. \tag{A.136}$$

The factor $V_{2212}^{(q_1,q_2)}(\mathbf{I} \mid \mathfrak{R})$, which accounts for the effects of the multiple reflections between the surfaces Γ_{G2}, Γ_{B12}, Γ_{B21}, Γ_{F1} and Γ_{F2} is given by,

$$V_{2212}^{(q_1,q_2)}(\mathbf{I} \mid \mathfrak{R}) = \begin{cases} V_{104}^{(q_1)}(\mathbf{I} \mid \mathfrak{R})\cdot\left[Q(\mathbf{I}, \mathfrak{R}, \beta_{\text{F1}})\right]^{p_2+1}\cdot\left[Q(\mathbf{I}, \mathfrak{R}, \beta_{\text{F2}})\right]^{p_2} \\ \qquad\qquad \text{for } q_1 = 2p_1+1 \text{ and } q_2 = 2p_2+1 \\ V_{104}^{(q_1)}(\mathbf{I} \mid \mathfrak{R})\cdot\left[Q(\mathbf{I}, \mathfrak{R}, \beta_{\text{F1}})\cdot Q(\mathbf{I}, \mathfrak{R}, \beta_{\text{F2}})\right]^{p_2} \\ \qquad\qquad \text{for } q_1 = 2p_1+1 \text{ and } q_2 = 2p_2 \end{cases}. \tag{A.137}$$

The illuminated zone of $\mathbf{E2}_{\underline{\text{B12-B21-F2-F1}}}^{(q_1,q_2)}$ is illustrated in figure A.39. The lines connecting the illuminated receivers with $\mathbf{E2}_{\underline{\text{B12-B21-F2-F1}}}^{(q_1,q_2)}$ should have an intersection with the line from $\left(x_{\text{E1-F2-F1}}^{(q_2)}, 0, -H\right)$ to $\left(x_{\text{E1-F2-F1}}^{(q_2)}, 0, H\right)$ and have no intersection with the line from $\left(x_{\text{E2-F2-F1}}^{(q_2)}, 0, -H\right)$ to $\left(x_{\text{E2-F2-F1}}^{(q_2)}, 0, H\right)$. The x-coordinate $x_{\text{E1-F2-F1}}^{(q_2)}$ can be calculated by equation A.40 while the x-coordinate $x_{\text{E2-F2-F1}}^{(q_2)}$ can be calculated by equation A.25.

Group 13 consists of image sources formed by multiple reflections between the surfaces Γ_{F1} and Γ_{F2} of the image sources $\mathbf{E2}_{\underline{\text{F2-B22}}}^{(q_1)}$ with odd q_1. They are denoted as,

$$\mathbf{E2}_{\underline{\text{F2-B22-F1-F2}}}^{(q_1,q_2)} \equiv \left(x_{\text{E2-F2-B22-F1-F2}}^{(q_1,q_2)}, 0, -H\right), \tag{A.138}$$

where $q_1 = 3,5,7,\cdots$ and $q_2 = 1,2,3,\cdots$. The subscript $\underline{\text{F2-B22-F1-F2}}$ indicates the surfaces of reflections involved and the underline in the subscript indicates the ground reflection. The order of reflections is starts from 3 as the image sources $\mathbf{E2}^{(1,q_2)}_{\underline{\text{F2-B22-F1-F2}}}$ are already considered as $\mathbf{E2}^{(q_2+1)}_{\underline{\text{F2-B22}}}$ already. After the last reflection by Γ_{F2} among the q_1 times multiple reflections between Γ_{F2} and Γ_{B22}, there would be q_2 times multiple reflections between Γ_{F1} and Γ_{F2}. For odd q_2, the image sources $\mathbf{E2}^{(q_1,2q_2+1)}_{\underline{\text{F2-B22-F1-F2}}}$, where $p_2 = 0,1,2,\ldots$, are reflected p_2+1 times by the surface Γ_{F1} and p_2 times by the surface Γ_{F2}. For even q_2, the image sources $\mathbf{E2}^{(q_1,2q_2)}_{\underline{\text{F2-B22-F1-F2}}}$, where $p_2 = 1,2,3,\ldots$, they are reflected p_2 times by both surfaces Γ_{F1} and Γ_{F2}. The x-coordinate $x^{(q_1,q_2)}_{\text{E2-F2-B22-F1-F2}}$ of the image source is given by,

$$x^{(q_1,q_2)}_{\text{E2-F2-B22-F1-F2}} = \begin{cases} -x^{(q_1)}_{\text{E2-F2-B22}} - (q_2 - 1)\cdot L & \text{for } q_2 = 1, 3, 5, \ldots \\ x^{(q_1)}_{\text{E2-F2-B22}} + (q_2)\cdot L & \text{for } q_2 = 2, 4, 6, \cdots \end{cases}. \tag{A.139}$$

The pressure contribution of $\mathbf{E2}^{(q_1,q_2)}_{\underline{\text{F2-B22-F1-F2}}}$ is calculated by,

$$P^{(q_1,q_2)}_{2213} = \sum_{n_1=0}^{\infty} \begin{bmatrix} V^{(n_1)}_{103}\left(\mathbf{I}^{(n_1)}_{\text{B1}} \mid \mathbf{E2}\right)\cdot V^{(q_1,q_2)}_{2213}\left(\mathbf{E2}^{(q_1,q_2)}_{\underline{\text{F2-B22-F1-F2}}} \mid \mathfrak{R}\right) \\ \cdot T\left(\mathbf{I}^{(n_1)}_{\text{B1}} \mid \mathbf{E2}, \mathbf{E2}^{(q_1,q_2)}_{\underline{\text{F2-B22-F1-F2}}} \mid \mathfrak{R}, \beta_{\text{B21}}, \beta_{\text{B22}}\right) \\ + V^{(n_1)}_{104}\left(\mathbf{I}^{(n_1)}_{\underline{\text{B1}}} \mid \mathbf{E2}\right)\cdot V^{(q_1,q_2)}_{2213}\left(\mathbf{E2}^{(q_1,q_2)}_{\underline{\text{F2-B22-F1-F2}}} \mid \mathfrak{R}\right) \\ \cdot T\left(\mathbf{I}^{(n_1)}_{\underline{\text{B1}}} \mid \mathbf{E2}, \mathbf{E2}^{(q_1,q_2)}_{\underline{\text{F2-B22-F1-F2}}} \mid \mathfrak{R}, \beta_{\text{B21}}, \beta_{\text{B22}}\right) \end{bmatrix}. \tag{A.140}$$

The factor $V^{(q_1,q_2)}_{2213}(\mathbf{I} \mid \mathfrak{R})$, which accounts for the effects of the multiple reflections between the surfaces Γ_{G2}, Γ_{B12}, Γ_{B21}, Γ_{F1} and Γ_{F2} is given by,

$$V^{(q_1,q_2)}_{2213}(\mathbf{I} \mid \mathfrak{R}) = \begin{cases} Q(\mathbf{I}, \mathfrak{R}, \beta_{\text{G2}})\cdot\left[Q(\mathbf{I}, \mathfrak{R}, \beta_{\text{B22}})\right]^{p_2}\cdot\left[Q(\mathbf{I}, \mathfrak{R}, \beta_{\text{F1}})\right]^{p_2}\cdot\left[Q(\mathbf{I}, \mathfrak{R}, \beta_{\text{F2}})\right]^{p_1+p_2+1} \\ \qquad\qquad \text{for } q_1 = 2p_1+1 \text{ and } q_2 = 2p_2+1 \\ Q(\mathbf{I}, \mathfrak{R}, \beta_{\text{G2}})\cdot\left[Q(\mathbf{I}, \mathfrak{R}, \beta_{\text{B22}})\right]^{p_2}\cdot\left[Q(\mathbf{I}, \mathfrak{R}, \beta_{\text{F1}})\right]^{p_2}\cdot\left[Q(\mathbf{I}, \mathfrak{R}, \beta_{\text{F2}})\right]^{p_1+p_2} \\ \qquad\qquad \text{for } q_1 = 2p_1+1 \text{ and } q_2 = 2p_2 \end{cases}. \tag{A.141}$$

The illuminated zone of $\mathbf{E2}^{(q_1,q_2)}_{\underline{\text{F2-B22-F1-F2}}}$ is illustrated in figure A.40. The lines connecting the illuminated receivers with $\mathbf{E2}^{(q_1,q_2)}_{\underline{\text{F2-B22-F1-F2}}}$ should have no intersection with the line from $\left(x^{(q_2)}_{\text{E2-F1-F2}},0,-H\right)$ to $\left(x^{(q_2)}_{\text{E2-F1-F2}},0,H\right)$ and have an intersection with the line from $\left(x^{(q_2+1)}_{\text{E2-F2-F1}},0,-H\right)$ to $\left(x^{(q_2+1)}_{\text{E2-F2-F1}},0,H\right)$. The x-coordinate $x^{(q_2)}_{\text{E2-F1-F2}}$ can be calculated by equation A.48 while the x-coordinate $x^{(q_2)}_{\text{E2-F2-F1}}$ can be calculated by equation A.25.

A.5 Overall Sound Pressure Level

In this section, we summarize the determination of the overall sound pressure by the image source model. The overall sound pressure at a particular receiver position would be the coherence summation of all the contribution from primary and secondary image sources which are illuminating the receiver. The cases with the parallel barriers in front of a façade surface would be a simplification of the case with the parallel barriers along a street canyon. In both cases, the overall sound pressure can be expressed as,

$$P(\boldsymbol{S},\Re) = P_{\text{Primary}} + P_{\text{Secondary,E1}} + P_{\text{Secondary,E2}}, \tag{A.142}$$

where, P_{Primary} is the overall primary contribution,

$P_{\text{Secondary, E1}}$ is the overall secondary contribution from **E1**,

$P_{\text{Secondary, E2}}$ is the overall secondary contribution from **E2**.

The details of the calculation of the terms P_{Primary}, $P_{\text{Secondary, E1}}$ and $P_{\text{Secondary, E2}}$ would be different for the two cases.

We first present the case with the parallel barriers in front of a façade surface discussed in Chapter 3. We denote it as case I to avoid confusion. The three terms of contribution $P_{\text{Primary (case I)}}$, $P_{\text{Secondary, E1 (case I)}}$ and $P_{\text{Secondary, E2 (case I)}}$ are determined respectively by,

$$\begin{aligned} P_{\text{Primary (case I)}} &= P_{101} + P_{102} + \sum_{n_1=1}^{\infty} P_{103}^{(n_1)} + \sum_{n_1=1}^{\infty} P_{104}^{(n_1)} + \sum_{n_1=1}^{\infty} P_{105}^{(n_1)} + \sum_{n_1=1}^{\infty} P_{106}^{(n_1)} \\ &\quad + \sum_{n_2=1}^{1} P_{107}^{(n_2)} + \sum_{n_2=1}^{1} P_{108}^{(n_2)} + \sum_{n_2}^{1}\sum_{n_1=1}^{\infty} P_{113}^{(n_1,n_2)} + \sum_{n_2}^{1}\sum_{n_1=1}^{\infty} P_{114}^{(n_1,n_2)} \end{aligned}, \tag{A.143}$$

$$\begin{aligned} P_{\text{Secondary,E1 (case I)}} &= P_{2101} + P_{2102} + \sum_{q_1=1}^{\infty} P_{2103}^{(q_1)} + \sum_{q_1=1}^{\infty} P_{2104}^{(q_1)} + \sum_{q_1=1}^{\infty} P_{2105}^{(q_1)} + \sum_{q_1=1}^{\infty} P_{2106}^{(q_1)} \\ &\quad + \sum_{q_2=1}^{1}\sum_{q_1=1}^{\infty} P_{2111}^{(q_1,q_2)} \end{aligned}, \text{ and} \tag{A.144}$$

$$P_{\text{Secondary,E2 (case I)}} = P_{2201} + P_{2202} + \sum_{q_1=1}^{\infty} P_{2205}^{(q_1)} + \sum_{q_1=1}^{\infty} P_{2206}^{(q_1)} + \sum_{q_2=1}^{1} P_{2207}^{(q_2)} + \sum_{q_2=1}^{1} P_{2208}^{(q_2)} + \sum_{q_2=1}^{1}\sum_{q_1=2}^{\infty} P_{2211}^{(q_1,q_2)} \quad . \tag{A.145}$$

The case with the parallel barriers along a street canyon discussed in Chapter 4 is denoted as case II. The three terms of contribution $P_{\text{Primary (case II)}}$, $P_{\text{Secondary, E1 (case II)}}$ and $P_{\text{Secondary, E2 (case II)}}$ are calculated respectively by,

$$\begin{aligned} P_{\text{Primary (case II)}} = {} & P_{101} + P_{102} + \sum_{n_1=1}^{\infty} P_{103}^{(n_1)} + \sum_{n_1=1}^{\infty} P_{104}^{(n_1)} + \sum_{n_1=1}^{\infty} P_{105}^{(n_1)} + \sum_{n_1=1}^{\infty} P_{106}^{(n_1)} \\ & + \sum_{n_2=1}^{\infty} P_{107}^{(n_2)} + \sum_{n_2=1}^{\infty} P_{108}^{(n_2)} + \sum_{n_2=1}^{\infty} P_{109}^{(n_2)} + \sum_{n_2=1}^{\infty} P_{110}^{(n_2)} \\ & + \sum_{n_2=1}^{\infty}\sum_{n_1=1}^{\infty} P_{111}^{(n_1,n_2)} + \sum_{n_2=1}^{\infty}\sum_{n_1=1}^{\infty} P_{112}^{(n_1,n_2)} + \sum_{n_2=1}^{\infty}\sum_{n_1=1}^{\infty} P_{113}^{(n_1,n_2)} + \sum_{n_2=1}^{\infty}\sum_{n_1=1}^{\infty} P_{114}^{(n_1,n_2)} \end{aligned} \quad , \tag{A.146}$$

$$\begin{aligned} P_{\text{Secondary,E1 (case II)}} = {} & P_{2101} + P_{2102} + \sum_{q_1=1}^{\infty} P_{2103}^{(q_1)} + \sum_{q_1=1}^{\infty} P_{2104}^{(q_1)} + \sum_{q_1=1}^{\infty} P_{2105}^{(q_1)} + \sum_{q_1=1}^{\infty} P_{2106}^{(q_1)} \\ & + \sum_{q_2=2}^{\infty} P_{2107}^{(q_2)} + \sum_{q_2=2}^{\infty} P_{2108}^{(q_2)} + \sum_{q_2=1}^{\infty} P_{2109}^{(q_2)} + \sum_{q_2=1}^{\infty} P_{2110}^{(q_2)} \\ & + \sum_{q_2=1}^{\infty}\sum_{q_1=1}^{\infty} P_{2111}^{(q_1,q_2)} + \sum_{q_2=1}^{\infty}\sum_{q_1=2}^{\infty} P_{2112}^{(q_1,q_2)} + \sum_{q_2=1}^{\infty}\sum_{q_1=3}^{\infty} P_{2113}^{(q_1,q_2)} \end{aligned} \quad \text{, and} \tag{A.147}$$

$$\begin{aligned} P_{\text{Secondary,E2 (case II)}} = {} & P_{2201} + P_{2202} + \sum_{q_1=1}^{\infty} P_{2203}^{(q_1)} + \sum_{q_1=1}^{\infty} P_{2204}^{(q_1)} + \sum_{q_1=1}^{\infty} P_{2205}^{(q_1)} + \sum_{q_1=1}^{\infty} P_{2206}^{(q_1)} \\ & + \sum_{q_2=1}^{\infty} P_{2207}^{(q_2)} + \sum_{q_2=1}^{\infty} P_{2208}^{(q_2)} + \sum_{q_2=2}^{\infty} P_{2209}^{(q_2)} + \sum_{q_2=2}^{\infty} P_{2210}^{(q_2)} \\ & + \sum_{q_2=1}^{\infty}\sum_{q_1=2}^{\infty} P_{2211}^{(q_1,q_2)} + \sum_{q_2=1}^{\infty}\sum_{q_1=1}^{\infty} P_{2212}^{(q_1,q_2)} + \sum_{q_2=1}^{\infty}\sum_{q_1=3}^{\infty} P_{2213}^{(q_1,q_2)} \end{aligned} \quad . \tag{A.148}$$

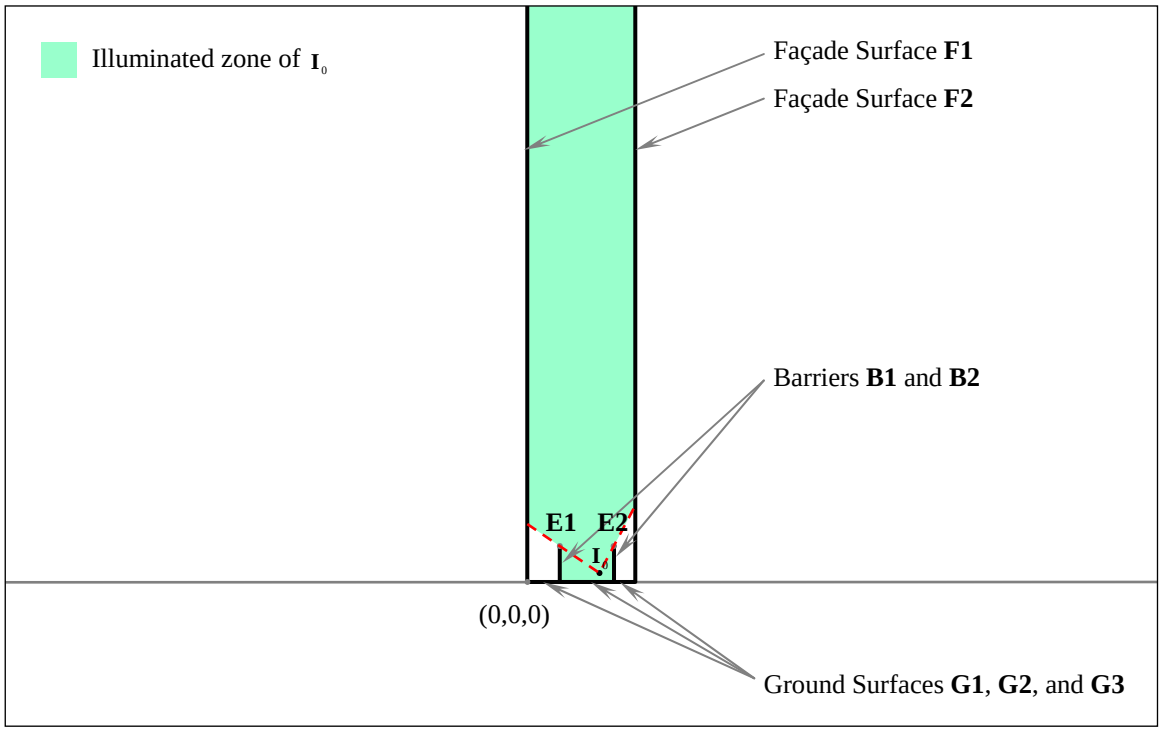

Figure A.1 Illustration of the secondary contribution from image source $\mathbf{I}_0$. The lines connecting $\mathbf{I}_0$ with the illuminated receivers should have no intersection with the line from $(L_1, 0, 0)$ to $(L_1, 0, H)$ and the line from $(L_1 + W, 0, 0)$ to $(L_1 + W, 0, H)$.

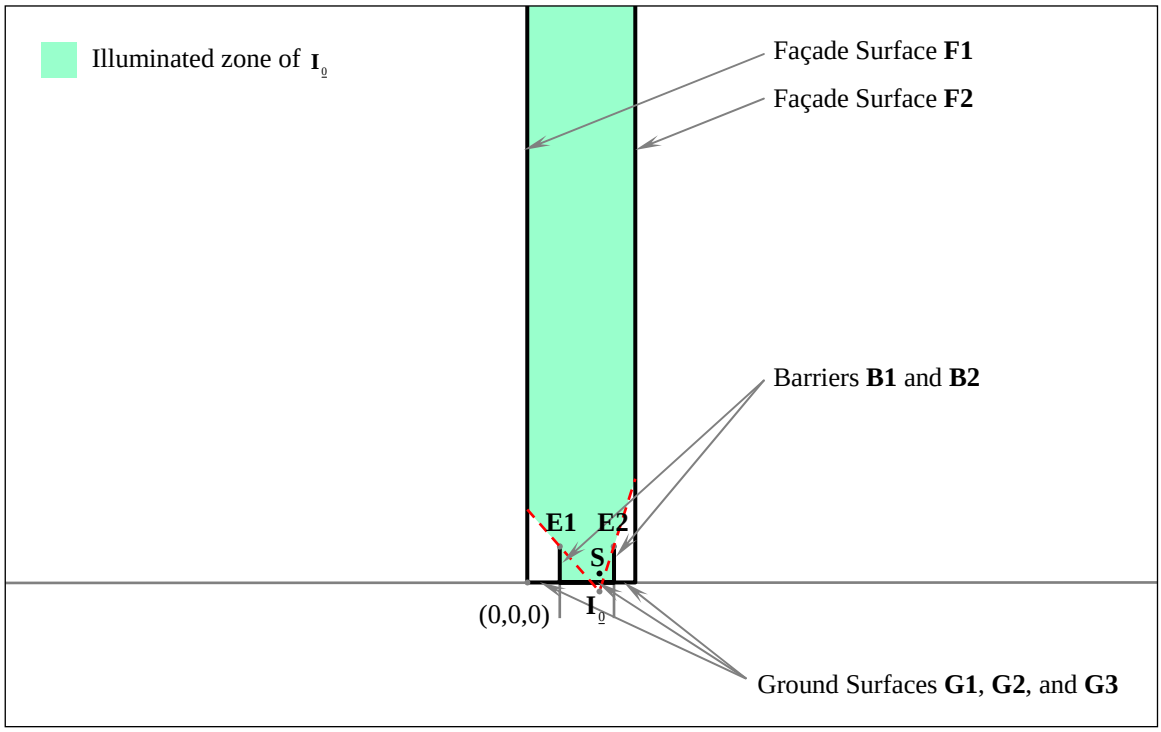

Figure A.2 Illustration of the secondary contribution from image source $\mathbf{I}_0$. The lines connecting $\mathbf{I}_0$ with the illuminated receivers should have no intersection with the line from $(L_1, 0, -H)$ to $(L_1, 0, H)$ and the line from $(L_1 + W, 0, -H)$ to $(L_1 + W, 0, H)$.

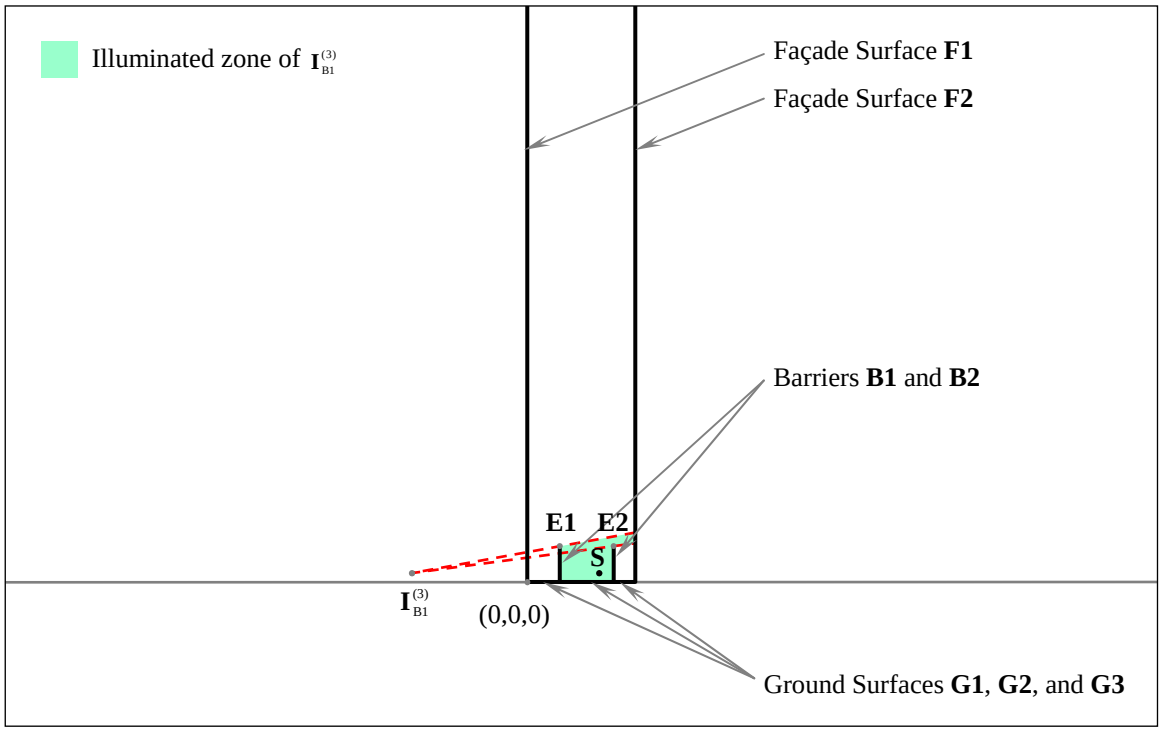

Figure A.3 Illustration of the secondary contribution from image sources $\mathbf{I}_{B1}^{(n_1)}$, where $n_1 = 1,2,3,\cdots$. The lines connecting $\mathbf{I}_{B1}^{(n_1)}$ with the illuminated receivers should have an intersection with the line from $(L_1, 0, 0)$ to $(L_1, 0, H)$ and have no intersection with the line from $(L_1 + W, 0, 0)$ to $(L_1 + W, 0, H)$.

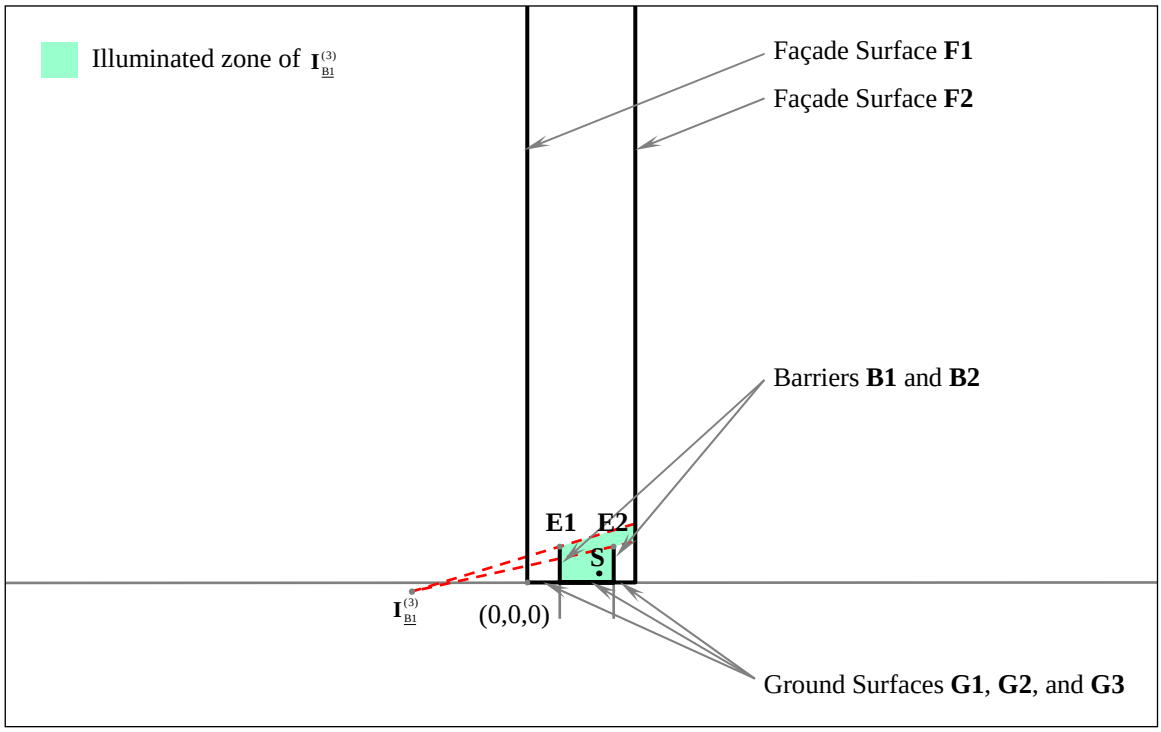

Figure A.4 Illustration of secondary the contribution from image sources $\mathbf{I}_{\underline{B1}}^{(n_1)}$, where $n_1 = 1,2,3,\cdots$. The lines connecting $\mathbf{I}_{\underline{B1}}^{(n_1)}$ with the illuminated receivers should have no intersection with the line from $(L_1, 0, -H)$ to $(L_1, 0, H)$ and have an intersection with the line from $(L_1 + W, 0, -H)$ to $(L_1 + W, 0, H)$.

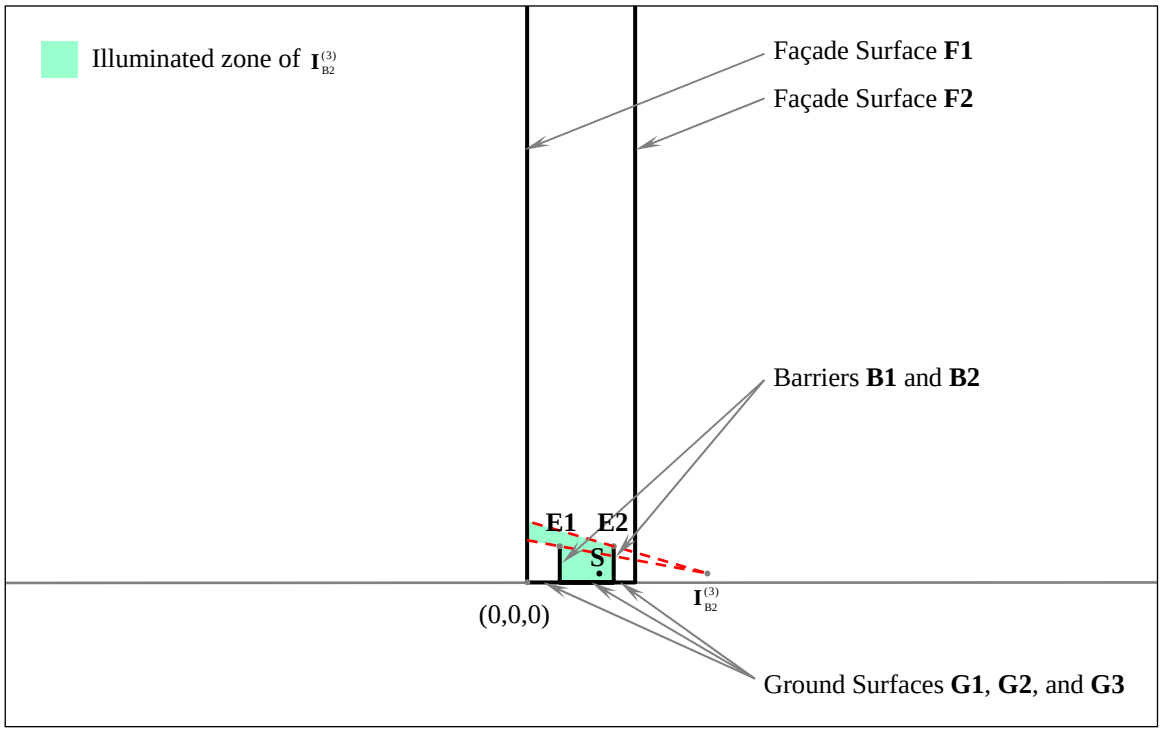

Figure A.5 Illustration of the secondary contribution from image sources $\mathbf{I}_{B2}^{(n_1)}$, where $n_1 = 1,2,3,\cdots$. The lines connecting $\mathbf{I}_{B2}^{(n_1)}$ with the illuminated receivers should have no intersection with the line from $(L_1, 0, 0)$ to $(L_1, 0, H)$ and have an intersection with the line from $(L_1 + W, 0, 0)$ to $(L_1 + W, 0, H)$.

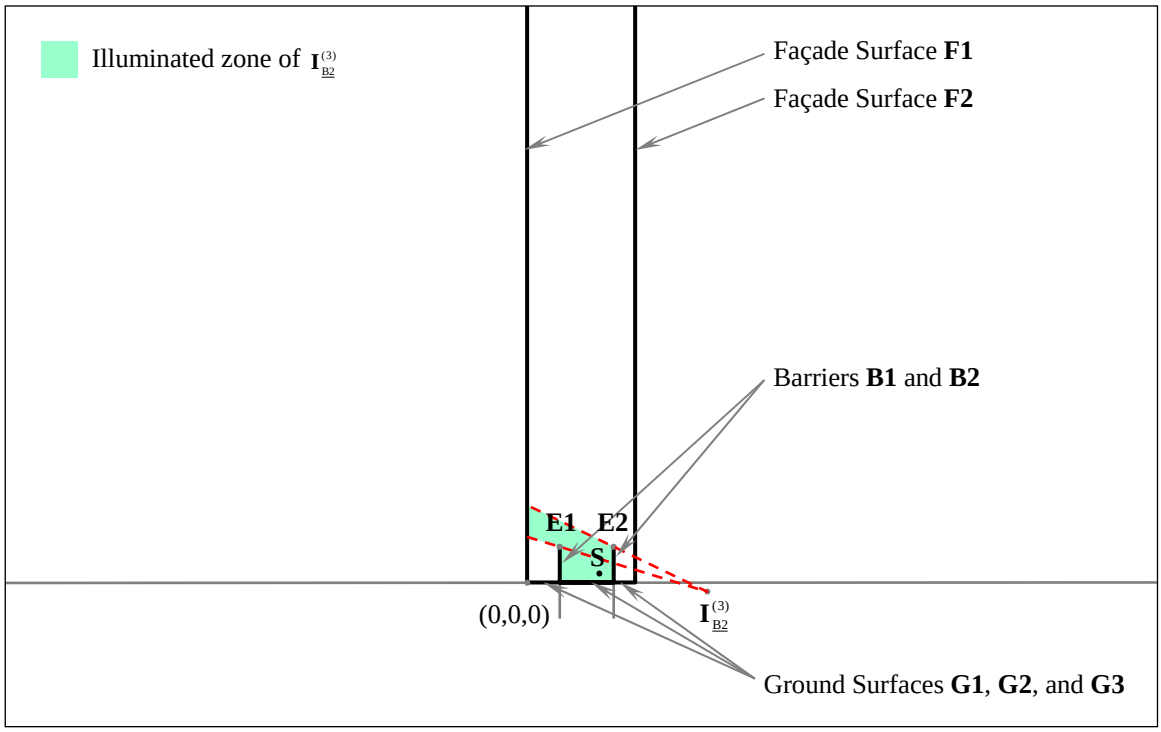

Figure A.6 Illustration of the secondary contribution from image sources $\mathbf{I}_{\underline{B2}}^{(n_1)}$, where $n_1 = 1,2,3,\cdots$. The lines connecting $\mathbf{I}_{\underline{B2}}^{(n_1)}$ with the illuminated receivers should have no intersection with the line from $(L_1, 0, -H)$ to $(L_1, 0, H)$ and have an intersection with the line from $(L_1 + W, 0, -H)$ to $(L_1 + W, 0, H)$.

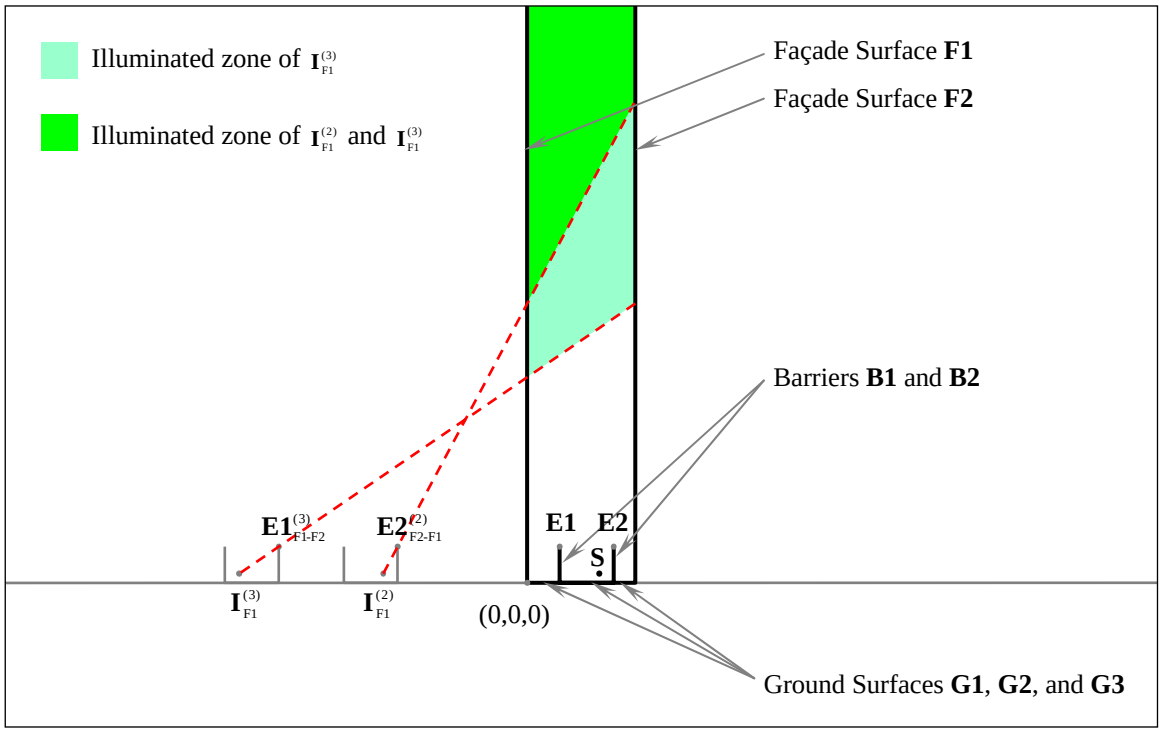

Figure A.7 Illustration of the secondary contribution from image sources $\mathbf{I}_{F1}^{(n_2)}$, where $n_2 = 1,2,3,\cdots$. For image sources $\mathbf{I}_{F1}^{(n_2)}$ with odd order n_2, the lines connecting $\mathbf{I}_{F1}^{(n_2)}$ with the illuminated receivers should have no intersection with the line from $\left(x_{E1\text{-}F1\text{-}F2}^{(n_2)}, 0, 0\right)$ to $\left(x_{E1\text{-}F1\text{-}F2}^{(n_2)}, 0, H\right)$. For image sources $\mathbf{I}_{F1}^{(n_2)}$ with even order n_2, the lines connecting $\mathbf{I}_{F1}^{(n_2)}$ with the illuminated receivers should have no intersection with the line from $\left(x_{E2\text{-}F2\text{-}F1}^{(n_2)}, 0, 0\right)$ to $\left(x_{E2\text{-}F2\text{-}F1}^{(n_2)}, 0, H\right)$.

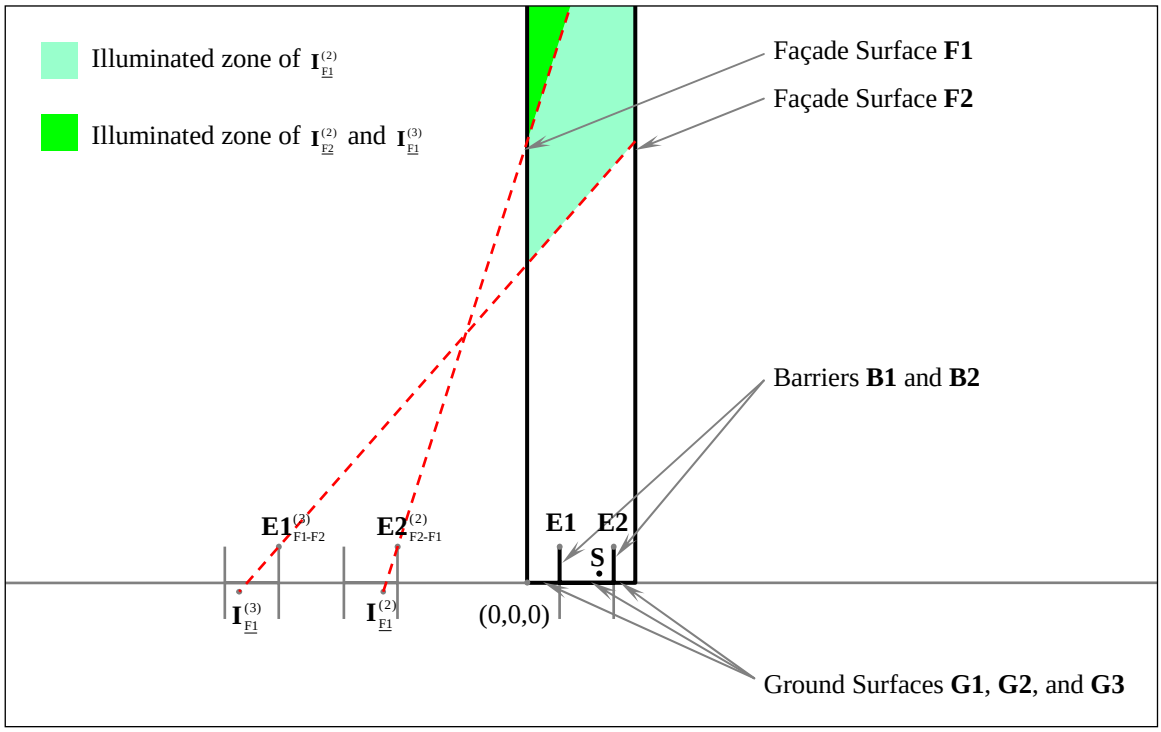

Figure A.8 Illustration of the secondary contribution from image sources $\mathbf{I}_{\underline{F1}}^{(n_2)}$, where $n_2 = 1,2,3,\cdots$. For image sources $\mathbf{I}_{\underline{F1}}^{(n_2)}$ with odd order n_2, the lines connecting $\mathbf{I}_{\underline{F1}}^{(n_2)}$ with the illuminated receivers should have no intersection with the line from $\left(x_{\text{E1-F1-F2}}^{(n_2)}, 0, -H\right)$ to $\left(x_{\text{E1-F1-F2}}^{(n_2)}, 0, H\right)$. For image sources $\mathbf{I}_{\underline{F1}}^{(n_2)}$ with even order n_2, the lines connecting $\mathbf{I}_{\underline{F1}}^{(n_2)}$ with the illuminated receivers should have no intersection with the line from $\left(x_{\text{E2-F2-F1}}^{(n_2)}, 0, -H\right)$ to $\left(x_{\text{E2-F2-F1}}^{(n_2)}, 0, H\right)$.

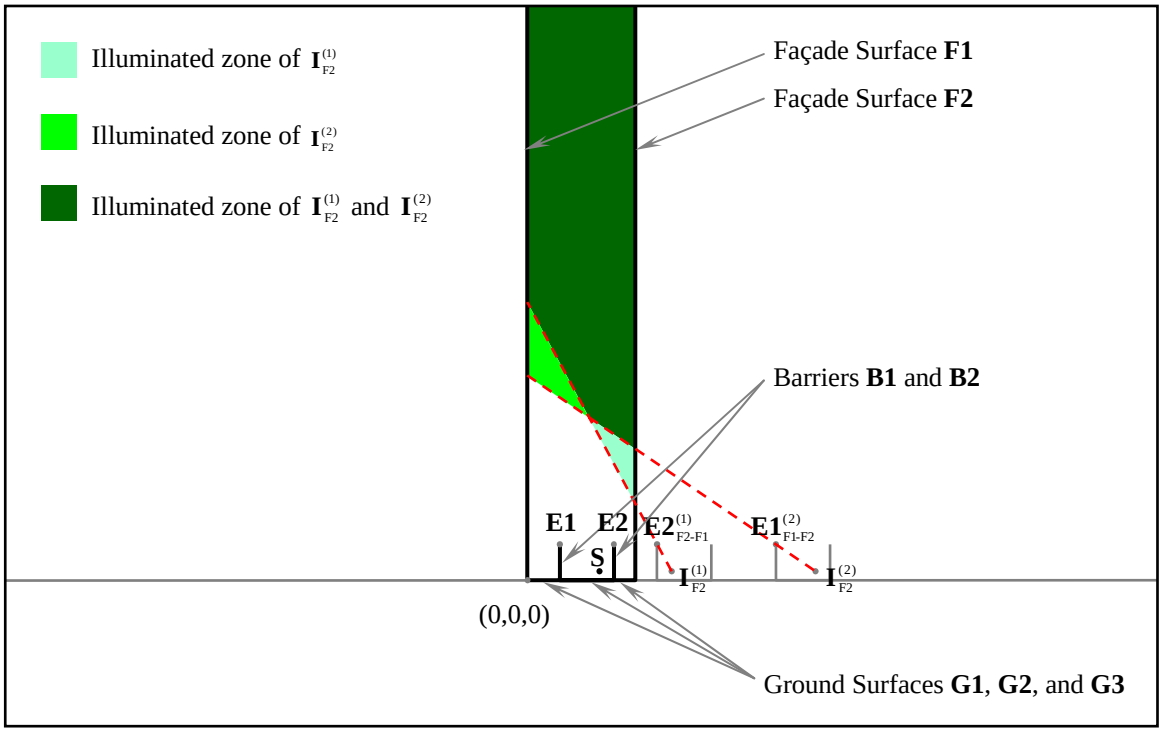

Figure A.9 Illustration of the secondary contribution from image sources $\mathbf{I}_{F2}^{(n_2)}$, where $n_2 = 1,2,3,\cdots$. For image sources $\mathbf{I}_{F2}^{(n_2)}$ with odd order n_2, the lines connecting $\mathbf{I}_{F2}^{(n_2)}$ with the illuminated receivers should have no intersection with the line from $\left(x_{E2\text{-}F2\text{-}F1}^{(n_2)}, 0, 0\right)$ to $\left(x_{E2\text{-}F2\text{-}F1}^{(n_2)}, 0, H\right)$. For image sources $\mathbf{I}_{F2}^{(n_2)}$ with even order n_2, the lines connecting $\mathbf{I}_{F2}^{(n_2)}$ with the illuminated receivers should have no intersection with the line from $\left(x_{E1\text{-}F1\text{-}F2}^{(n_2)}, 0, 0\right)$ to $\left(x_{E1\text{-}F1\text{-}F2}^{(n_2)}, 0, H\right)$.

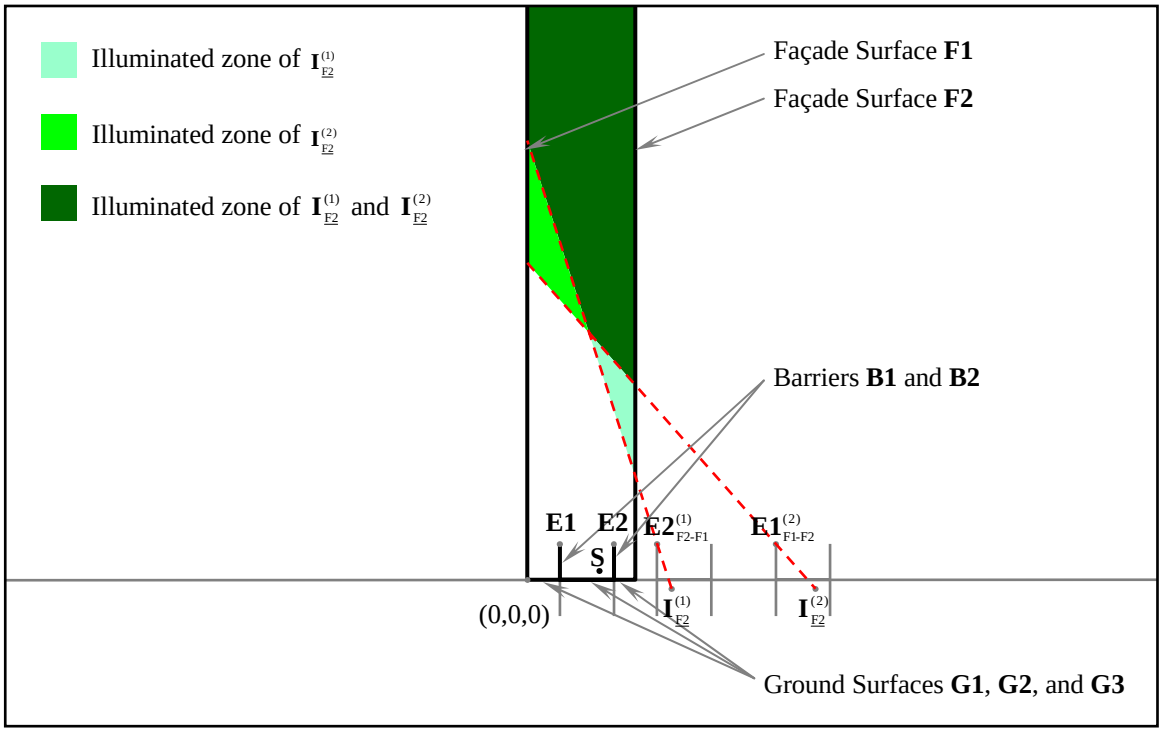

Figure A.10 Illustration of the secondary contribution from image sources $\mathbf{I}_{\underline{F2}}^{(n_2)}$, where $n_2 = 1,2,3,\cdots$. For image sources $\mathbf{I}_{\underline{F2}}^{(n_2)}$ with odd order n_2, the lines connecting $\mathbf{I}_{\underline{F2}}^{(n_2)}$ with the illuminated receivers should have no intersection with the line from $\left(x_{\text{E2-F2-F1}}^{(n_2)}, 0, -H\right)$ to $\left(x_{\text{E2-F2-F1}}^{(n_2)}, 0, H\right)$. For image sources $\mathbf{I}_{\underline{F2}}^{(n_2)}$ with even order n_2, the lines connecting $\mathbf{I}_{\underline{F2}}^{(n_2)}$ with the illuminated receivers should have no intersection with the line from $\left(x_{\text{E1-F1-F2}}^{(n_2)}, 0, -H\right)$ to $\left(x_{\text{E1-F1-F2}}^{(n_2)}, 0, H\right)$.

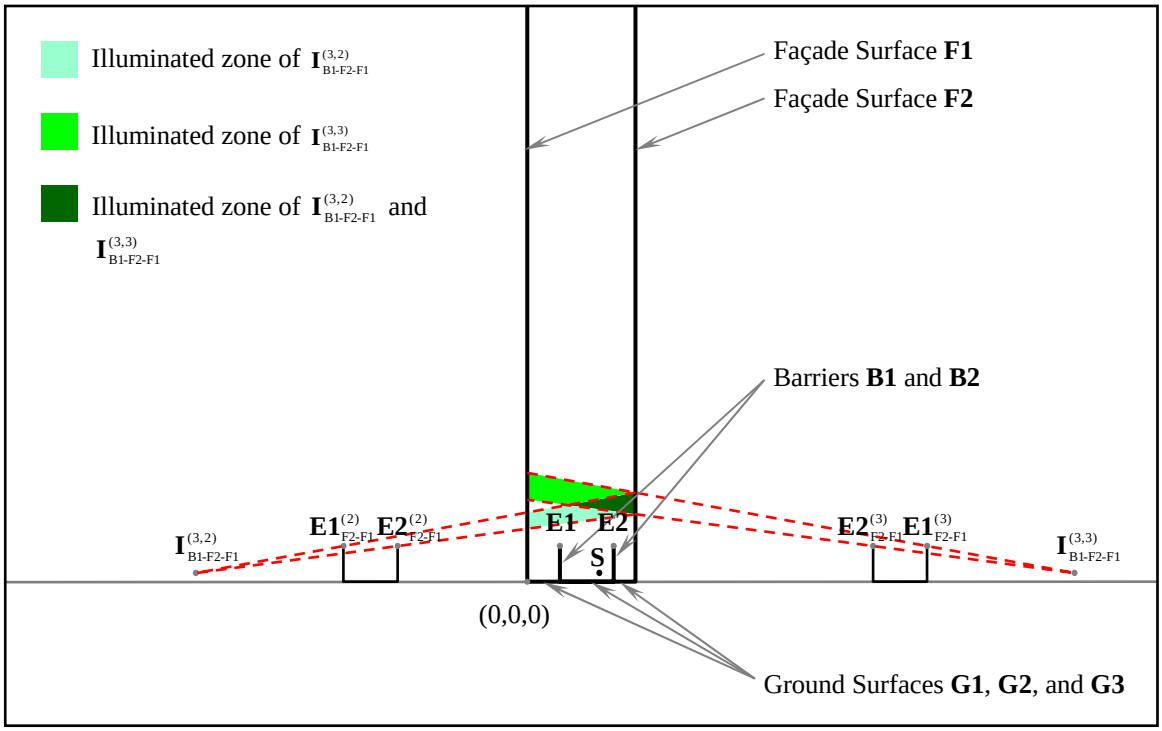

Figure A.11 Illustration of the secondary contribution from image sources $\mathbf{I}^{(n_1,n_2)}_{\text{B1-F2-F1}}$, where $n_1 = 1,2,3,\cdots$ and $n_2 = 1,2,3,\cdots$. The lines connecting $\mathbf{I}^{(n_1,n_2)}_{\text{B1-F2-F1}}$ with the illuminated receivers should have an intersection with the line from $\left(x^{(n_2)}_{\text{E1-F2-F1}},0,0\right)$ to $\left(x^{(n_2)}_{\text{E1-F2-F1}},0,H\right)$ and have an intersection with the line from $\left(x^{(n_2)}_{\text{E2-F2-F1}},0,0\right)$ to $\left(x^{(n_2)}_{\text{E2-F2-F1}},0,H\right)$.

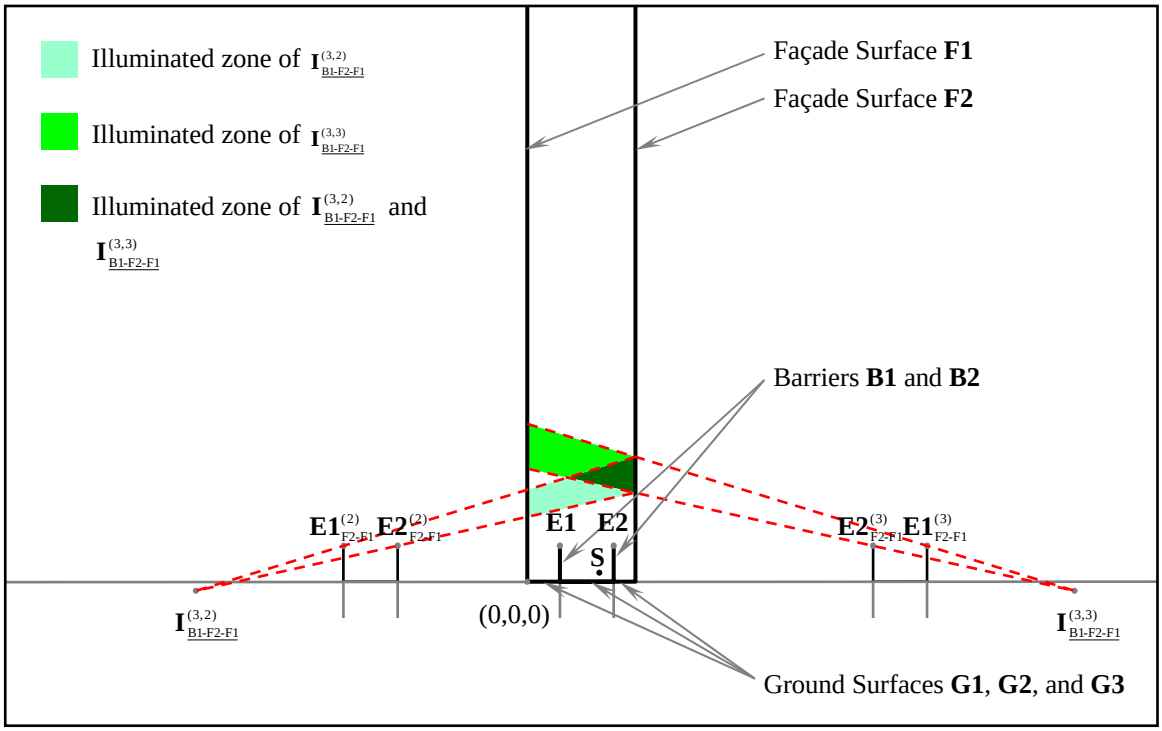

Figure A.12 Illustration of the secondary contribution from image sources $\mathbf{I}^{(n_1,n_2)}_{\underline{\text{B1-F2-F1}}}$, where $n_1 = 1,2,3,\cdots$ and $n_2 = 1,2,3,\cdots$. The lines connecting $\mathbf{I}^{(n_1,n_2)}_{\underline{\text{B1-F2-F1}}}$ with the illuminated receivers should have no intersection with the line from $\left(x^{(n_2)}_{\text{E1-F2-F1}},0,-H\right)$ to $\left(x^{(n_2)}_{\text{E1-F2-F1}},0,H\right)$ and have an intersection with the line from $\left(x^{(n_2)}_{\text{E2-F2-F1}},0,H\right)$ to $\left(x^{(n_2)}_{\text{E2-F2-F1}},0,H\right)$.

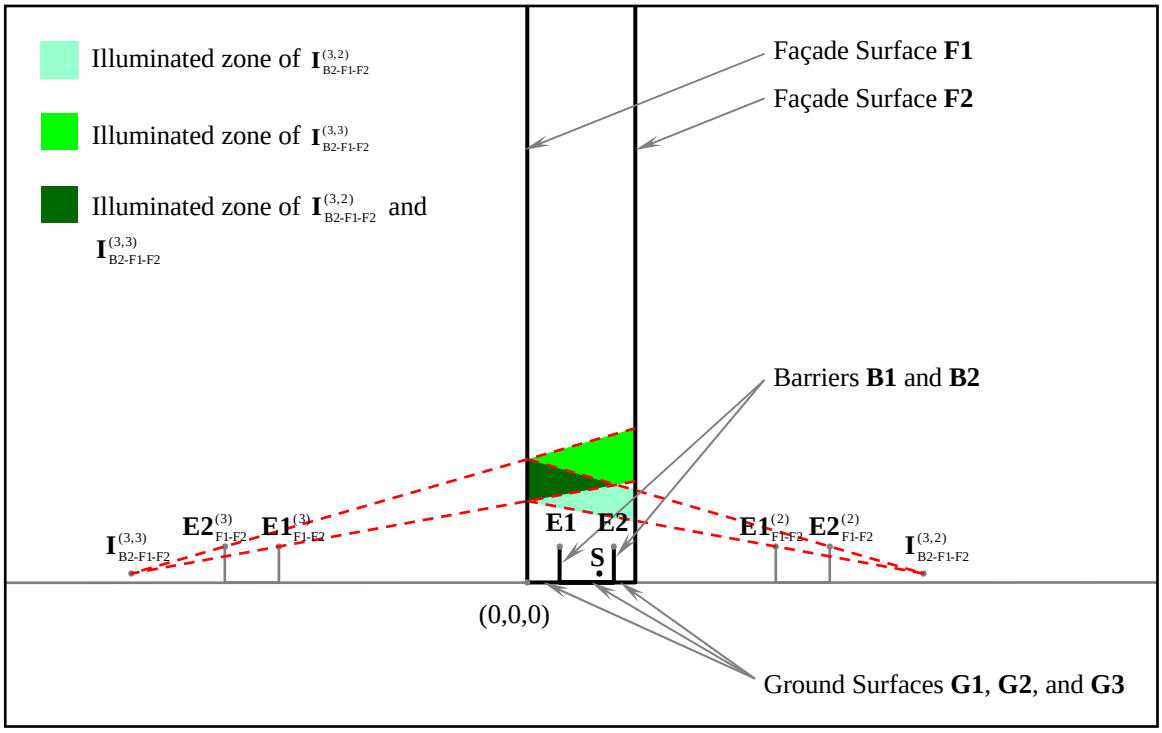

Figure A.13 Illustration of the secondary contribution from image sources $\mathbf{I}^{(n_1,n_2)}_{\text{B2-F1-F2}}$, where $n_1 = 1,2,3,\cdots$ and $n_2 = 1,2,3,\cdots$. The lines connecting $\mathbf{I}^{(n_1,n_2)}_{\text{B2-F1-F2}}$ with the illuminated receivers should have no intersection with the line from $\left(x^{(n_2)}_{\text{E1-F1-F2}},0,0\right)$ to $\left(x^{(n_2)}_{\text{E1-F1-F2}},0,H\right)$ and have an intersection with the line from $\left(x^{(n_2)}_{\text{E2-F1-F2}},0,0\right)$ to $\left(x^{(n_2)}_{\text{E2-F1-F2}},0,H\right)$.

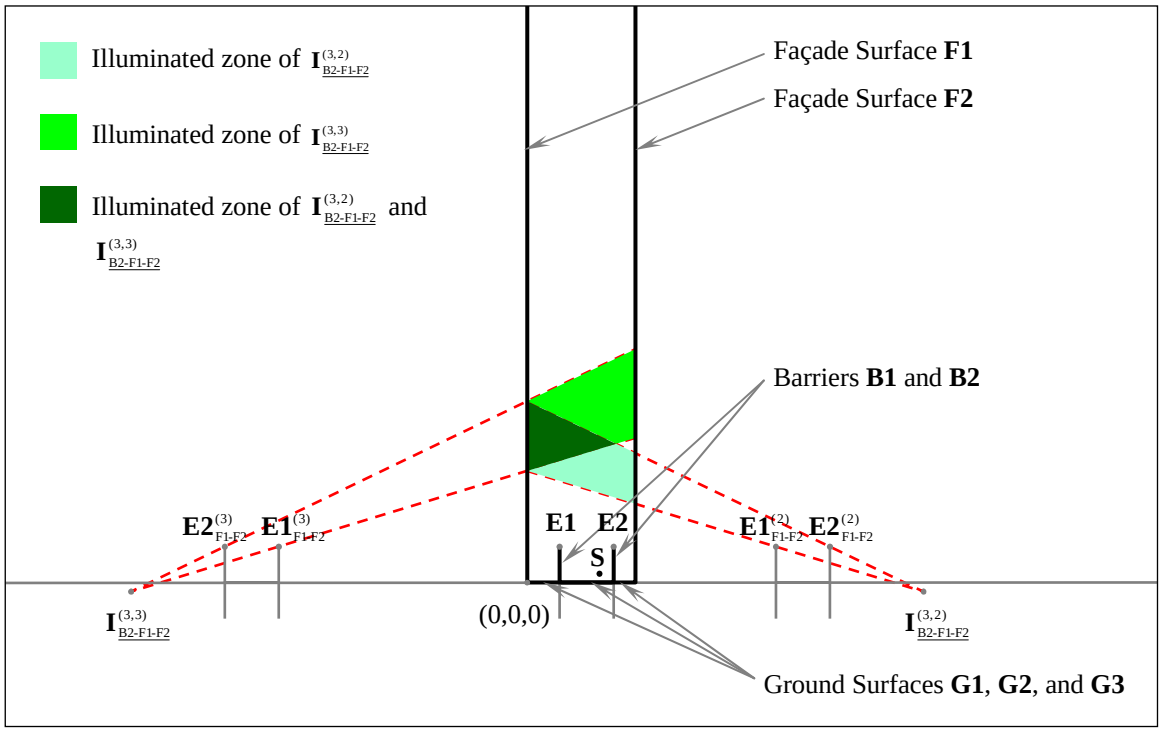

Figure A.14 Illustration of the secondary contribution from image sources $\mathbf{I}^{(n_1,n_2)}_{\underline{\text{B2-F1-F2}}}$, where $n_1 = 1,2,3,\cdots$ and $n_2 = 1,2,3,\cdots$. The lines connecting $\mathbf{I}^{(n_1,n_2)}_{\text{B2-F1-F2}}$ with the illuminated receivers should have no intersection with the line from $\left(x^{(n_2)}_{\text{E1-F1-F2}},0,-H\right)$ to $\left(x^{(n_2)}_{\text{E1-F1-F2}},0,H\right)$ and have an intersection with the line from $\left(x^{(n_2)}_{\text{E2-F1-F2}},0,-H\right)$ to $\left(x^{(n_2)}_{\text{E2-F1-F2}},0,H\right)$.

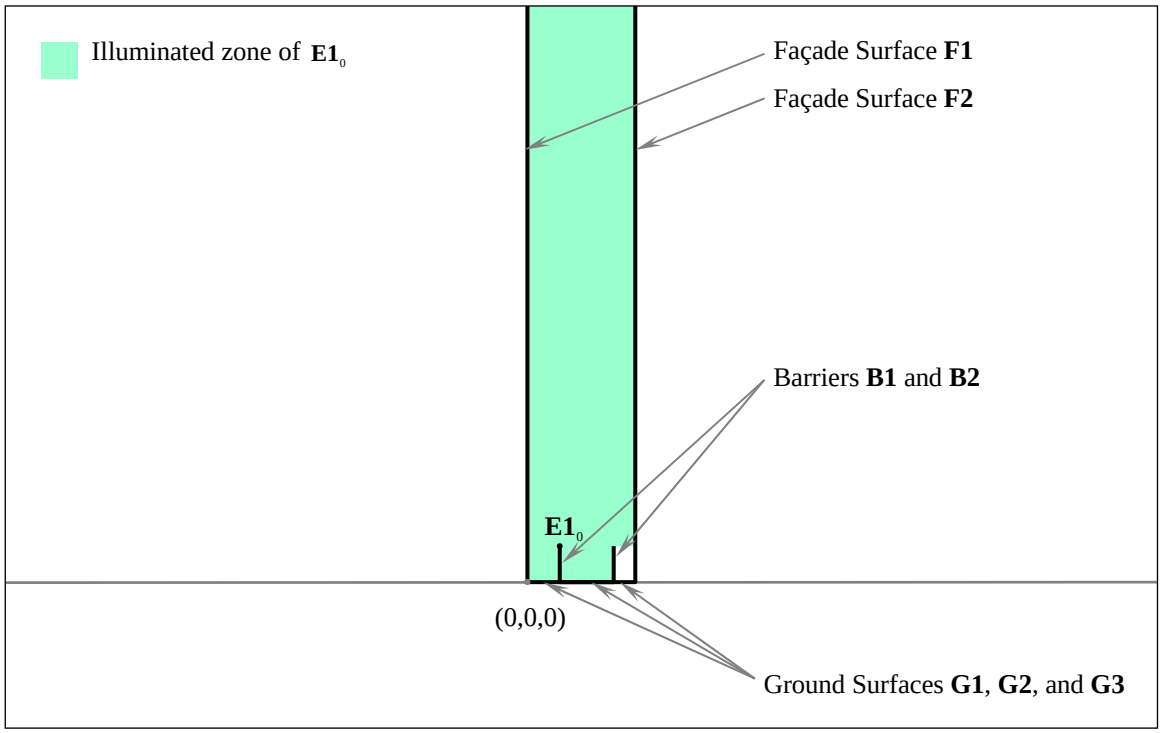

Figure A.15 Illustration of the secondary contribution from image sources $\mathbf{E1}_0$. The lines connecting the illuminated receivers with $\mathbf{E1}_0$ should have no intersection with the line from $(L_1 + W, 0, H)$ to $(L_1 + W, 0, 0)$.

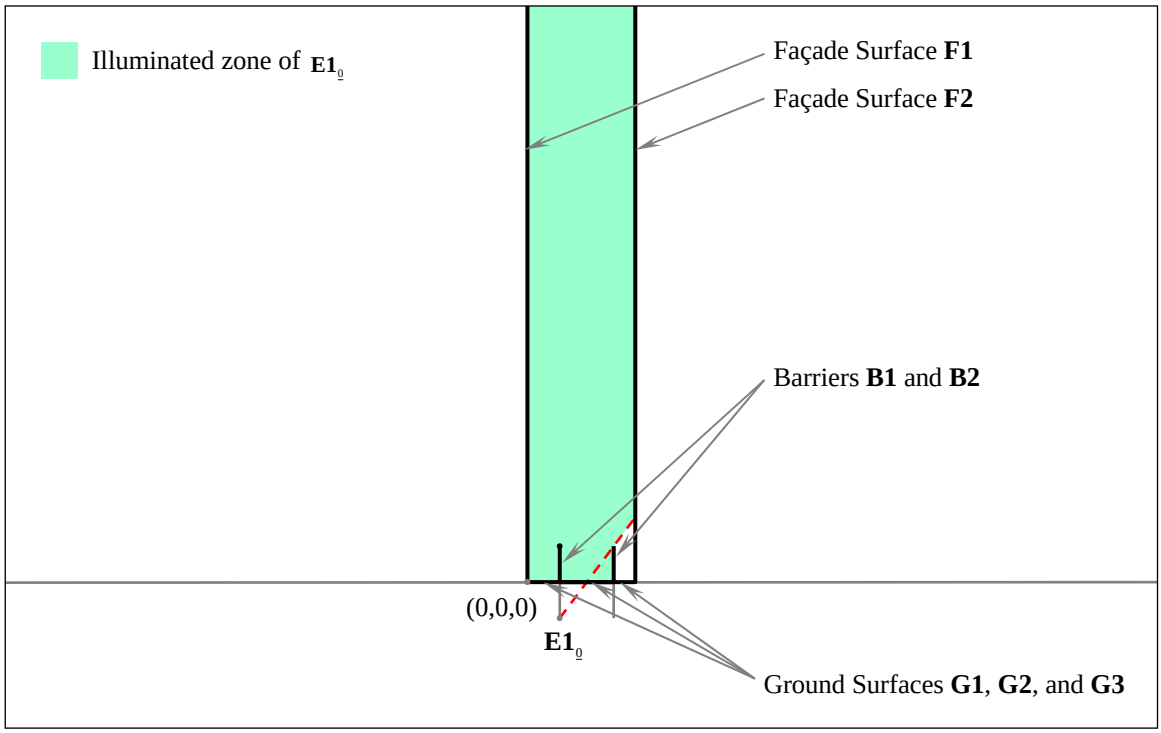

Figure A.16 Illustration of the secondary contribution from image sources $\mathbf{E1}_0$. The lines connecting the illuminated receivers with $\mathbf{E1}_0$ should have no intersection with the line from $(L_1 + W, 0, H)$ to $(L_1 + W, 0, -H)$.

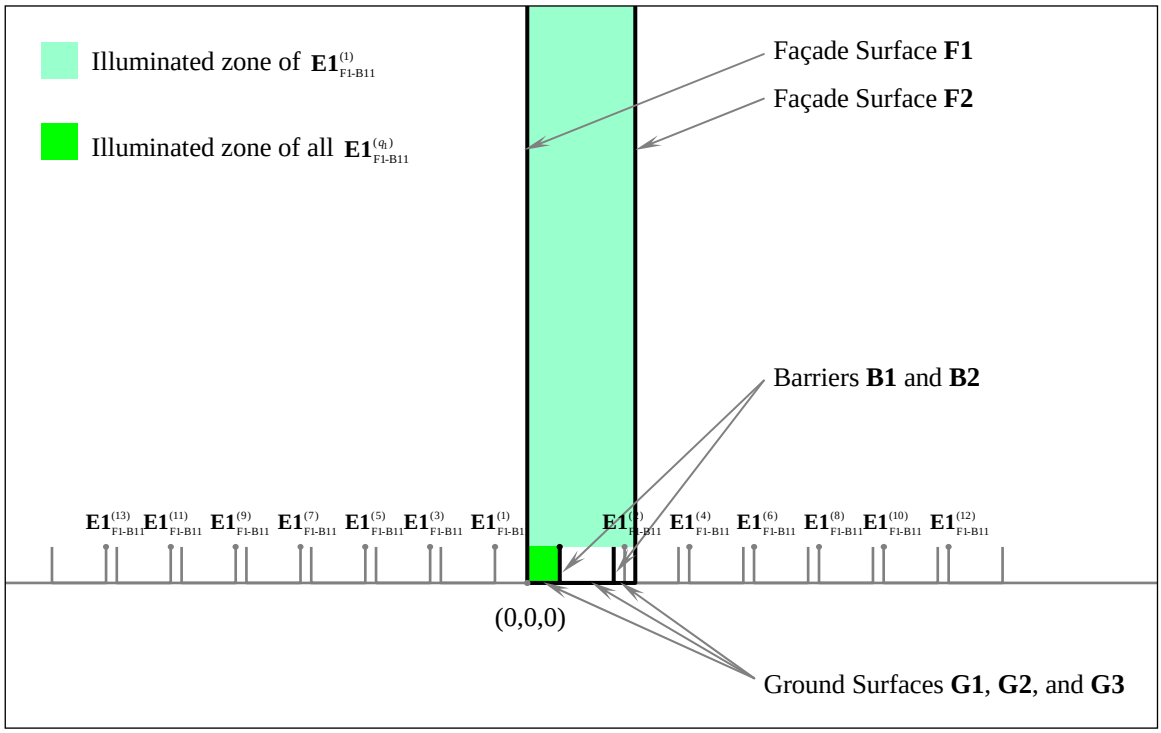

Figure A.17 Illustration of the secondary contribution from image edges $\mathbf{E1}^{(q_1)}_{\text{F1-B11}}$, where $q_1 = 1,2,3,\cdots$. Receivers having a height lower than H and located between the façade surface Γ_{F1} and the barrier **B1** should be illuminated by all $\mathbf{E1}^{(q_1)}_{\text{F1-B11}}$. Especially for $\mathbf{E1}^{(1)}_{\text{F1-B11}}$, receivers located higher than H are also illuminated.

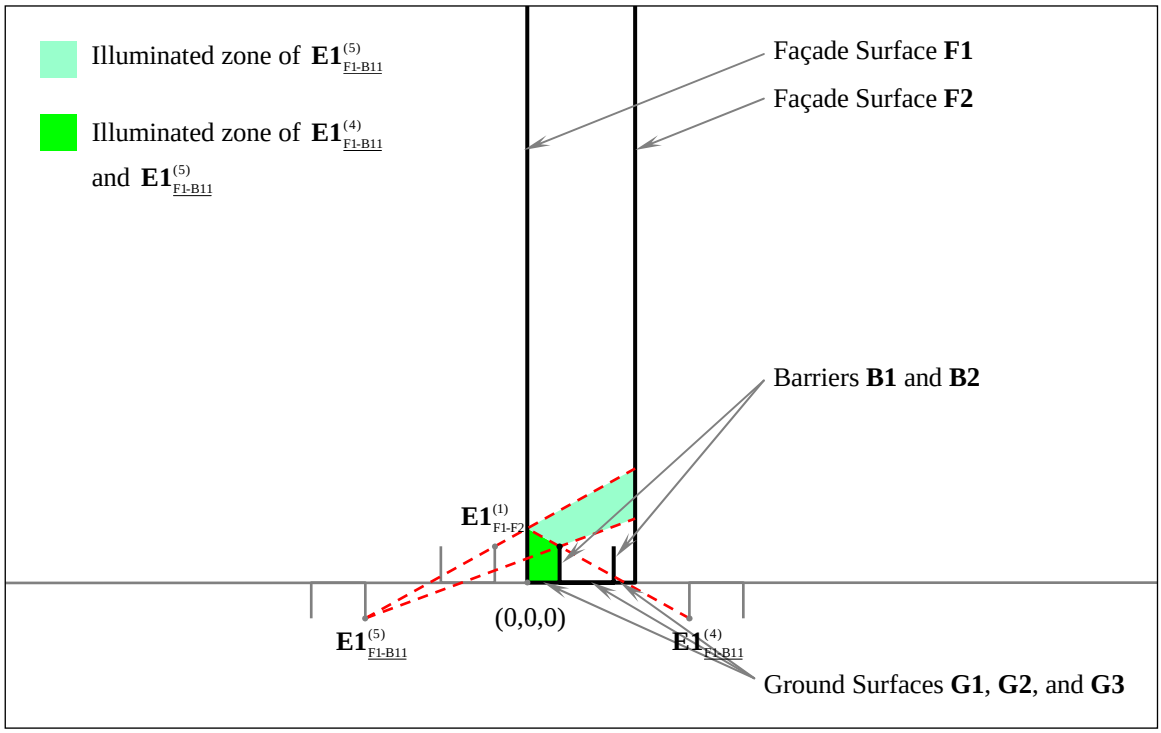

Figure A.18 Illustration of the secondary contribution from image sources $\mathbf{E1}^{(q_1)}_{\text{F1-B11}}$, where $q_1 = 1,2,3,\cdots$. For the $\mathbf{E1}^{(q_1)}_{\text{F1-B11}}$ with odd q_1, the lines connecting the illuminated receivers with $\mathbf{E1}^{(q_1)}_{\text{F1-B11}}$ should have an intersection with the line from $(-L_1,0,-H)$ to $(-L_1,0,H)$ and have no intersection with the line from $(L_1,0,-H)$ to $(L_1,0,H)$. For the $\mathbf{E1}^{(q_1)}_{\text{F1-B11}}$ with even q_1, the lines connecting the illuminated receivers with $\mathbf{E1}^{(q_1)}_{\text{F1-B11}}$ should have an intersection with the line from $(L_1,0,-H)$ to $(L_1,0,H)$.

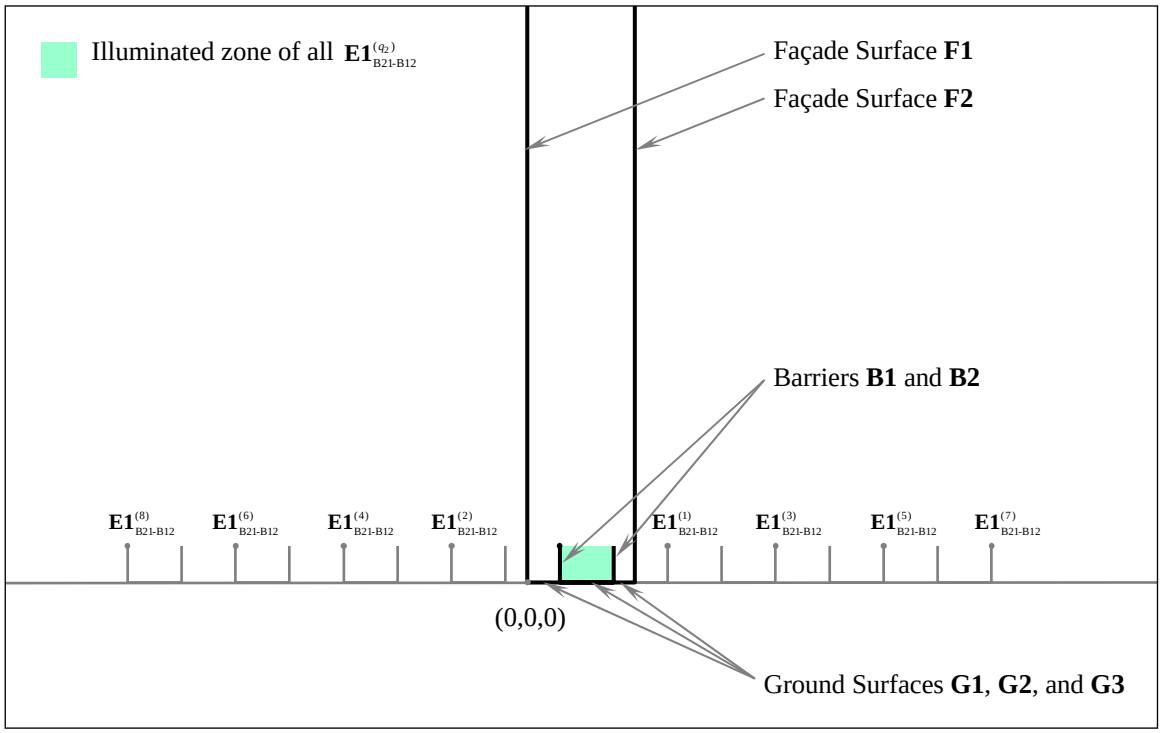

Figure A.19 Illustration of the secondary contribution from image sources $\mathbf{E1}_{\text{B21-B12}}^{(q_1)}$, where $q_1 = 1,2,3,\cdots$. The illuminated receivers should be located between the two barriers **B1** and **B2** and have a height lower than H.

`

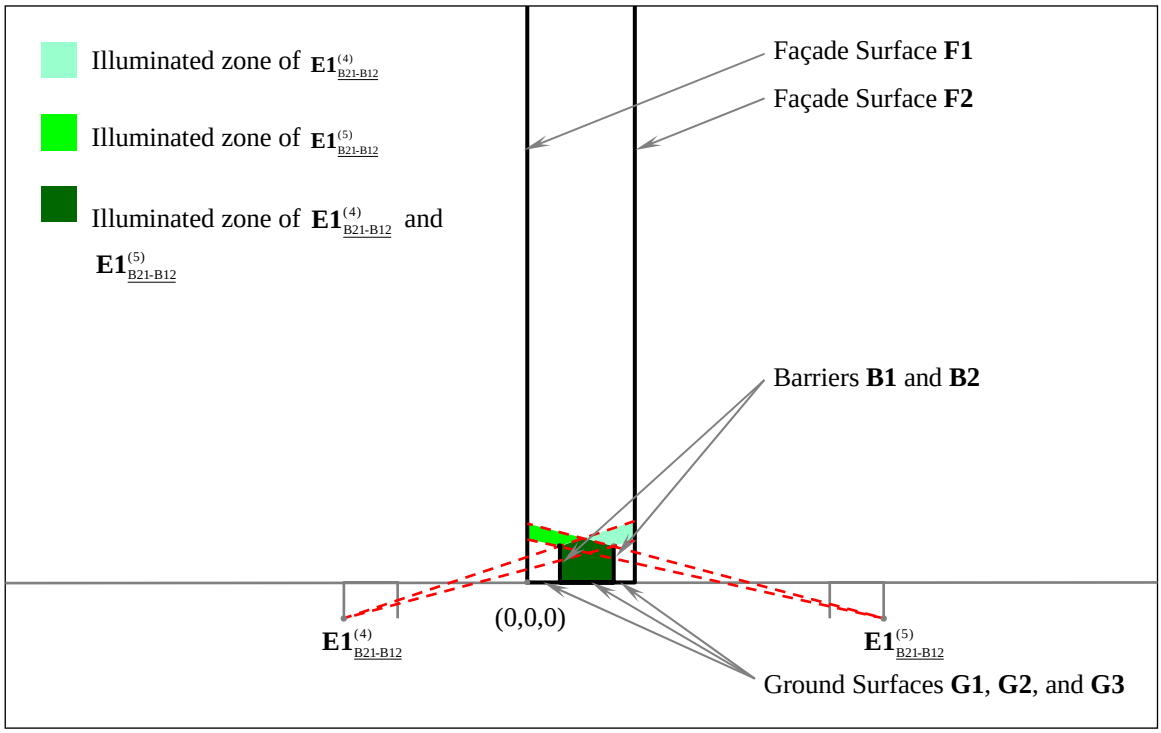

Figure A.20 Illustration of the secondary contribution from image sources $\mathbf{E1}^{(q_1)}_{\underline{\text{B21-B12}}}$, where $q_1 = 1,2,3,\cdots$. For the $\mathbf{E1}^{(q_1)}_{\underline{\text{B21-B12}}}$ with odd q_1, the lines connecting the illuminated receivers with $\mathbf{E1}^{(q_1)}_{\underline{\text{B21-B12}}}$ should have no intersection with the line from $(L_1,0,-H)$ to $(L_1,0,H)$ and have an intersection with the line from $(L_1+W,0,-H)$ to $(L_1+W,0,H)$. For the $\mathbf{E1}^{(q_1)}_{\underline{\text{B21-B12}}}$ with even q_1, the lines connecting the illuminated receivers with $\mathbf{E1}^{(q_1)}_{\underline{\text{B21-B12}}}$ should have an intersection with the line from $(L_1,0,-H)$ to $(L_1,0,H)$ and have no intersection with the line from $(L_1+W,0,-H)$ to $(L_1+W,0,H)$.

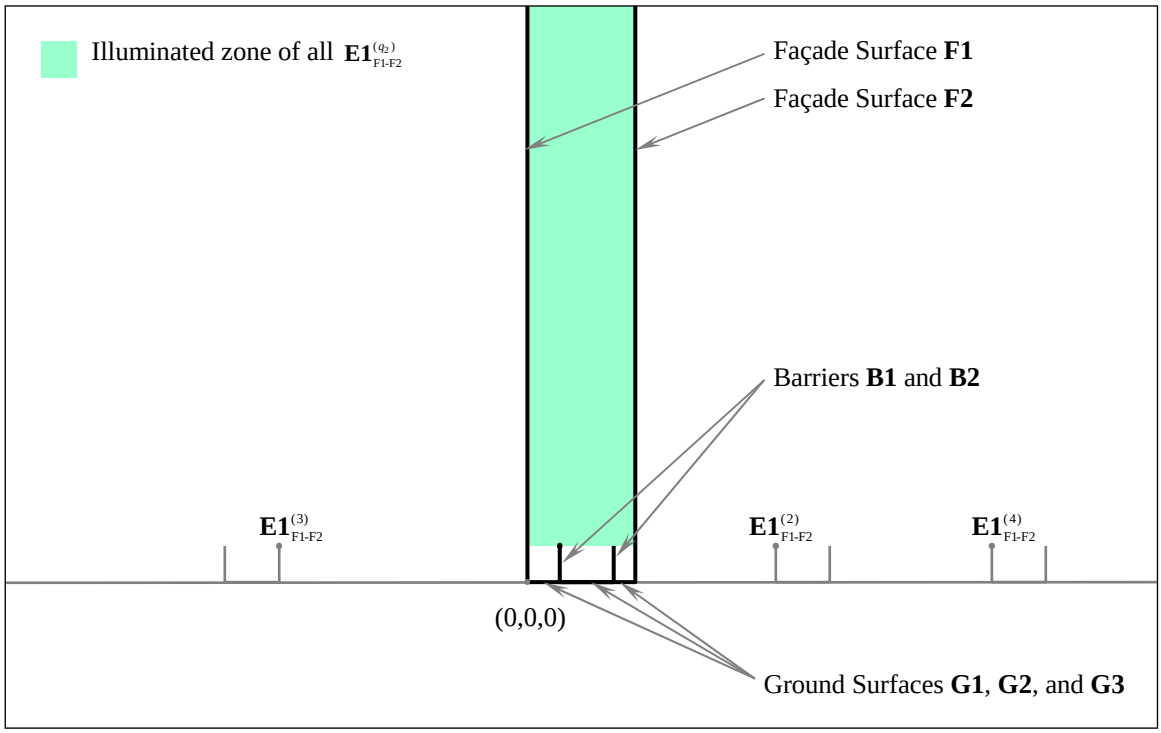

Figure A.21 Illustration of the secondary contribution from image sources $\mathbf{E1}^{(q_2)}_{\text{F1-F2}}$, where $q_2 = 2,3,4,\cdots$. Note that q_2 starts from 2 as $\mathbf{E1}^{(1)}_{\text{F1-F2}}$ is already considered as $\mathbf{E1}^{(1)}_{\text{F1-B11}}$. For all $\mathbf{E1}^{(q_2)}_{\text{F1-F2}}$, the illuminated receivers should have a height higher than H.

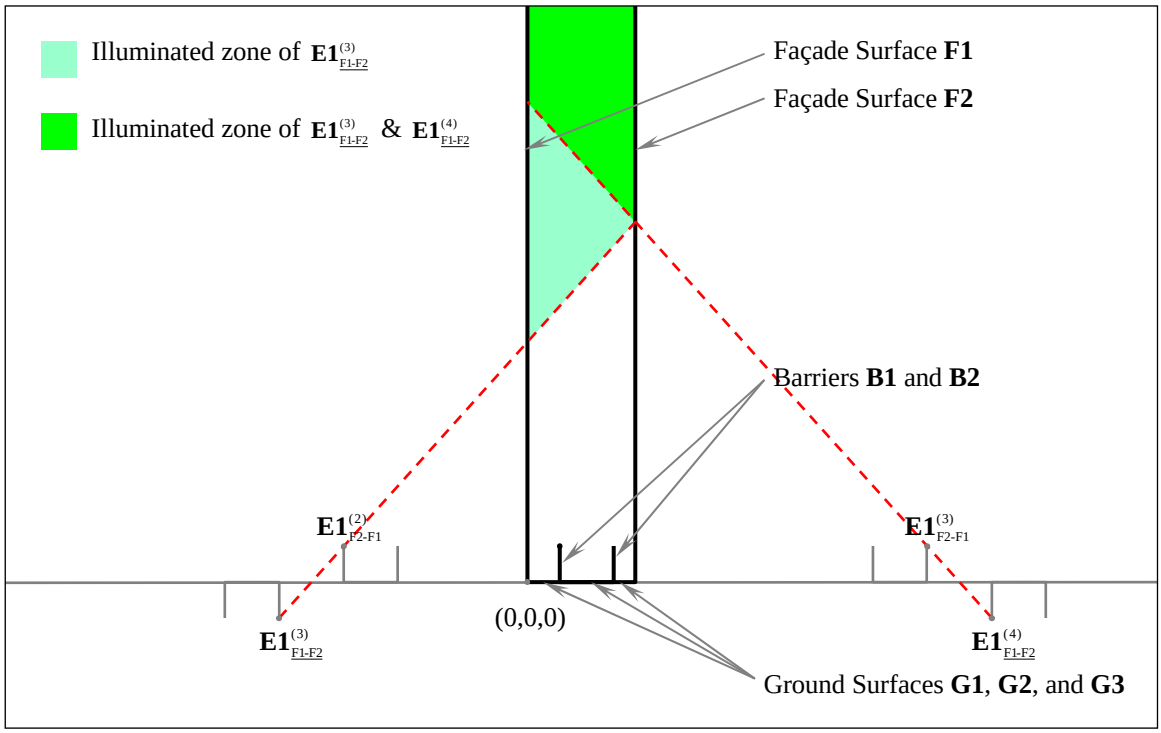

Figure A.22 Illustration of the secondary contribution from image sources $\mathbf{E1}^{(q_2)}_{\underline{\text{F1-F2}}}$, where $q_2 = 2,3,4,\cdots$. Note that q_2 starts from 2 as $\mathbf{E1}^{(1)}_{\underline{\text{F1-F2}}}$ is already considered as $\mathbf{E1}^{(1)}_{\underline{\text{F1-B11}}}$. The lines connecting the illuminated receivers with $\mathbf{E1}^{(q_2)}_{\underline{\text{F1-F2}}}$ should have no intersection with the line from $\left(x^{(q_2-1)}_{\text{E1-F2-F1}},0,-H\right)$ to $\left(x^{(q_2-1)}_{\text{E1-F2-F1}},0,H\right)$.

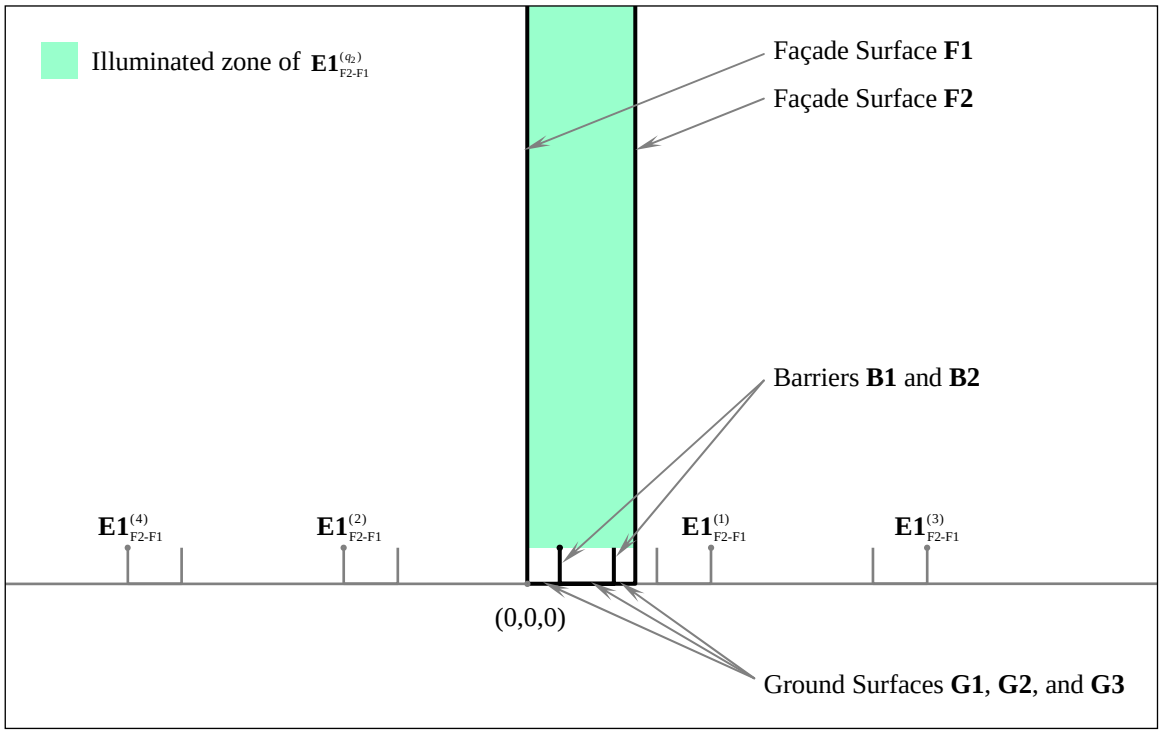

Figure A.23 Illustration of the secondary contribution from image sources $\mathbf{E1}^{(q_2)}_{\text{F2-F1}}$, where $q_2 = 1,2,3,\cdots$. The illuminated receivers should have a height higher than H.

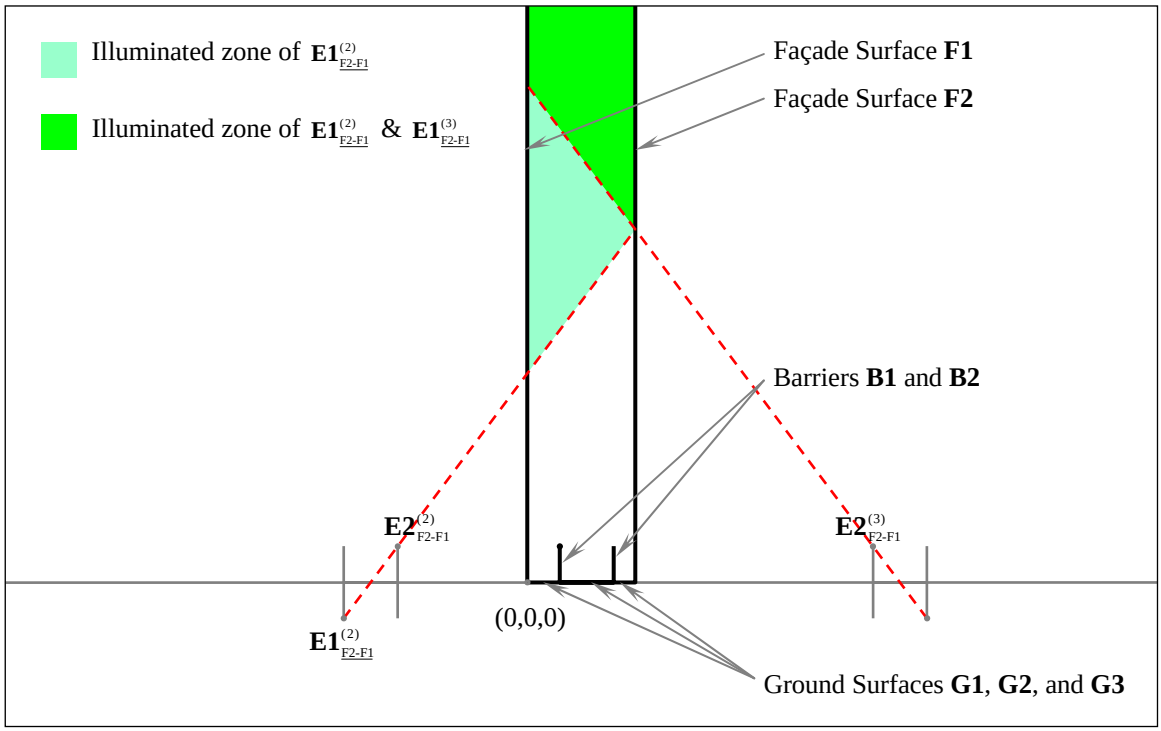

Figure A.24 Illustration of the secondary contribution from image sources $\mathbf{E1}^{(q_2)}_{\underline{\text{F2-F1}}}$, where $q_2 = 1,2,3,\cdots$. The lines connecting the illuminated receivers with $\mathbf{E1}^{(q_2)}_{\underline{\text{F2-F1}}}$ should have no intersection with the line from $\left(x^{(q_2)}_{\text{E2-F2-F1}},0,-H\right)$ to $\left(x^{(q_2)}_{\text{E2-F2-F1}},0,H\right)$.

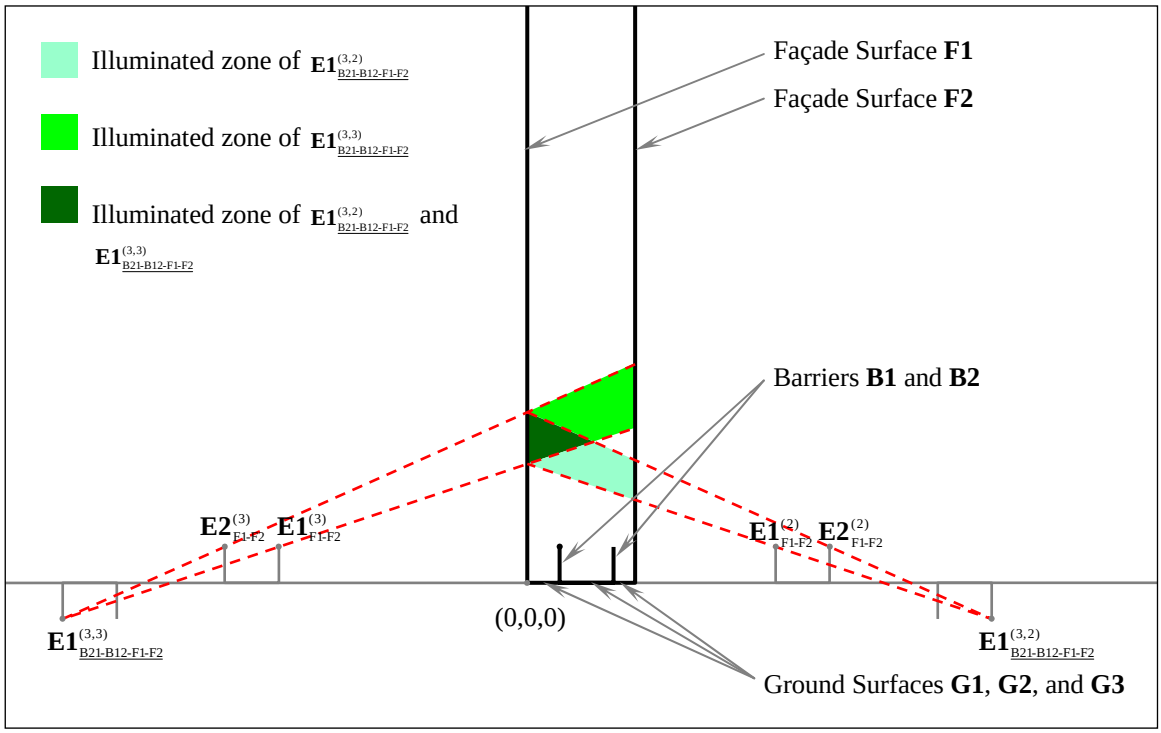

Figure A.25 Illustration of the secondary contribution from image sources $\mathbf{E1}^{(q_1,q_2)}_{\text{B21-B12-F1-F2}}$, where $q_2 = 1,3,5,\cdots$ and $q_2 = 1,2,3,\cdots$. The lines connecting the illuminated receivers with $\mathbf{E1}^{(q_1,q_2)}_{\text{B21-B12-F1-F2}}$ should have no intersection with the line from $\left(x^{(q_2)}_{\text{E1-F1-F2}},0,-H\right)$ to $\left(x^{(q_2)}_{\text{E1-F1-F2}},0,H\right)$ and have an intersection with the line from $\left(x^{(q_2)}_{\text{E2-F1-F2}},0,-H\right)$ to $\left(x^{(q_2)}_{\text{E2-F1-F2}},0,H\right)$.

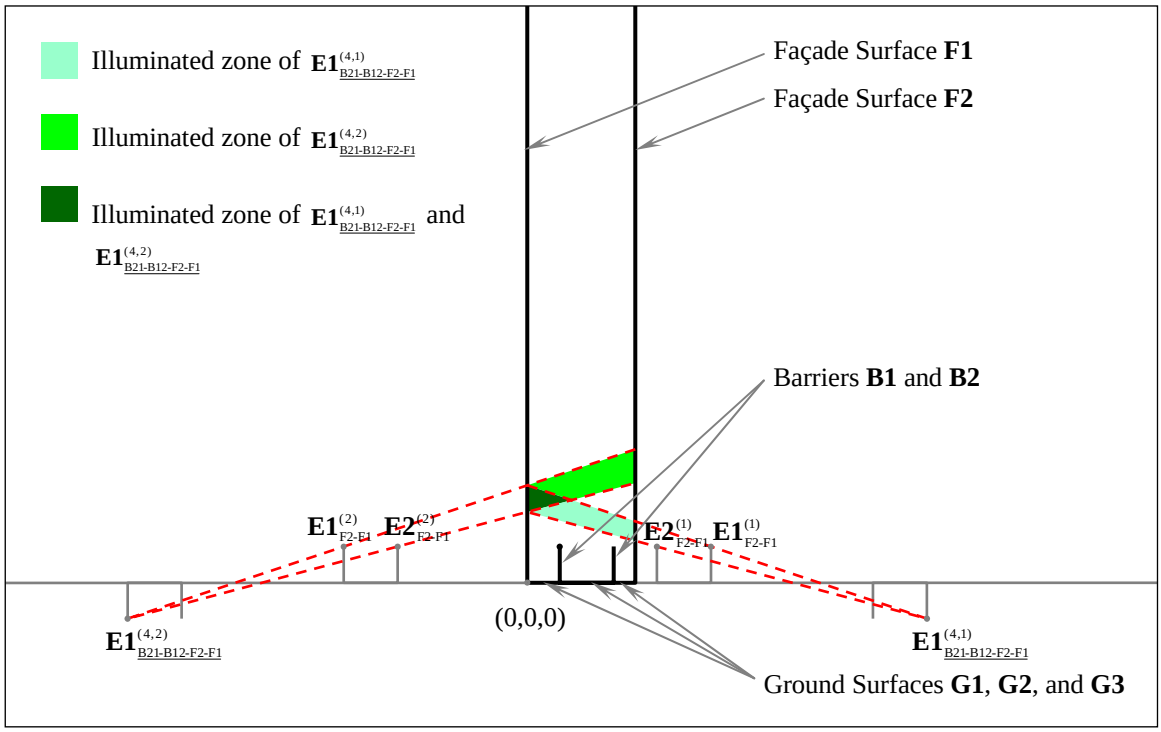

Figure A.26 Illustration of the secondary contribution from image sources $\mathbf{E1}^{(q_1,q_2)}_{\text{B21-B12-F2-F1}}$ where $q_1 = 2,4,6,\cdots$ and $q_2 = 1,2,3,\cdots$. The lines connecting the illuminated receivers with $\mathbf{E1}^{(q_1,q_2)}_{\text{B21-B12-F2-F1}}$ should have an intersection with the line from $\left(x^{(q_2)}_{\text{E1-F2-F1}},0,-H\right)$ to $\left(x^{(q_2)}_{\text{E1-F2-F1}},0,H\right)$ and have no intersection with the line from $\left(x^{(q_2)}_{\text{E2-F2-F1}},0,-H\right)$ to $\left(x^{(q_2)}_{\text{E2-F2-F1}},0,H\right)$.

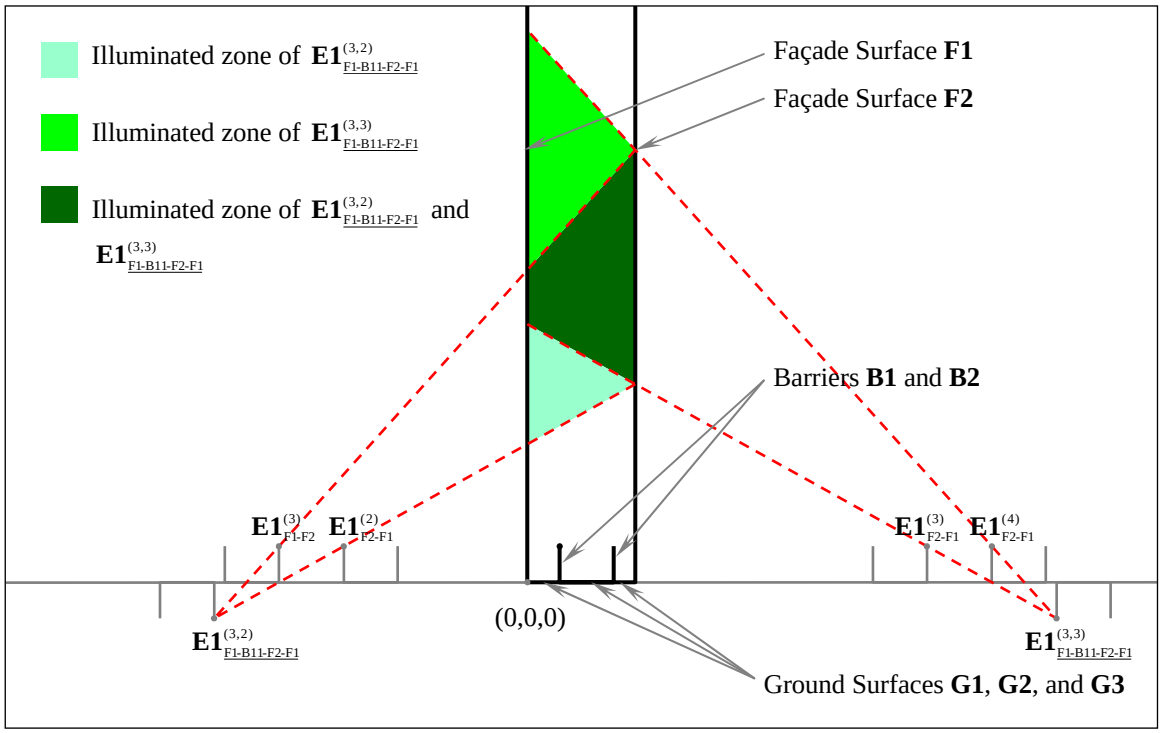

Figure A.27 Illustration of the secondary contribution from image sources $\mathbf{E1}^{(q_1,q_2)}_{\text{F1-B11-F2-F1}}$, where $q_1 = 3,5,7,\cdots$ and $q_2 = 1,2,3,\cdots$. Note that q_1 starts from 3 as $\mathbf{E1}^{(1,q_2)}_{\text{F1-B11-F2-F1}}$ is already considered as $\mathbf{E1}^{(q_2+1)}_{\text{F1-F2}}$. The lines connecting the illuminated receivers with $\mathbf{E1}^{(q_1,q_2)}_{\text{F1-B11-F2-F1}}$ should have no intersection with the line from $\left(x^{(q_2)}_{\text{E1-F2-F1}},0,-H\right)$ to $\left(x^{(q_2)}_{\text{E1-F2-F1}},0,H\right)$ and have an intersection with the line from $\left(x^{(q_2+1)}_{\text{E1-F1-F2}},0,-H\right)$ to $\left(x^{(q_2+1)}_{\text{E1-F1-F2}},0,H\right)$.

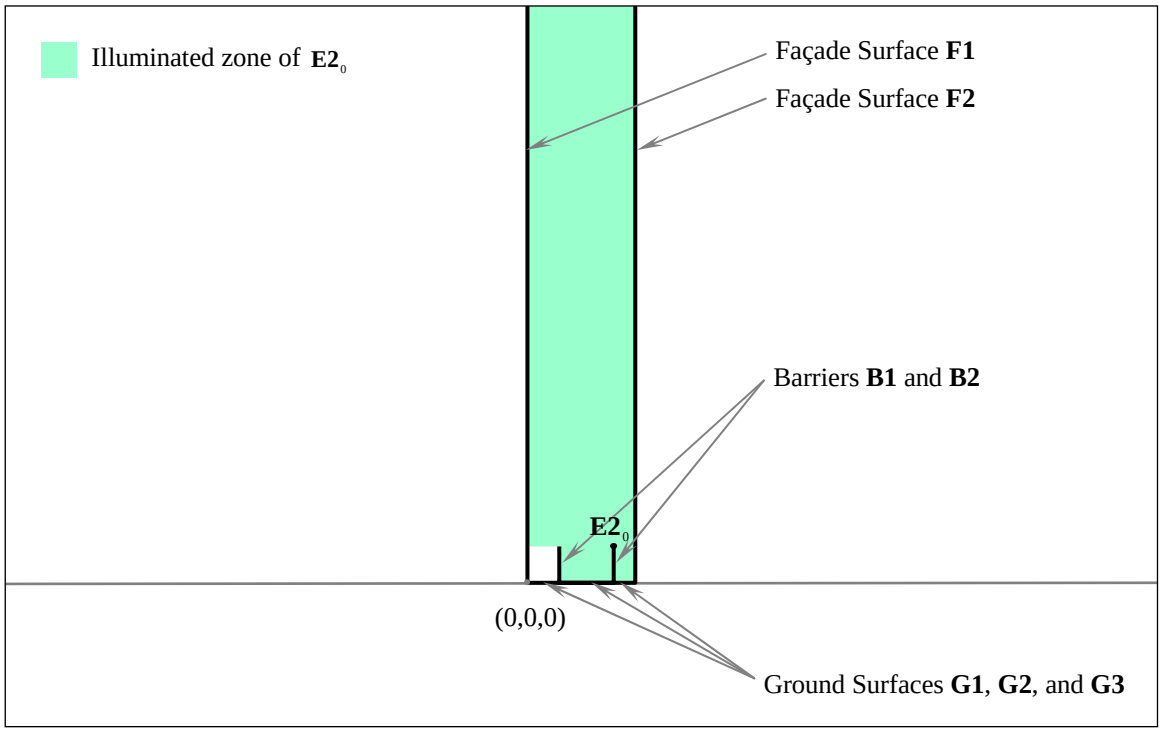

Figure A.28 Illustration of the secondary contribution from image source $\mathbf{E2}_0$. The lines connecting $\mathbf{E2}_0$ and the illuminated receivers should have no intersection with the line from $(L_1, 0, 0)$ to $(L_1, 0, H)$.

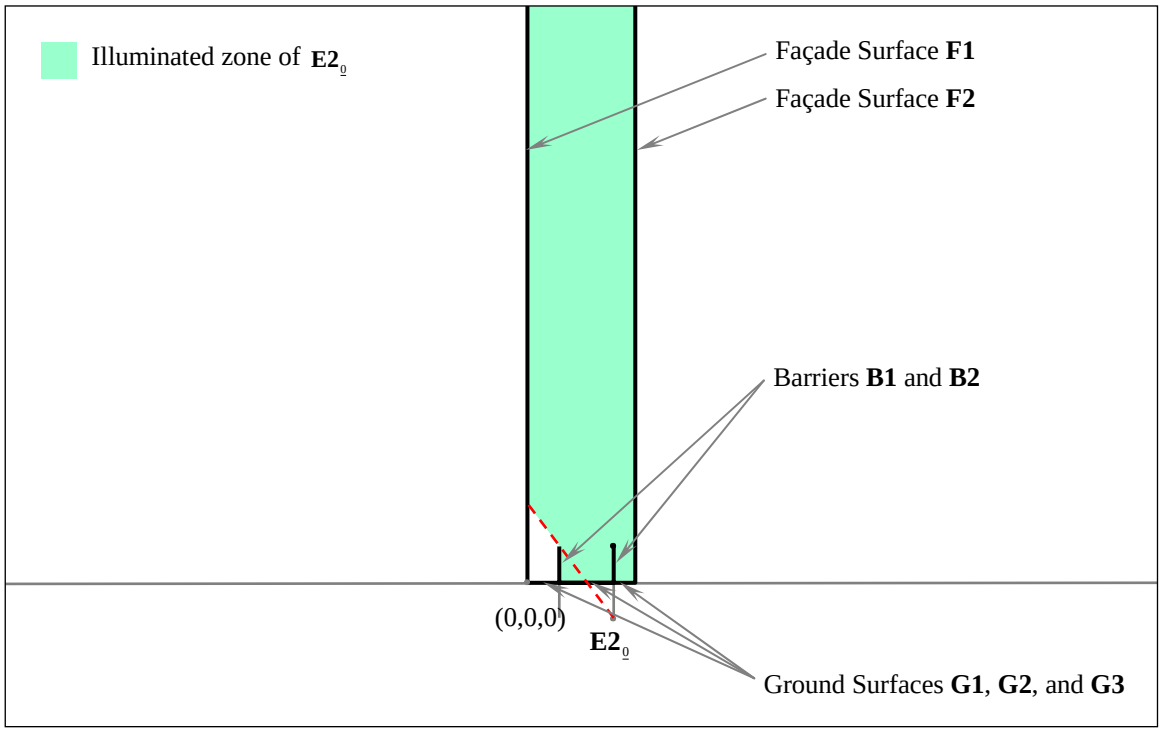

Figure A.29 Illustration of the secondary contribution from image source $\mathbf{E2}_0$. The lines connecting $\mathbf{E2}_0$ and the illuminated receivers should have no intersection with the line from $(L_1, 0, -H)$ to $(L_1, 0, H)$.

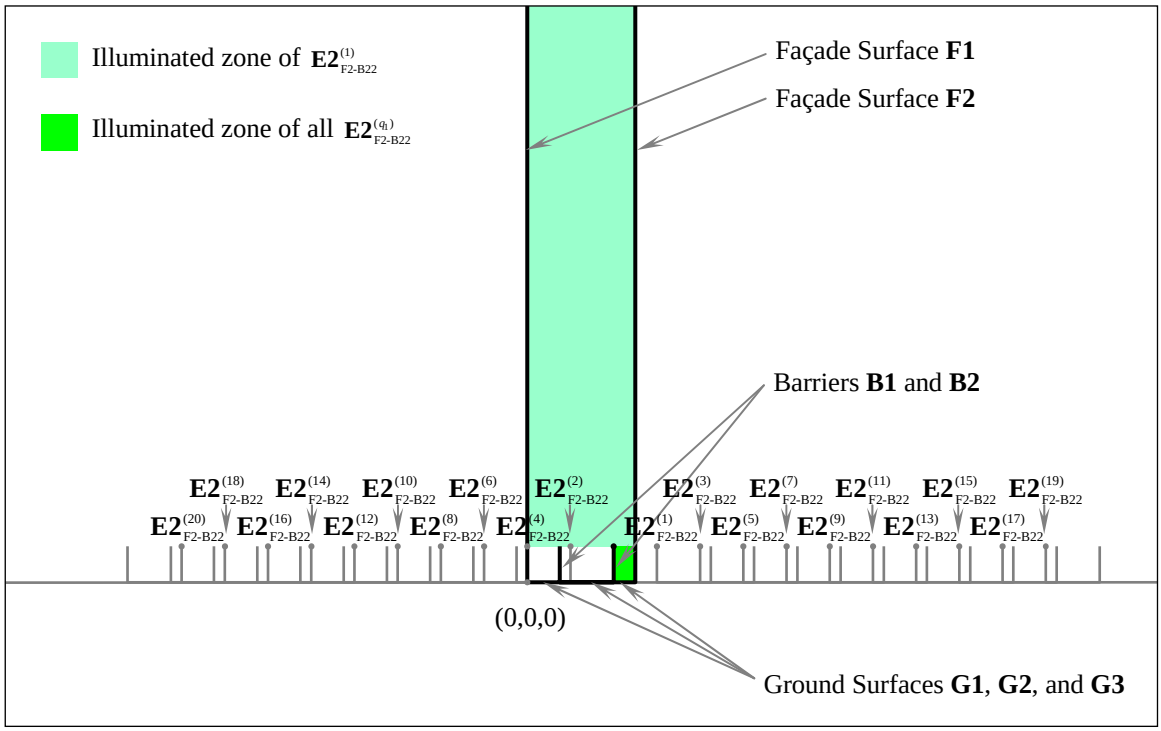

Figure A.30 Illustration of the secondary contribution from image sources $\mathbf{E2}^{(q_1)}_{\text{F2-B22}}$, where $q_1 = 1,2,3,\cdots$. Receivers having a height lower than H and located between the façade surface Γ_{F2} and the barrier **B2** should be illuminated by all $\mathbf{E2}^{(q_1)}_{\text{F2-B22}}$. Especially for $\mathbf{E2}^{(1)}_{\text{F2-B22}}$, receivers located higher than H are also illuminated.

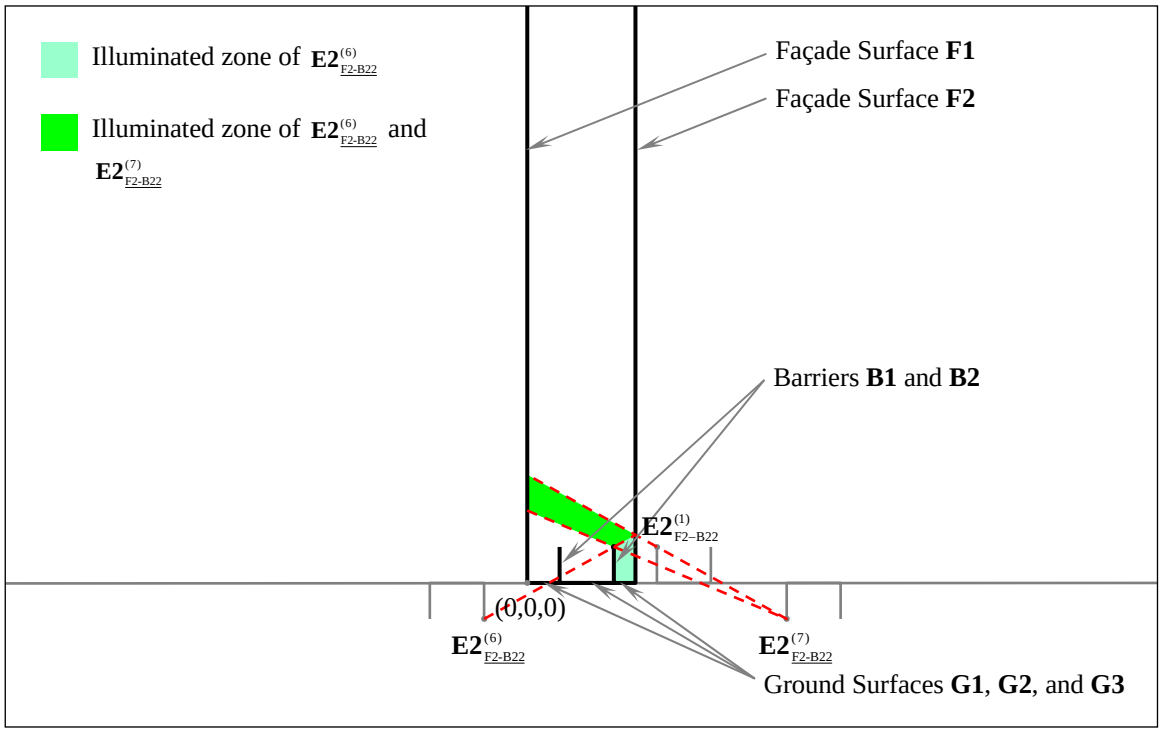

Figure A.31 Illustration of the secondary contribution from image sources $\mathbf{E2}^{(q_1)}_{\text{F2-B22}}$, where $q_1 = 1,2,3,\cdots$. For image sources $\mathbf{E2}^{(q_1)}_{\text{F2-B22}}$ with odd order q_1, the lines connecting the illuminated receivers with $\mathbf{E2}^{(q_1)}_{\text{F2-B22}}$ should have an intersection with the line from $(L+L_2,0,-H)$ to $(L+L_2,0,H)$ and have no intersection with the line from $(L_1+W,0,-H)$ to $(L_1+W,0,H)$. For the $\mathbf{E2}^{(q_1)}_{\text{F2-B22}}$ with even q_1, the lines connecting the illuminated receivers with $\mathbf{E2}^{(q_1)}_{\text{F2-B22}}$ should have an intersection with the line from $(L_1+W,0,-H)$ to $(L_1+W,0,H)$.

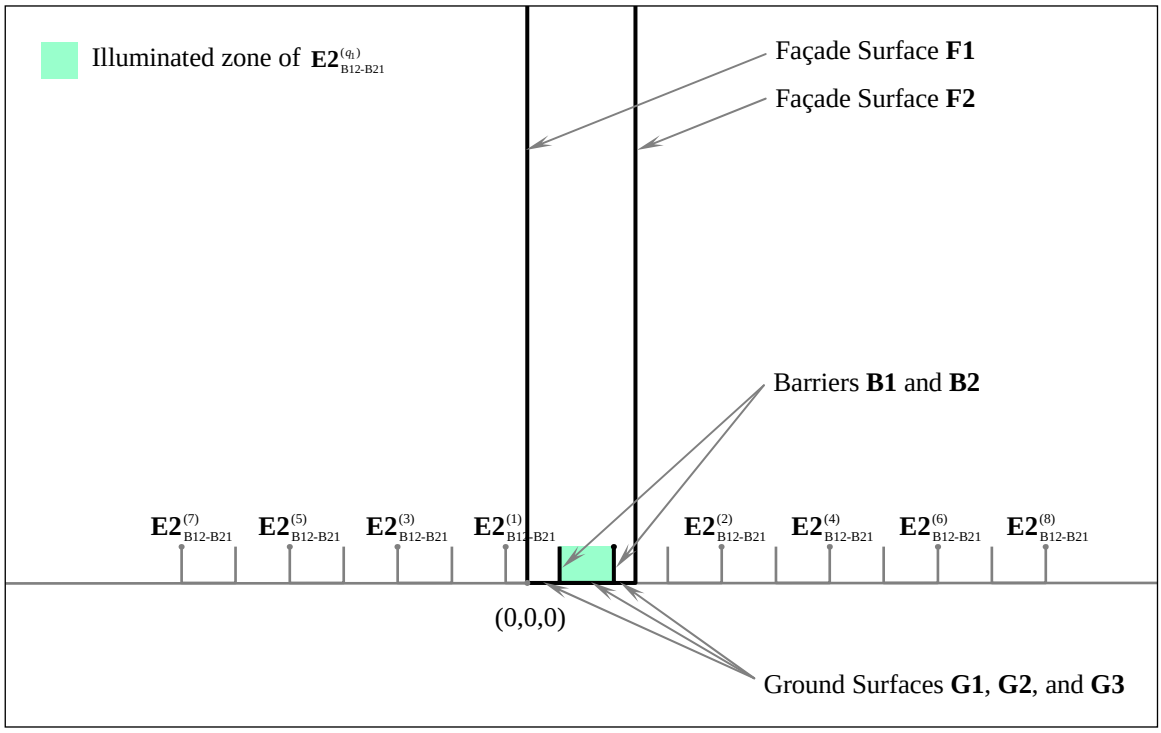

Figure A.32 Illustration of the secondary contribution from image sources $\mathbf{E2}^{(q_1)}_{\text{B12-B21}}$, where $q_1 = 1,2,3,\cdots$. The illuminated receivers should be located between the two barriers **B1** and **B2** and have a height lower than H.

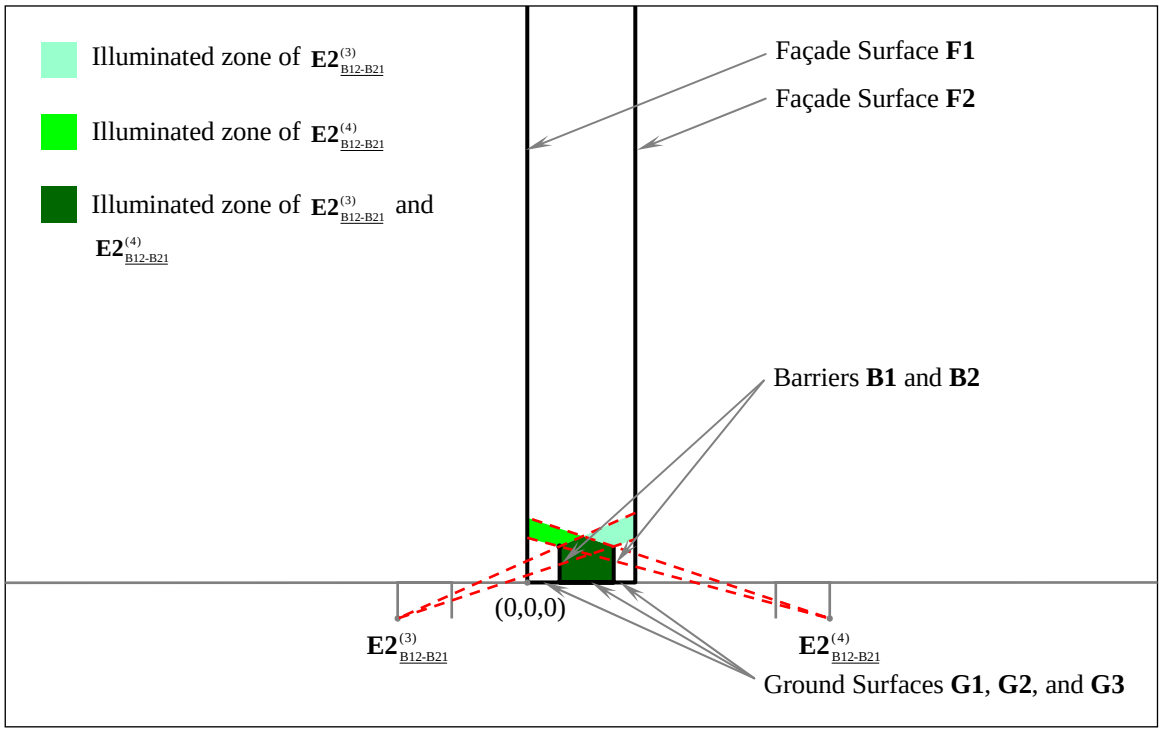

Figure A.33 Illustration of the secondary contribution from image sources $\mathbf{E2}^{(q_1)}_{\underline{\text{B12-B21}}}$, where $q_1 = 1,2,3,\cdots$. For the $\mathbf{E2}^{(q_1)}_{\underline{\text{B12-B21}}}$ with odd q_1, the lines connecting the illuminated receivers with $\mathbf{E2}^{(q_1)}_{\underline{\text{B12-B21}}}$ should have an intersection with the line from $(L_1,0,-H)$ to $(L_1,0,H)$ and have no intersection with the line from $(L_1+W,0,-H)$ to $(L_1+W,0,H)$. For the $\mathbf{E2}^{(q_1)}_{\underline{\text{B12-B21}}}$ with even q_1, the lines connecting the illuminated receivers with $\mathbf{E2}^{(q_1)}_{\underline{\text{B12-B21}}}$ should have no intersection with the line from $(L_1,0,-H)$ to $(L_1,0,H)$ and have an intersection with the line from $(L_1+W,0,-H)$ to $(L_1+W,0,H)$.

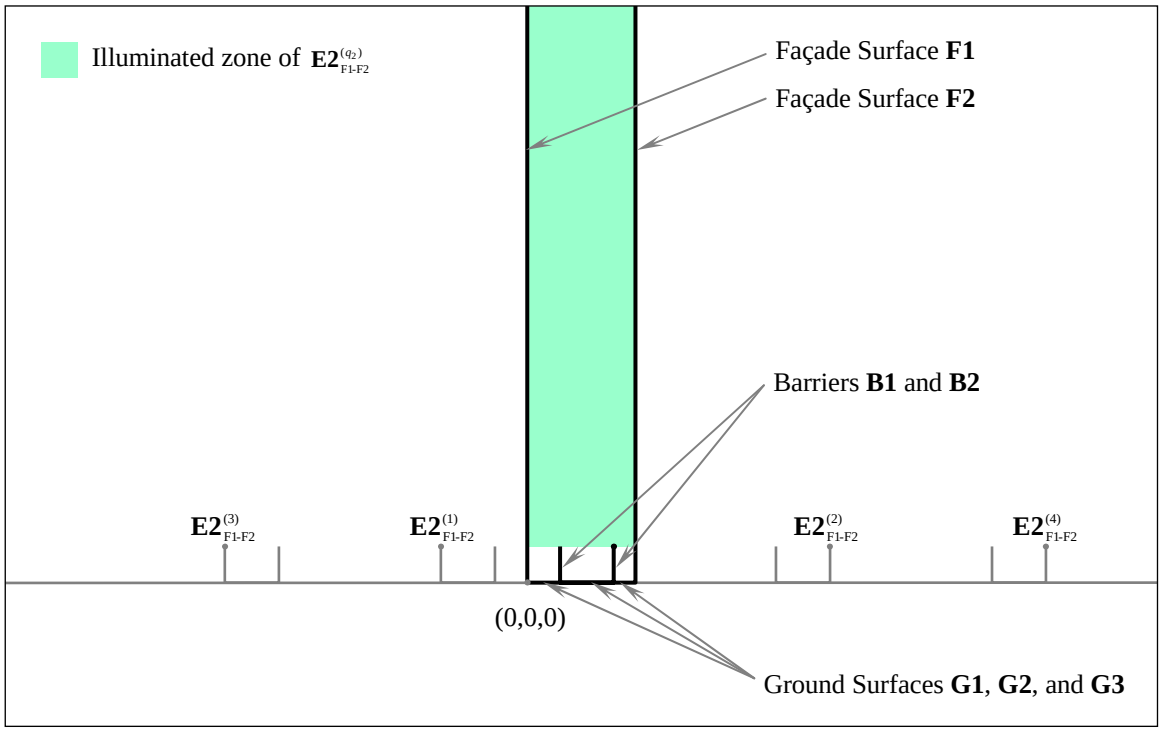

Figure A.34 Illustration of the secondary contribution from image sources $\mathbf{E2}^{(q_2)}_{\text{F1-F2}}$, where $q_2 = 1,2,3,\cdots$. The illuminated receivers should have a height higher than H.

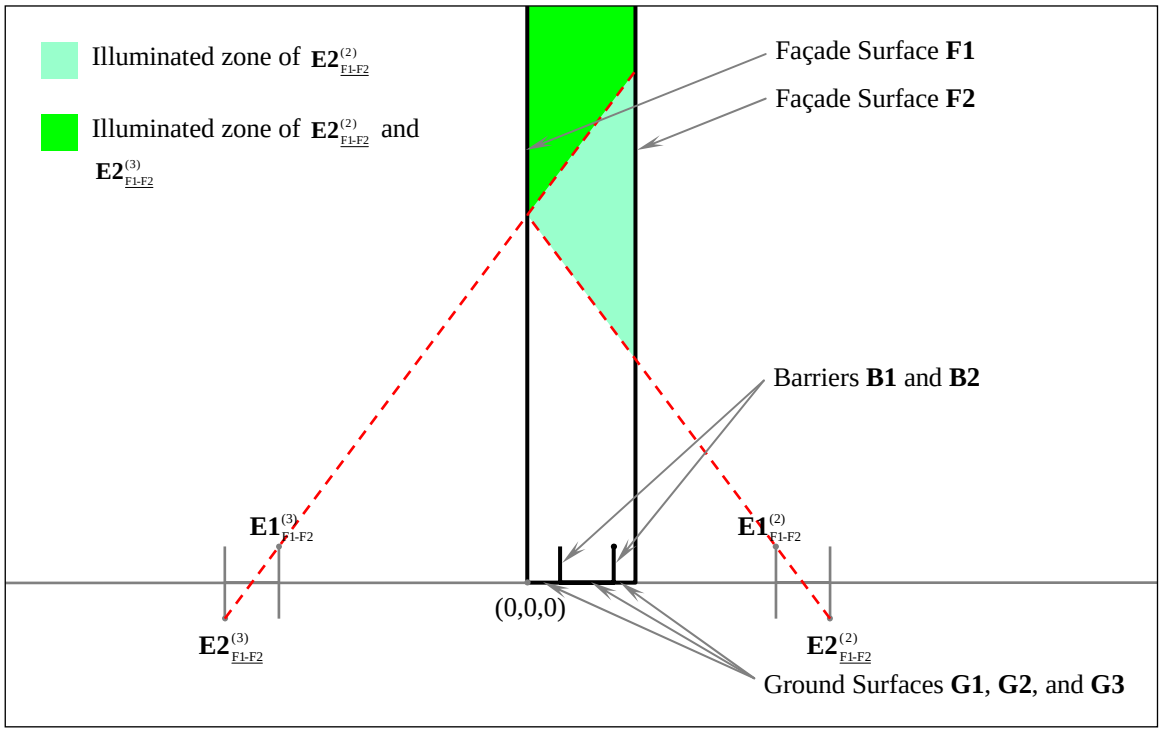

Figure A.35 Illustration of the secondary contribution from image sources $\mathbf{E2}^{(q_2)}_{\underline{\text{F1–F2}}}$, where $q_2 = 1,2,3,\cdots$. The lines connecting the illuminated receivers with $\mathbf{E2}^{(q_2)}_{\underline{\text{F1–F2}}}$ should have no intersection with the line from $\left(x^{(q_2)}_{\text{E1-F1-F2}},0,-H\right)$ to $\left(x^{(q_2)}_{\text{E1-F1-F2}},0,H\right)$.

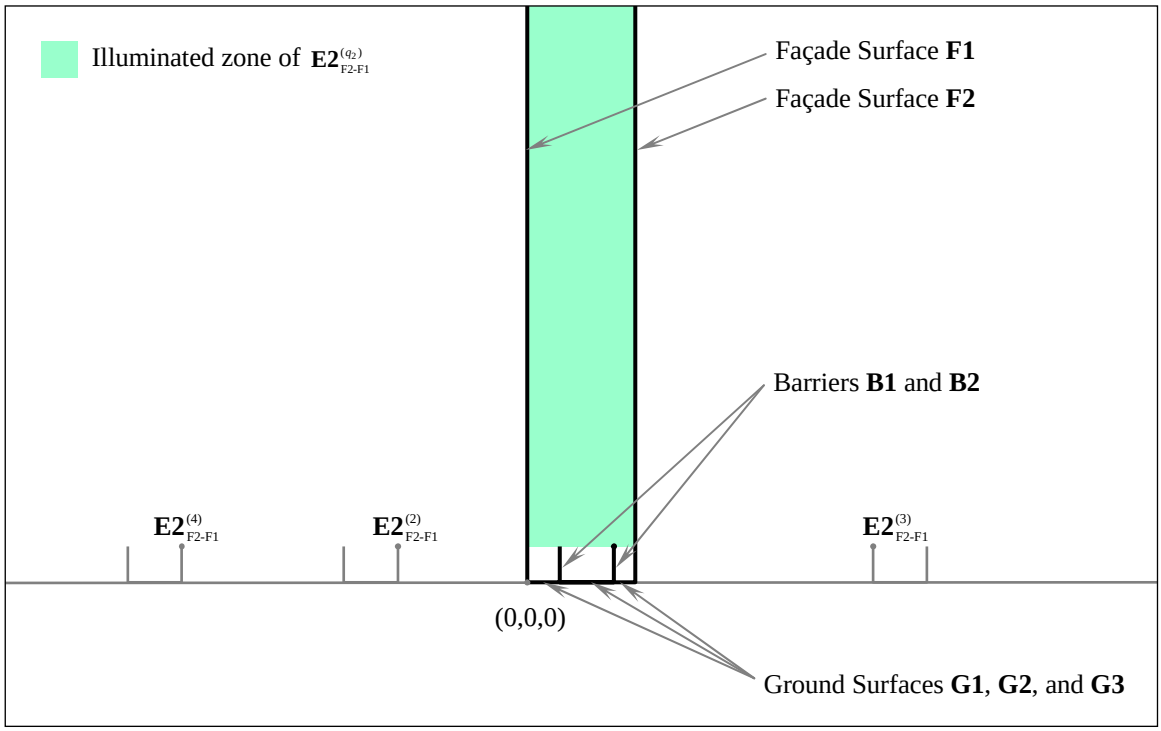

Figure A.36 Illustration of the secondary contribution from image sources $\mathbf{E2}^{(q_2)}_{\text{F2-F1}}$, where $q_2 = 2,3,4,\cdots$. The starting number of reflection is 2 to avoid duplication with $\mathbf{E2}^{(1)}_{\text{F2-B22}}$. The illuminated receiver should have a height higher than H.

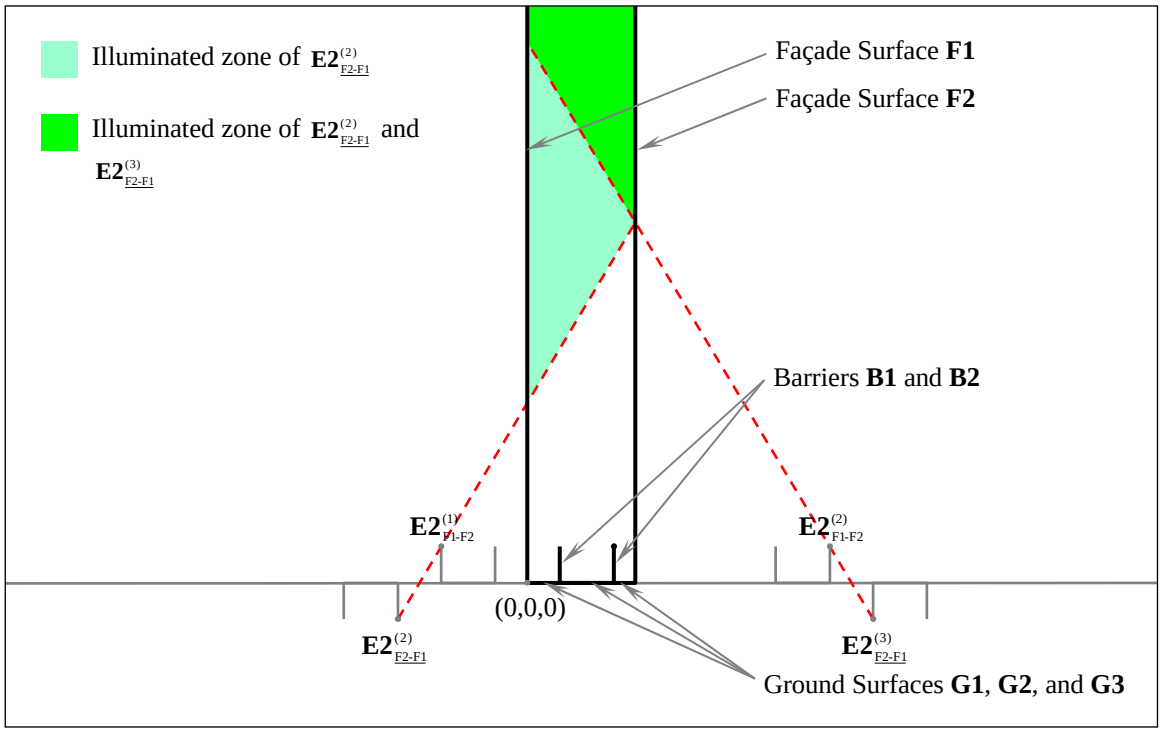

Figure A.37 Illustration of the secondary contribution from image sources $\mathbf{E2}^{(q_2)}_{\underline{\text{F2-F1}}}$, where $q_2 = 2,3,4,\cdots$. The starting number of reflection is 2 to avoid duplication with $\mathbf{E2}^{(1)}_{\underline{\text{F2-B22}}}$. The lines connecting the illuminated receivers with $\mathbf{E2}^{(q_2)}_{\underline{\text{F2-F1}}}$ should have no intersection with the line connecting $\left(x^{(q_2-1)}_{\text{E2-F1-F2}},0,-H\right)$ and $\left(x^{(q_2-1)}_{\text{E2-F1-F2}},0,H\right)$.

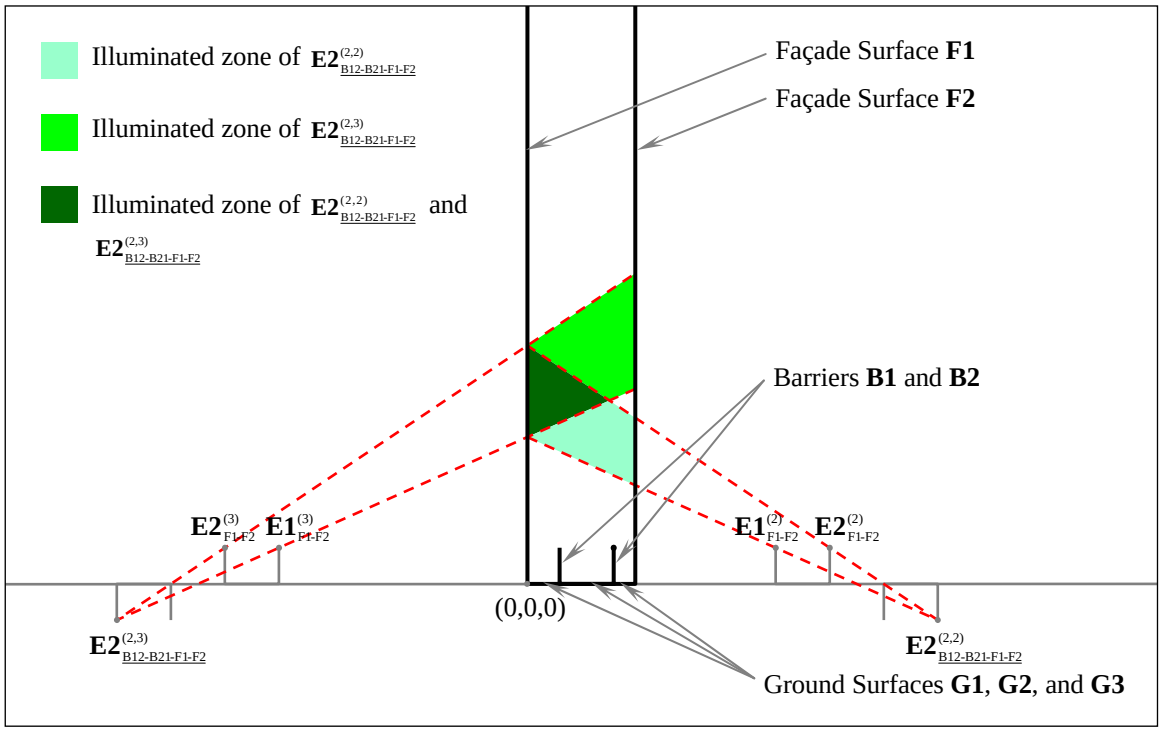

Figure A.38 Illustration of the secondary contribution from image sources $\mathbf{E2}^{(q_1,q_2)}_{\text{B12-B21-F1-F2}}$, where $q_1 = 2,4,6,\cdots$ and $q_2 = 1,2,3,\cdots$. The lines connecting the illuminated receivers with $\mathbf{E2}^{(q_1,q_2)}_{\text{B12-B21-F1-F2}}$ should have no intersection with the line from $\left(x^{(q_2)}_{\text{E1-F1-F2}},0,-H\right)$ to $\left(x^{(q_2)}_{\text{E1-F1-F2}},0,H\right)$ and have an intersection with the line from $\left(x^{(q_2)}_{\text{E2-F1-F2}},0,-H\right)$ to $\left(x^{(q_2)}_{\text{E2-F1-F2}},0,H\right)$.

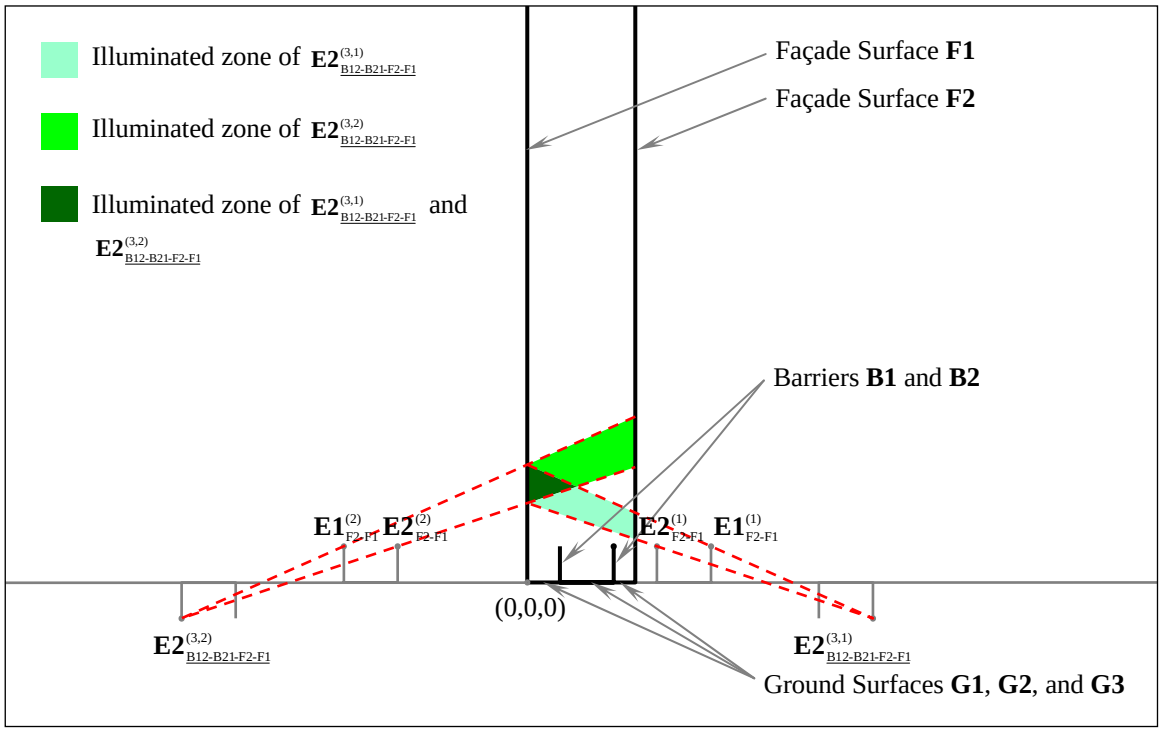

Figure A.39 Illustration of the secondary contribution from image sources $\mathbf{E2}^{(q_1,q_2)}_{\text{B12-B21-F2-F1}}$ where $q_1 = 1,3,5,\cdots$ and $q_2 = 1,2,3,\cdots$. The lines connecting the illuminated receivers with $\mathbf{E2}^{(q_1,q_2)}_{\text{B12-B21-F2-F1}}$ should have an intersection with the line from $\left(x^{(q_2)}_{\text{E1-F2-F1}},0,-H\right)$ to $\left(x^{(q_2)}_{\text{E1-F2-F1}},0,H\right)$ and have no intersection with the line from $\left(x^{(q_2)}_{\text{E2-F2-F1}},0,-H\right)$ to $\left(x^{(q_2)}_{\text{E2-F2-F1}},0,H\right)$.

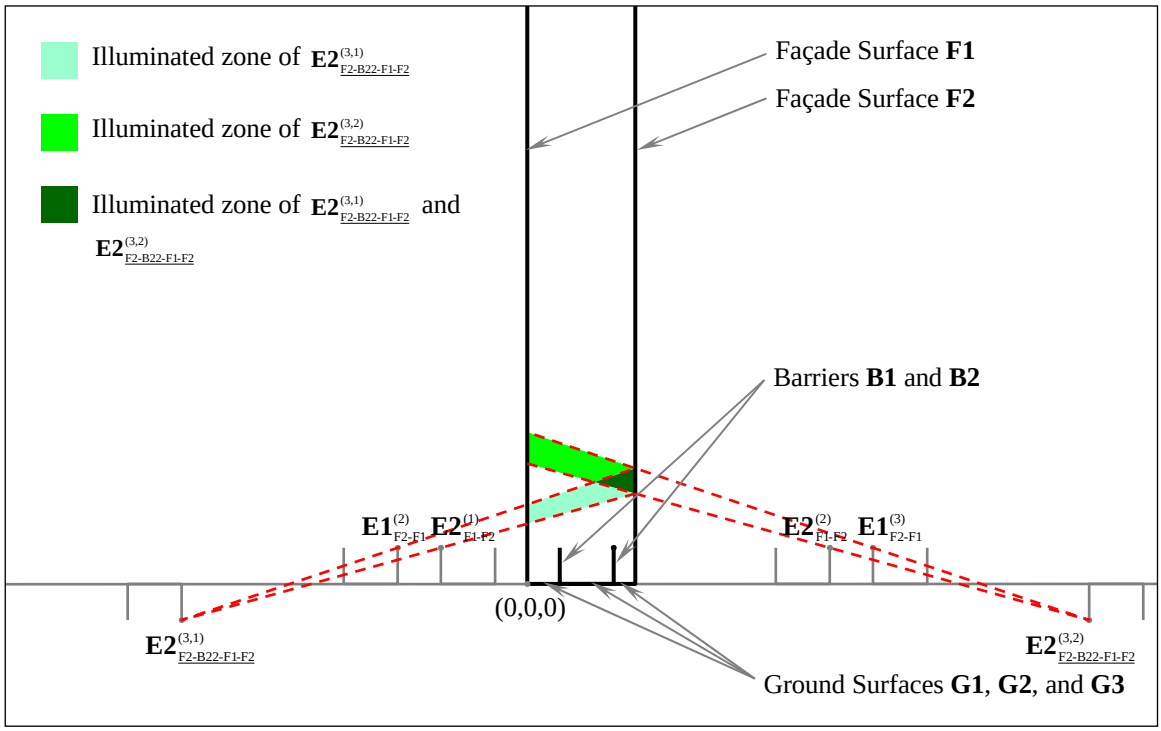

Figure A.40 Illustration of the secondary contribution from image sources $\mathbf{E2}^{(q_1,q_2)}_{\text{F2-B22-F1-F2}}$, where $q_1 = 3,5,7,\cdots$ and $q_2 = 1,2,3,\cdots$. Note that q_1 starts from 3 as $\mathbf{E2}^{(1,q_2)}_{\text{F2-B22-F1-F2}}$ is already considered as $\mathbf{E2}^{(q_2+1)}_{\text{F2-B22}}$. The lines connecting the illuminated receivers with $\mathbf{E2}^{(q_1,q_2)}_{\text{F2-B22-F1-F2}}$ should have no intersection with the line from $\left(x^{(q_2)}_{\text{E2-F1-F2}},0,-H\right)$ to $\left(x^{(q_2)}_{\text{E2-F1-F2}},0,H\right)$ and have an intersection with the line from $\left(x^{(q_2+1)}_{\text{E2-F2-F1}},0,-H\right)$ to $\left(x^{(q_2+1)}_{\text{E2-F2-F1}},0,H\right)$.

References

1. Abramowitz M. and Stegun I. A., “Handbook of Mathematical Functions, with Formulas, Graphs, and mathematical Tables,” New York, Wiley, pp. 890, (1972)
2. Allard J. F. and Sieben B., “Measurements of acoustic impedance in a free field with two microphones and a spectrum analyer,” J. Acoust. Soc. Am. 77(4), 1617-1618, (1985).
3. Allard J. F., Champoux Y., “In situ two-microphone technique for the measurement of the acoustic surface impedance of materials,” Noise. Con Eng. J., 31, 15-23, (1989).
4. Allard J. F., Gareton V., Henry M., Jansens G., and Lauriks W., “Impedance evaluation from pressure measurements near grazing incidence for nonlocally reacting porous layers,” Acust. Acta Acust., 89, 595-603, (2003).
5. Allard J. F., Henry M., Gareton V., Jansens J., and Lauriks W., “Impedance measurement around grazing incidence for nonlocally reacting thin porous layers,” J. Acoust. Soc. Am., 113(3), 1210-1215, (2003).
6. ASTM C384-04, Standard Test Method for Impedance and Absorption of Acoustical Materials by Impedance Tube Method, 2004
7. ASTM C423-02A, Standard Test Method for Sound Absorption and Sound Absorption Coefficients by the Reverberation Room Method, 2003
8. Attenborough K., Hayek S. I., and Lawther J.M., “Propagation of sound above a porous half-space,” J. Acoust. Soc. Am., 68(5), 1493-1501, (1980).
9. Attenborough K., “Acoustical characteristics of rigid fibrous absorbents and grannular materials,” J. Acoust. Soc. Am., 73(3), 785-799, (1983).

10. Attenborough K., “Review of ground effects on outdoor sound propagation from continuous broadband sources,” Appl. Acoust., 24, 289-319, (1988).

11. Attenborough K., “Ground parameter information for propagation modeling,” J. Acoust. Soc. Am., 92(1), 418-427 (1992). See also: Raspet R. and Attenborough K., “Erratum: ground parameter information for propagation modeling,” J. Acoust. Soc. Am., 92(5), 3007, (1992).

12. Attenborough K. and Waters-Fuller T., “Effective impedance of rough porous ground surfaces,” J. Acoust. Soc. Am., 108(3), 949-956, (2000).

13. Attenborough K. and Boulanger P., “Template and Direct Measurements of Ground Impedance,” ICA conference proceedings (2004).

14. Attenborough K., “Ground Impedance Models: A Review,” ICA conference proceedings, (2004).

15. Blumrich R. and Altmann J., “Ground Impedance Measurement Over a Range of 20 m,” Acust. Acta Acust., 85, 691-700, (1999).

16. Boulanger P. and Attenborough K., “Effective impedance spectra for predicting rough sea effects on atmospheric impulsive sounds,” J. Acoust. Soc. Am., 117(2), 751-762, (2005).

17. Boulanger P., Attenborough K., and Qin Q., “Effective impedance of surfaces with porous roughness: Models and data,” J. Acoust. Soc. Am., 117(3), 1146-1156, (2005).

18. Bowman J. J., Senior T. B. A., and Uslenghi P. L. E., “Electromagnetic and acoustic scattering by simple shapes,” North-Holland, Amsterdam, 29, (1969).

19. Brazier-Smith P. R. and Scott J. F. M., “On the determination of the roots of dispersion equations by use of winding number integrals,” J. Sound Vib., 145(3), 503-510, (1991).

20. BS 1793-5, Road traffic noise reducing devices — Test method for determining the acoustic performance — Part 5: Intrinsic characteristics — In situ values of sound reflection and airborne sound insulation, 2003

21. Carslaw H. S., “Some multiform solutions of the partial differential equations of physical mathematics and their applications,” Proc. London Math. Soc., 30, 121-161, (1899).

22. Carslaw H. S., “Diffraction of waves by a wedge of any angle,” Proc. London Math. Soc., 18, 1291-1306, (1920).

23. Chandler-Wilde S. N. and Hothersall D. C., “Sound propagation above an inhomogeneous impedance plane,” J. Sound Vib., 98(4), 475-491, (1985).

24. Cheng W. F. and Ng C. F., “The acoustic performance of an inclined barrier for high-rise residents,” J. Sound Vib., 242, 295-308, (2001).

25. Chessell C. I., “Propagation of noise along a finite impedance boundary,” J. Acoust. Soc. Am., 62(4), 825-834, (1977).

26. Chew C. H., “Prediction of traffic noise from expressways -Part II : Building flanking both sides of expressways,” Appl. Acoust., 32, 61- 72, (1991).

27. Chien C. F. and Soroka W. W., “A note on the calculation of sound propagation along an impedance surface,” J. Sound Vib., 69(2), 340-343, (1980).

28. Chien C. F. and Soroka W. W., “Sound propagation along an impedance plane,” J. Sound Vib., 43(1), 9-20, (1975).

29. Copson E. T., “On an integral equation arising in the theory of diffraction,” Quart. J. Math., 17, 19-34, (1946).

30. Crighton D. G., Williams J. E., Dowling A. P., Heckl M. A., and Leppington F. A., “Modern methods in analytical acoustics: lecture notes,” Springer-Verlag, (1996).

31. Daigle G. A., Nicolas J., and Berry J.-L., “Propagation of noise above ground having an impedance discontinuity,” J. Acoust. Soc. Am., 77(1), 127-138, (1985).

32. Davies H. G., “Multiple-reflection diffuse-scattering model for noise propagation in streets,” Acoust. Soc. Am., 64(3), 517-521, (1978).

33. Davies J. C., Mulholland K. A., “An impulse method of measuring normal impedance at oblique incidence,” J. Sound Vib., 67, 135-149, (1979).

34. Delany M. E. and Bazley E. N., “Acoustical properties of fibrous absorbent materials,” Appl. Acoust., 3, 105-116, (1970).

35. Delany M. E., “Sound propagation in the atmosphere: a historical review,” Acustica 38, 201-223, (1977).

36. Embleton T. F. W., “Line integral theory of barrier attenuation in the presence of the ground,” J. Acoust. Soc. Am, 67(1), 42-45, (1980).

37. Embleton T. F. W., “Tutorial on sound propagation outdoors,” J. Acoust. Soc. Am., 100(1), 31-48, (1996).

38. Fleming G. and Rickley E., “Parallel barrier effectiveness under free-flowing traffic conditions,” US federal highway administration, Report FHWA-RD-92-068, McLean, V A, USA, (1992).

39. Garai M., “Measurement of the sound absorption coefficient in situ, the reflex method using periodic pseudo random sequences of maximum length,” Appl. Acoust., 39, 119-139, (1993).

40. Godinho L., Antonio J. and Tadeu A., “3D sound scattering by rigid barriers in the vicinity of tall buildings,” Appl. Acoust., 62, 1229-1248, (2001).

41. Hadden W. J. and Pierce A. D., “Plane wave diffraction by a wedge with finite impedance,” J. Acoust. Soc. Am., 63 (1), 17-27, (1978).

42. Hadden W. J. and Pierce A. D., “Sound diffraction around screens and wedges for arbitrary point-source locations”, J. Acoust. Soc. Am., 69 (5), 1266-1276, (1981). See also: Hadden W. J. and Pierce A. D., “Erratum: Sound diffraction around screens and wedges for arbitrary point-source locations,” J. Acoust. Soc. Am., 71(5), 1290, (1982).

43. Hajek J. I., “Performance of parallel noise barrier Yonge Street to Bayview Avenue,” Ontario Ministry of Transportation and Communication, Ottawa, (1980).

44. Halliwell R. E., “Field performance of parallel barriers,” Canadian Acoust., 10, 9-18, (1980).

45. Hothersall D. C., Chandler-Wilde S. N., and Hajmirzae M. N., “Efficiency of single noise barriers,” J. Sound Vib., 146(2), 303-322, (1991).

46. Hothersall D. C., Crombie D. H. and Chandler-Wilde S. N., “The performance of T-profile and associated noise barriers,” Appl. Acoust., 32, 269-287, (1991).

47. Hurst C. J., “Sound transmission between absorbing parallel planes,” J. Acoust. Soc. Am., 67(1), 206-213, (1980).

48. Hutchins D. A. and Pitcarn D, “A laser study of multiple reflections within parallel noise barriers,” J. Acoust. Soc. Am., 73(6), 2216-2218, (1983).

49. Hutchins D. A., Jones H. W., Paterson B., and Russell L. T., “Studies of parallel barrier performance by acoustical modeling,” J. Acoust. Soc. Am., 77(2), 536-546, (1985).

50. Ingard U., “On the reflection of a spherical sound wave from a finite plane,” J. Acoust. Soc. Am., 23(3), 329-335, (1951).

51. Ingard U., Bolt R. H., “A Free field method of measuring the absorption coefficient of acoustic materials,” J. Acoust. Soc. of Am., 25(3), 509-516, (1951).

52. Isei T., “Absorptive noise barrier on finite impedance ground,” J. Acoust. Soc. Jpn. (E), 1, 3-10, (1980).

53. Isei T., Embleton T. F. W. And Piercy J. E., “Noise reduction by barriers on finite impedance ground,” J. Acoust. Soc. Am., 67(1), 46-58, (1980).

54. ISO 10534-1, Acoustics — Determination of sound absorption coefficient and impedance in impedance tubes — Part 1: Method using standing wave ratio, 2001

55. ISO 10534-2, Acoustics — Determination of sound absorption coefficient and impedance in impedance tubes — Part 2: Transfer-function method, 2001

56. ISO 354, Acoustics — Measurement of sound absorption in a reverberation room, 2003

57. Janczur R., Walerian E. and Czecnowicz M., “Sound levels forecasting for city-centers. Part III: A road lane structure influence on sound level within urban canyon,” Appl. Acoust., 62, 493-513, (2001).

58. Janczur R., Walerian E. and Czecnowicz M., “Sound levels forecasting for city-centers Part IV. Vehicles stream parameters influence on sound level distribution within a canyon street,” Appl. Acoust., 62, 645-664, (2001).

59. Johnasson H. G., “Sound reduction by barriers on the ground,” J. Sound Vib., 22(1), 113-126, (1972).

60. Kawai T., Hidaka T. and Nakajima T., “Sound propagation above an impedance boundary,” J. Sound Vib., 83(1), 125-138, (1982).

61. Keller J. B., “Diffraction by an aperture,” J. Appl. Phys., 28, 426-444, (1957).

62. Keller J. B., “The geometrical theory of diffraction,” J. Opt. Soc., 52, 116-130, (1962).

63. Kwok M. P., Li K. M., Tang S. H., and Frommer G. H., “Acoustic performance of parallel barriers in urban environments,” Proc. Inter-Noise 2003, 1802-1809, (2003)

64. Koers P., “Diffraction by an absorbing barrier or by an impedance transition,” Proc. INTER-NOISE 83, 311-314, (1983).

65. Kurze U. J. and Anderson G. S., “Sound attenuation by barriers,” Appl. Acoust., 4, 35-53, (1971).

66. Kurze U. J., “Noise reduction by barriers,” J. Acoust. Soc. Am., 55(3), 504-518, (1974).

67. Lam Y. W., “Using Maekawa's chart to calculate finite length barrier insertion loss,” Appl. Acoust., 42, 29-40, (1994).

68. Lawhead R. B. and Rudnick I., “Acoustic wave propagation along a constant normal impedance boundary,” J. Acoust. Soc. Am., 23(5), 546-549, (1951).

69. Levine H. and Schwinger J., “On the theory of diffraction by an aperture in an infinite plane screen. I,” Phys. Rev., 74, 958-974, (1948).

70. Levine H. and Schwinger J., “On the theory of diffraction by an aperture in an infinite plane screen. II,” Phys. Rev. 75, 1423-1432, (1949).

71. Li J. F. and Pascal J. C., “The Influence of Microphone Vents on Measurements of Acoustic Intensity and Impedance,” J. Acoust. Soc. Am. 99(2), 969-978, (1996).

72. Li J. F. and Hodgson M., “Use of pseudo-random sequences and a single microphone to measure surface impedance at oblique incidence,” J. Acoust. Soc. Am. 102(4), 2200-2210, (1997).

73. Li K. M., Waters-Fuller T., and Attenborough K., “Sound propagation from a point source over extended-reaction ground,” J. Acoust. Soc. Am., 104(2), 679-685, (1998).

74. Li K. M. and Tang S. H., “The predicted barrier effects in the proximity of tall buildings,” J. Acoust. Soc. of Am., 114(2), 821-832, (2003).

75. Macdonald H. M., “A class of diffraction problems,” Proc. London Math. Soc., 14, 410-427, (1915).

76. Maekawa Z., “Noise reduction by screens,” Appl. Acoust., 1, 157-173, (1968).

77. Menounou P., “A correction to Maekawa’s curve for the insertion loss behind barriers,” J. Acoust. Soc. Am., 110 (4), 1828-1838, (2001).

78. Miki Y., “Acoustical properties of porous materials -modification of Delany-Bazley models,” J. Acoust. Soc. Jpn.(E), 11, 19-24, (1990).

79. Mommertz E., “Angle dependant in situ measurement of the complex reflection coefficient using a subtraction technique,” Appl. Acoust., 46, 251-263, (1995).

80. Morgan P. A., Hothersall D. C., and Chandler-Wilde S. N., “Influence of shape and absorbing surface - a numerical study of railway noise barriers,” J. Sound Vib., 217(3), 405-417, (1998).

81. Muradali A. and Fyfe K. R., “A study of 2D and 3D barrier insertion loss using improved diffraction-based methods,” Appl. Acoust., 53, 49-75, (1998).

82. Nelson P. M., Abbott P. G. and Saridge C., “Acoustic performance of the M6 noise barriers,” Transport Research Laboratory Report, LR 731, Crowthorne, UK, (1976).

83. Nicolas J., Embleton T. F. W. and Piercy J. E., “Precise model measurements versus theoretical prediction of barrier insertion loss in presence of the ground,” J. Acoust. Soc. Am., 73(1), 44-54, (1983).

84. Nicolas J. and Berry J. L., “Propagation of sound above a finite layer of snow,” J. Acoust. Soc. Am., 77, 67-73, (1985).

85. Nobile M. A. and Hayek S. I., “Acoustic Propagation Over an Impedance Plane,” J. Acoust. Soc. Am. 78(4), 1325-1336, (1985).

86. Nocke C., Mellert V., Waters-Fuller T., Attenborough K, Li K. M., “Impedance deduction from broadband, point-source measurements at grazing incidence,” Acta Acustica, 82, 1085-1090, (1997).

87. Nocke C., “Improved impedance deduction from measurement near grazing incidence,” Acust. Acta Acust., 85, 586-590, (1999).

88. Nocke C., “In-situ acoustic impedance measurement using a free-field transfer function method,” Appl. Acoust., 59, 253-264, (2000).

89. Panneton R., L 'Esperance A., Nicolas J. and Daigle G. A., “Development and validation of a model predicting the performance of hard or absorbent parallel noise barriers,” J. Acoust. Soc. Jpn. (E), 14, 251-258, (1993).

90. Pierce A. D., “Diffraction of sound around corners and over wide barriers”, J. Acoust. Soc. Am., 55 (5), 941-955, (1974).

91. Piercy J. E., Embleton T. F. W. and Sutherland L. C., “Review of noise propagation in the atmosphere,” J. Acoust. Soc. Am., 61(6), 1403-1416, (1977).

92. Pirinchieva R. K., “Model study of sound propagation over ground of finite impedance,” J. Acoust. Soc. Am., 90 (5), 2678-2682, (1991).

93. Press W. H., “Numerical recipes in FORTRAN: the art of scientific computing,” Cambridge University Press, 1992.

94. Pyett J. S., “The Acoustic Impedance of a Porous Layer at Oblique Incidence,” Acust. Acta Acust., 3, 375-382, (1953).

95. Rathe E. J., “Note on two common problems of sound propagation,” J. Sound Vib., 10,472-479, (1969).

96. Redfearn S. W., “Some acoustical source-observer problems,” Phil. Mag., 30, 223-236, (1940).

97. Rubinowicz A., “Die Beugungswelle in der Kirchhoffschen theorie der beugungserscheinungen,” Annalen de Physik, 53, 257-278 (1917).

98. Rudnick I., “The propagation of an acoustic wave along a boundary”, J. Acoust. Soc. Am., 19(2), 348-356, (1947).

99. Sakurai Y., Walerian E. and Morimoto H., “Noise barrier for a building façade,” J. Acoust. Soc. Jpn. (E), 11, 257-265, (1990).

100. Salomons E. M., Geerlings A. C. and Duhamel D.; “Comparison of a ray model and a Fourier-boundary element method for traffic noise situations with multiple diffractions and reflections,” Acustica, 83, 35-47, (1997).

101. Salomons E. M., “Sound Propagation in Complex Outdoor Situations with a Non-Refracting Atmosphere: Model Based on Analytical Solutions for Diffractions and Reflections,” Acustica, 83, 436-454, (1997).

102. Scholes W. E., Salvidge A. C. and Sargent J. W., “Field performance of a noise barrier,” J. Sound Vib., 16, 627-642, (1971).

103. Slutsky S and Bertoni H, “Analysis and programs for assessment of absorptive and tilted barriers,” Transportation Research Record 1176, Washington, (1988).

104. Sommerfeld A, “Mathematische theorie der diffraction,” Math. Ann., 47, 317-374, (1896).

105. Sutherland L. C. and Daigle G. A., “Atmospheric Sound Propagation,” in Handbook of acoustics edited by Crocker M. J., John Wiley & Son, New York, 305-329, (1998).

106. Taherzadeh S., Attenborough K., “Deduction of ground impedance from measurements of excess attenuation spectra,” J. Acoust. Soc. of Am., 105(3), 2039-2042, (1999).

107. Tamura M., “Spatial Fourier transform method of measuring reflection coefficients at oblique incidence. I: theory and numerical examples,” J. Acoust. Soc. of Am., 88(5), 2259-2264, (1990).

108. Tamura M, Allard J. F. , Lafarge D., “Spatial Fourier transform method for measuring reflection coefficients at oblique incidence. II: experimental results,” J. Acoust. Soc. of Am., 97(4), 2255-2262, (1995).

109. Thomasson S. I., “Reflection of waves from a point source by an impedance boundary,” J. Acoust. Soc. Am., 59(4), 780-785, (1976).

110. Thomasson S. I., “Sound-propagation above a layer with a large refraction,” J. Acoust. Soc. Am., 61(3), 659-674, (1977).

111. Thomasson S. I., “Diffraction by a screen above an impedance boundary”, J. Acoust. Soc. Am., 63(6), 1768-1781, (1978).

112. Tolstoy I., “Diffraction by a hard truncated wedge and a Strip,” IEEE Journal of Ocean Engineering, 14(1), 4-16, (1989).

113. Tolstoy I., “Exact, explicit solutions for diffraction by hard sound barriers and seamounts,” J. Acoust. Soc. Am., 85(2), 661-669, (1989).

114. Walerian E. and Janczur R., “Acoustical field in a space with obstacles. Part II: Propagation between buildings,” Acustica, 78, 210-219, (1993).

115. Walerian E., Czechowicz M. and Janczur R., “Barriers’ Efficiency Dependence on Types of Environments,” Appl. Acoust., 44, 291-324, (1995).

116. Walerian E., Janczur R. and Czechowicz M., “The effectiveness of screens in an urban area,”, Appl. Acoust., 58, 153-172, (1999).

117. Walerian E., Janczur R. and Czechowicz M., “Sound levels forecasting for city-centers. Part I: Sound level dueto,aroad within an urban canyon,” Appl. Acoust., 62, 359-380, (2001).

118. Walerian E., Janczur R. and Czechowicz M., “Sound levels forecasting for city-centers. Part II: Effect of source model parameters on sound level in built-up area,” Appl. Acoust., 62, 461-492, (2001).

119. Watts G. R., “Acoustic performance of parallel traffic noise barriers,” Appl. Acoust., 47, 95-119, (1996).

120. Wenzel A. R., “Propagation of waves along an impedance boundary,” J. Acoust. Soc. Am., 55(5), 956-963, (1974).

121. Wilms U. and Heinz R., “In-situ Messung komplexer Reflexionfaktoren von Wandflächen,” Acustica, 75, 28-39, (1991).

122. Yusawa M., “A method of obtaining the oblique incident reflection coefficient through an on the spot measurement,” Appl. Acoust., 8, 27-41, (1975).